Department of Information Engineering, Electronics and Telecommunications (D.I.E.T.)

PhD in Mathematical Models for Engineering, Electromagnetics and Nanosciences
XXX cycle

SAPIENZA
UNIVERSITÀ DI ROMA

Metamaterial, Nanophotonic and Plasmonic components for applications in Integrated Optics

Badrul Alam

Supervisors: Prof F. Frezza
Dr. A. Benedetti

Rome, Italy, 2017

To all who believed in me

Acknowledgments

These years as PhD student have been quite stormy; I am happy to have been able to navigate everything in the correct way, and I am very proud of my activity. Despite the difficulties, at the end of my studentship I emerge tougher in personality, and professionally more skilled and articulate. This was thanks to the support of many persons, who I wish to thank.

First of all, I wish to thank **Dr. Andrea Veroli** and **Dr. Alessio Benedetti**, respectively my colleague and my mentor, who are also my close friends; we handled various projects together, and I could always count on their competence and professionality; our work together was stimulating and also fun.

Many thanks also to **Maria Denise Astorino**, **Alessio Buzzin**, **Emilija Petronijevic**, **Dr. Marco Muzi** and **Dr. Pietro Monsurrò** for the good times together and the warm climate at the offices.

I wish to thank **Prof. Daniele Andreucci, Prof.ssa Paola Loreti** and **Prof. Luigi Palumbo** for the support and guidance they gave to all PhD student, and thanks to **Prof. Fabrizio Frezza** for including me into his group.

I'd like to express my gratitude also to **Prof. Pierre Berini** from University of Ottawa for believing in my projects, and for giving me access to the resources to develop them; into his group I could avail from the expertise of **Dr. Ewa Lisicka-Shzek** and **Howard Northfield**, as well as **Prof. Sun Xiaoqiang** from Jilin University. Special thanks go also to **Dr. Luca Maiolo** from CNR-Artov Roma, **Dr. Francesco Mura** from CNIS Sapienza, and **Dr. Lorenzo Dominici** from CNR-Nanotec for giving us access to their instruments and their expertise.

On a more general note, I wish to thank **my mother** and my relatives: uncle **Shiblee**, **Dalia** auntie and **Mala** auntie; having their backing reassured me when I was down, and helped me to not derail from the right path.

Introduction

We live in an era of great change, inside societies heavily reliant on technological innovation. We are now in the middle of the information revolution: the increasing amount of data created, processed, stored and moved, as well as the related technological platforms, are profoundly changing economy, markets, and industry structures. Scientific achievements from multiple disciplines, in particular in life sciences and physics, grow expectations on further revolutions.

In this framework, optical technologies are a major driving force in research, necessary not only to respond to the increasing demands from telecommunications and computation, but also for new areas of big interest and expectations such as biology, chemistry, medicine and metrology. A special role in this is expected from integrated optics, which aims to build optical devices by combining components such as waveguides, optical filters, modulators, amplifiers, lasers, photodetectors, etc [1]. Classical technologies to construct such optical elements are Silicon Photonics, InP or InGaAsP, and the "exotic" Photonics crystals [1]; although those achieved many interesting scientific results, and allowed to build some high-performance devices for telecommunications [2,3], the long-term goal of reaching the complexity of micro/nano electronics is yet to be fulfilled, because of limitations due to optical losses, incapacity to reduce dimensions under the wavelength, and impossibility to miniaturize some optical elements [1,4].

In the last two decades, three sub-disciplines of Integrated Optics that defy the aforementioned limitations, namely optical metamaterials, nanophotonics and plasmonics [5,6], have grown greatly thanks to the use of the fabrication tools and methods developed initially for electronic scaling, as well as the introduction of powerful computers on a mass scale; despite being researched ever since the '50s and '60s, and being considered as minor and exotic options until 15 years ago, the scientific feats they demonstrated in the last years make the scientists envision also

industrial success in various directions, in particular on intra/inter-chip-communication, computation and chemical/biological sensing.

Some devices are already established at an industrial level [7], but the core potential of those fields is still under research; in general, the components obtained from those technologies focus on one, or a combination, of the following effects: the particular physics of nanometric sizes [8,9], enhanced sensitivity of resonances [10], the possibility of localizing the electromagnetic field in small regions [11], the possibility to tailor specific non-conventional optical effects [12], and the possibility to integrate with other types of systems [13] in order to produce inexpensive and reusable measurement systems. The most popular and relevant topics of research are: subwavelength waveguides [14, 15], optical nanoantennas [16 – 18], elements for computation [9, 19], slow light [20], active elements, optical tweezers [21], superlenses [22, 23], optical invisibility cloaks [24, 25], hyperlenses [26, 27], planar magnifying hyperlens and light concentrators [28, 29]. While those are still at research level, most of them are moving away fast from the proof-of-principle stage towards that of mature applications [5].

Many potential devices have been presented in literature, and there are usually multiple technological solutions in the same topic (i.e. there are many types of waveguiding systems [30], or various possible geometries for circular dichroism sensors). Defining the best option for specific applications (choice between different configurations, parameters, physics) is also important, nowadays. Also, while research in those fields may be mature from a theoretical perspective (including analytical and computational tools), the synthesis into fabricated elements becomes sometimes challenging due not only to limitations of the technologies themselves, but also to the non-idealities of the fabrication processes; in this case, the boost of the sensibility of metamarerials, plasmonics and nanophotonics backfires, as the behavior of the devices may be significantly altered due to fickle working conditions and/or compromised repeatability. In order to design actual devices, it is important to take into account of this, which means an increase of computational complexity.

In this thesis I present my research activity as a PhD student, which is composed of a variety of projects concerning Metamaterials, Plasmonics and Nanophotonics for various types of application. My work was focused in numerical/analytical study of designed devices or experimental data, and in micro/nano-fabrication; I also handled measurements on some of the investigated structures, while others were operated

by collaborators. My main projects involve improved coupling method for intra-chip communication, and highly dichroic metasurfaces for potential applications as biosensors. My research includes also study on efficient edge coupling between fiber and plasmonic waveguides and strongly directional optical antenna. Most of my design efforts were focused on structures using surface plasmons, in particular LR-SPPs, since the related phenomena and structures offer great flexibility, and because many technological concepts may be imported from microwave devices, scaled down to micro/nanometers. As for fabrication, I have adopted a top-down approach for the construction of my devices.

Overall, the multidisciplinary aspect of these works was handled by managing feedbacks from each step, which quantitatively increased the complexity of the design process. Logistics was another difficulty that needed to be handled, since the many resources needed for fabrication and measurements required the collaboration with multiple institutions:

- **CNIS, Sapienza**, for access to Electron Beam Lithography machine;
- **University of Ottawa-SITE**, with the group of Prof. Berini, for the access to clean room with instrumentations focused on surface plasmons, as well as related expertise; in Canada I have been supported also by the expertise of prof. Sun from **Jilin University, China**.
- **CNR-ARTOV** for access to clean room;
- **CNR-IFN** for access to another EBL and evaporators;
- **DIET, Sapienza** (Department of Information Engineering, Electronics and Telecommunications) for logistic support;
- **CNR-Nanotech**, operated FIBID fabrication and optical measurements.
- **Department SBAI** for optical and photoacoustic measurements;

This thesis is organized as follows. Chapter 2 contains the fundamentals of plasmonics (with particular regard for long range surface plasmon polaritons), metamaterials, circular dichroism, fabrication tools. In chapter 3 I have presented a scheme for intra-chip communication by using multilayer optical routing through vertical directional couplers; it contains an analysis of vertical directional couplers (material from the paper [31] “Analysis on vertical directional couplers with long range surface plasmons for multilayer optical routing”), fabrication processes flow operated on a plasmonic signal bridging system, as well as schemes for measurements. Chapter 4 contains a numerical analysis on a strongly directional

optical antenna based on leaky wave antenna theory. In chapter 5 I have reported the results of the analysis on the circular dichroism of a metamaterial composed of an array of nano-helices, published as [32] “Precise detection of circular dichroism in a cluster of nano-helices by photoacoustic measurements”. In Chapter 6 a new planar geometry for dichroic filters (named “nano-beans”) is presented, with design, fabrication, and first measurements. Finally, in chapter 7 I will draw the conclusions of this work. In Appendix I have presented some content of interest of the projects that have been moved away from the chapters for the sake of readability, or some additional minor works: A1 contains the study of plasmonic chirped gratings, in A2 I have shown the analytical development of Green’s Tensor used in chapter 4, in A3 I have presented the fabrication processes required to build a nanoscopic sieve for the mechanical separation of cells within lab-on-chips, and in A4 I have presented the supplementary information of the numerical and analytical analysis done for the chapter 5.

References

[1] R. Hunsperger, “Integrated Optics”, Springer, (2009)

[2] R. Stabile, A. Albores-Mejia, A. Rohit, K.A. Williams, “Integrated optical switch matrices for packet data networks”, Microsyst. Nanoeng. 2, 15042 (2016).

[3] P.de Dobbelaere, Silicon Photonics: Applications and High volume Manufacturing Platform," Frontiers in Optics 2016, OSA technical digest, FF3E.1, (2016)

[4] J.Bowers, “Trends, Possibilities and Limitations of Silicon Photonic Integrated Circuits and Devices”, IEEE-CIC Conference, 13895732 (2013)

[5] C.E.Png, Y.Akimov, “Nanophotonics and Plasmonics: An Integrated View”, CRC Press (2017)

[6] F.Monticone, and A.Alù, “Metamaterial, plasmonic and nanophotonic devices”, Rep. Prog. Phys. (IOP Science) 80 036401, (2017)

[7] Y.Liu, Q.Liu, S.Chen, F.Cheng, H.Wang, and W.Peng, “Surface Plasmon Resonance Biosensor Based on Smart Phone Platforms”, Scientific Reports 5, 12864 (2015)

[8] T.G.Tiecke, J.D.Thompson, N.P.de Leon, L.R. Liu, V. Vuletić, and M.D.Lukin,

“Nanophotonic quantum phase switch with a single atom”, Nature, 508, 241–244, (2014)

[9] T.J.Davis, D.E.Gómez, A.Roberts, “Plasmonic circuits for manipulating optical information”, Nanophotonics, 6(3), 543–559, 2017

[10] H.H.Nguyen, J.Park, S.Kang, and M.Kim, “Surface Plasmon Resonance: A Versatile Technique for Biosensor Applications”, Sensors, 15(5), 10481-10510 (2015)

[11] S.A. Maier and H.A. Atwater, “Plasmonics: Localization and guiding of electromagnetic energy in metal/dielectric structures”, Journal of Applied Physics, 98, 011101 (2005)

[12] W.Cai, V.Shalaev, “Optical Metamaterials Fundamentals and Applications”, Springer (2010)

[13] O.Tokel, U.H.Yildiz, F.Inci, N. G.Durmus, O.O.Ekiz, B.Turker, C.Cetin, S.Rao, K.Sridhar, N.Natarajan, H.Shafiee, A.Dana, and U. Demircia, “Portable Microfluidic Integrated Plasmonic Platform for Pathogen Detection”, Scientific Reports, 5, 9152 (2015)

[14] S.A. Maier, P.G. Kik, H.A.Atwater, S.Meltzer, E.Harel, B.E.Koel, and A.A.G. Requicha, “Local detection of electromagnetic energy transport below the diffraction limit in metal nanoparticle plasmon waveguides” Nat. Mater.2, 229–232 (2003)

[15] S.I.Bozhevolnyi, V.S.Volkov, E.Devaux, J.-Y.Laluet, and T.W.Ebbesen, “Channel plasmon subwavelength waveguide components including interferometers and ring resonators”, Nature,440, 508–511 (2006)

[16] W.Rechberger, A.Hohenau, A.Leitner, J.R.Krenn, B.Lamprecht and F.R.Aussenegg, “Optical properties of two interacting gold nanoparticles”, Opt. Commun., 220, 137–141 (2003)

[17] D.P.Fromm, A.Sundaramurthy, P.J.Schuck, G.Kino, and W.E.Moerner, “Gap-dependent optical coupling of single "bowtie" nanoantennas resonant in the visible”, Nano Lett., 4, 957–961 (2004)

[18] T. Atay, J.H.Song, and A.V.Nurmikko, “Strongly Interacting Plasmon Nanoparticle Pairs: From Dipole-Dipole Interaction to Conductively Coupled Regime”, Nano Lett., 4, 1627–1632 (2004)

[19] H.Fan, R.Buckley, and P.Berini, “Passive long-range surface plasmon-polariton devices in Cytop”, Applied Optics, 51 (10), pp. 1459-1467 (2012)

[20] K.L. Tsakmakidis, A.D.Boardman, and Ortwin Hess, “'Trapped rainbow' storage of light in metamaterials”, Nature 450, 397-401 (2007)

[21] M.L Juan, M.Righini, and R.Quidant, “Plasmon nano-optical tweezers”, Nature Photonics 5, 349–356 (2011)

[22] J.B. Pendry. “Negative refraction makes a perfect lens”, Phys. Rev. Lett., 85, 3966–3969 (2000)

[23] N. Fang, H.Lee, C.Sun, X.Zhang, “Sub-diffraction-limited optical imaging with a silver superlens”, Science, 308, 534– 537 (2005)

[24] U. Leonhardt, “Optical conformal mapping”, Science, 312, 1777–1780 (2006)

[25] A.Alù and N.Engheta, “Theory and potentials of multi-layered plasmonic covers for multi-frequency cloaking”, Phys. Rev. Lett., 100, 113901 (2008)

[26] A. Salandrino and N. Engheta, “Far-field sub diffraction optical microscopy using metamaterial crystals: theory and simulation”, Phys. Rev. B, 74, 75103 (2006)

[27] Z. Liu, H.Lee, Y.Xiong, C.Sun, X. Zhang, “Far-Field Optical Hyperlens Magnifying Sub-Diffraction Limited Objects”, Science, 315, 1686–1686 (2007)

[28] A.V. Kildishev and V.M. Shalaev. “Engineering space for light via transformation optics”. Opt. Lett. 33, 43–45 (2008).

[29] Y. Xiong, “A simple design of flat hyperlens for lithography and imaging with half-pitch resolution down to 20 nm”, Appl. Phys. Lett., 94, 203108 (2009).

[30] X.Wang, C.Yin, Z. Cao, “Progress in Planar Optical Waveguides”, Springer Tracts in Modern Physics (2016)

[31] B. Alam, A. Veroli, and A. Benedetti, “Analysis on vertical directional couplers with long range surface plasmons for multilayer optical routing”, Journal of Applied Physics, 120, 083106 (2016)

[32] A. Benedetti, B. Alam, M. Esposito, V. Tasco, G. Leahu, A. Belardini, R. Li Voti, A.Passaseo, and C. Sibilia, “Precise detection of circular dichroism in a cluster of nano-helices by photoacoustic measurements”, Scientific Reports 7, 5257 (2017)

2 Fundamentals

This chapter contains the fundamentals of the works presented in this thesis: section 2 contains the base theory of plasmonics, with particular focus to long range surface plasmons, in section 3 a classification of metamaterials has been presented, in section 4 I presented the base formulas to study chirality, and in section 4 I describe the main fabrication tools I have used.

2.1 Plasmonics: background theory

When an electromagnetic wave at optical frequencies impinges on the interface between a metal and a dielectric, oscillations of the conduction band electrons are formed as a result, in a physical phenomenon conventionally called “Surface Plasmon Polaritons” (SPPs); it should be underlined that Surface Plasmons are actually a type of Polariton, which means that the convention is actually a repetition. Such phenomenon displays many interesting and important properties, in particular it’s capability to strongly confine electromagnetic field, which allows increased sensitivity to changes in the local environment and the ability to localize energy to tiny volumes not restricted by the wavelength of the exciting light; also, many possible waveguiding solutions can be implemented with plasmonics, although most of the options present high propagation losses. Because of these reasons, SPPs are mainly researched with the objective of producing sensors for chemistry, biology, and medicine, or as an enhancement of specific desired effects.

In this section we present the background theory of plasmonics, regardless of the possible application; we will have a special interest in Long Range SPPs, which allows to overcome the issue of the propagation loss. Although most of the content of this paragraph is obtainable from the main textbooks on plasmonics [1], I wanted to recall and reorganize them in a fashion that I judge profitable. Sub-section 2.1.1 presents Maxwell’s equation and the base electromagnetic relations; in 2.1.2 I describe briefly the problem of propagation inside a metallic medium, starting from Drude model; in 2.1.3 I describe analytically the surface plasmon polaritons (SPPs) on

flat interfaces between conductors and dielectrics; sub-section 2.1.4 applies what described previously for single interface metal-dielectrics (slab), later formalized in a more popular form in 2.1.5; in sub-section 2.1.6, I presented the analytical representation of multilayer systems composed of multilayer interfaces, in particular metal-insulator-metal and insulator-metal-insulator; in 2.1.7 long-range-SPPs are defined, and I present a comparison between an approximated analytical formula with the numerical results.

2.1.1 Maxwell's Equations and Electromagnetic Wave Propagation

Metallic nanostructures down to sizes of few nanometers can still be described without a need to resort to quantum mechanics, since the high density of free carriers results in very small spacing of the electron energy levels compared to thermal excitations of energy k_BT at room temperature. In general, the optics of metals falls within the realms of the classical theory; however, this does not prevent a rich and often unexpected variety of optical phenomena from occurring, due to the strong dependence of the optical properties on frequency.

It is general knowledge [1] that, for frequencies up to the infrared, metals are highly reflective and do not allow electromagnetic waves to propagate through them; for this reason, they are traditionally used for the construction of waveguides operating in microwave and far-infrared frequencies, as the perfect or good conductor approximation of infinite or fixed finite conductivity is valid for most purposes. At higher frequencies towards the near-infrared and visible part of the spectrum, field penetration increases significantly, leading to increased dissipation, and prohibiting a simple size scaling of photonic devices that work well at low frequencies to this regime; there is a change in the phase of the induced currents with respect to the driving field for frequencies approaching $1/\tau$, where τ is the characteristic electron relaxation time of the metal. At ultraviolet frequencies, metals acquire dielectric character and allow the propagation of electromagnetic waves, with varying degrees of attenuation, depending on the details of the electronic band structure. Alkali metals exhibit an ultraviolet transparency, while noble metals such as gold or silver show strong absorption in this regime.

These dispersive properties can be described via a complex dielectric function ε(ω), which provides the basis of all phenomena discussed in this text.

Our first approach in this work would be to recall the basic equations governing the electromagnetic response, the macroscopic Maxwell equations, and then extract ε(ω) in a useful way where a microscopic description can be obtained from a macroscopic analysis.

The starting point of Maxwell's equations of macroscopic electromagnetism is:

$$\vec{\nabla} \cdot \vec{D} = \rho_{ext} \qquad (2.1.1.1.a)$$

$$\vec{\nabla} \cdot \vec{B} = 0 \qquad (2.1.1.1.b)$$

$$\vec{\nabla} \times \vec{E} = -\frac{\partial \vec{B}}{\partial t} \qquad (2.1.1.1.c)$$

$$\vec{\nabla} \times \vec{H} = \overrightarrow{J_{ext}} + \frac{\partial \vec{D}}{\partial t} \qquad (2.1.1.1.d)$$

where D is the dielectric displacement, E the electric field, H is the magnetic field, B is the magnetic induction, ρ_{ext} is external charge density and J_{ext} is the external current density. Additionally, we can define:

$$\rho_{tot} = \rho_{ext} + \rho \qquad (2.1.1.2.a)$$

$$J_{tot} = J_{ext} + J \qquad (2.1.1.2.b)$$

where are ρ and J are internal charge and current density, and ρ_{tot} and J_{tot} are the total ones.

The four macroscopic fields are further linked via the polarization P and magnetization M by

$$\vec{D} = \varepsilon_0 \vec{E} + \vec{P} \qquad (2.1.1.3a)$$

$$\vec{H} = \frac{1}{\mu_0} \vec{B} - \vec{M} \qquad (2.1.1.3b)$$

where ε_0 and μ_0 are the electric permittivity and magnetic permeability of vacuum, respectively. Here we will only treat nonmagnetic media, we need not consider a magnetic response represented by M, but can limit our description to electric polarization effects. P describes the electric dipole moment per unit volume inside the material, caused by the alignment of microscopic dipoles with the electric field. It is related to the internal charge density via $\nabla \cdot P = -\rho$. Charge conservation

(∇·J=−∂ρ/∂t) further requires that the internal charge and current densities are linked via

$$\vec{J} = \frac{\delta \vec{P}}{\delta t} \qquad (2.1.1.4).$$

By inserting the first of (2.1.3) into the first of (2.1.1), we would have a form that allows to have both the internal and external densities of charge:

$$\nabla \cdot E = \frac{\rho_{tot}}{\varepsilon_0} \qquad (2.1.1.5).$$

We will limit ourselves to linear, isotropic and non-magnetic media. Thus, one can define the constitutive relations

$$D = \varepsilon_0 \varepsilon E \qquad (2.1.1.6a)$$
$$B = \mu_0 \mu H \qquad (2.1.1.6b)$$

where ε is the dielectric constant or relative permittivity and μ = 1 the relative permeability of the nonmagnetic medium. Another way to represent the linear relationship between P, D and E is to confront the first of (2.1.6) with the first of (2.1.3):

$$P = \varepsilon_0 X E \qquad (2.1.1.7)$$

where ε=1+X makes the linearity explicit. Another important linear relationship is:

$$J = \sigma E \qquad (2.1.1.8)$$

where σ represents the conductivity.

The inclusion of dispersion in space and in time makes ε and σ dependent on r-r' and t-t', and D(r,t) and J(r,t) are obtained by the convolutions of (2.1.1.6) and (2.1.1.8). This complication can be easily resolved by transforming in Fourier with respect to $\int dt\, dr\, e^{i(Kr-\omega t)}$, which turns the convolutions into multiplications. This means decomposing the fields into many individual plane wave components of wave vector K and angular frequency ω. Thus we have:

$$D(K,\omega) = \varepsilon_0 \varepsilon(K,\omega) E(K,\omega) \qquad (2.1.1.9a)$$
$$J(K,\omega) = \sigma(K,\omega) E(K,\omega) \qquad (2.1.1.9b).$$

Using equations (2.1.1.3), (2.1.1.4) and (2.1.1.9) and recognizing that in the Fourier domain ∂/∂t →−iω, we finally arrive at the fundamental relationship between the relative permittivity and the conductivity:

$$\varepsilon(K,\omega) = 1 + \frac{i\sigma(K,\omega)}{\varepsilon_0 \omega} \qquad (2.1.1.10).$$

At low frequencies, ε is usually used for the description of the response of bound charges to a driving field, leading to an electric polarization, while σ describes the contribution of free charges to the current flow. At optical frequencies however, the distinction between bound and free charges is blurred.

In general, ε(ω) and σ(ω) are complex valued functions of angular frequency ω, linked via (2.1.10):

$$\varepsilon(\omega) = \varepsilon_1(\omega) + \mathrm{i}\varepsilon_2(\omega) \qquad (2.1.1.11a)$$

$$\sigma(\omega) = \sigma_1(\omega) + \mathrm{i}\,\sigma_2(\omega) \qquad (2.1.1.11b).$$

At optical frequencies, ε can be experimentally determined for example via reflectivity studies and the determination of the complex refractive index $\tilde{n}(\omega)$ of the medium:

$$\tilde{n}(\omega) = \mathrm{n}(\omega) + \mathrm{i}\kappa(\omega) \qquad (2.1.1.12a)$$

$$\tilde{n}(\omega) = \sqrt{\varepsilon} \qquad (2.1.1.12b)$$

So, overall, we have:

$$\varepsilon_1(\omega) = n^2 - \kappa^2 \qquad (2.1.1.13a)$$

$$\varepsilon_2(\omega) = 2n\kappa \qquad (2.1.1.13b)$$

$$n^2 = \frac{\varepsilon_1}{2} + \frac{1}{2}\sqrt{\varepsilon_1^2 + \varepsilon_2^2} \qquad (2.1.1.13c)$$

$$\kappa = \frac{\varepsilon_2}{2n} \qquad (2.1.1.13d)$$

κ is called the extinction coefficient and determines the optical absorption of electromagnetic waves propagating through the medium. It is linked to the absorption coefficient α of Beer's law (describing the exponential attenuation of the intensity of a beam propagating through the medium via $I(x) = I_0 e^{-\alpha x}$) by the relation

$$I(x) = I_0 e^{-\alpha x} \qquad (2.1.1.14a)$$

$$\alpha(\omega) = \frac{2\kappa(\omega)\omega}{c} \qquad (2.1.1.14b)$$

Therefore, the imaginary part ε_2 of the dielectric function determines the amount of absorption inside the medium. For $|\varepsilon 1| >> |\varepsilon 2|$, the real part n of the refractive index, quantifying the lowering of the phase velocity of the propagating waves due to polarization of the material, is mainly determined by ε_1. Examination of (2.1.1.10) thus reveals that the real part of σ determines the amount of absorption, while the imaginary part contributes to ε1 and therefore to the amount of polarization.

2.1.2 Electromagnetic fields in metals

In the previous subsection we have presented models of an electromagnetic wave propagating inside a linear, isotropic and non-magnetic media material; here, we will describe briefly the problem of propagation inside a metallic medium, starting from Drude model. According to this model, in a metal the atomic nuclei and the core electrons that are linked to them are fixed, whereas the valence electrons are free to wander around almost like a free electron "gas" on the backdrop of the immobile ions.

The structure of metals may be more complicated, but despite this big approximation Drude model does still account for the DC and AC conductivity of metals, the Hall effect and magnetoresistance and thermal conductivity due to electrons. Below is a list of the relevant assumptions of the Drude model:

1. Except for the collisions, the interaction between electrons and other electrons, as well as the interaction between electrons and the fixed ions, is negligible. These are known as the *independent electron approximation* and the *free electron approximation*, respectively.
2. The collisions of the electrons are instantaneous
3. The probability of an electron collision in the time interval dt is $\frac{dt}{\tau}$, where τ is the average time between two collisions, called *mean free time*.

An electron in the presence of an external field E moves by following the equation of motion:

$$m\frac{\delta^2 r}{\delta t^2}+\frac{m}{\tau}\frac{\delta r}{\delta t}=-eE \tag{2.1.2.1}$$

where m is the mass of an electron and r is the coordinate of the electron.

If the driving field has a form of E, then the displacement of the electron will also follow r.

$$-m\omega^2 r-\frac{i\omega m}{\tau}r=-eE \tag{2.1.2.2a}$$

$$r=\frac{e\tau}{m(\omega^2\tau+i\omega)}E \tag{2.1.2.2b}$$

The contribution of the displaced electrons to the polarization P is given by:

$$P=-ner \tag{2.1.2.3}$$

where n is the number of electrons per unit of volume. Combining (2.1.2.2) with (2.1.2.3), we have:

$$P=-\frac{n\frac{e^2}{m}}{\omega^2+i\frac{\omega}{\tau}}E \tag{2.1.2.4a}$$

$$D=\varepsilon_0\left(1-\frac{n\frac{e^2}{m\varepsilon_0}}{\omega^2+i\frac{\omega}{\tau}}\right)E \tag{2.1.2.4b}$$

The term $ne^2/m\varepsilon_0$ is called plasma frequency:

$$\omega_p=n\frac{e^2}{m\varepsilon_0} \tag{2.1.2.5}$$

From (2.1.2.4b) we also have the complex relative permittivity: $\hat{\varepsilon}_r=\frac{\hat{\varepsilon}}{\varepsilon_0}$:

$$\hat{\varepsilon}_r=1-\frac{\omega_p^2}{\omega^2+i\omega/\tau} \tag{2.1.2.6}$$

We can separate the complex relative permittivity into its real and imaginary parts $\hat{\varepsilon}_r=\varepsilon_r'+i\varepsilon_r''$, as done in the previous sub-section with (2.1.1.10);

$$\varepsilon_r'=1-\frac{\omega_p^2\tau^2}{1+\omega^2\tau^2} \tag{2.1.2.7a}$$

$$\varepsilon_r''=\frac{\omega_p^2\tau}{\omega(1+\omega^2\tau^2)} \tag{2.1.2.7b}$$

In the optical regime we have $\omega\tau >> 1$ which leads to:

$$\varepsilon_r' = 1 - \frac{\omega_p^2}{\omega^2} \qquad (2.1.2.8)$$

The plasmon frequency ω_p is the limit at which a Drude metal becomes transparent: if $\omega < \omega_p$, the electromagnetic radiation cannot propagate through the metal and is reflected if $\omega << \omega_p$; on the other hand, if $\omega > \omega_p$, metal will allow passage of the electromagnetic radiation. As pointed out earlier, the Drude model is not suitable for describing high-frequency regimes in real metals as it fails to account for interband electron transitions.

2.1.3 The Wave Equation

To describe analytically the surface plasmon polaritons (SPPs), it is advantageous to focus on flat interfaces between conductors and dielectrics. Before proceeding, it is useful to cast the equations in a general form applicable to the guiding of electromagnetic waves, the "wave equation".

In the absence of external charge and current densities, the curl equations from (2.1.1.1) can be combined in:

$$\vec{\nabla} \times \vec{\nabla} \times \vec{E} = -\mu_0 \frac{\partial^2 \vec{D}}{\partial t^2} \qquad (2.1.3.1)$$

Using the identities $\vec{\nabla} \times \vec{\nabla} \times \vec{E} = \vec{\nabla}\left(\vec{\nabla} \cdot \vec{E}\right) - \nabla^2 \vec{E}$, as well as $\vec{\nabla} \cdot \left(\varepsilon \vec{E}\right) \equiv \vec{E} \cdot \vec{\nabla}\varepsilon + \varepsilon \vec{\nabla} \cdot \vec{E}$ and remembering that due to the absence of external stimuli $\vec{\nabla} \cdot \vec{D} = 0$, $\overrightarrow{J_{ext}} = 0$, we obtain:

$$\vec{\nabla}\left(-\frac{1}{\varepsilon}\vec{E} \cdot \vec{\nabla}\varepsilon\right) - \nabla^2 \vec{E} = \mu_0 \varepsilon_0 \varepsilon \frac{\partial^2 \vec{E}}{\partial t^2} \qquad (2.1.3.2)$$

For negligible changes of the dielectric profile $\varepsilon = \varepsilon(\boldsymbol{r})$ over distances on the order of one optical wavelength, (2.1.3.3) simplifies to the central equation of electromagnetic wave theory:

$$\nabla^2\vec{E} - \frac{\varepsilon}{c^2}\frac{\partial^2\vec{E}}{\partial t^2} = 0 \qquad (2.1.3.3)$$

This equation has to be solved separately in regions of constant ε, and the obtained solutions have to be matched using appropriate boundary conditions. To cast (2.1.3.3) in a form suitable for the description of confined propagating waves, we proceed in two steps.

First, we assume in all generality a harmonic time dependence of the electric field: $\vec{E}(\vec{r},t) = \vec{E}(\vec{r})e^{-jwt}$. Inserted into (2.1.3.3) we obtain the "Helmholtz equation":

$$\nabla^2\vec{E} + k_0^2\varepsilon\vec{E} = 0 \qquad (2.1.3.4)$$

where $k_0 = \frac{\omega}{c}$ is the wave vector of the propagative wave in vacuum.

Next, we have to define the propagation geometry. We assume for simplicity a one-dimensional problem, i.e. ε depends only on one spatial coordinate. Specifically, the waves propagate along the x-direction of a Cartesian coordinate system, and show no spatial variation in the perpendicular, in-plane y-direction (see Fig. 2.1); therefore, $\varepsilon = \varepsilon(z)$.

Applied to electromagnetic surface problems, the plane $Z = 0$ coincides with the interface sustaining the propagating waves, which can now be described as $\vec{E}(x,y,z) = \vec{E}(z)e^{j\beta x}$.

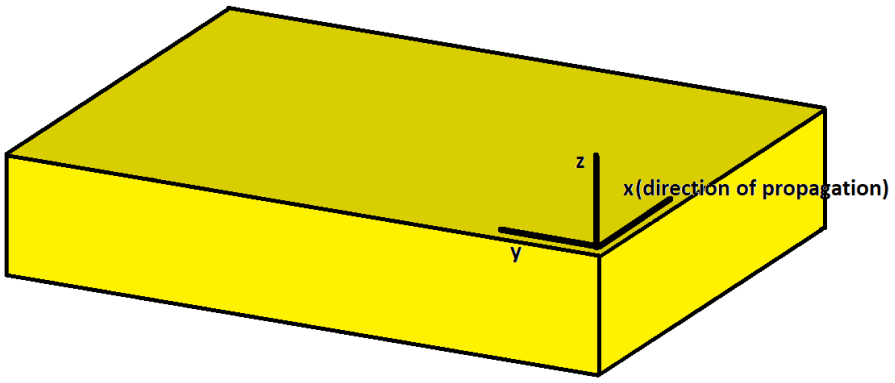

Figure 2.1 Definition of a planar waveguide geometry. The waves propagate along the x direction in a cartesian coordinate system.

The complex parameter $\beta = k_x$ is called the propagation constant of the travelling waves and matches to the component of the wave vector in the direction of

propagation. Inserting this expression into (2.1.3.4) we obtain the desired form of the wave equation:

$$\frac{d^2\vec{E}(z)}{dz^2} + (k_0^2\varepsilon - \beta^2)\vec{E}(\vec{r}) = 0 \qquad (2.1.3.5)$$

a dual equation exists for the magnetic field $\vec{H}$.

Equation (2.1.3.5) is the starting point for the general analysis of guided electromagnetic modes in waveguides. In order to use the wave equation for determining the spatial field profile and dispersion of propagating waves, now we are going to find explicit expressions for the different field components of $\vec{E}(\vec{r})$ and $\vec{H}(\vec{r})$. This can be done using the third and fourth component of the Maxwell equation (2.1.1.1).

For harmonic time dependence $\left(\frac{\partial}{\partial t} = -i\omega\right)$, we arrive at the following set of coupled equations:

$$\frac{\partial E_z}{\partial y} - \frac{\partial E_y}{\partial z} = i\omega\mu_0 H_x \qquad (2.1.3.6a)$$

$$\frac{\partial E_x}{\partial z} - \frac{\partial E_z}{\partial x} = i\omega\mu_0 H_y \qquad (2.1.3.6b)$$

$$\frac{\partial E_y}{\partial x} - \frac{\partial E_x}{\partial y} = i\omega\mu_0 H_z \qquad (2.1.3.6c)$$

$$\frac{\partial H_z}{\partial y} - \frac{\partial H_y}{\partial z} = -i\omega\varepsilon_0\varepsilon E_x \qquad (2.1.3.6d)$$

$$\frac{\partial H_x}{\partial z} - \frac{\partial H_z}{\partial x} = -i\omega\varepsilon_0\varepsilon E_y \qquad (2.1.3.6e)$$

$$\frac{\partial H_y}{\partial x} - \frac{\partial H_x}{\partial y} = -i\omega\varepsilon_0\varepsilon E_z \qquad (2.1.3.6f)$$

For propagation along the x-direction $\left(\frac{\partial}{\partial x} = i\beta\right)$ and homogeneity in the y direction $\left(\frac{\partial}{\partial y} = 0\right)$ this system of equation simplifies to:

$$\frac{\partial E_y}{\partial z} = -i\omega\mu_0 H_x \qquad (2.1.3.7a)$$

$$\frac{\partial E_x}{\partial z} - i\beta E_z = i\omega\mu_0 H_y \qquad (2.1.3.7b)$$

$$i\beta E_y = i\omega\mu_0 H_z \qquad (2.1.3.7c)$$

$$\frac{\partial H_y}{\partial z} = i\omega\varepsilon_0\varepsilon E_x \tag{2.1.3.7d}$$

$$\frac{\partial H_x}{\partial z} - i\beta H_z = -i\omega\varepsilon_0\varepsilon E_y \tag{2.1.3.7e}$$

$$i\beta H_y = -i\omega\varepsilon_0\varepsilon E_z \tag{2.1.3.7f}$$

This system allows two sets of self-consistent solutions with different polarization properties of the propagating waves. The first set is composed by the transverse magnetic (*TM* or *p*), modes, where only the field components E_x, E_z and H_y are nonzero, and the second set the transverse electric (*TE* or *s*) modes, with only H_x, H_z and E_y being nonzero. For *TM* modes, the system of governing equations (2.1.3.7) reduces to

$$E_x = -i\frac{1}{\omega\varepsilon_0\varepsilon}\frac{\partial H_y}{\partial z} \tag{2.1.3.8a}$$

$$E_z = -\frac{\beta}{\omega\varepsilon_0\varepsilon}H_y \tag{2.1.3.8b}$$

and the wave equation for *TM* modes is

$$\frac{\partial^2 H_y}{\partial z^2} + (k_0^2\varepsilon - \beta^2)H_y = 0 \tag{2.1.3.8c}$$

For *TE* modes the analogous set is

$$H_x = i\frac{1}{\omega\mu_0}\frac{\partial E_y}{\partial z} \tag{2.1.3.9a}$$

$$H_z = \frac{\beta}{\omega\mu_0}E_y \tag{2.1.3.9b}$$

with the *TE* wave equation

$$\frac{\partial^2 E_y}{\partial z^2} + (k_0^2\varepsilon - \beta^2)E_y = 0 \tag{2.1.3.9c}$$

2.1.4 Surface plasmon polaritons at a single interface

Now we shall examine the simplest configuration that can that can support SPPs: a single flat interface (Fig. 2.2) between a dielectric non-absorbing half space *(Z >0)* with positive real dielectric constant ε_2 and an adjacent conducting half space (*Z<0*) described via a dielectric function $\varepsilon_1(\omega)$. We have a metallic character, so $Re[\varepsilon_1]<0$. We are looking for propagating wave solutions confined to the interface, i.e. with evanescent decay in the perpendicular z-direction.

We start with the *TM* solutions. Using the equation set (2.2.8) in both half spaces we obtain:

$$H_y(z) = A_2 e^{i\beta x} e^{-k_2 z} \tag{2.1.4.1a}$$

$$E_x(z) = iA_2 \frac{1}{\omega \varepsilon_0 \varepsilon_1} k_2 e^{i\beta x} e^{-k_2 z} \tag{2.1.4.1b}$$

$$E_z(z) = -A_2 \frac{\beta}{\omega \varepsilon_0 \varepsilon_2} e^{i\beta x} e^{-k_2 z} \tag{2.1.4.1c}$$

for *Z>0* and

$$H_y(z) = A_1 e^{i\beta x} e^{k_1 z} \tag{2.1.4.2a}$$

$$E_x(z) = -iA_1 \frac{1}{\omega \varepsilon_0 \varepsilon_1} k_1 e^{i\beta x} e^{k_1 z} \tag{2.1.4.2b}$$

$$E_z(z) = -A_1 \frac{\beta}{\omega \varepsilon_0 \varepsilon_2} e^{i\beta x} e^{-k_1 z} \tag{2.1.4.2c}$$

for $Z<0$, $k_i \equiv k_{z,i} (i = 1,2)$ is the component of the wave vector perpendicular to the interface in the two media. Its reciprocal value, $\hat{z} = \frac{1}{|k_z|}$, defines the evanescent decay length of the fields perpendicular to the interface, which quantifies the confinement of the wave. The continuity of $\varepsilon_i E_z$ at the interface requires that $A_1=A_2$ and

$$\frac{k_2}{k_1} = -\frac{\varepsilon_2}{\varepsilon_1} \tag{2.1.4.3}$$

It should be noted that with our convention of the signs in the exponents in (2.1.4.1, 2.1.4.2), confinement to the surface demands $Re[\varepsilon_1]<0$ if $\varepsilon_2>0$ the surface waves exist only at interfaces between materials with opposite signs of the real part of their dielectric permittivities, i.e. between a conductor and an insulator.

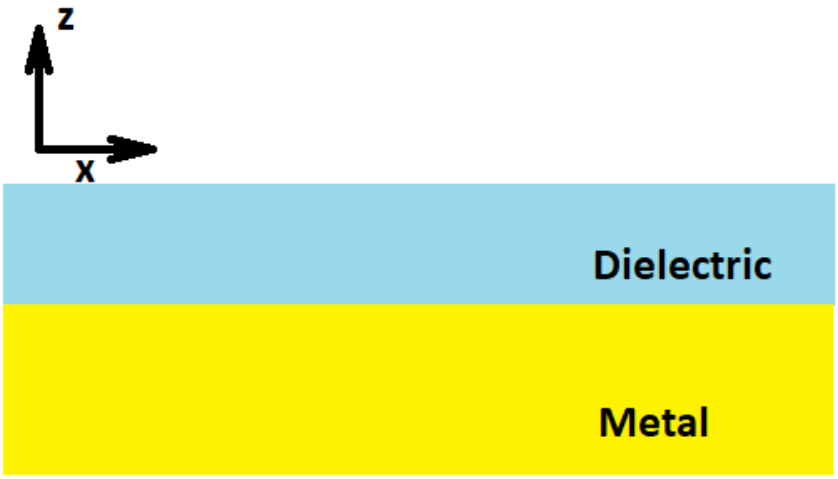

Figure 2.2 Geometry for SPP propagation at a single interface between a metal and a dielectric.

The expression for H_y further has to fulfill the wave equation (2.1.3.8c):

$$k_1^2 = \beta^2 - k_0^2\varepsilon_1 \qquad (2.1.4.4a)$$

$$k_2^2 = \beta^2 - k_0^2\varepsilon_2 \qquad (2.1.4.4b)$$

Combining this and (2.3.3) we arrive at the central result of this subsection, the dispersion relationship of *SPPs* propagating at the interface between the two half spaces:

$$\beta = k_0\sqrt{\frac{\varepsilon_1\varepsilon_2}{\varepsilon_1+\varepsilon_2}} \qquad (2.1.4.5)$$

This expression is valid both for real and complex ε_1, i.e. for conductors without and with attenuation.

We shall now briefly analyze *TE* surface modes. Using (2.1.3.9), the expressions for the field components become:

$$E_y(z) = A_2 e^{i\beta x} e^{-k_2 z} \qquad (2.1.4.6a)$$

$$H_x(z) = -iA_2\frac{1}{\omega\mu_0}k_2 e^{i\beta x} e^{-k_2 z} \qquad (2.1.4.6b)$$

$$H_z(z) = A_2\frac{\beta}{\omega\mu_0} e^{i\beta x} e^{-k_2 z} \qquad (2.1.4.6c)$$

for *Z>0*, and:

$$E_y(z) = A_1 e^{i\beta x} e^{k_1 z} \qquad (2.1.4.7a)$$

$$H_x(z) = iA_1 \frac{1}{\omega\mu_0} k_1 e^{i\beta x} e^{k_1 z} \quad (2.1.4.7b)$$

$$H_z(z) = A_1 \frac{\beta}{\omega\mu_0} e^{i\beta x} e^{-k_1 z} \quad (2.1.4.7c)$$

for $Z<0$. Continuity of E_y and H_x at the interface leads to the condition:

$$A_1(k_1 + k_2) = 0 \quad (2.1.4.8)$$

Since confinement to the surface requires $Re[k_1]>0$ and $Re[k_2]>0$, this condition is only fulfilled if $A_1=0$, so that also $A_1=A_2=0$. Therefore, no surface modes exists for *TE* polarization; for this reason, surface plasmon polaritons only exist for *TM* polarization.

2.1.5 SPP Propagation

In general, two quantities describe the propagation of a SPP along an interface: *propagation length* and *evanescent decay length*. The propagation length describes the attenuation of the surface plasmon in the direction of travel; it is defined as the distance after which the intensity of the electric field has decreased by a factor of $1/e$, which is roughly to 37% of the original amplitude. The propagation length L is given by:

$$L = \frac{1}{2Im(\beta)} \quad (2.1.5.1)$$

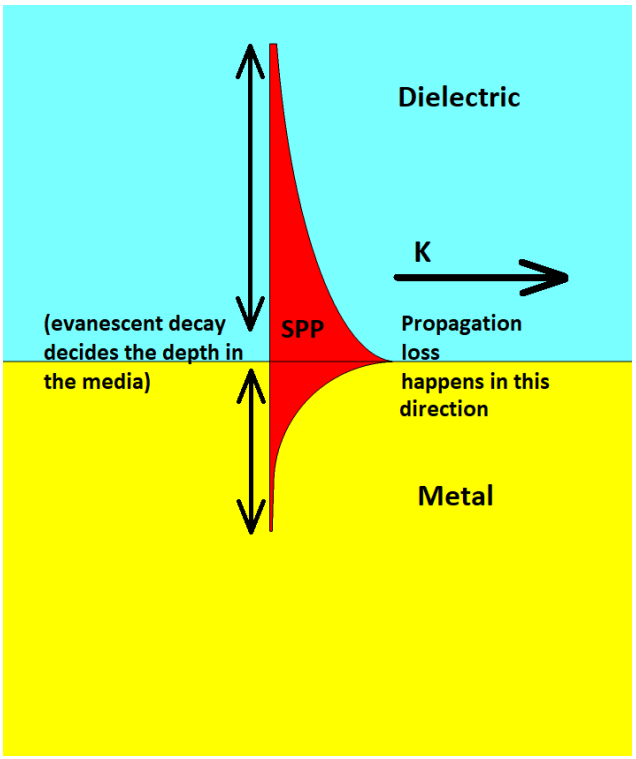

Figure 2.3 Characteristics of SPP propagation at a single interface between a metal and a dielectric.

The evanescent decay length indicates how far the plasmon penetrates into the two media, on either side of the interface, perpendicular to the direction of propagation. The evanescent decay length $\hat{z}_i$, with $i = 1,2$ for the two media, is defined as the distance after which the amplitude of the electric field, in the direction perpendicular to the propagation direction, has decreased by a factor of $1/e$, and is given by the formula:

$$\hat{z}_i = \frac{1}{|k_i|} \qquad (2.1.5.2)$$

2.1.6 Multilayer system

In a multilayer system composed of alternating conducting and dielectric thin films each single interface can support bound SPPs. When the separation between adjacent interfaces is comparable to or smaller than the decay length $\hat{z}$ of the interface mode, interactions between SPPs give rise to coupled modes. The complexity of the calculations increase with the number of layers.

Here we will focus on two types of three layered system, depicted in Fig. 2.4. The first one we will consider has a thin metallic layer (**I**) sandwiched between two (infinitely) thick dielectric claddings (**II**) and (**III**) that realize an insulator/metal/insulator (*IMI*) heterostructure. The second system has a thin dielectric core layer (**I**) sandwiched between two metallic claddings (**II**,**III**) a metal/insulator/metal (*MIM*) heterostructure.

Figure 2.4. Geometry of a three-layer system consisting of a thin layer sandwiched between two infinite half spaces II and III.

We are only interested in the lowest-order bound modes, so we start with a general description of *TM* modes that are non-oscillatory in the z-direction normal to the interfaces, using (2.1.3.8).

For $z > a$ the field components are:

$$H_y = Ae^{i\beta x}e^{-k_3 z} \tag{2.1.6.1a}$$

$$E_x = iA\frac{1}{\omega\varepsilon_0\varepsilon_3}k_3 e^{i\beta x}e^{-k_3 z} \tag{2.1.6.1b}$$

$$E_z = -A\frac{\beta}{\omega\varepsilon_0\varepsilon_3}e^{i\beta x}e^{-k_3 z} \tag{2.1.6.1c}$$

while for $z < a$ we have:

$$H_y = Be^{i\beta x}e^{k_2 z} \tag{2.1.6.2a}$$

$$E_x = -iB\frac{1}{\omega\varepsilon_0\varepsilon_2}k_2 e^{i\beta x}e^{k_2 z} \tag{2.1.6.2b}$$

$$E_z = -B\frac{\beta}{\omega\varepsilon_0\varepsilon_2}e^{i\beta x}e^{k_2 z} \qquad (2.1.6.2c).$$

Thus, we demand that the field decay exponentially in the cladding (**II**) and (**III**). We have defined the component of the wave vector perpendicular to the interface simply $k_i=k_{z,i}$.

In the core region $-\alpha<Z<\alpha$, the modes localized at the bottom and top interface couple:

$$H_y = Ce^{i\beta x}e^{k_1 z} + De^{i\beta x}e^{-k_1 z} \qquad (2.1.6.3a)$$

$$E_x = -iC\frac{1}{\omega\varepsilon_0\varepsilon_1}k_1 e^{i\beta x}e^{k_1 z} + iD\frac{1}{\omega\varepsilon_0\varepsilon_1}k_1 e^{i\beta x}e^{-k_1 z} \qquad (2.1.6.3b)$$

$$E_z = C\frac{\beta}{\omega\varepsilon_0\varepsilon_1}e^{i\beta x}e^{k_1 z} + D\frac{\beta}{\omega\varepsilon_0\varepsilon_1}e^{i\beta x}e^{-k_1 z} \qquad (2.1.6.3c)$$

the requirement of continuity of H_y and E_x leads to

$$Ae^{-k_3 a} = Ce^{k_1 a} + De^{-k_1 a} \qquad (2.1.6.4a)$$

$$\frac{A}{\varepsilon_3}k_3 e^{-k_3 a} = -\frac{C}{\varepsilon_1}k_1 e^{k_1 a} + \frac{D}{\varepsilon_1}k_1 e^{-k_1 a} \qquad (2.1.6.4b)$$

at $z=a$, and:

$$Be^{-k_2 a} = Ce^{-k_1 a} + De^{k_1 a} \qquad (2.1.6.5a)$$

$$-\frac{B}{\varepsilon_2}k_2 e^{-k_2 a} = -\frac{C}{\varepsilon_1}k_1 e^{-k_1 a} + \frac{D}{\varepsilon_1}k_1 e^{k_1 a} \qquad (2.1.6.5b)$$

at $z= -a$, a linear system of four coupled equations. H_y further has to fulfill the wave equation (1.9c) in the three distinct regions, through:

$$k_i^2 = \beta^2 - k_0^2\varepsilon_i \qquad (2.1.6.6)$$

with $i=1,2,3$. Solving this system of linear equations results in an implicit expression for the dispersion relation linking β and ω via

$$e^{-4k_1 a} = \frac{k_1/\varepsilon_1+k_2/\varepsilon_2}{k_1/\varepsilon_1-k_2/\varepsilon_2}\frac{k_1/\varepsilon_1+k_3/\varepsilon_3}{k_1/\varepsilon_1-k_3/\varepsilon_3} \qquad (2.1.6.7).$$

For infinite thickness ($\alpha\to\infty$), (2.1.6.7) reduces to (2.1.4.3), the equation of two uncoupled *SPP* at the respective interfaces.

At this point we can consider the interesting special case where the sub- and the superstrates (**II**) and (**III**) are equal in terms of their dielectric response, i.e. $\varepsilon_2=\varepsilon_3$ and thus $k_2=k_3$. In this case, the dispersion relation (2.1.6.7) can be split into a pair of equations:

$$\tanh k_1 a = -\frac{k_2 \varepsilon_1}{k_1 \varepsilon_2} \qquad (2.1.6.8a)$$

which describes modes of *odd* vector parity ($E_x(z)$, $H_Y(z)$, $E_Z(z)$ are even functions), and

$$\tanh k_1 a = -\frac{k_1 \varepsilon_2}{k_2 \varepsilon_1} \qquad (2.1.6.8b)$$

which describes modes of *even* vector parity ($E_X(z)$, $H_Y(z)$, $E_Z(z)$ are odd functions). Usually, *odd* and *even* modes are also called *antisymmetric* and *symmetric*, respectively.

MIM and *IMI* structures have been developed, and have their own functionality. In the present thesis we will focus on the former, other than the single interfaced structures.

2.1.7 Long Range Surface Plasmons

(Analytical approximation model for LRSPP from a Slab IMI waveguide)

In order to find the effective index of the even mode, corresponding to the symmetric solutions of (2.1.6.7), we need to solve the formula (2.1.6.8b). In what follows we will show analytically that the reduction of the thickness of the metal in an IMI system reduces significantly propagation loss of the symmetric TM mode, and makes *it Long Range Surface Plasmon Polaritons*.

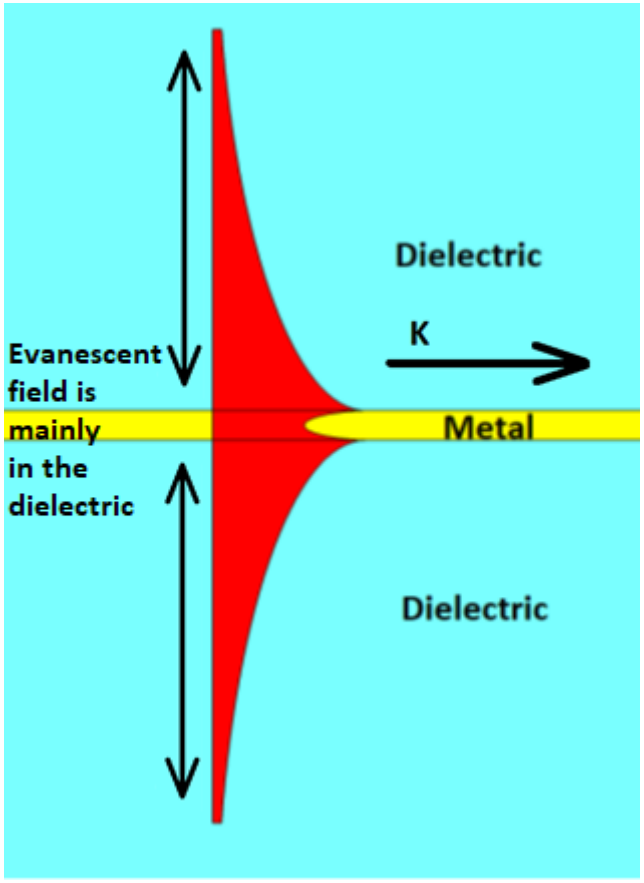

Figure 2.5. Characteristics of Long Range-SPP propagation at double interface with dielectric-metal-dielectric.

Computation on calculators is hindered by the hyperbolic function, since it gives an approximation error for big arguments. At the same time, if we consider $a \to 0$, we can approximate to $\tanh(x) = x$, which is true numerically with a very low error if the argument is lower than "0.5" (the approximation is 4% bigger than the actual value).

Thus, with $a \to 0$, equation (2.1.6.8b) can be approximated:

$$(k_1 a) = -\frac{k_2 \varepsilon_1}{k_1 \varepsilon_2} \tag{2.1.7.1a}$$

$$k_1{}^2 = -\frac{k_2 \varepsilon_1}{a \varepsilon_2} \tag{2.1.7.1b}$$

$$(\beta^2 - k_0^2 \varepsilon_1) = -\frac{\sqrt{(\beta^2 - k_0^2 \varepsilon_2)} \varepsilon_1}{a \varepsilon_2} \tag{2.1.7.1c}$$

$$(n_{eff}^2 - \varepsilon_1) = -\frac{\sqrt{(n_{eff}^2-\varepsilon_2)\varepsilon_1}}{a\varepsilon_2 k_0} \qquad (2.1.7.1d)$$

$$(n_{eff}^2 - \varepsilon_1)^2 = \frac{(n_{eff}^2-\varepsilon_2){\varepsilon_1}^2}{(a\varepsilon_2 k_0)^2} = (n_{eff}^2 - \varepsilon_2)\left(\frac{\varepsilon_1}{\varepsilon_2}\right)^2\left(\frac{1}{ak_0}\right)^2 \qquad (2.1.7.1e)$$

It must be noticed that $\left(\frac{1}{ak_0}\right)^2$ is very big since $a \to 0$ and this may help for further passages. By solving the last equation, it's possible to find the approximated value of n_{eff}:

$$n_{eff} \cong \left(\frac{\varepsilon_1}{\sqrt{\varepsilon_2}}\right)\left(\frac{1}{ak_0}\right) \qquad (2.1.7.2)$$

Again, if the condition $(n_{eff}^2 - \varepsilon_1) * k_0 * a \leq 0.5$ is satisfied, the result of the last equation can be considered reliable.

Simulations with mode solvers such as Eigen Mode Expansion (EME) or Finite Element Method (FEM) are already very precise for the real part of n_{eff}; formula (2.1.7.2) will be used mainly to find the imaginary part of n_{eff}. A validation can be given by Fig.2.6:

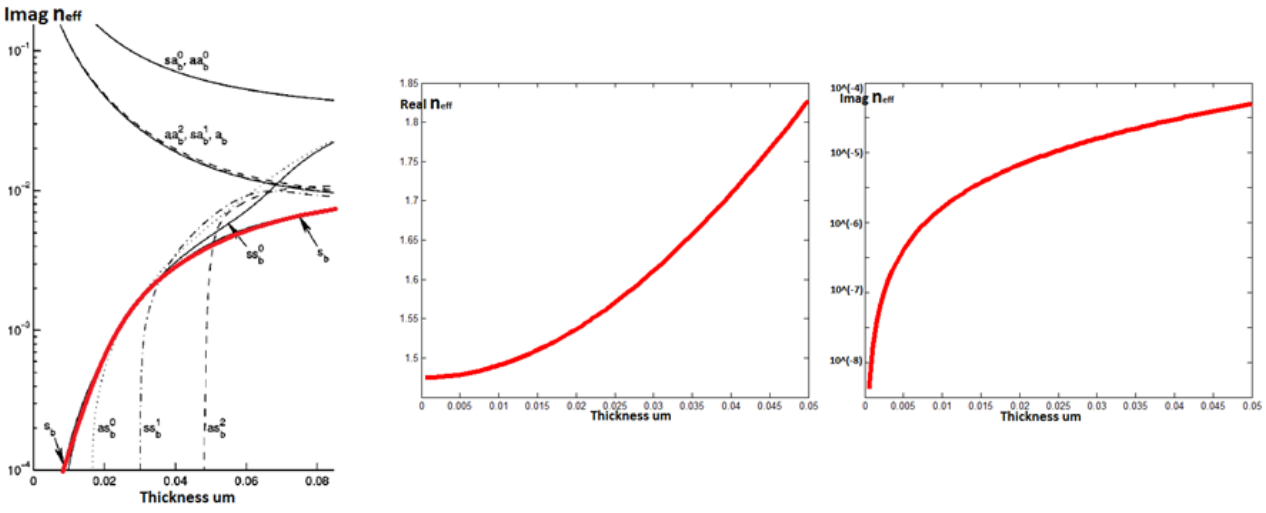

Figure 2.6. Result of the simulations on LR-SPPs, presented with the red lines. On the left image, the black lines are the values present in literature.

By using the approximation (which has been estimated to be reliable if the thickness is lower than 50nm), the real and imaginary values of the "IMI" structure have been calculated, and are shown in fig.2.6 (center and right).

Until now we have presented SPPs propagating along the interface between a metal and a dielectric, and concluded that a LRSPP (the symmetric mode propagating at a dielectric/metal/dielectric interface) yields the longest propagation length and is best suited for our application. However, we have only studied slabs, where an LRSPP propagating along an 'infinitely-wide' (from the plasmons' point of view) interface would have the possibility to quickly dissipate sideways. If we introduce lateral confinement, as demonstrated through calculation by ref.[2] and experimentally by ref.[3], we would have four fundamental quasi-TM modes; one of these four fundamental modes is a non-radiative and bound mode that is symmetric in both x and y directions; this mode is the LRSPP mode. The modal study of such metal stripe cannot be operated analytically, but through numerical methods such as [FEM, EME, Method of Lines].

The EME solver used on a LR-SPP waveguide with a finite width (specifically Width=8μm) and a thickness=25nm gives a reliable real value of the effective index, while it gives errors on the imaginary part. In this kind of situation, it has been decided to adopt the slab's "Imag neff" as the imaginary value; such a choice is reasonable, since Width>>thickness, so the resulting "*ssb*" mode from the 3D waveguide shall be similar to the slab's "*sb*".

The propagation loss can be calculated by:

$$PL(dB/m) = \frac{10*2*k_0*Im(n_{eff})}{\ln(10)}; \qquad (2.1.7.3)$$

With the given values the expected propagation loss is around 7dB/cm. This has the same order of magnitude of the results from literature. The losses reduce with the thickness.

2.2 Metamaterials

Metamaterials are a class of materials engineered to produce properties that don't occur naturally. A conventional material present in nature has its electromagnetic behavior defined by its own atomic configuration. On the other hand, a metamaterial is an assembly of multiple individual elements (sometimes referred as "meta-atoms") with sizes under the wavelength of the electromagnetic waves considered; meta-atoms can be composed of many types of materials (i.e. metals, dielectrics, semiconductors), although the core properties of metamaterials do not depend on the specific composition, but from the pattern given to the structures: their precise shape, geometry, size, orientation and arrangement affects electromagnetic waves of light to create material properties that are unachievable with just the materials.

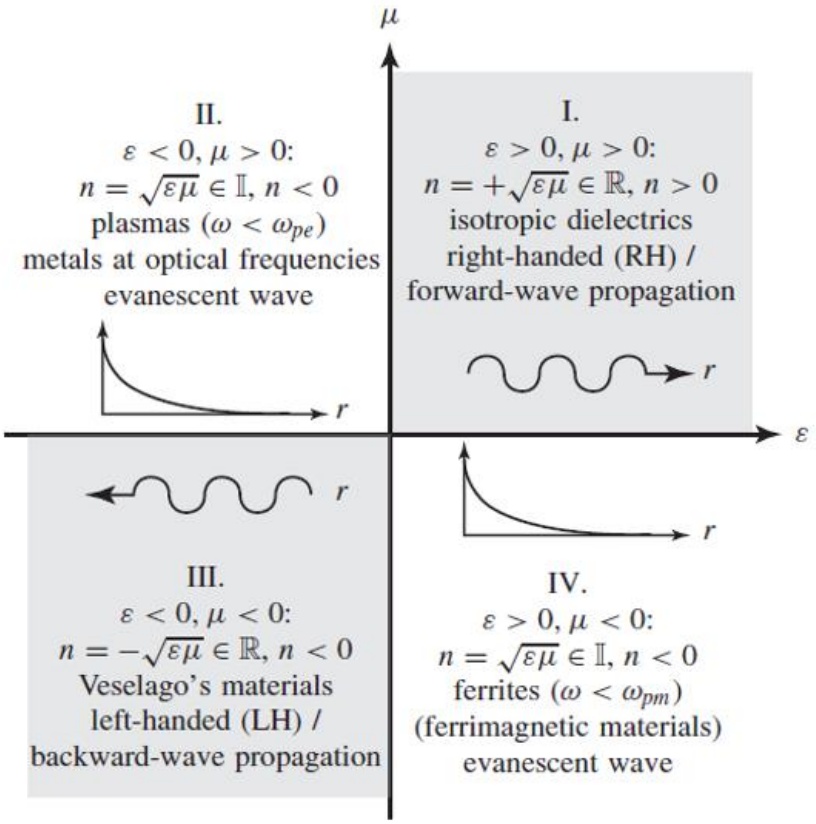

Figure 2.7. Classification of metamaterials based on the sign of the permittivity and permeability

On the basis of permittivity ε and permeability μ, the metamaterials are classified in following four groups [5] as shown in Fig.2.7.

I. Double Positive (DPS) Material: The materials which have both permittivity & permeability greater than zero (ε > 0, μ > 0) are called as double positive (DPS) materials. Most occurring media (e.g. dielectrics) fall under this designation.

II. Epsilon Negative (ENG) Material: If a material has permittivity less than zero and permeability greater than zero (ε < 0, μ > 0) it is called as epsilon negative (ENG) material. In certain frequency regimes, many plasmas exhibit these characteristics.

III. Mu Negative(MNG) Material: If a material has permittivity greater than zero & permeability less than zero (ε > 0, μ < 0) it is called as mu negative (MNG) material. In certain frequency regimes, some gyrotropic material exhibits these characteristics.

IV. Double Negative (DNG) Material: If a material has permittivity & permeability less than zero (ε < 0, μ < 0) it is termed as double negative (DNG) material. This class of materials can only be produced artificially.

Research in metamaterials is active in multiple directions, and it is hard to sort the enormous quantity of papers on the topic. In general, it is possible to classify some macro research lines, which may intermingle.

Metamaterials at microwave frequencies are already a mature field; optical frequencies and terahertz are being researched in these years, and multiple types have been demonstrated experimentally. “Electromagnetic Metamaterials”, other than classical applications as band pass filters, lenses, couplers, antennas, beam steerers, etc., are being researched also for more exotic applications, such as cloaking [6], hologram forming [7], biosensors, fast electronics, etc.; in those cases, the focus is to induce behaviors such as: single/double negative permittivity or permeability [8,9], band gap [10], bi-isotropy/bi-anisotropy, [11] and non-linearities.

Metamaterials that induce chirality are also of great interest; other than the more popular gammadion structures [12], there are various types of proposed structures [13] capable of elliptically polarizing linearly polarized incident light.

Tunable and Frequency-Selective Metamaterials have also attracted a lot of interest [14].

Between the many and various directions in the field of metamaterials, in this thesis we will work mainly with chiral metamaterials.

2.3 Expressions of circular dichroism

Chirality refers to the geometric property of a structure lacking any mirror symmetry plane. It exists in many forms in nature, ranging from molecules, to proteins, and to crystals. In contrast, a structure is achiral if it is indistinguishable or superimposable on its mirror image.

Due to the interest in chiral molecules, optical dichroism properties of natural and artificial materials have become a hot research topic. In this section I present the analytical background and the representation forms for circular dichroic materials.

2.3.1 Tellegen's Formula and gyrotropic media

Circular dichroism can be expressed in 2 possible forms: Tellegen's and gyrotropic media's, which adopts a tensor permittivity instead of a scalar one. In Tellegen's form, it is expected that the relationship between electric displacement D, magnetic induction B, electric field E and magnetic field H is as follows:

$$\begin{aligned}\vec{D} &= \varepsilon_0 \varepsilon_r \vec{E} + \frac{\iota\kappa}{c_0}\vec{H} \\ \vec{B} &= -\frac{\iota\kappa}{c_0}\vec{E} + \mu_0 \mu_r \vec{H}\end{aligned} \qquad (2.3.1.1).$$

Commonly, in gyrotropic form, circular dichroism of a chiral media is represented from the source of the chirality, which is inside the electric field E and in its interaction with scatterers:

$$\begin{aligned}\vec{D} &= \varepsilon_0 \overline{\overline{\varepsilon_r}} \bullet \vec{E} \\ \vec{B} &= \mu_0 \mu_r \vec{H}\end{aligned} \qquad (2.3.1.2).$$

Obviously the meaning given to the permittivity and permeability in (1.2) is not the same of those of Tellegen's form.

Despite those formal definitions allow a big variety of hypothetic materials, and the possibility to define an isotropically dichroic media in 4π steradians, it is still almost impossible to obtain ''precisely'' such a material, and usually metamaterials allow to have an equivalent gyrotropic media. If we consider those two forms with a purely vertical propagation (along $\hat{z}$), and we suppose a tensorial permittivity in (2.3.1.2) such as:

$$\overline{\overline{\varepsilon_r}} = \begin{pmatrix} a & -\imath b & 0 \\ +\imath b & a & 0 \\ 0 & 0 & c \end{pmatrix} \tag{2.3.1.3}$$

and if we confine the analysis to the two cartesian components perpendicular to the propagation (such as x and y), we can compare the parameters of the two types of representation. As for Tellegen, we have:

$$\begin{aligned} &\vec{\nabla} \wedge \vec{\nabla} \wedge \vec{E} = +\imath\omega\vec{\nabla} \wedge \vec{B} = +\imath\omega\vec{\nabla} \wedge \left(-\frac{\imath\kappa}{c_0}\vec{E} + \mu_0\mu_r\vec{H} \right) = \\ &= +\imath\omega\left(-\frac{\imath\kappa}{c_0}\vec{\nabla} \wedge \vec{E} + \mu_0\mu_r\vec{\nabla} \wedge \vec{H} \right) = +\imath\omega\left(\frac{\omega\kappa}{c_0}\vec{B} - \imath\omega\mu_0\mu_r\vec{D} \right) = \\ &= +\imath\omega\left[\frac{\omega\kappa}{c_0}\left(-\frac{\imath\kappa}{c_0}\vec{E} + \mu_0\mu_r\vec{H} \right) - \imath\omega\mu_0\mu_r\left(\varepsilon_0\varepsilon_r\vec{E} + \frac{\imath\kappa}{c_0}\vec{H} \right) \right] = \\ &= k_0^2\left(\kappa^2 + \mu_r\varepsilon_r \right)\vec{E} + 2\imath\frac{\kappa\mu_0\mu_r\omega^2}{c_0}\vec{H} \end{aligned} \tag{2.3.1.4}$$

which is also known as Helmholtz vectorial equation for Electric field. On the other hand, if we see the gyroscopic version of this, and limiting the analysis to the lack of the z components, we have:

$$\vec{\nabla}\wedge\vec{\nabla}\wedge\vec{E}=+\imath\omega\vec{\nabla}\wedge\vec{B}=+\imath\omega\mu_0\mu_r\vec{\nabla}\wedge\vec{H}=$$
$$=\omega^2\mu_0\varepsilon_0\mu_r\overline{\overline{\varepsilon_r}}\vec{E}=\omega^2\mu_0\varepsilon_0\mu_r\begin{pmatrix}a & -\imath b\\ +\imath b & a\end{pmatrix}\begin{pmatrix}E_x\\ E_y\end{pmatrix}=$$
$$=\omega^2\mu_0\varepsilon_0\mu_r\left[\begin{pmatrix}a & 0\\ 0 & a\end{pmatrix}\begin{pmatrix}E_x\\ E_y\end{pmatrix}+\begin{pmatrix}0 & -\imath b\\ +\imath b & 0\end{pmatrix}\begin{pmatrix}E_x\\ E_y\end{pmatrix}\right]= \qquad (2.3.1.5)$$
$$=\omega^2\mu_0\varepsilon_0\mu_r\left(a\vec{E}+\imath b\hat{z}\wedge\vec{E}\right)=k_0^2\mu_r\left(a\vec{E}+\frac{b}{k}\imath\vec{k}\wedge\vec{E}\right)=k_0^2\mu_r\left(a\vec{E}+\frac{b}{k}\vec{\nabla}\wedge\vec{E}\right)=$$
$$=k_0^2\mu_r a\vec{E}+k_0^2\frac{\imath\omega b\mu_0\mu_r^2}{k}\vec{H}=k_0^2\mu_r a\vec{E}+k_0^2\frac{\imath b\mu_0 c_0\mu_r^2}{n}\vec{H}$$

Here, we have considered:

$$k=k_0 n \qquad (2.3.1.6)$$

with n as the effective index of the linearly polarized wave. By comparing (2.3.1.4) with (2.3.1.5) we discern that:

$$\begin{cases}k_0^2\ \kappa^2+\mu_r\varepsilon_r\ =k_0^2\mu_r a\\ 2\iota\dfrac{\kappa\mu_0\mu_r\omega^2}{c_0}=k_0^2\dfrac{\imath b\mu_0 c_0\mu_r^2}{n}\end{cases}\rightarrow\begin{cases}\kappa^2+\mu_r\varepsilon_r=\mu_r a\\ \kappa=\dfrac{b\mu_r}{2n}\end{cases} \qquad (2.3.1.7).$$

It should be noticed the direct proportionality between chirality parameters k and b in the last equation of (2.3.1.7), as those represent circular dichroism of the two forms.

2.3.2 Refractive indexes of circular modes

We will start from gyrotropic form, where refractive indexes can be discerned easily. First, we transform the electromagnetic vectorial components from the Cartesian representation to the circular:

$$\begin{pmatrix} v_+ \\ v_- \end{pmatrix} = \begin{pmatrix} 1 & -\iota \\ 1 & +\iota \end{pmatrix} \begin{pmatrix} v_x \\ v_y \end{pmatrix}, \quad \begin{pmatrix} v_x \\ v_y \end{pmatrix} = \frac{1}{2} \begin{pmatrix} 1 & 1 \\ +\iota & -\iota \end{pmatrix} \begin{pmatrix} v_+ \\ v_- \end{pmatrix} \tag{2.3.2.1}$$

to obtain:

$$\begin{pmatrix} D_+ \\ D_- \end{pmatrix} = \begin{pmatrix} 1 & -\iota \\ 1 & +\iota \end{pmatrix} \begin{pmatrix} D_x \\ D_y \end{pmatrix} = \begin{pmatrix} 1 & -\iota \\ 1 & +\iota \end{pmatrix} \begin{pmatrix} a & -\iota b \\ +\iota b & a \end{pmatrix} \begin{pmatrix} E_x \\ E_y \end{pmatrix} =$$
$$= \begin{pmatrix} 1 & -\iota \\ 1 & +\iota \end{pmatrix} \begin{pmatrix} a & -\iota b \\ +\iota b & a \end{pmatrix} \frac{1}{2} \begin{pmatrix} 1 & 1 \\ +\iota & -\iota \end{pmatrix} \begin{pmatrix} E_+ \\ E_- \end{pmatrix} = \tag{2.3.2.2}$$
$$= \begin{pmatrix} a+b & 0 \\ 0 & a-b \end{pmatrix} \begin{pmatrix} E_+ \\ E_- \end{pmatrix}$$

Since in this form magnetism is represented from a scalar permeability (=1 when magnetism is absent), refractive indexes of the two directions are:

$$n_\pm = \sqrt{\mu_r \ a \pm b} \tag{2.3.2.3}$$

Using (2.3.1.7), we have in Tellegen:

$$n_\pm = \sqrt{\mu_r \ a \pm b} = \sqrt{\mu_r \left[\left(\frac{\kappa^2}{\mu_r} + \varepsilon_r \right) \pm \frac{2n}{\mu_r} \kappa \right]} = \sqrt{\left[\kappa^2 + \varepsilon_r \mu_r \ \pm 2n\kappa \right]} \tag{2.3.2.4}$$

where it was presumed:

$$n^2 = \varepsilon_r \mu_r \tag{2.3.2.5}$$

Thus, supposing the scalar permittivity from Tellegen's form:

$$n_{\pm} = \sqrt{\kappa^2 \pm 2n\kappa + n^2} = n \pm \kappa \qquad \text{(2.3.2.6).}$$

The effects of chirality are expressed with κ, which detracts or adds to the original refractive index n.

2.3.3 Reflective coefficients

Suppose a plane wave propagating vertically downward (towards negative z), and impinging on a perfectly flat and smooth etalon with gyrotropic permittivity on both faces, as in (2.3.1.3). The wave is polarized on x.

If we reduce the study area on only an interface air-gyroid, and a wave impinging on vertically, there will be a reflection with a rotation of linear polarization, so reflected field will not be parallel to x axis, but it will have also a component in y. Reflection coefficients will be:

$$r_{xx} = \frac{\alpha - \gamma}{\alpha + \gamma}, \quad r_{yx} = 2\iota \frac{2 - \alpha}{\alpha + \gamma} \qquad \text{(2.3.3.1)}$$

with *α* e *γ* given from:

$$\alpha = \frac{n_+ + n_- + 2}{n_- + 1}, \qquad \gamma = \frac{n_+ + n_- + 2n_+ n_-}{n_- + 1} \qquad \text{(2.3.3.2).}$$

On the other hand, transmission coefficients:

$$t_+ = \frac{2}{\alpha + \gamma}, \quad t_- = 2\frac{\alpha - 1}{\alpha + \gamma} \qquad \text{(2.3.3.3).}$$

If the impinging wave on the gyroid-air interface is circularly polarized, the reflection coefficient will be dependent on the rotation direction:

$$r_+ = \frac{n_+ - 1}{n_- + 1}, \quad r_- = \frac{n_- - 1}{n_+ + 1} \tag{2.3.3.4}$$

While transmission coefficient will be:

$$\begin{aligned} t_{+x} &= \frac{n_+ + n_-}{n_- + 1}, & t_{+y} &= +\iota t_{+x} \\ t_{-x} &= \frac{n_+ + n_-}{n_+ + 1}, & t_{-y} &= -\iota t_{+x} \end{aligned} \tag{2.3.3.5}$$

With this information, it is easy to deduce reflection and transmission coefficients for linearly polarized plane wave, which will be:

$$\begin{aligned} R_{xx} &= r_{xx} + \frac{t_+ r_+ t_{+x} + t_- r_- t_{-x}}{1 - r_+ r_- e^{\iota k_0 (n_+ + n_-) d}} e^{\iota k_0 (n_+ + n_-) d} \\ R_{yx} &= r_{yx} + \iota \frac{t_+ r_+ t_{+x} - t_- r_- t_{-x}}{1 - r_+ r_- e^{\iota k_0 (n_+ + n_-) d}} e^{\iota k_0 (n_+ + n_-) d} \\ T_{xx} &= \frac{t_+ t_{+x} e^{\iota k_0 n_+ d} + t_- t_{-x} e^{\iota k_0 n_- d}}{1 - r_+ r_- e^{\iota k_0 (n_+ + n_-) d}} \\ T_{yx} &= +\iota \frac{t_+ t_{+x} e^{\iota k_0 n_+ d} - t_- t_{-x} e^{\iota k_0 n_- d}}{1 - r_+ r_- e^{\iota k_0 (n_+ + n_-) d}} \end{aligned} \tag{2.3.3.6}$$

Since a circularly polarized planar wave is given from the sum of two orthogonal linearly polarized waves with 90° phase shift, it is possible to calculate reflection and transmission coefficients for a circularly polarized wave from (2.3.3.6). Before going through with the calculations, it is better to recall the particular case of circularly polarized planar waves impinging downward:

$$\begin{aligned} E_x &= e^{-\iota k_0 n_0 z} \qquad E_y = \mp \iota e^{-\iota k_0 n_0 z} \\ H_x &= \frac{-\frac{dE_y}{dz}}{\iota \omega \mu_0} = \mp \iota n_0 \frac{e^{-\iota k_0 n_0 z}}{\zeta_0} \qquad H_y = \frac{\frac{dE_x}{dz}}{\iota \omega \mu_0} = -n_0 \frac{e^{-\iota k_0 n_0 z}}{\zeta_0} \end{aligned} \tag{2.3.3.7}$$

For an achiral media and for a vertical propagation upward we have:

$$E_x = e^{+\iota k_0 n_0 z} \qquad E_y = \pm \iota e^{+\iota k_0 n_0 z}$$
$$H_x = \frac{-\frac{dE_y}{dz}}{\iota\omega\mu_0} = \mp \iota n_0 \frac{e^{+\iota k_0 n_0 z}}{\zeta_0} \qquad H_y = \frac{\frac{dE_x}{dz}}{\iota\omega\mu_0} = +n_0 \frac{e^{+\iota k_0 n_0 z}}{\zeta_0} \tag{2.3.3.8}.$$

A chiral media has different laws. Magnetic field is obtained from electric field from:

$$\vec{\nabla} \wedge \vec{E} = \iota\omega\vec{B} = \iota\omega\left(\mu_0\mu_r\vec{H} - \iota\frac{\kappa}{c}\vec{E}\right)$$
$$\rightarrow \frac{\left(\frac{dE_z}{dy} - \frac{dE_y}{dz} - k_0\kappa E_x, \frac{dE_x}{dz} - \frac{dE_z}{dx} - k_0\kappa E_y, \frac{dE_y}{dx} - \frac{dE_x}{dy} - k_0\kappa E_z\right)}{\iota\omega\mu_0\mu_r} = H_x, H_y, H_z \tag{2.3.3.9}.$$

For a vertical downward in a chiral media we have:

$$E_x = e^{-\iota k_0 n_\pm z} \qquad E_y = \mp \iota e^{-\iota k_0 n_\pm z}$$
$$H_x = \frac{-\frac{dE_y}{dz} - k_0\kappa E_x}{\iota\omega\mu_0\mu_r} = \mp\iota\frac{n_\pm e^{-\iota k_0 n_\pm z} \mp \kappa e^{-\iota k_0 n_\pm z}}{\zeta_0\mu_r} \tag{2.3.3.10}.$$
$$H_y = \frac{\frac{dE_x}{dz} - k_0\kappa E_y}{\iota\omega\mu_0\mu_r} = -\frac{n_\pm e^{-\iota k_0 n_\pm z} \mp \kappa e^{-\iota k_0 n_\pm z}}{\zeta_0\mu_r}$$

For a vertical propagation upward in chiral media we have:

$$E_x = e^{+\iota k_0 n_\pm z} \qquad E_y = \pm \iota e^{+\iota k_0 n_\pm z}$$
$$H_x = \frac{-\frac{dE_y}{dz} - k_0\kappa E_x}{\iota\omega\mu_0\mu_r} = \mp\iota\frac{n_\pm e^{+\iota k_0 n_\pm z} \mp \kappa e^{+\iota k_0 n_\pm z}}{\zeta_0\mu_r} \tag{2.3.3.11}.$$
$$H_y = \frac{\frac{dE_x}{dz} - k_0\kappa E_y}{\iota\omega\mu_0\mu_r} = \frac{n_\pm e^{+\iota k_0 n_\pm z} \mp \kappa e^{+\iota k_0 n_\pm z}}{\zeta_0\mu_r}$$

So, if there is a planar wave impinging from a non-chiral dielectric media with index n_0 on a chiral media, the following relation is valid:

$$z > 0 \rightarrow \left\{\begin{array}{l} E_x = e^{+\iota k_0 n_0 z} + r_{0\pm} e^{-\iota k_0 n_0 z} \\ E_y = \mp \iota e^{-\iota k_0 n_0 z} \mp r_{0\pm} \iota e^{+\iota k_0 n_0 z} \\ H_x = \mp \iota n_0 \frac{e^{-\iota k_0 n z}}{\zeta_0} \pm r_{0\pm} \iota n_0 \frac{e^{+\iota k_0 n_0 z}}{\zeta_0} \\ H_y = -n_0 \frac{e^{-\iota k_0 n_0 z}}{\zeta_0} + r_{0\pm} n_0 \frac{e^{+\iota k_0 n_0 z}}{\zeta_0} \end{array}\right\} z < 0 \rightarrow \left\{\begin{array}{l} E_x = t_{0\pm} e^{-\iota k_0 n_\pm z} \\ E_y = \mp t_{0\pm} \iota e^{-\iota k_0 n_\pm z} \\ H_x = \mp t_{0\pm} \iota \frac{n_\pm e^{-\iota k_0 n_\pm z} \mp \kappa e^{-\iota k_0 n_\pm z}}{\zeta_0\mu_r} \\ H_y = -t_{0\pm} \frac{n_\pm e^{-\iota k_0 n_\pm z} \mp \kappa e^{-\iota k_0 n_\pm z}}{\zeta_0\mu_r} \end{array}\right\}$$

$$\rightarrow \begin{cases} 1+r_{0\pm}=t_{0\pm} \\ 1-r_{0\pm}=t_{0\pm}\dfrac{n_{\pm}\mp\kappa}{n_0\mu_r} \end{cases} \rightarrow \begin{cases} r_{0\pm}=\dfrac{n_0\mu_r-\ n_{\pm}\mp\kappa}{n_0\mu_r+\ n_{\pm}\mp\kappa}=\dfrac{n_0\mu_r-n}{n_0\mu_r+n} \\ t_{0\pm}=\dfrac{2n_0\mu_r}{n_0\mu_r+\ n_{\pm}\mp\kappa}=\dfrac{2n_0\mu_r}{n_0\mu_r+n} \end{cases} \qquad (2.3.3.12).$$

If, on the other hand, the wave impinges from chiral media into a non-chiral one, the coefficients become:

$$z>0 \rightarrow \begin{cases} E_x=e^{-\iota k_0 n_{\pm} z}+r_{\pm 0}e^{+\iota k_0 n_{\mp} z} \\ E_y=\pm\iota e^{-\iota k_0 n_{\pm} z}\pm r_{\pm 0}\iota e^{+\iota k_0 n_{\mp} z} \\ H_x=\mp\iota\dfrac{n_{\pm}e^{-\iota k_0 n_{\pm} z}\mp\kappa e^{-\iota k_0 n_{\pm} z}}{\zeta_0\mu_r}\pm\iota r_{\pm 0}\dfrac{n_{\mp}e^{-\iota k_0 n_{\mp} z}\pm\kappa e^{-\iota k_0 n_{\mp} z}}{\zeta_0\mu_r} \\ H_y=-\dfrac{n_{\pm}e^{-\iota k_0 n_{\pm} z}\mp\kappa e^{-\iota k_0 n_{\pm} z}}{\zeta_0\mu_r}+r_{\pm 0}\dfrac{n_{\mp}e^{+\iota k_0 n_{\mp} z}\pm\kappa e^{+\iota k_0 n_{\mp} z}}{\zeta_0\mu_r} \end{cases} z<0 \rightarrow \begin{cases} E_x=t_{\pm 0}e^{+\iota k_0 n_0 z} \\ E_y=\mp t_{\pm 0}\iota e^{+\iota k_0 n_0 z} \\ H_x=\mp t_{\pm 0}\iota n_0\dfrac{e^{+\iota k_0 n_0 z}}{\zeta_0} \\ H_y=-t_{\pm 0}n_0\dfrac{e^{+\iota k_0 n_0 z}}{\zeta_0} \end{cases}$$

$$\rightarrow \begin{cases} 1+r_{\pm 0}=t_{\pm 0} \\ \dfrac{n_{\pm}\mp\kappa}{n_0\mu_r}-r_{\pm 0}\dfrac{n_{\mp}\pm\kappa}{n_0\mu_r}=t_{\pm 0} \end{cases} \rightarrow \begin{cases} r_{\pm 0}=\dfrac{n_{\pm}\mp\kappa-n_0\mu_r}{n_{\mp}\pm\kappa+n_0\mu_r}=\dfrac{n-n_0\mu_r}{n+n_0\mu_r} \\ t_{\pm 0}=\dfrac{n_{\pm}\mp\kappa+n_{\mp}\pm\kappa}{n_{\mp}\pm\kappa+n_0\mu_r}=\dfrac{2n}{n+n_0\mu_r} \end{cases} \qquad (2.3.3.13).$$

By comparing (2.3.3.12-13), we have:

$$\begin{aligned} r_{0\pm}&=-r_{\pm 0} \\ t_{0\pm}&=1+r_{0\pm}=1-r_{\pm 0}=2-t_{\pm 0} \end{aligned} \qquad (2.3.3.14).$$

It should be noticed that these coefficients are independent from polarization, even considering the different index for the two circular polarizations. Since transmission and reflection coefficients are more linked to characteristic impedance of the media, rather than the refractive index, we can deduce that the two circularly polarized waves experience the same impedance, despite their rotation direction. By using (2.3.3.12-13), we can obtain the reflection and transmission for the entire etalon of thickness d:

$$\begin{aligned} R_{\pm}&=r_{0\pm}+\frac{t_{0\pm}r_{\pm 0}t_{\mp 0}e^{\iota k_0\ n_{+}+n_{-}\ d}}{1-r_{\pm 0}r_{\mp 0}e^{\iota k_0\ n_{+}+n_{-}\ d}}=r_{0\pm}\frac{1-\ r_{\pm 0}r_{\mp 0}+t_{0\pm}t_{\mp 0}\ \ e^{\iota k_0\ n_{+}+n_{-}\ d}}{1-r_{\pm 0}r_{\mp 0}e^{\iota k_0\ n_{+}+n_{-}\ d}} \\ T_{\pm}&=\frac{t_{0\pm}t_{\pm 0}e^{\iota k_0 n_{\pm} d}}{1-r_{\pm 0}r_{\mp 0}e^{\iota k_0\ n_{+}+n_{-}\ d}} \end{aligned} \qquad (2.3.3.15).$$

Despite transmission coefficient is different for the two rotation directions (just because of the different phase shift for a single starting point of the propagation), the reflection coefficient is still the same.

2.3.4 Calculation of Tellegen's parameters from measured coefficients

If the 4 transmission and reflection coefficient are given, it is possible to calculate the parameters of Tellegen's model for chiral media, by walking backwards the path described previously. From the previous formulas, specifically (2.3.3.15) and (2.3.3.12-13):

$$\frac{T_+}{T_-}=\frac{t_{0+}t_{+0}e^{\iota k_0 n_+ d}}{t_{0-}t_{-0}e^{\iota k_0 n_- d}}=e^{\iota 2k_0\kappa d}\ \rightarrow\ \ \kappa=\frac{-\iota}{2k_0 d}\ln\left(\frac{T_+}{T_-}\right) \tag{2.3.4.1}.$$

We rewrite (2.3.3.12-13):

$$\begin{aligned} r_{0\pm}&=\frac{n_0\mu_r-\sqrt{\mu_r}\sqrt{\varepsilon_r}}{n_0\mu_r+\sqrt{\mu_r}\sqrt{\varepsilon_r}}=\frac{n_0\sqrt{\mu_r}-\sqrt{\varepsilon_r}}{n_0\sqrt{\mu_r}+\sqrt{\varepsilon_r}}=\frac{n_0Z-1}{n_0Z+1}\\ t_{0\pm}&=\frac{2n_0\mu_r}{n_0\mu_r+\sqrt{\mu_r}\sqrt{\varepsilon_r}}=\frac{2n_0\sqrt{\mu_r}}{n_0\sqrt{\mu_r}+\sqrt{\varepsilon_r}}=2\frac{n_0Z}{n_0Z+1}\\ r_{\pm 0}&=\frac{1-n_0Z}{1+n_0Z}\\ t_{\pm 0}&=2\frac{1}{n_0Z+1} \end{aligned} \tag{2.3.4.2}.$$

So, coefficients for etalon become:

$$R=R_\pm=r_{0\pm}\frac{1-\ r_{\pm0}^2+t_{0\pm}t_{\mp0}\ \ e^{\iota k_0\ n_++n_-\ d}}{1-r_{\pm0}^2e^{\iota k_0\ n_++n_-\ d}}=$$

$$=\frac{n_0Z-1}{n_0Z+1}\frac{1-\left[\left(\frac{n_0Z-1}{n_0Z+1}\right)^2+\frac{4n_0Z}{n_0Z+1^{\ 2}}\right]e^{\iota 2k_0nd}}{1-\left(\frac{n_0Z-1}{n_0Z+1}\right)^2e^{\iota 2k_0nd}}=\frac{n_0Z-1}{n_0Z+1}\frac{n_0Z+1^{\ 2}-\left[\ n_0Z-1^{\ 2}+4n_0Z\right]e^{\iota 2k_0nd}}{n_0Z+1^{\ 2}-\ n_0Z-1^{\ 2}e^{\iota 2k_0nd}}=$$

$$= \frac{n_0 Z - 1}{n_0 Z + 1} \frac{n_0 Z + 1^{\,2} - n_0 Z + 1^{\,2} e^{\iota 2 k_0 n d}}{n_0 Z + 1^{\,2} - n_0 Z - 1^{\,2} e^{\iota 2 k_0 n d}} = \frac{\left[n_0 Z^{\,2} - 1 \right] 1 - e^{\iota 2 k_0 n d}}{n_0 Z + 1^{\,2} - n_0 Z - 1^{\,2} e^{\iota 2 k_0 n d}} \qquad (2.3.4.3a)$$

$$T_{\pm} = \frac{t_{0\pm} t_{\pm 0} e^{\iota k_0 \, n \pm k \, d}}{1 - r_{\pm 0}^2 e^{\iota k_0 \, n_+ + n_- \, d}} = \frac{\frac{4 n_0 Z}{n_0 Z + 1^{\,2}} e^{\iota k_0 \, n \pm k \, d}}{1 - \left(\frac{n_0 Z - 1}{n_0 Z + 1} \right)^2 e^{\iota 2 k_0 n d}} = \frac{4 n_0 Z e^{\iota k_0 \, n \pm k \, d}}{n_0 Z + 1^{\,2} - n_0 Z - 1^{\,2} e^{\iota 2 k_0 n d}} \qquad (2.3.4.3b)$$

By combining (2.3.4.3 a-b) and defining $t = n_0 Z$, we can compose many passages. First, we will multiply the two transmission coefficients in the two circular directions:

$$T_+ T_- = \left[\frac{4 t e^{\iota k_0 n d}}{t + 1^{\,2} - t - 1^{\,2} e^{\iota 2 k_0 n d}} \right]^2 \qquad (2.3.4.4a).$$

By using again parameter t we will use also reflection coefficient in (2.3.4.3 a), and from this we will explicit the exponential at denominator of (2.3.4.4 a):

$$R = \frac{t^2 - 1 \;\; 1 - e^{\iota 2 k_0 n d}}{t + 1^{\,2} - t - 1^{\,2} e^{\iota 2 k_0 n d}} \rightarrow \frac{R \;\; t + 1^{\,2} - t^2 - 1}{R \;\; t - 1^{\,2} - t^2 - 1} = e^{\iota 2 k_0 n d} \qquad (2.3.4.4b).$$

So, (2.3.4.4 a) changes in:

$$T_+ T_- = \frac{16 t^2 e^{\iota 2 k_0 n d}}{\left[t + 1^{\,2} - t - 1^{\,2} e^{\iota 2 k_0 n d} \right]^2} = \frac{16 t^2 \frac{R \;\; t + 1^{\,2} - t^2 - 1}{R \;\; t - 1^{\,2} - t^2 - 1}}{\left[t + 1^{\,2} - t - 1^{\,2} \frac{R \;\; t + 1^{\,2} - t^2 - 1}{R \;\; t - 1^{\,2} - t^2 - 1} \right]^2} =$$

$$= \frac{16 t^2 \left[R (t+1)^2 - \left(t^2 - 1 \right) \right] \left[R (t-1)^2 - \left(t^2 - 1 \right) \right]}{\left[(t+1)^2 \left[R (t-1)^2 - \left(t^2 - 1 \right) \right] - (t-1)^2 \left[R (t+1)^2 - \left(t^2 - 1 \right) \right] \right]^2} =$$

$$= \frac{16 t^2 \left[R (t+1)^2 - \left(t^2 - 1 \right) \right] \left[R (t-1)^2 - \left(t^2 - 1 \right) \right]}{\left[(t+1)^2 R (t-1)^2 - (t+1)^2 \left(t^2 - 1 \right) - R (t+1)^2 (t-1)^2 + (t-1)^2 \left(t^2 - 1 \right) \right]^2} =$$

$$= \frac{16 t^2 \left[R (t+1)^2 - \left(t^2 - 1 \right) \right] \left[R (t-1)^2 - \left(t^2 - 1 \right) \right]}{16 t^2 \left(t^2 - 1 \right)^2} =$$

$$= \frac{R^2\left(t^2-1\right)^2+\left(t^2-1\right)^2-2R\left(t^2+1\right)\left(t^2-1\right)}{\left(t^2-1\right)^2} = R^2+1-2R\frac{t^2+1}{t^2-1} \qquad (2.3.4.4c).$$

Formula (2.3.4.4 c) is a simple first order equation in t^2:

$$\begin{aligned} & T_+T_- = R^2+1-2R\frac{t^2+1}{t^2-1} \\ & \rightarrow T_+T_-\ t^2-1 = R^2+1\ \ t^2-1 -2R\ t^2+1 \\ & \rightarrow\ T_+T_- +2R-R^2-1\ t^2 = T_+T-R^2-1-2R \\ & \rightarrow t^2 = \frac{T_+T-\ R+1^{\ 2}}{T_+T_-\ -\ R-1^{\ 2}} \end{aligned} \qquad (2.3.4.4d)$$

from which we obtain:

$$Z = \frac{1}{n_0}\sqrt{\frac{T_+T-\ R+1^{\ 2}}{T_+T_-\ -\ R-1^{\ 2}}} \qquad (2.3.4.5).$$

Square root in Complex domain leaves an ambiguity in the sign. Luckily, we are obligated, because of the passivity of the media, to impose the real part of the impedance as not negative. By inserting (2.3.4.4b) inside (2.3.4.3b), we have:

$$T_\pm = \frac{4te^{\imath k_0 n_\pm d}}{\left(t+1\right)^2-\left(t-1\right)^2 e^{\imath 2k_0 nd}} = \frac{4te^{\imath k_0 n_\pm d}}{\left(t+1\right)^2-\left(t-1\right)^2\frac{R\left(t+1\right)^2-\left(t^2-1\right)}{R\left(t-1\right)^2-\left(t^2-1\right)}} =$$

$$= \frac{4te^{\imath k_0 n_\pm d}\left[R\left(t-1\right)^2-\left(t^2-1\right)\right]}{-\left(t^2-1\right)\left(t+1\right)^2+\left(t-1\right)^2\left(t^2-1\right)} = \frac{4te^{\imath k_0 n_\pm d}\left[R\left(t-1\right)^2-\left(t^2-1\right)\right]}{-\left(t^4+2t^3-2t-1\right)+\left(t^4-2t^3+2t-1\right)} =$$

$$= \frac{4te^{\imath k_0 n_\pm d}\left[R\left(t-1\right)^2-\left(t^2-1\right)\right]}{-\left(t^2-1\right)4t} = \frac{e^{\imath k_0 n_\pm d}\left[\left(t^2-1\right)-R\left(t-1\right)^2\right]}{\left(t^2-1\right)} = e^{\imath k_0 n_\pm d}\left(1-R\frac{t-1}{t+1}\right)$$

$$\rightarrow n_\pm = +\frac{\iota}{k_0 d}\ln\left[\frac{1}{T_\pm}\left(1-R\frac{t-1}{t+1}\right)\right]+m\frac{2\pi}{k_0 d} = +\frac{\iota}{k_0 d}\ln\left[\frac{1}{T_\pm}\left(1-R\frac{n_0 Z-1}{n_0 Z+1}\right)\right]+m\frac{2\pi}{k_0 d} \qquad (2.3.4.6).$$

The presence of the logarithm applied to a complex number introduces another ambiguity, connected to the phase of the argument of the logarithm itself, which leaves a proportional factor to the coefficient m. This ambiguity is not resolvable with

the present formulation, and could be deduced from the indexes inside (2.3.4.3) in the exponential function.

At this point all the coefficients are known (except from the ambiguous m inside (2.3.4.6), because from chirality factor in (2.3.4.1), and from the circular polarization index expressed in (2.3.4.6), it is possible to deduct the linear polarization without the chiral effects in n; this is also the average of the two index, while chirality factor is the semi-difference.

In our works we have used the following figure of merit as circular dichroic factor (CDF), because of its popularity:

$$CDF = 2\frac{T^+ - T^-}{T^+ + T^-} \qquad (2.3.4.7a)$$

or, alternatively, we focus on the absorption

$$CDF = 2\frac{A^+ - A^-}{A^+ + A^-} \qquad (2.3.4.7a).$$

Another way to indicate CD is just the difference, although less popular.

2.4 Fabrication Tools

The components presented in this thesis have been fabricated by using a top-down approach. In this section I present the fabrication instrumentations I have used the most; in order to obtain a good film quality, I have often employed lift-off process.

2.4.1 Spin coaters and hot plates

Spin coaters, or spinners, allow to depose thin films of liquid or viscous materials (usually polymers) on flat substrates, by using centrifugal force. Typically, a small portion of coating material is applied on the center of the substrate, which is either spinning at low speed or not spinning at all; then, the substrate rotated at high

speed in order to spread the coating material by centrifugal force; the rotations continue while the fluid spins off the edges of the substrate and the desired thickness of the film is achieved, Fig.2.8. The applied solvent is usually volatile, and simultaneously evaporates. So, the higher the angular speed of spinning, the thinner the film. The thickness of the film also depends on the viscosity and concentration of the solution and the solvent.

Depending on the type of solvent, after spin coating it may be necessary to bake the deposed material in order to change its nature from liquid to solid; for this use a *hot plate* is used. It is a portable self-contained tabletop small appliance that features one, two or more electric heating elements or gas burners; in laboratory settings, hot plates are generally used to heat glassware or its contents. Some hot plates also contain a magnetic stirrer, allowing the heated liquid to be stirred automatically.

Temperatures depend on the specific chemical reaction of the solvent. It is usually useful to distinguish between a *soft bake*, where a material is just dried off without changing its nature too much, and a *hard bake*, where the temperature allows the material to completely change.

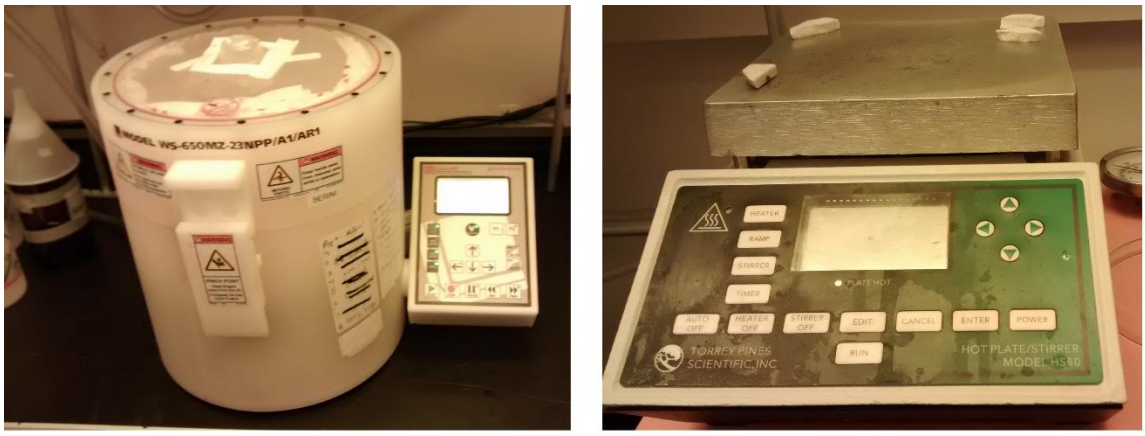

(a) (b)

Figure 2.8. Images of the spinner (a) and one of the hot plates (b) used for the structures presented in chapter 3 and 4.

2.4.2 Vacuum Evaporator

Deposition through evaporation is called also *vacuum evaporation*, since it involves vapors of metal in a chamber with a very low pressure; this method allows to depose

very flat and very thin layers of metals atom-by-atom or molecule-by-molecule on solid surfaces.

Evaporation consists in two physical processes: a hot source material *evaporates* and then it *condenses* on the substrate. The name of the vacuum evaporation process can be qualified based on the vapor source: in *thermal* evaporation the metal material is placed on a crucible in the form of pellets, and then fused when though heating due to radiation by electric filament. The low pressure (usually between 10^{-4} Pa and 10^{-6} Pa for nanometric thicknesses) of the chamber allows the vapor to move without colliding with other gasses. Once the gas reaches the substrate, it condenses on it little by little with time. Greater flatness and purity of the metal layer is obtained by choosing small deposition rates (i.e. 0.5 Angstrom/s) and by having very low pressures.

In general, a vacuum evaporator is a system composed of a chamber with vacuum pump, a metal holder, a substrate holder, and a system that evaporates the metal; a shutter and a thickness monitors help to control the deposition rate, etc. Fig. 2.9.a.

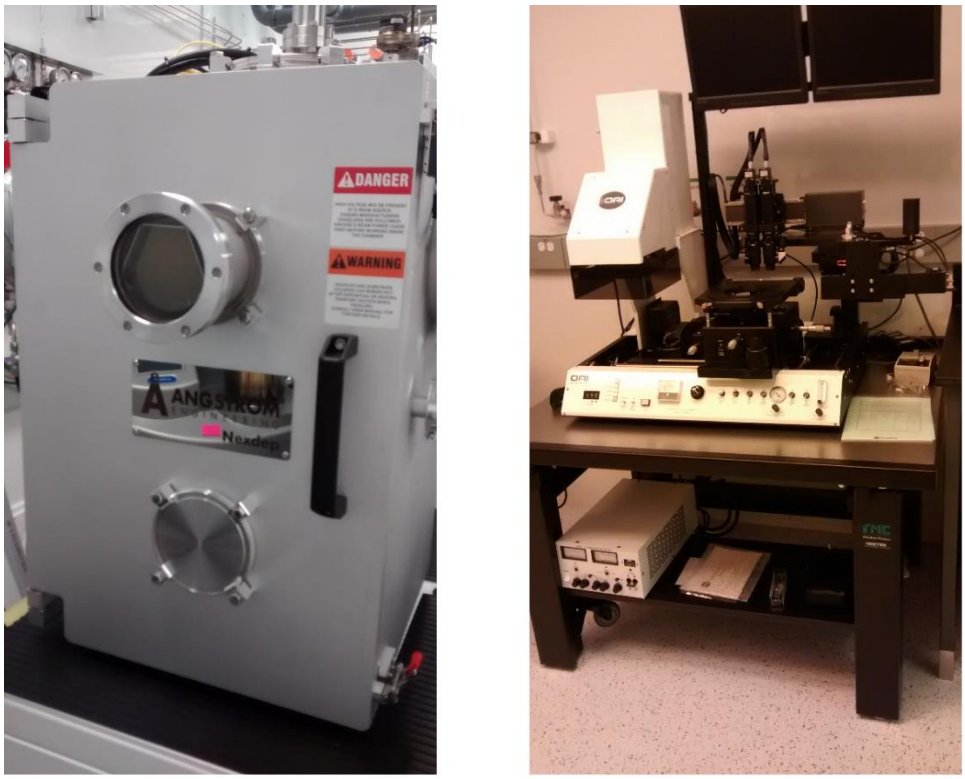

(a) (b)

Figure 2.9. (a) Model of evaporator, and (b) aligner used for the structures presented in chapter 3 and 4.

2.4.3 Photolithography: Mask Aligner and related processes

Photolithography, is a sequence of processes operated to transfer a geometric pattern from a photomask to a light-sensitive chemical, the *photoresist* (called also *resist*), by exposing it with UV light. It is extensively popular in micro/nano-fabrication, and has been widely used in electronic industry (i.e. in complex integrated circuits a modern CMOS wafer will go through the photolithographic cycle up to 50 times); the same apparatus is now used successfully in photonics.

Depending on the frequency of the light used, it is called *UV-lithography* or *deep-UV-lithography*; some frequencies/wavelength are more popular and are signed as letters (i.e. I line uses a 265nm light source), so the lithography may also be named after such letter. The desired geometries are imprinted to the photoresist through a *photomask*: an opaque plate with holes or transparencies that allow light to shine through in a defined pattern.

A series of chemical treatments are needed prior and after the exposure to engrave a pattern on a photoresist; a single photolithography is composed by a sequence of several steps:

I. *Preparation*: the substrate is cleaned and put at an appropriate temperature for the photoresists. Some adhesion promoter may be applied, in some cases; i.e. HMDS is useful to promote the adhesion of Cytop (a polymeric dielectric) on Silicon.

II. *Photoresist application*: the wafer is covered with photoresist by spin coating. The photo resist-coated wafer is then prebaked to drive off excess photoresist solvent, typically at 90 to 100 °C for 30 to 60 seconds on a hotplate.

III. *Exposure and development*: inside the mask aligner (Fig.2.9.b) the photoresist is exposed to a pattern of intense light. The exposure to light causes a chemical change that allows some of the photoresist to be removed by a special solution, called "developer". *Positive photoresists* become soluble in the developer when exposed, while in *negative photoresists* unexposed regions remain soluble in the developer. Sometimes it is better to "hard-bake" the resulting wafer in order to solidify the remaining photoresist, thus making a more durable protecting layer in future ion implantation, wet chemical etching, or plasma etching.

IV. *Photoresist removal*: after a photoresist is no longer needed, it must be removed from the substrate. This usually requires a liquid "resist stripper", which chemically alters the resist so that it no longer adheres to the substrate. Another method for dry etch the photoresist is made by using plasma containing oxygen, which oxidizes it; this process is called *ashing*.

The advantage of UV-lithography is that it allows to imprint large areas of wafers, and thus it can be used in industrial scale process flow. The optical instrumentation and the frequency of the exposure light decide the shape; today, deep-UV-lithographic technique have allowed to reach 8nm pitch size, a precision achievable with very few other technologies. Other than the cost of equipment, a non-indifferent cost is the price to produce masks, which depends on the size of the areas and the required precision; the success of Photolithography in the industry depends from the fact that such cost is scalable with the quantities.

2.4.4 Electron Beam Lithography

Electron Beam Lithography (EBL) is the method which uses a focused beam of electron to draw custom shapes on a surface covered with an electron sensitive film called e-resist (a similar operation is done also with Ion Beam Lithography, where the “ions” are charged positively). The electron beam changes the solubility of the e-resist, enabling selective removal of either the exposed or non-exposed regions of the resist by immersing it in a solvent (there is a distinction between *positive* and *negative* resists, just like photolithography). This allows to create very small structures in the resist that can subsequently be transferred to the substrate material with other processes; high resolutions have been obtained with EBL (dimensions under 10nm are achievable with this process); also, since there is no requirement for masks, there is no additional cost related to the production of single chips.

One of the limits of EBL is the time for “writing” the shapes with the electron beam, as this requires to expose all the required areas; for “dense” systems, this can be very time-consuming; EBL machines containing multiple beams would be faster, but the equipment is much more expensive. Another limiting factor is the scattering of electrons: as those penetrate the resist, they experience many small angle scattering events called *forward scattering*, which tends to broaden the initial beam

diameter; also, once the electrons penetrate through the resist into the substrate, they occasionally undergo large angle scattering events: *backscattering*. Scattering events are probabilistic, and can be calculated through numerical tools (fig. 2.10), but their effects cannot be removed completely, and need particular attention, as they create undercuts in the resists.

Popular electron beam resists are PMMA (positive) and SU-8 (negative). The choice between the two depends usually from the amount of resist polymer to remove: if it's a lot, then a negative one is needed, otherwise a positive one is better.

The exposure is needs to be dosed; in general, the main parameter is the area dose, which is the amount of energy of the beam imping on a surface.

$$Area\ Dose = \frac{Beam\ Current \times Area\ Dwell\ Time}{Step\ Size \times Line\ Spacing} \tag{2.6}$$

where the beam current is given by the electron source, the step size and the line spacing provides the step of the stage movement respectively for each dot and in line, and the *area dwell time* is the time to expose each point of the geometry. For example, to expose an area with a beam current of 110pAand dwell time of $4*10^{-4}$s it takes 14.5µC/cm^2 for each point.

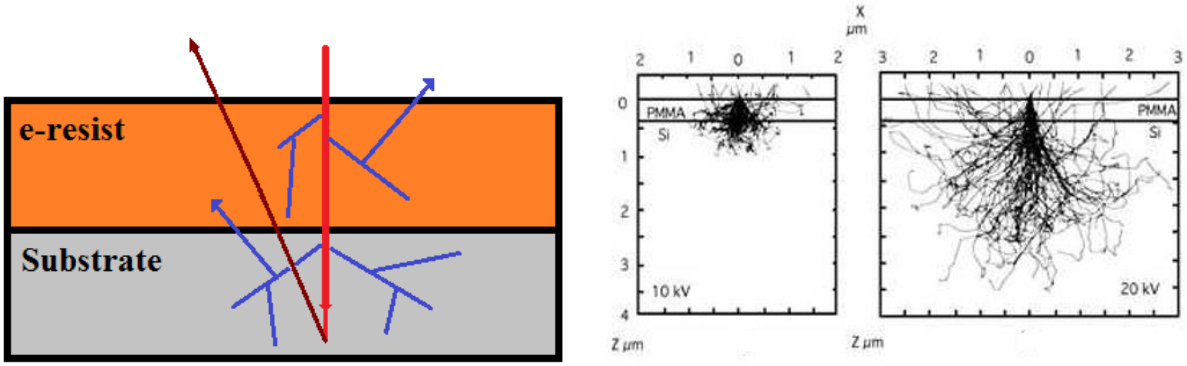

(a) *(b)*

Figure 2.10. (a)Electron trajectories in e-resist: An incident electron (red) produces secondary electrons (blue); the incident electron may itself be backscattered as shown here and leave the surface of the resist (purple). (b) Monte Carlo simulation of electron scattering in PMMA on a silicon substrate at 10 KeV and 20 KeV [48].

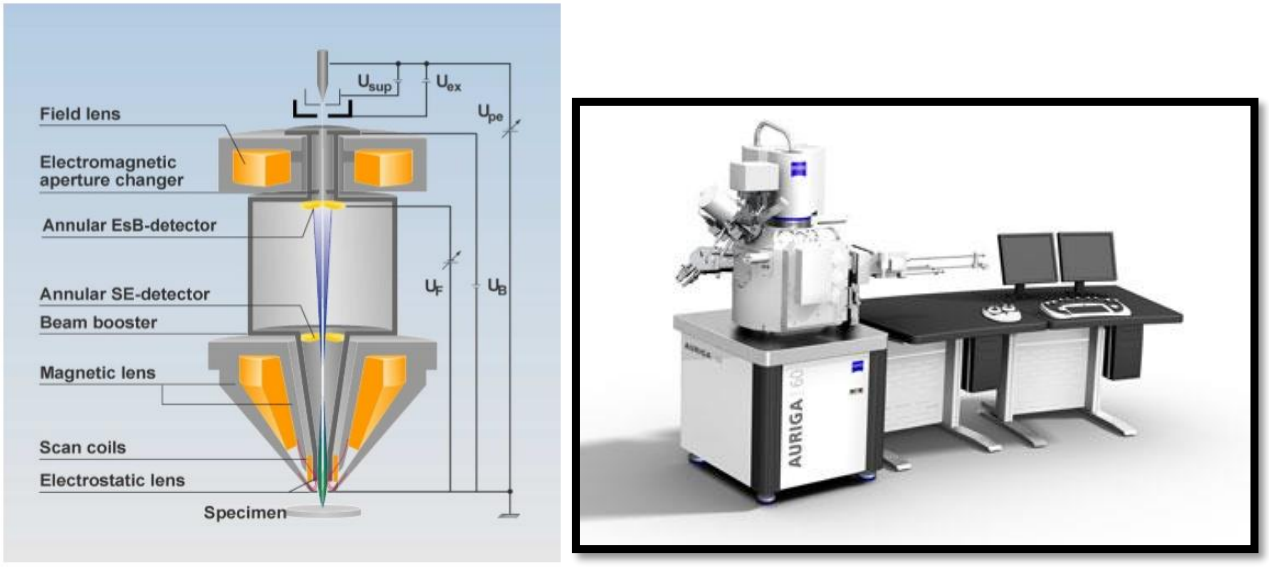

(a) *(b)*

Figure 2.11. (a)Electron optical setup of the Zeiss Gemini column optimized for low energy elctrons. (b) FESEM Zeiss Auriga model located in the La Sapienza's C.N.I.S laboratory.

2.4.5 Plasma Etcher

Between the various methods to etch (remove) materials from substrates, we can define two main branches: *wet etching* and *dry etching* (the first involves chemical reactions, the second a more physical approach); also, we can talk about two different directionalities: isotropic etching means that the removal acts toward all directions, while anisotropic means that there is a preferred direction (usually towards the gravity). While etching is an important topic in fabrication, and usually requires bigger spaces for the description, in this thesis we will focus only in the plasma etching (Fig.2.12).

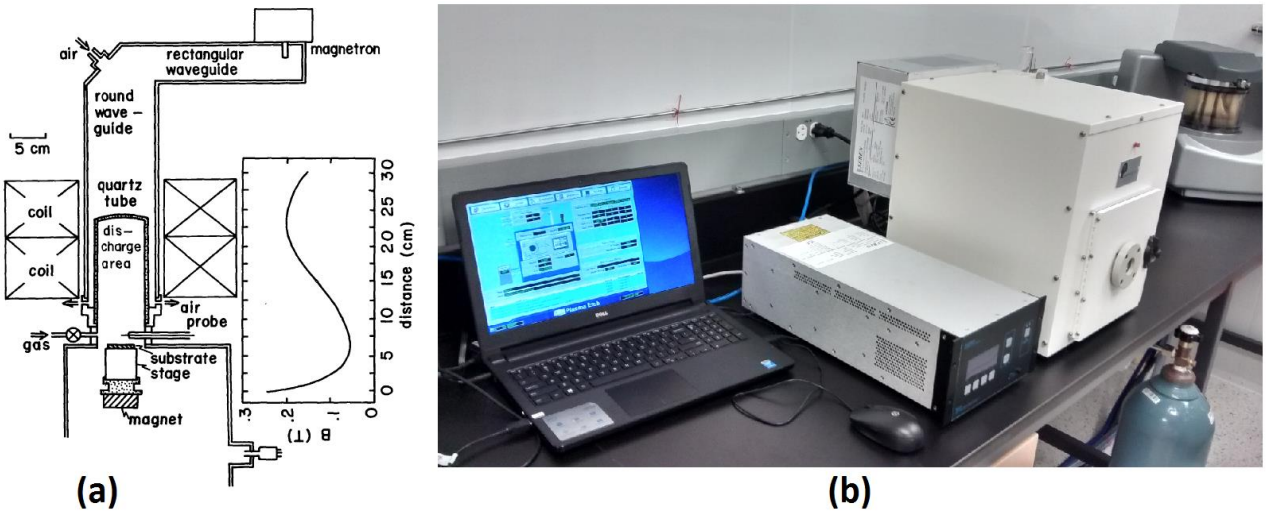

Figure 2.12. (a) Scheme and (b) photo of the plasma etcher I have used

Plasma etching removes layers of materials in order to create micro designs on the surface

Plasma etching is done using low-pressure plasma systems. Ion precursors (i.e. argon or oxygen) are used as the precursor gas and are channeled into the vacuum chamber with the wafer. Then, high power radio waves are applied in the chamber and this, along with the low pressure of the vacuum chamber, cause the ion precursors to ionize, forming plasma. The plasma generates volatile etch products at room temperature from the chemical reactions between the elements of the material etched and the reactive species generated by the plasma; eventually the atoms of the shot element embed themselves at or just below the surface of the target, thus modifying the physical properties of the target; i.e. Oxygen plasma creates Silicon dioxide with Si, or etches the polymers by turning them into ash. Additional products (i.e. ashes) are removed through the vacuum pump.

References

[1] S.A.Maier, “Plasmonics: fundamentals and applications”, Springer, 2009

[2] P.Berini, “Plasmon-polariton waves guided by thin lossy metal films of finite width: Bound modes of symmetric structures”, Phys. Rev. B 61, 10484-10503 (2000)

[3] R. Charbonneau, P. Berini, E. Berolo, and E. Lisicka-Shrzek, “Experimental observation of plasmon–polariton waves supported by a thin metal film of finite width”, Optics Letters, 25(11), pp. 844-846 (2000)

[4] R. Charbonneau, C. Scales, I. Breukelaar, S. Fafard, N. Lahoud, G. Mattiussi, P. Berini, “Passive integrated optics elements based on long-range surface plasmon polaritons”, Journal of Lightwave Technology, 24(1), (2006)

[5] G. Singh, Rajni, A. Marwaha, “A Review of Metamaterials and its Applications”, IEEE-IJETT, 19(6), pp.305-310 (2015)

[6] R. Fleury, and A. Alù, “Cloaking and invisibility: a review”, Forum for Electromagnetic Research Methods and Application Technologies(FERMAT), 1, 1–24 (2014)

[7] N. Yu and F. Capasso, “Flat optics with designer metasurfaces”, Nat. Mater., 13, 139–50 (2014)

[8] S. Zhang, W. Fan, N. Panoiu, K. Malloy, R. Osgood, and S. Brueck, “Experimental demonstration of near-infrared negative-index metamaterials”, Phys. Rev. Lett., 95 (13), p.137404 (2005)

[9] E. Nader, and R.W. Ziolkowski, "A positive future for double-negative metamaterials”, IEEE Transactions on Microwave Theory and Techniques, 53, pp. 1535-1556 (2005)

[10] D.J. Norris, “Photonic Crystals: A view of the future”, Nature Materials, 6, 177 - 178 (2007)

[11] D. Cohen, and R. Shavit, “Bi-anisotropic Metamaterials Effective Constitutive Parameters Extraction Using Oblique Incidence S-Parameters Method”, IEEE-Transactions on antennas and propagation, 63(5) (2015)

[12] V.K. Valev, J. Baumberg, B. De Clercq, N. Braz, X. Zheng, E. Osley, S. Vandendriessche, M. Hojeij, C. Blejean, and J. Mertens, “Nonlinear superchiral meta-surfaces: tuning chirality and disentangling non-reciprocity at the nanoscale”, Adv. Mater., 26, 4074–81 (2014)

[13] M. Esposito, V. Tasco, F. Todisco, M. Cuscunà, A. Benedetti, D. Sanvitto, and A. Passaseo, “Triple-helical nanowires by tomographic rotatory growth for chiral photonics”, Nat. Commun., 6, 6484 (2015)

[14] N.I. Zheludev, “Obtaining optical properties on demand”, Science, 348 973 (2015)

3 Analysis on vertical directional couplers with long range surface plasmons for multilayer optical routing

Introduction

The realization of efficient Optical Integrated Circuits is one of the key efforts in order to respond to the increasing demand of high speed signal transfer and manipulation. An alternative technology to the more popular dielectric waveguide-based devices is represented by Surface Plasmon Polaritons based systems, which have been extensively researched for various applications [1– 3]. Long Range Surface Plasmon Polaritons (LR-SPPs) have received special attention, mainly due to the fact that they offer reduced propagation losses and easier interfacing with standard optical fibers, compared to the strong-confinement of SPP-based structures [4, 5]. Many LR-SPP based devices operating at telecom wavelengths have been realized and presented in the literature [1]; measurements on some specific geometries demonstrated a high data transmission capability [6 – 8] and a good coupling with Single Mode Optical Fibers [2, 9, 10]; electrical switching has been demonstrated [2]; and optical switching is possible [11].

Those devices consist of very thin metal stripes (width >> thickness) inside a homogenous dielectric medium and usually perform their operations in a planar geometry [1]. The bound modes propagate along the dielectric/metal interface, and most of the field is localized on the dielectric side. While classical dominant technologies based on dielectric cores require multiple lithography steps, accurate deposition processes, and a good control over doping [1, 2], LR-SPP based devices need care only to the deposition of ultrathin metal layer, as the dielectric growth and lithography are more lenient on precision [2]. Moreover, when nonpolymeric dielectrics are used in dielectric core based devices, the thickness of the films acts as a major limiting factor, as it is proportional to the costs and because of the mechanical stress for values exceeding ~ 1μm; on the other hand, polymeric dielectrics can act as a very good medium for LR-SPPs and can be easily deposited on films several micrometers thick without incurring in significant mechanical stress [12]. In practice, LR-SPP technology is much cheaper than its counterpart and allows to vertically "stack" multiple layers, which is a key requirement for multilayer optical routing.

Directional coupling is one of the fundamental passive operations, and LR-SPP based directional couplers have been extensively studied [13 – 17]. Most of the

devices are expected to operate at a single plane, so Lateral Directional Couplers (LDC) have been developed and optimized. Vertical Directional Couplers (VDC) between LR-SPPs has also been studied in Refs. 18 and 19; in the former work, an interferometer using such a phenomenon has been experimentally demonstrated, showing significant increase in interaction, while in the latter a comparative study with LDC has been done by taking into account the effect of the main topological (geometrical) parameters. Both works underline the potentialities of this process in the creation of multilayer photonic routing, as well as the reduction of Coupling Length, which means shorter devices and thus lower losses due to propagation.

The bend radius of the sample built in Ref. 18 was too small (~ 600 μm as can be estimated from the images), which resulted in a significant amount of power loss due to radiation and transition, as also stated by the authors; the results lose a quantitative meaning, making the work a good qualitative proof-of-principle. The increased interaction makes the device more sensitive to geometrical nonidealities due to fabrication imprecisions; also, the analyses have been done on vertical coupling between two straight paths and ignored the interaction on the bent part, which we demonstrate to be significant. Thus, in Refs. 18 and 19, the authors needed further parameters in order to describe all the main characteristics of the VDCs.

In the present work, a Vertical Directional Coupler (VDC) structure working in the third window ($\lambda = 1.55\ \mu m$) is proposed and analyzed with the aim of achieving efficient optical routing. Differently from previous works, in order to obtain exhaustive information about the overall behavior of the device, this analysis comprises also the important topic of the additional interaction on the bent part: a practical method is presented and applied in order to engineer the correct combinations of geometrical parameters to reach the desired final amount of signal exchange, even in the presence of small geometrical parameter's variations due to fabrication issues. The scheme of the device presented here is designed in order to minimize propagation losses thanks to the presence of one only S-Bend. Between the various possible applications, we underline that the abilities to easily "stack" multiple planar circuits, and enabling them to communicate through these efficient VDCs, make LR-SPP technology a good option for the production of cheap and high density network systems [20].

In Section 2, the scheme of the device is presented along with the main parameters and settings of the calculations. In Section 3, the computation of the coupling coefficients of the different paths of the device is shown; in particular, the method used to compute the additional coupling of S-Bend is presented. In Section 4, the relationship between fabrication tolerances and relative performance to the change of some parameters is evaluated. Finally, the main summary and conclusions are drawn.

3.2 Schematic and settings

The calculations presented in this chapter have been carried out at telecom wavelength of $\lambda = 1.55$ µm and will be focused on the fundamental, symmetric, bound quasi-*TM* modes [1, 2, 4, 5]. There are many possible geometries that can implement vertical directional coupling [18, 19, 21 – 25]; in the present work, the analysis is focused on a structure represented by two elements in two different layers: a "long" straight stripe on a layer, while on another layer two "short" straight stripes are connected on the ends of a S-bend (Figs. 3.1(a)–1(c) show the unscaled scheme of the whole structure).

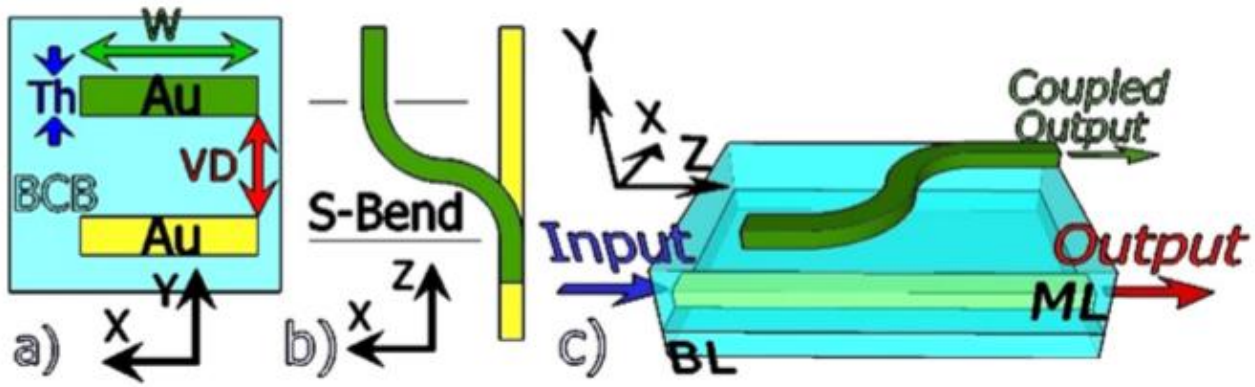

Figure 3.1. Different unscaled views of the device, with Cartesian axes. (a) Transverse view of the scheme, with the main parameters. (b) Scheme of the structure from top view. (c) 3-D view of the structure, with signal paths; top dielectric is not shown for graphical purposes.

The two layers are positioned in order to guarantee that one of the "short" straight stripes is parallel on both the vertical and horizontal directions with the "long" one (from a top view, they are overlapped); this is the region where the "straight coupling" will take place. In the region where the long straight stripe will interact with the bent stripe, "additional coupling" shall take place. These two couplings compose the total signal exchange of the device, since on the other ends the stripes are far enough to approximate the interaction to zero.

The analyzed structure has three signal ports: input, output, and coupled output. The long straight waveguide (on layer 1- in yellow) is connected on both ends with external signal paths (i.e., single mode optical fiber), which are the input and

output; the S-bend (layer 2 in green in Fig. 3.1) is connected only through the coupled output.

This scheme has been decided in order to minimize insertion loss, which is the sum of all propagation, radiation, and transition losses. Big bend radii allow to reduce power loss due to radiation and transition [26], while the propagation length is reduced by increasing the interaction (as shown in Sections 5.3A and 5.3B) and by reducing the total path length; this element requires a single S-bend, differently than most directional couplers [15 – 18]; thus, it propagates on shorter paths.

In what follows, the main geometrical parameters that will be engineered are: vertical distance (VD) between the layers, the bending radius (R) of the S-bend, the single stripes' width (W), and thickness (T). The horizontal displacement of the S-bend (distance between output and coupled output) has been fixed at 250 μm.

Once the main rule of having very low thickness is satisfied, the other geometrical shapes (W, R, VD) can be controlled to adjust the selected performance of the device. The geometrical dimensions of this analysis have been chosen to be around the range of the landmark structures present in literature [16, 17]; here *Au* stripes ($\epsilon_r = -93.0839 + i*11.1097$ at $\lambda = 1.55\mu m$) are embedded within polymer cladding ($n = 1.443$ at $\lambda = 1.55\ \mu m$), with widths between 4 μm and 10 μm and thicknesses between 15nm and 25nm. Since those structures have a low propagation loss, a low coupling loss with SM-fiber and proven measurement values, it is easier to make comparisons.

3.3 Parameter Evaluation

3.3.A Coupling length of the straight path

In order to compute the (co)directional coupling between the strips, a supermode approach to coupled mode theory has been used [24]; the same method has been successfully used with LR-SPPs in Refs. 16, 23, 25, and 27, showing very good matching between experiments and calculations. Through Finite Element analysis (2-D) on two

vertically parallel strips, the effective indexes of the symmetric and antisymmetric supermodes related to the fundamental quasi-TM mode have been extracted; from that, the "coupling length" (L_C), which is the minimum length necessary for two parallel paths to completely transfer an input signal from one to another, and the corresponding coupling coefficient (K) can be obtained from Ref. 24

$$L_C = \frac{2\pi}{Re[\beta_s - \beta_{As}]} = \frac{\pi}{2K} \tag{3.1}$$

with β_S and β_{As} the symmetric (even) and antisymmetric (odd) propagation constants, respectively, of the overall structure. As can be discerned from (1), an increase in L_C corresponds to a decrease of K and interaction. Once K or L_C are obtained, the exchange of power between the two straight stripes through the interaction path can be calculated through Ref. 24

$$P_1 = P_0 \times \cos^2(K_Z),$$
$$P_2 = P_0 \times \sin^2(K_Z) \tag{3.2}$$

being P_1 and P_2 the input and coupled stripes' power, and Z is the longitudinal axis. The relation between the computed L_C and the VD between the two straight paths is shown in Fig. 3.2; stripes with different widths (thickness is fixed at 20nm) in Fig. 3.2(a) and thicknesses (width is fixed at 8 µm) in Fig. 3.2(b) are shown.

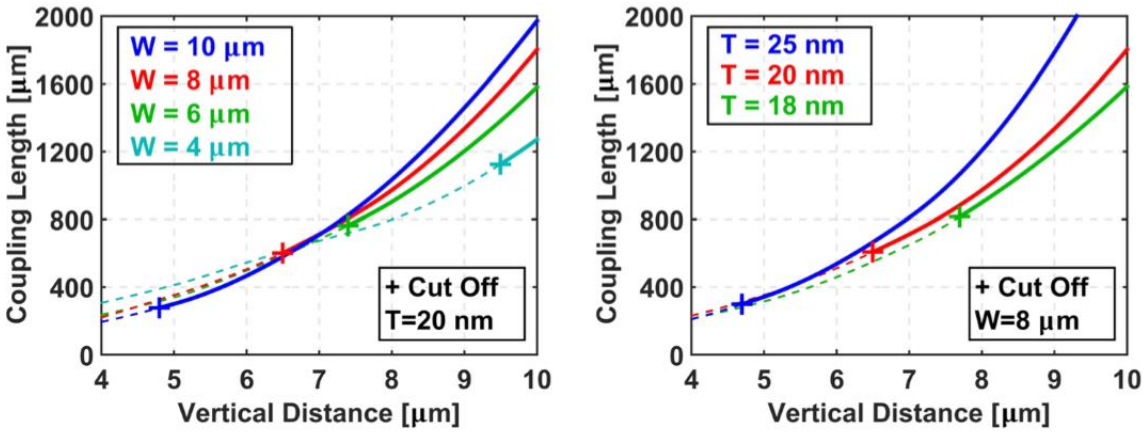

Figure 3.2. (a) Coupling Length as a function of the vertical distance for a fixed *T* = 20nm and for *W* = 10 µm (blue line), *W* = 8 µm (red line), *W* = 6 µm (green line), and *W* = 4 µm (cyan line). (b) Coupling Length as a function of the vertical distance for a fixed *W* = 8 µm and for *T* = 25nm (blue line), *T* = 20nm (red line), and *T* = 18nm (green line).

L_C is shorter than LDCs since the mode field is distributed more in the vertical direction than lateral: the overlap areas are increased, resulting in enhanced interactions [5,

18, 28]. A small L_C allows to have a reduced straight path and thus low overall propagation losses (but this also makes the additional coupling on the bent part more significant, as shown in Section 3.3B). As reported in Ref. 18, a limit value of VD has been found, under which the odd supermode reaches its cut-off limit and becomes leaky (dotted line in Figs. 3.2(a) and 3.2(b)). It can be observed that the increase in the size of the single stripes' width and thickness may decrease the cut-off VD value, allowing to reduce L_C more, but this needs to be counterweighted with increased losses [1, 2, 4, 5, 19].

3.3.B Additional coupling computation and control

In order to have negligible radiation and transition losses, LR-SPP strip based devices and circuits have very big bending radii, on the order of tens of millimeters [16, 23, 26].

This means that the separation of the two strips in the bent part of VDCs will be slow, so a relevant amount of additional coupling is expected, due also to the strong interaction along the vertical direction. Thus, while in conventional LDCs the additional coupling has a small influence on the overall device, in VDCs it is significant and needs to be taken into account. Thus, an approximated method has been introduced in order to calculate it through the same theory, tools, and simplified relations used for the straight path coupling.

The calculation of the additional coupling has been done after several steps: at first, the relation between L_C and the Lateral Distance (LD) has been computed by means of the discussed method in Section 3.3.A (Figs. 3.3(a) and 3.3(b)); then, the values have been interpolated; finally, after approximating a bend into many small straight segments, each with a specific LD calculated from the straight strip (Fig. 3.3(c)), the total signal exchange has been obtained by combining together all contributions from the segments.

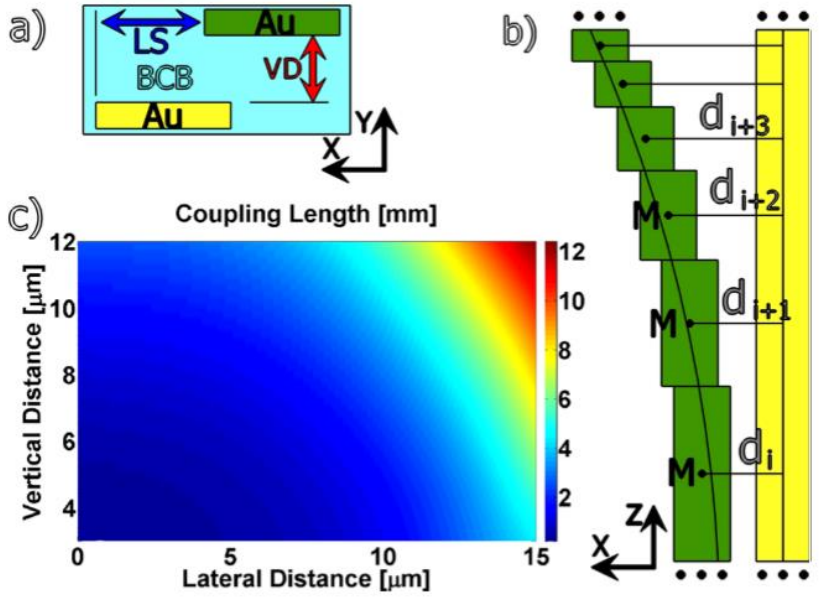

Figure 3.3. (a) Transverse unscaled view of the scheme used for the 2D Finite Element analysis, with the main parameters. (b) Geometrical description of the mathematical method: the bend is divided into many small segments (each one is laterally shifted from the previous and the next by a very small value); the length of the segments shrinks as the lateral shift grows. (c) Plot of the Coupling Length as a function of the lateral distance among the waveguides for different vertical distance values.

The different losses due to propagation through the two different paths have been taken into account: while on the straight line the attenuation loss of each segment is proportional to the length dz, on the S-bend the corresponding segment has a proportionality to dz*dϑ.

Since the interaction decreases exponentially with LD, the variations of δK have been neglected for LD > 27 µm: over that point, the directional coupling is too weak, and the biggest differentiation between the "main" and "coupled" signals is given by the different path length (and thus propagation loss). Since the stripes are still almost parallel when the calculation is truncated, expressions (1) and (2) keep valid, and consequently this method can be assumed as genuine for the chosen range of R.

This approach has been applied on LR-SPP stripes with W = 8 µm, T = 20nm, VD = 7 µm, LD < 20 µm, with various R (ranging from 8 mm to 40 mm) in order to find the optimum value for the desired coupling ratio, as shown in Fig. 3.4; on the plot, Z = 0 represents the starting point of the bend; normalized power ($P_{main}/(P_{main} + P_{coupled})$, $P_{coupled}/(P_{main}+P_{coupled})$) is shown in order to focus more on the power ratio. Since the final lateral shift between the output and the coupled output is fixed (at 250 µm), each value of R changes the longitudinal length of the S-bend

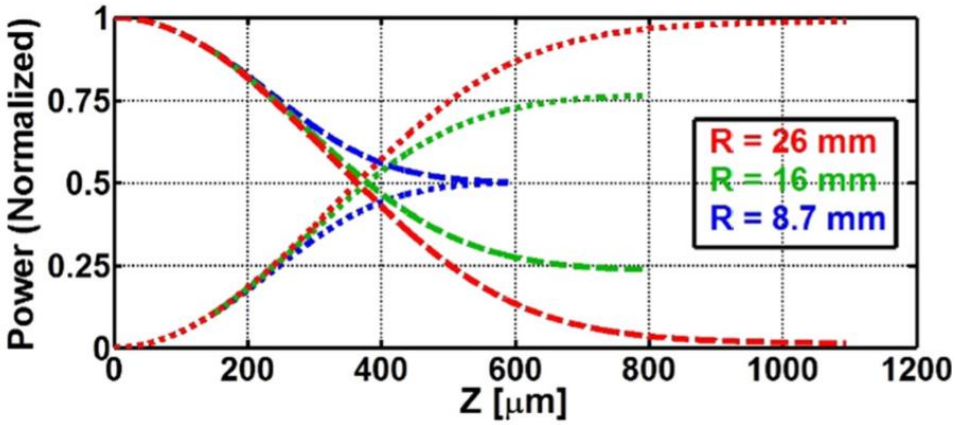

Figure 3.4. Normalized power exchange between the two stripes as a function of the length of the straight stripe (dashed line: $P_{main}/(P_{main}+P_{coupled})$, dotted line: $P_{main}/(P_{main}+P_{coupled})$). In the analyses, the stripes have *W* = 8 μm, *T* = 20nm, VD = 7 μm, *propagation loss = 13.42 dB/cm (*corresponding to measurements done as in Ref. 13), and several Rs. The calculation interrupts when LD = 20 μm. As can be seen, the final signal ratio can be adjusted by selecting R. The length of the device is also related to R, since the final LD is fixed.

With VD fixed, it is possible to choose the correct final power ratios (usually 50–50 or 100–0) by setting the value of R (Fig. 3.5); the only condition is that R needs to be high enough to guarantee that bend losses are due mainly to the propagation. As can be seen, there are ample areas of optimal topological choice for 100–0.

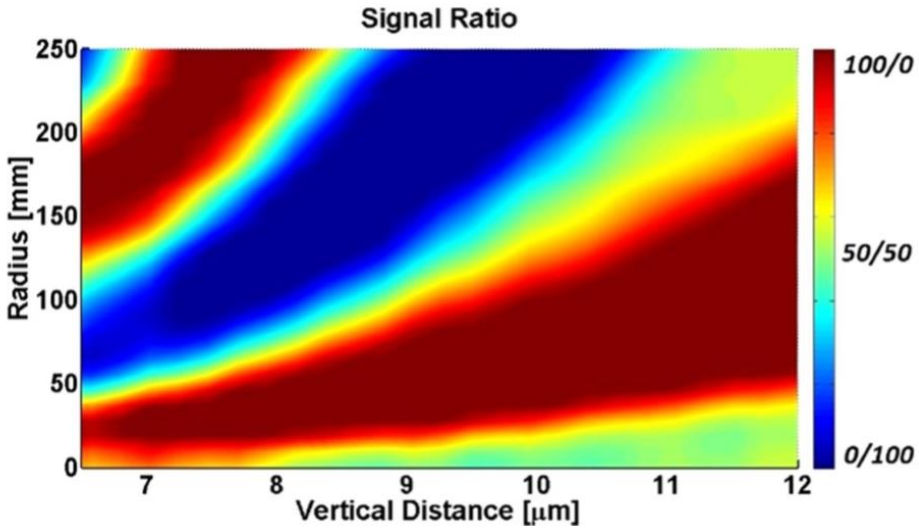

Figure 3.5. Final signal ratio of the S-Bend as a function of VD and R, with *W* = 8 μm and *T* = 20nm. The calculation has been done by following the method presented above. The optimum value of R can be chosen from this graph, in combination with the length of the straight path.

At the same time, the straight part's coupling ratio can be controlled with its length (Fig. 3.2). The total coupling of the device is given by the linear combination of the straight and S-bend parts.

Fig. 3.6 shows the coupling in the first part of S-bend when the input signal is set at the straight stripe, and W = 8 µm, T = 20nm, VD = 7 µm, R = 30mm, and LD < 20 µm; power has been extracted 100nm from the stripes. After a certain LD, the interaction becomes negligible, and the coupled power is subject mainly to propagation loss; it should be noticed that, if X and Z axis had the same scale, they would be almost parallel (at LD = 20 µm, they would be tilted by 2°).

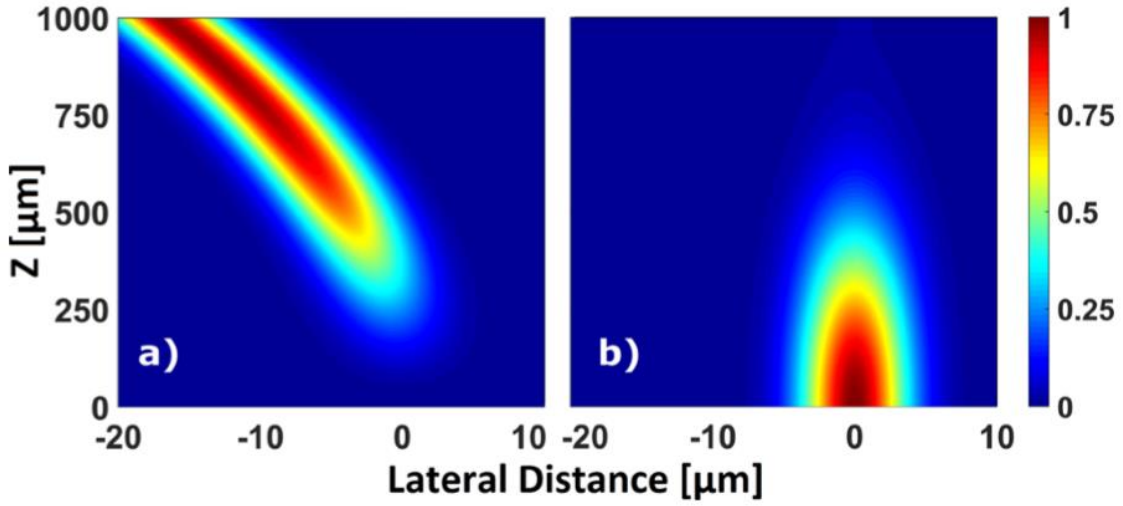

Figure 3.6. Optical power propagation extracted at 100 nm above and below the top and bottom stripes, respectively, for the 100–0 operation on the bend region up to a 20 µm LD, when W = 8 µm, T = 20nm, VD = 7 µm, and R = 30mm. (a) Power 100nm upon the S-Bend; from LD = 20 µm to 250 µm, this path carries almost the entirety of the total power, affected mainly by propagation loss from that point on. (b) Power below the straight stripe, which loses almost all power.

3.4 Fabrication tolerances

There are in the literature many techniques, materials, and methods to fabricate ultra-thin-strip based systems on a single layer [21, 29, 30]. As shown in Sections 5.3A and 5.3B, when a multilayer interaction is involved, many geometrical parameters influence the operations, and need a specific degree of precision: stripes' width and thickness, flatness of the deposited layers, the thickness of the middle dielectric layer (VD), and the alignment between layers.

A good control over the deposited *Au* strips' thickness at nanometric scale is expected to be easily achievable with standard sputtering or evaporation machines, although at those dimensions the strips' flatness may be hindered by the presence of small lumps and cracks, whose main consequence is an additional propagation loss [31]. The relaxed sizes of the circuits (multi-micrometric width and multimillimetric bending radii) ease photolithographic processes with the currently available technologies, thus allowing repeatable results and a good control over the width. From Fig. 3.2, it is possible to discern that there are ideal VD values that allow to minimize the fabrication errors' effects; i.e., we notice from Fig. 3.2(a) that by choosing VD = 7 µm, *W* = 8 µm and *T* = 20nm, it is possible to reduce significantly the effects of width variations.

VD has a significant influence on vertical Directional Coupling, as already shown in Sections 3.3A and 3.3B. Unfortunately, the cut-off values for VD are higher than the growth limits of particularly stable materials that can be deposed through accurate low-temperature fabrication processes (i.e., chemical vapor deposition grown SiO2 [32]). The most viable materials seem to be polymeric dielectrics such as Benzocyclobutene, Cytop, or poly-methyl methacrylate, which can be deposed through spin coating, although a certain degree of inaccuracy of the film thickness (VD) is expected because of environmental conditions. By using the same methods described in Sections 3.3A and 3.3B, it is also possible to foresee the effects of the VD variations on the power exchange; while the straight coupling's characteristics are compromised, it is possible to compute for the S-Bend an optimum R that can minimize the variation of the final signal ratio. This is proven by Fig. 3.7, where the influence of a VD variation of 0.5 µm is shown, with all the other parameters fixed: *W* = 8 µm, *T* = 20nm, and R = 23mm. The chosen value of R makes allows to reduce, in the S-Bend, the effects of the variations on the final coupling ratio.

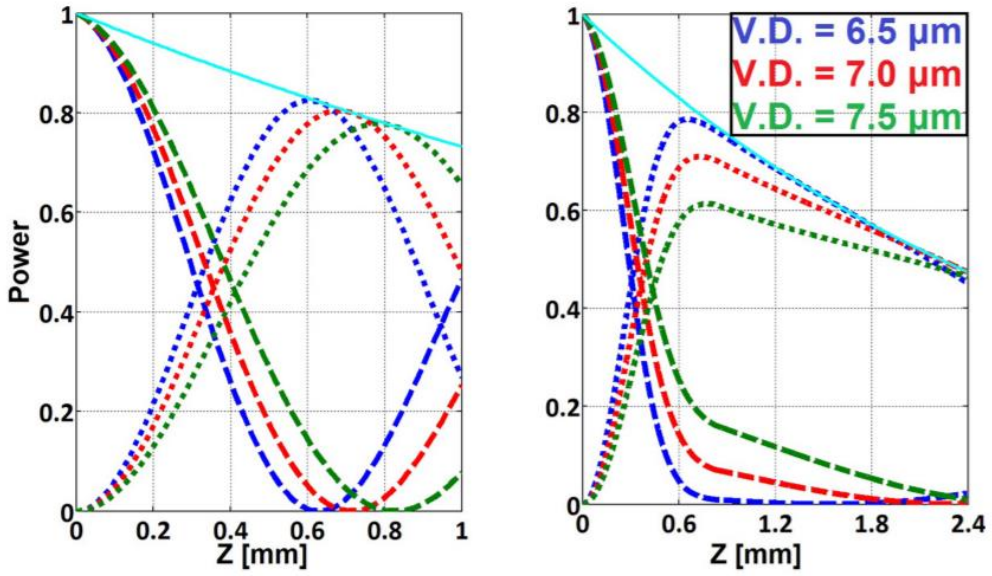

Figure 3.7. Power exchange for VDCs with *W* = 8 µm, *T* = 20nm, with different VDs; dashed line represents main path signal, and dotted line represents the coupled path signal. (a) On the straight coupling region VD variations change significantly the L_C. (b) In the additional coupling region, there are little changes to the final coupling ratio if R = 23mm.

Since this structure involves the patterning of two different layers, a certain amount of misalignment is expected. Just like VD variations, there is an optimum bend radius value that minimizes, in the S-Bend, the effects of misalignments; on the straight path L_C increases the same independently from the direction of the misalignment.

In Fig. 3.8, the resulting effects are shown, with *W* = 8 µm, *T* = 20nm, and R = 23mm, VD = 7 µm; positive misalignment represents the unwanted lateral shift of the layer towards the direction of the bend, while negative is on the opposite side.

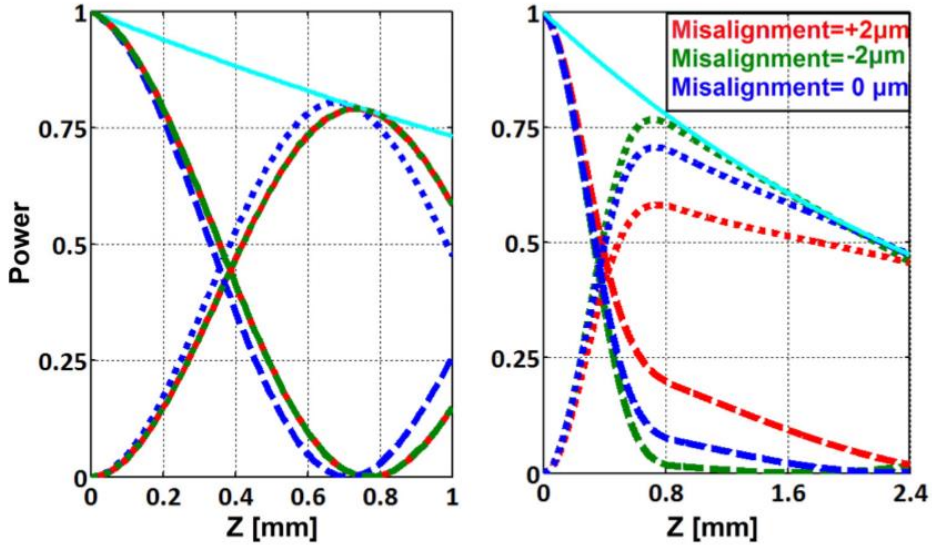

Figure 3.8. Power exchange for VDCs with *W* = 8 μm, *T* = 20nm, and VD = 7μm with different misalignments; positive misalignment values represent the lateral shift of the layer towards the direction of the bend, while negative is on the opposite side. Dashed line represents main path signal, and dotted line represents the coupled path signal. (a) On the straight coupling region, misalignment variations increase LC, regardless of the direction. (b) In the additional coupling region, there are little changes to the final coupling ratio if it is close to the optimum, such as R = 23mm.

3.5 Conclusions of the analysis and future developments

From the present analysis, it is possible to discern general information regarding VDCs and the methods to design them. We have introduced and used a pragmatic method to compute the interaction in the s-bend region; the approximations used within this method are coherent with the features of the most popular LR-SPP based systems. It is clear that, differently than LDCs, the interaction on the first parts of bends in VDCs is relevant and cannot be neglected. We have shown also that this "additional" coupling can be controlled by tuning the geometrical parameters, in particular, bend radius.

The major fabrication issues are those that affect the repeatability of the devices: the precision of the middle dielectric layer deposition and the misalignment between layers; their effect regards mainly the straight path, as the final coupling ratio of the bent path can be optimized through an optimum R calculated through the aforementioned method. Fig. 3.5 shows that if 100–0 additional coupling ratio is chosen for the s-bend, there is an ample range of values of bend radii to choose, like those used for Figs. 3.7 and 3.8. Lower governability of the straight path's coupling ratio makes us expect more crosstalk in VDC than LDC, which can be reduced only by an increased amount of fabrication accuracy, and consequently costs.

Overall, while VDCs exhibit smaller propagation loss than LDCs, they require more fabrication complexity (still lower than standard dielectric based optical integrated circuits) and have lower precision in signal transmission. As formerly stated, to our opinion, the main reason to produce them should be the undeniable topological advantage they can give to LR-SPP optical circuits. The ability to easily stack different layers of optical integrated circuits which communicate through VDCs

makes LR-SPP technology a good option for the production of complex network systems.

3.6 Plasmonic Bridging System by means of vertical directional coupler with long range surface plasmons

Profiting from the topological advantages given from 3.1-3.7, I have proposed a new system where vertical directional coupler may find useful application: signal bridging from one point of a chip to another. An example of the proposed scheme is shown in fig. 3.9a.

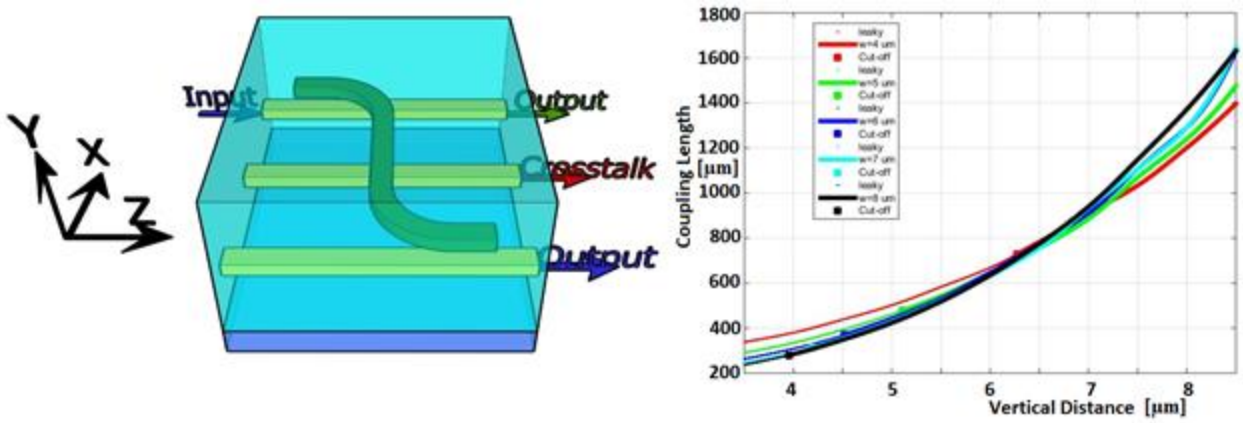

Figure 3.9. (Left) Sample device I proposed: the signal input power needs to be transfrered fully (100/0) or half (50/50) from the first stripe to the third. Crosstalk to other stripes (the second) needs to be low. The stripes at the bottom planar layer are shown in yellow, while the top planar layer, containing the "bridge", is shown in green. (Right) Lc vs Vd for stripes with t=20nm and with different widths. Red: w=4[µm]. Green: w=5. Blue: w=6[µm]. Cyan: w=7[µm]. Black: w=8[µm]. Crosses are the cut-offs.

Such structure contains two VDCs, and allows to move a part of the input signal contained in a waveguide to another waveguide far away without compromising other waveguides in the middle; the VDCs are needed to allow the communication between the bottom circuit (shown in yellow) and the top circuit containing the "bridge" (green). The scheme shown in fig.3.9 allows to study the possible crosstalk inside the middle stripe. The two VDCs need a precise design as stated in sections 3.1-3.7, in order to work as designed.

I have produced a process flows for the fabrication of such structures by using a lift-off process; the plan includes the materials: Au stripes within a Su-8 dielectric environment (n=1.573). The calculations presented in 3.1-3.7 have been repeated with the new material; the result of the analysis is shown in Fig.3.9.

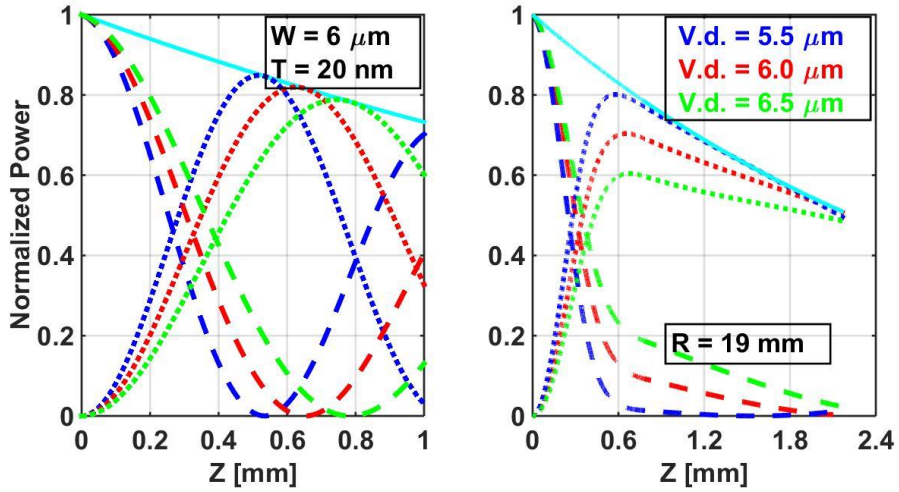

Figure 3.10. Power exchange with straight path (Left) and s-bend (Right) with Au stripes within Su-8, when Vertical Distance is changed (due to possible material deposition errors).

Between the various options, shown in table 3.1, I have chosen w=6µm and t=20nm, as this allowed me to have good propagation loss and safe bend losses; due to mode mismatch, fiber-to-stripe coupling is 50%, which forced us to create a taper as a mode adapter (see next chapter).

W	t	Pout/Pin [%]	CL [dB]	Re(neff)	Xr(R=25mm) [µm]	PL [1/m]	Imag(neff)	Xr (R=19mm) [µm]
8	20	50,90%	2,9	1,574725	34	1,35E+03	3,85E-05	25,84
	15	66,5	1.80	1,573772	19	5,17E+02	1,47E-05	14,4
Leaky as	10	86,9	0,61	1,573126	3,15	2,16E+02	6,14E-06	2,394
6	20	50,2	2,99	1,574276	31	1,17E+03	3,32E-05	23,56
Leaky as	15	68,43	1,647	1,573483	12	4,32E+02	1,23E-05	9,12
4	20	56,6	2.47	1,573621	15	8,00E+02	2,27E-05	11,4
Leaky as	15	77,8	1,09	1,573119	2,97	3,18E+02	9,03E-06	2,2572

Tab 3.1: Parameters obtained from simulations on structures with different width and thickness.

Lift-off has been chosen over the more traditional subtracting techniques like etching for various reasons: to obtain good control over the width of the structure, avoid sidewall non-uniformity because of etching, and to ensure repeatability. The process flow for a standard lift-off, as applied to a vertical coupler, is shown in Fig. 3.11.

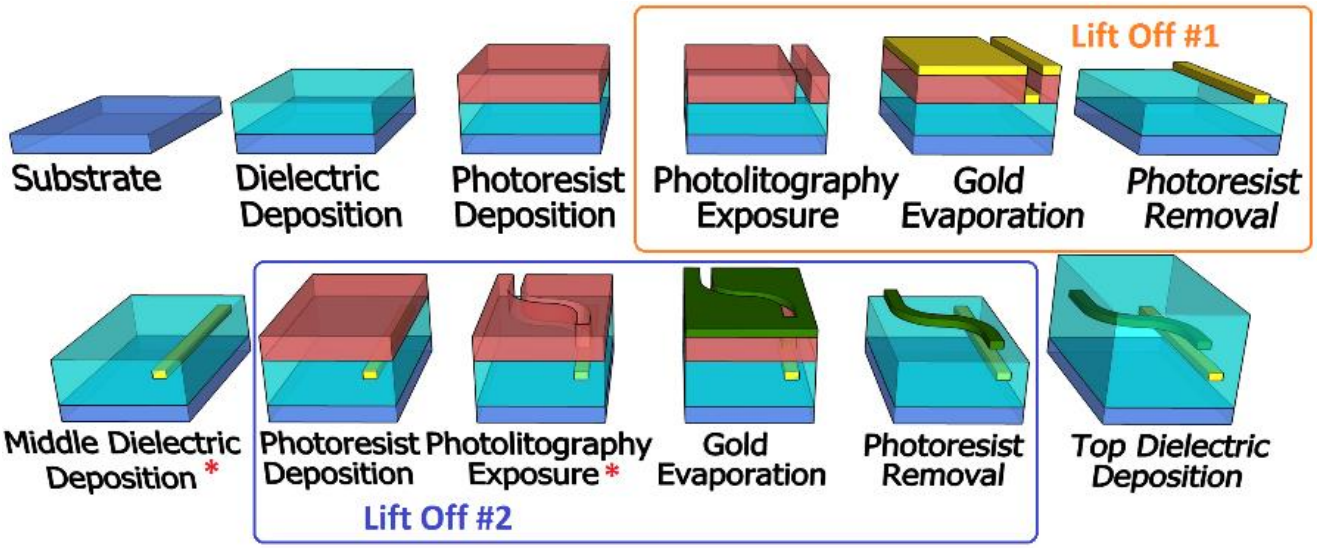

Figure 3.11. Fabrication process flow of the multilayer circuit, presented in the form of a vertical directional coupler. Lift-off process is used to construct the Au stripe.

It can be seen that we need two lift-off processes. As stated in section 3.4, and as shown in Fig.3.10, particular care needs to be given to the thickness of the middle dielectric layer to avoid dis-uniformity between design and fabricated structure. I chose middle dielectric as 6.25µm in order to reduce the effect of width variation (due to photolithography aleatory imprecisions).

3.7 Mask design

The scheme in Fig.3.9.left, along other structures, has been implemented and drawn using graphical programs such as Autocad; the result has been exported in GDSII standard through DW2000, another Cad program. This bi-planar circuit needs two masks, corresponding to the planar circuits stacked together.

The resulting masks are shown in Fig.3.12; particular attention has been given to the markers, which are needed for the alignment of the second circuit with the first

(Fig. 3.13.a). There are also markers for EBL fabrication and Dicing mark (Fig.3.13.b); the latter is necessary to the dicing.

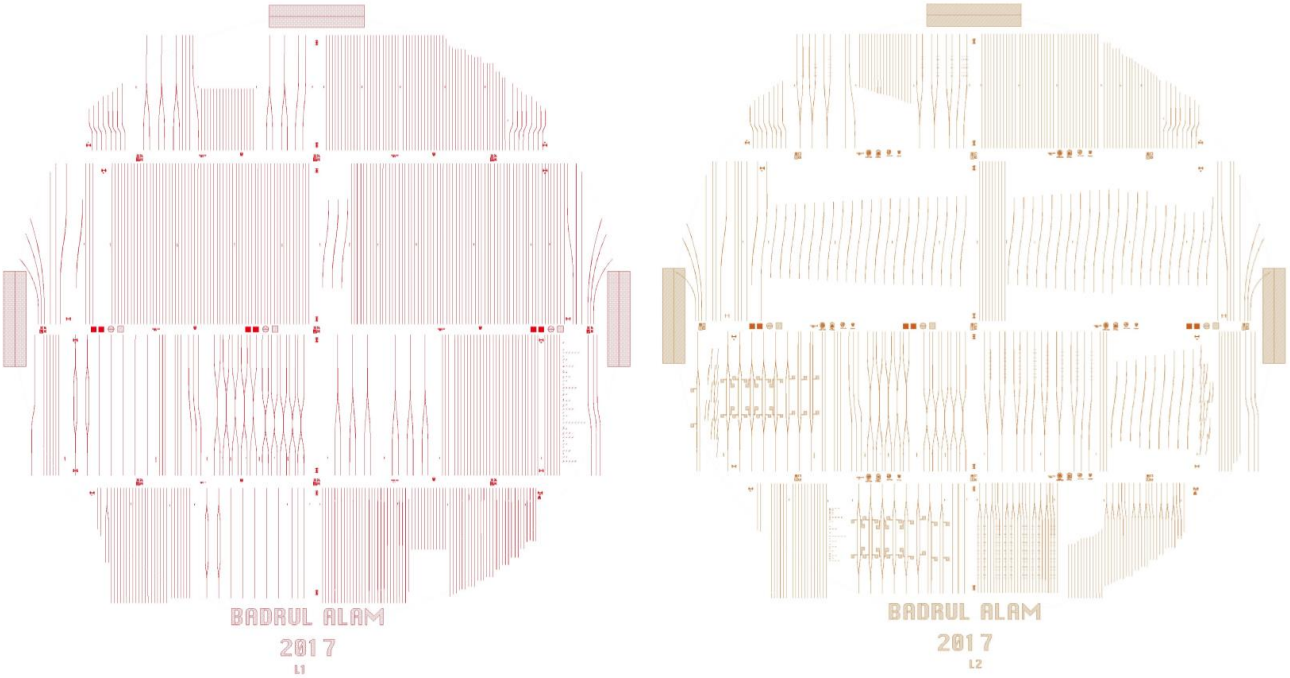

Figure 3.12. Masks outline for the two schemes.

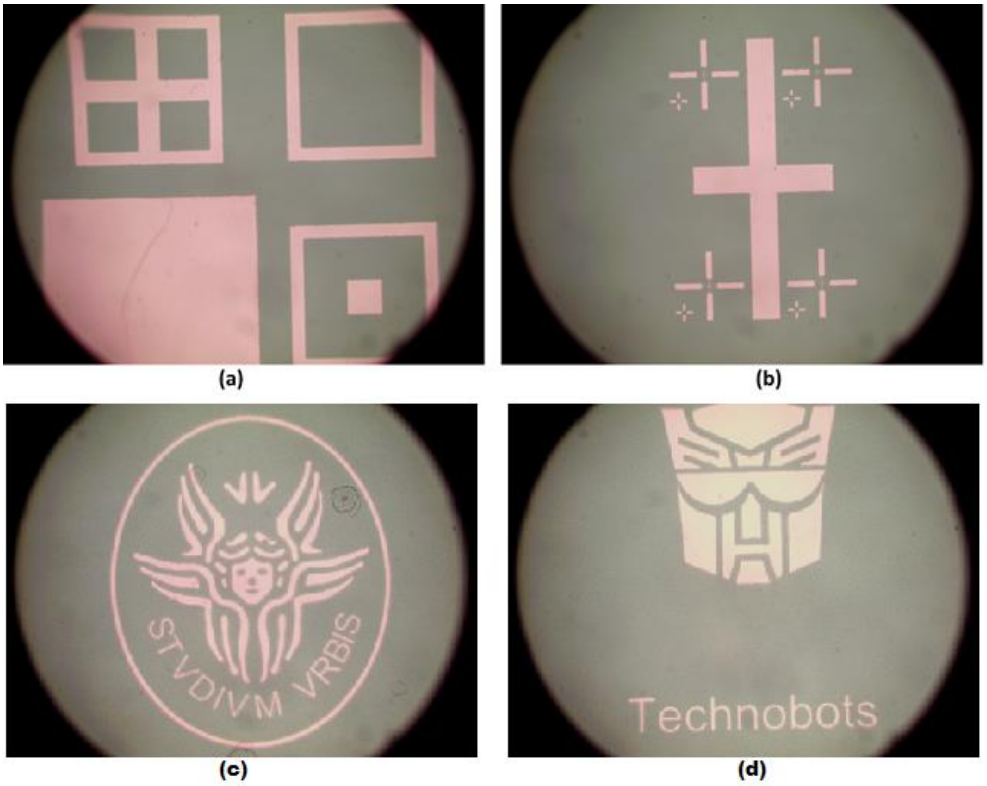

Figure 3.13. Alignment markers for photolithography (a) and dicing/EBL (b), (c) and (d) are additional markers

3.8 Bilayer lift-off process flow

As an evolution of standard lift-off, *bilayer lift-off* has been chosen as our method to fabricate the LR-SPP waveguide system on SU-8 because it has previously proven effective with other polymers, and because we expect it to become a repeatable process flow. An alternative way of producing the same type of circuits can be found in literature, where a metal (Au) layer is deposed and, after defining the pattern with photolithography, wet etched; the merit of that method is the flatness of the metal layer, while the flaw is in the wet etching itself: the difficulty in handling and in the possibility to have inhomogeneous sidelines.

The optical elements we have produced had stripes with different widths (2.25µm, 6 µm, 10 µm), tapers with different profiles and lengths, bends, overall length of one or more cm, and we expected a thickness of 20nm; also, we have stacked two circuits together, which translated into stacking multiple layers of SU-8. We used SU-8 2005 from Microchem, which helps to achieve a thickness of 3 to 7µm. The bottom and top claddings usually need a higher thickness (>10µm) to reduce leakage with the substrate, so we stacked two SU-8 layers; in order to guarantee adhesion, we used plasma (more detail are in the following sections).

3.9 Fabrication of plasmonics signal bridge

3.9.1 SU-8: polymer handling

SU-8 is an epoxy based negative resist with relatively good optical transparency and is sensitive to near UV radiation. While we utilized it as a substrate, it is usually used as a negative resist, which needs to be exposed and baked in order to guarantee crosslinking. Cured films of SU-8 are highly resistant to solvents, acids and bases and have excellent thermal and mechanical stability, making it well suited for permanent use applications, in particular in MEMS and microfluidics; also, it is less expensive than

other more popular polymers for surface plasmons: BCB, ZEP, Cytop. The refractive index is 1.573.

As datasheets suggest, after being spun on a substrate, SU-8 needs to be pre-baked in a hotplate at 95°C for a few minutes, then exposed to UV radiation around I-line, and then post-baked at 95°C for another few minutes; it is possible to hard-bake at 150°C-200°C for 5-30minutes to make sure that the properties will not change (we did not need a hard-bake, although we indirectly used it, as photolithography process needed a baking of 180°C for 3 mins). We changed some values from the datasheets, in particular we extended the bake time and temperature; after spinning, we first baked at 65°C for 5 minutes and then at 95°C for 10 minutes; this ensured graduality, and allowed to reduce the probability of having small holes due to fast temperature variation (actually, in the final devices, we used the same hotplates, and changed the temperature from 65°C to 95°C, ramping ~4 deg/min, and did not have those holes at all). After exposure, we baked 10min at 65°C and 20min at 95°C. During (flood) exposure, to ensure penetration of the light inside the whole thickness of the SU-8 layer, we increased a little bit (less than 10%) the amount of energy suggested by the datasheet; but we must underline that also tests with bigger amount to exposure energies (2x) did not give us any tangible issue. In fig.3.13(left), we have the interpolated graph of the energy vs thickness, as suggested by datasheets and as used by us.

We poured SU-8 directly from the bottle, as this guaranteed the absence of bubbles; if pipettes were used as middle carriers, there was always a chance to have small bubbles, which may ruin the quality of the material as dielectric; with a small stick (we suggest to use the final part of a pipette), by sliding it through the perimeter, we ensured the spread of the polymer throughout the whole area of the sample. It is advisable to wait a certain amount of time (in our case, 1 min) after pouring, to allow the dense fluid to settle on the whole substrate, and some other time (in our case, 1 min) right after spinning has been completed, to allow the fluid on the sample to rest.

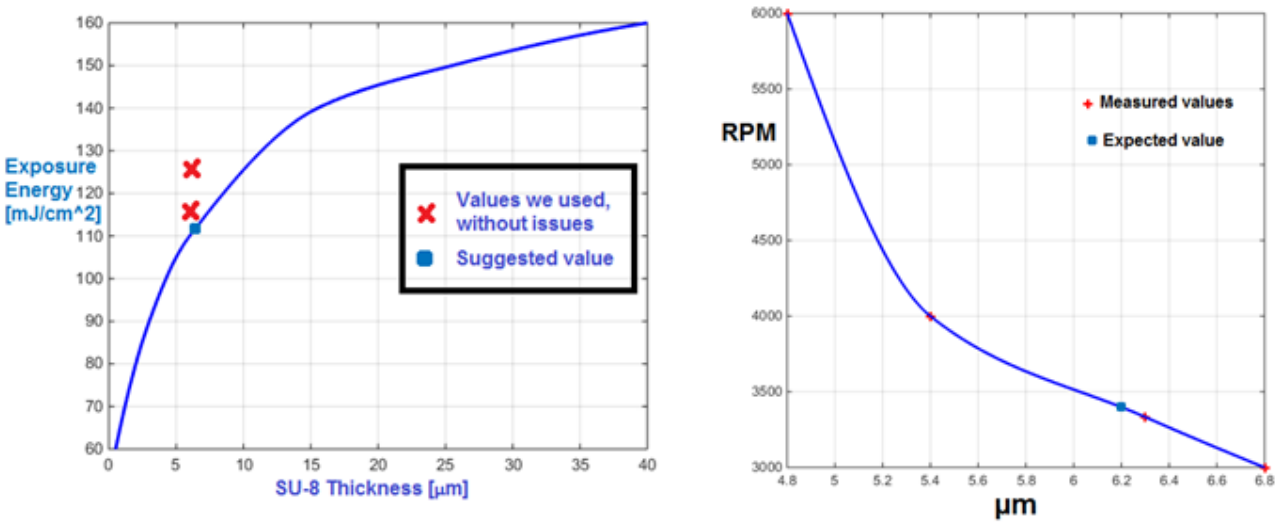

Figure 3.13. Left: Exposure energy vs thickness, as suggested by datasheet, on Si substrate. Right: Spin speed vs Thickness, of Su-8 layer on Su-8 layer, as measured after tests.

With SU-8 2005, and with the spinner at our disposal, we had good spins if they were > 1500RPM, for more than 30÷40seconds; before increasing the spin speed, it is good to have a middle values for 10 seconds. Spins > 3000 RPM usually guaranteed a reduced edge bead; when stacking multiple layers of SU-8, the "cumulative" edge bead may become an issue for both the following spins and exposure (actually, for our project, there was no trouble with it). Since in our project the middle dielectric layer's thickness is critical, we made various tests with SU-8 deposed upon other SU-8; the resulting graph is shown in fig.1(right); in general, we can state that SU-8 deposed upon Si has a little bit lower adhesion, but similar.

Sometimes, when multiple SU-8 layers are stacked or when we have a very thick layer, there may arise issues with adhesion with other polymers or even with itself; in such situations, it is advisable to treat the surface with O_2 plasma in order to increase roughness. We used 25W for 15 seconds to obtain a roughness of Rq=0.385nm, in the final device; higher values of power and time are not advisable because it may remove too much SU-8 and create un-manageable roughness values: i.e. 50W for 3 minutes removed around 70nm, and created a roughness of Rq=2.5nm. If SU-8 is exposed to PG Remover, the roughness may increase too. Roughness management with plasma treatment has proved important for the success of a multilayer, stacked structure.

Once deposed, removing SU-8 may prove very difficult due to its high chemical resistance. Right after spinning, it is possible to remove it if the wafer is inserted

within a bath of acetone and IPA, and splashed repeatedly through a pipette. If it has been soft baked (95°C), and/or it has been exposed, it can be removed after putting it in 80°C PG Remover, and ultrasonic 37KHz for 30 min; we managed to do something similar with 80°C water and ultrasonic 37KHz for 40 min, because in that specific situation our exposure did not penetrate enough; if a sample has been hard-baked, it's SU-8 removal may not be successful.

3.9.2 Bilayer lift-off methodology

As already stated, the circuit has been constructed by stacking multiple layers of SU-8 (5 in total: 2 for the bottom cladding, 1 for the middle, and 2 for the top cladding), and 2 photolithographic processes.

A bilayer liftoff process was used, in which a layer of LOR-1A is first spun and baked and then a layer of positive photoresist (Shipley S1805) is spun on top of it. LOR-1A and S1805 have no interlayer mixing. After exposure of the S1805, the pattern was developed in Shipley MF-321 developer. After the exposed photoresist is dissolved, the developer will start dissolving the underlying LOR-1A, resulting in a controllable undercut. This undercut makes the liftoff process repeatable and reliable.

In general, development time is related to the roughness of the underlying SU-8, as this influences the thickness of LOR-1A to remove. Since LOR-1A has a relatively slow dissolution rate, compared to other resists like PMGI, it guarantees a bigger amount of development time (in our case, 110 seconds); but, at the same time, since we have different stripe widths, the control of the development time and method has been critical for the quality of the stripes: in particular, being the chemical dissolution weak, the movement defined the "fluido-dynamics" of the removed materials, and the correct development of specific areas. In general, the outer borders of the wafers had more development that the center; less importantly, sometimes the stripes with the smaller width seemed to have less development. Wings usually resulted from under-development and from over-development. We adopted a movement of the wafer inside the developer (MF-321) as shown in fig.3.14(Left); it may seem trivial,

but the results from a well performed movement and an ill performed one is very tangible: see remaining images from Fig.3.14.

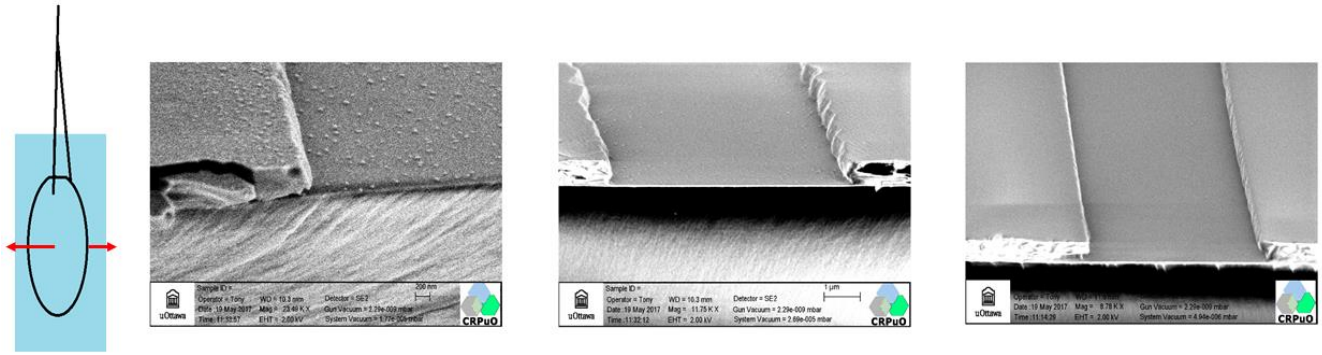

Figure 3.14. Left: movement of the wafer within the developer. Remaining: SEM image of a channel after development with insufficient movement (Center Left: the flatness of the gold will be ruined by the bits and dirt at nm level), insufficient flow (Center right: the sides of the stripe will be irregular, and there will be wings), and with correct movement (Right: Sufficient undercut and no dirt, thus having a successful stripe).

If the aligner is handled correctly, the alignment and the exposure should not be big issues. We used contact aligning, and it proved reliable and repeatable on the long run.

** The trick with our specific aligner is to rely mainly on the contact vacuum and avoid pressing even slightly the mask: if there is any pressure before the activation of the contact vacuum, the resulting connection will not be efficient (the value will be less than 10); if the sample is very close to the mask, but still not contacting, when the contact vacuum is activated, the contact will be more effective (the value will be more than 20). Some care must be dedicated to the sample holder: if it is not flat and parallel to the mask, and if the contact vacuum is not activated correctly, entire areas of the sample/wafer may be exposed incorrectly, or not exposed at all… **

3.9.3 Fabrication recipe

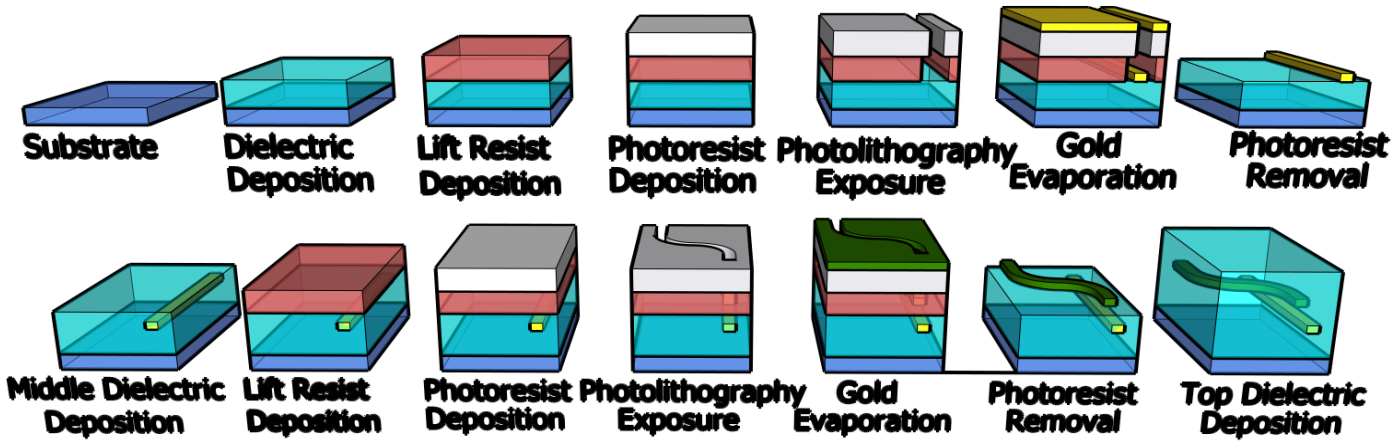

Figure 3.15. Fabrication of the two circuit levels through bilayer lift-off.

<u>Bottom Cladding deposition</u>:

This first layer is the bottom cladding; this needs to be highest possible; we used a double spin of 3400RPM, because it was a high enough value to ensure reduced edge bead. After each deposition, we plasma treated the sample to control the roughness to guarantee good adhesion with the next layer.

SU8 Layer 1:

- Silicon substrate cleaning:
  - Plasma O2 Etching, «Preen», 10 min, 50W.
  - Dehydration: hotplate 200°C, 10 min (Prof. Sun 30min @120°C)
- SU-8 2005 Spin coating:
  - Pour the SU-8 directly from the bottle, and spread it
  - (1 minute wait)
  - (13sec@200r/s)+(10sec@2600rpm)+(4sec@200r/s)+(40sec@3400rpm)+(7sec@500 r/s)
  - (1 minute wait)
- Prebake: 5 min @ 65°C + 10 min @ 95°C
- Exposure:
  - (For 6µm): 115mJ/cm² (I-line): 5,6s @ intensity 20,32 mW/cm².
- Post exposure bake: 10min @ 65°C + 20 min @ 95°C (according to paper, 3-4 minutes)

- Plasma treatment: 0, 15 sec @ 25W. (To gain roughness of Rq = 0,385 nm)

SU8 Layer 2: Repeat SU-8 Layer 1.

<u>Circuit LV1</u>:

All the processes shown here are repeatable, although a particular care must be given to the development; in general, the development time between the center and the borders of the sample/wafer will differ slightly.

Photolithography:

- **LOR-1A:**

- Pour with pipette
- (1 min wait)
- Fast Spin: (15sec@200r/s)+(10sec@3000rpm) +(15sec@200r/s) +(30sec@6000rpm) + (6sec@ -1000r/s)
- (1 minute wait)
- Bake: 3 min @ 180°C

- **S1805:**

- Pour with pipette
- (1 min wait)
- Fast Spin: (15sec@200r/s)+(10sec@3000rpm) +(15sec@200r/s) +(30sec@6000rpm) + (6sec@ -1000r/s)
- (1 minute wait)
- Bake: 3 min @ 115°C

- **Expose**:

- Set up wafer inside aligner
- Expose: 64mJ/cm² (I-line) or as indicated (or 64,5mJ/cm² for a little bit of overexposure)

- **Develop**:
    - MF-321 for 110sec or indicated time.

- Water right after development, to turn off the process; then dry

- **AU Deposition**:
  - 20nm Thermal Evaporation
- **Lift Off**:
  - PG Remover, for 4 minutes; when finished, ultrasonic 37KHz, for 10÷15 sec
  - Acetone bath, ~20 sec, remove PG by flowing it
  - IPA bath, ~20 sec
  - DI-H_2O bath; and dry it

Middle dielectric layer:

Since we needed a thickness of 6.25µm, we used a spin speed of 3400 RPM.

SU8 Layer 3:

- SU-8 2005 Spin :
  - Pour the SU-8 directly from the bottle, and spread it
  - (1 minute wait)
  - (13sec@200r/s)+(10sec@2600rpm)+(4sec@200r/s)+(40sec@3400rpm)+(7sec@500 r/s)
  - (1 minute wait)
- Prebake: 5 min @ 65°C + 10 min @ 95°C
- Exposure:
  - (For 6µm): 115mJ/cm² (I-line): 5,6s @ intensity 20,32 mW/cm².
- Post exposure bake: 10min @ 65°C + 20 min @ 95°C (according to paper, 3-4 minutes)
- Plasma treatment: 0, 15 sec @ 25W. (To gain roughness of Rq = 0,385 nm)

Circuit LV2:

This is the same as the previous layer, except for one critical thing: the correct alignment with the previous circuit. Given the small thickness variations between the various regions of the sample/wafer, there should not be any alignment issue, if soft contact is used correctly.

Photolithography:

- **LOR-1A:**

- Pour with pipette
- (1 min wait)
- Fast Spin: (15sec@200r/s)+(10sec@3000rpm) +(15sec@200r/s) +(30sec@6000rpm) + (6sec@ -1000r/s)
- (1 minute wait)
- Bake: 3 min @ 180°C

- **S1805:**

- Pour with pipette
- (1 min wait)
- Fast Spin: (15sec@200r/s)+(10sec@3000rpm) +(15sec@200r/s) +(30sec@6000rpm) + (6sec@ -1000r/s)
- (1 minute wait)
- Bake: 3 min @ 115°C

- **Expose**:

- Set up wafer inside aligner
- Expose: 64mJ/cm² (I-line) or as indicated (or 64,5mJ/cm² for a little bit of overexposure)

- **Develop**:

    - MF-321 for 110sec or indicated time.
    - Water right after development, to turn off the process; then dry

- **AU Deposition**:
    - 20nm Thermal Evaporation
- **Lift Off**:
    - PG Remover, for 4 minutes; when finished, ultrasonic 37KHz, for 10÷15 sec
    - Acetone bath, ~20 sec, remove PG by flowing it
    - IPA bath, ~20 sec
    - DI-H_2O bath; and dry it

<u>Top Cladding Deposition:</u>

Again, we use a double deposition of SU-8 to ensure a high enough thickness.

SU8 Layer 4:

- SU-8 2005 Spin :
    - Pour the SU-8 directly from the bottle, and spread it
    - (1 minute wait)
    - (13sec@200r/s)+(10sec@2600rpm)+(4sec@200r/s)+(40sec@3400rpm)+(7sec@500 r/s)
    - (1 minute wait)
- Prebake: 5 min @ 65°C + 10 min @ 95°C
- Exposure:
    - (For 6µm): 115mJ/cm² (I-line): 5,6s @ intensity 20,32 mW/cm².
- Post exposure bake: 10min @ 65°C + 20 min @ 95°C (according to paper, 3-4 minutes)
- Plasma treatment: 0, 15 sec @ 25W.

SU8 Layer 5: Repeat SU-8 Layer 4.

Additional: preparation for dicing

Before sending the sample/wafer to the dicing step, it is better to cover it with another resist, which will protect it from the debris. After dicing, it can be removed. SPR220 is perfect for this task.

SPR220 deposition:

- SPR220 Spin :
    - Pour the SU-8 directly from the bottle, in the middle
    - (1 minute wait)
    - (10sec@200r/s)+(30sec@2000rpm)+(4sec@-500r/s)
    - (1 minute wait)
- Bake:
    - 30 min @ room temperature
    - change the temperature to 100°C
    - 20 min @ 100°C
    - Change temperature from 100°C to room temperature

Dicing: to a private company

3.9.4 Fabrication Results

By following the recipe of the previous sub-section I obtained profiles of the waveguides similar to the expectations (Fig.3.16); the Au film is flat and sidewall profiles are uniform. Some small profiles still displayed “wings” and dirt, proof that the development is not uniform in all areas of the wafer; also, tapers and waveguides with different widths demonstrated to have different optimum development time.

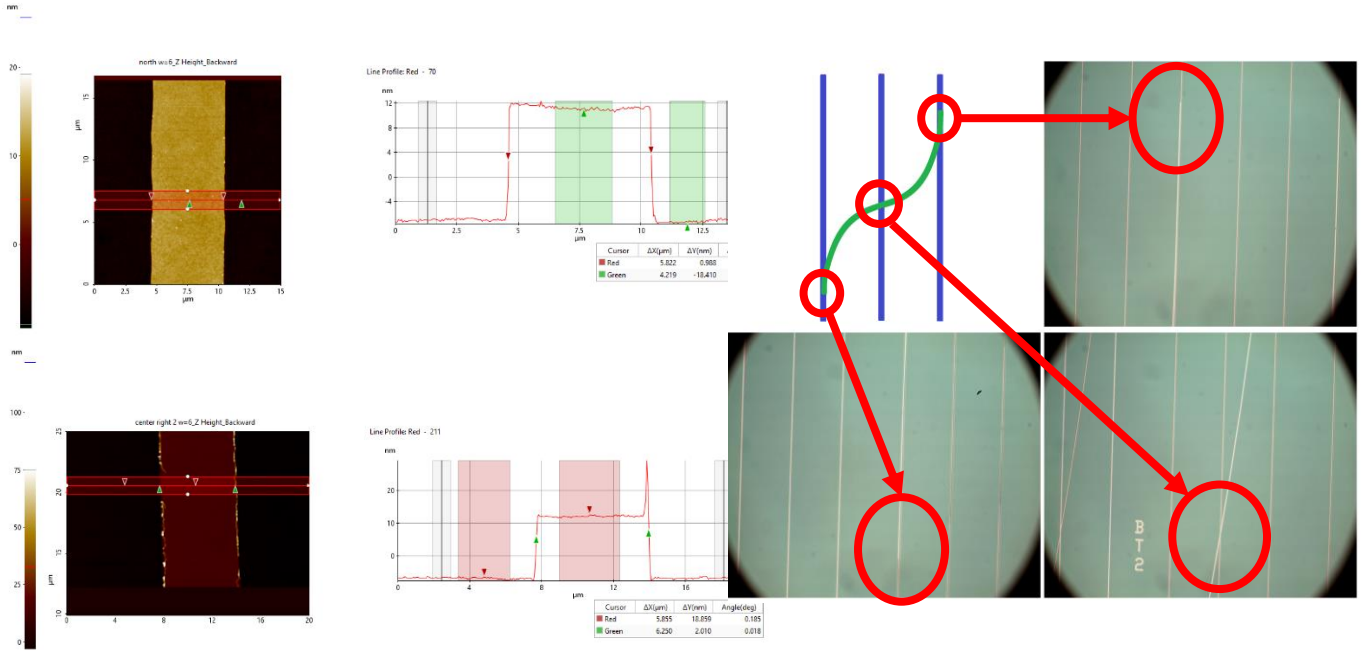

Figure 3.16. Left: AFM images of the metal stripes; some "wings" are present at the sides of the stripes. Right: Microscopy images of the signal bridge.

Dicing may have traumatic effects on the dielectric's adhesion or on their facets, as shown in Fig.3.7. The quality of the facets is critical for the measurements, as an opaque facet may scatter the input signals from the fibers.

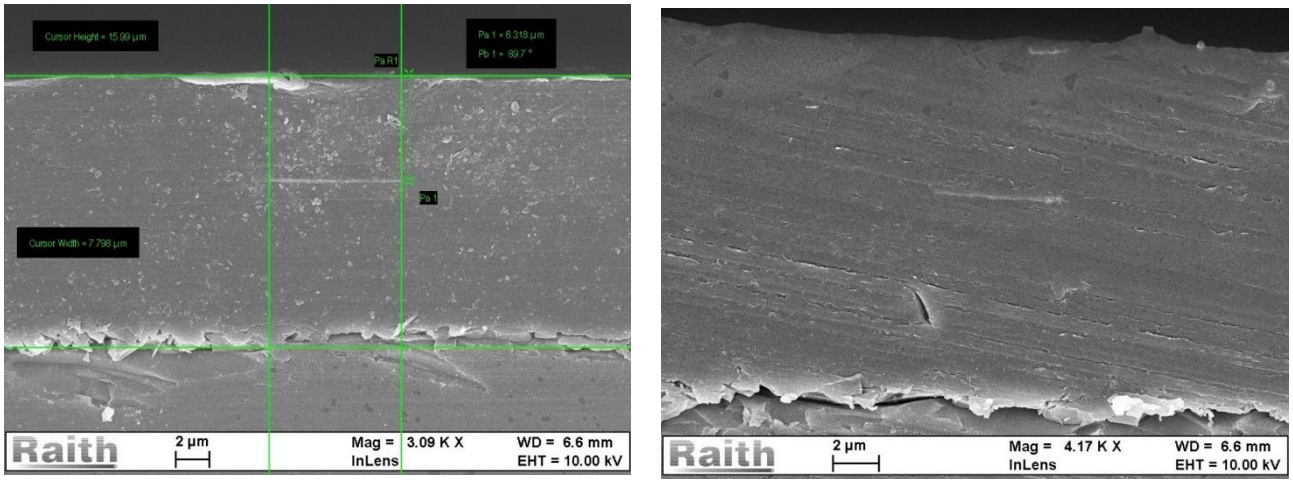

Figure 3.17. SEM images of the facets. Left: A polished facet; Right: a facet with significant roughness.

3.10 Measurements

The setup used here is represented schematically in fig.3.18, while the physical implementation is shown in fig.3.19; as can be seen, in addition to the concept idea's elements, the real setup required additional elements for the alignment, in particular another laser (Helium-Neon, 633nm) and two additional cameras (one for a top-view of the samples, another at the output).

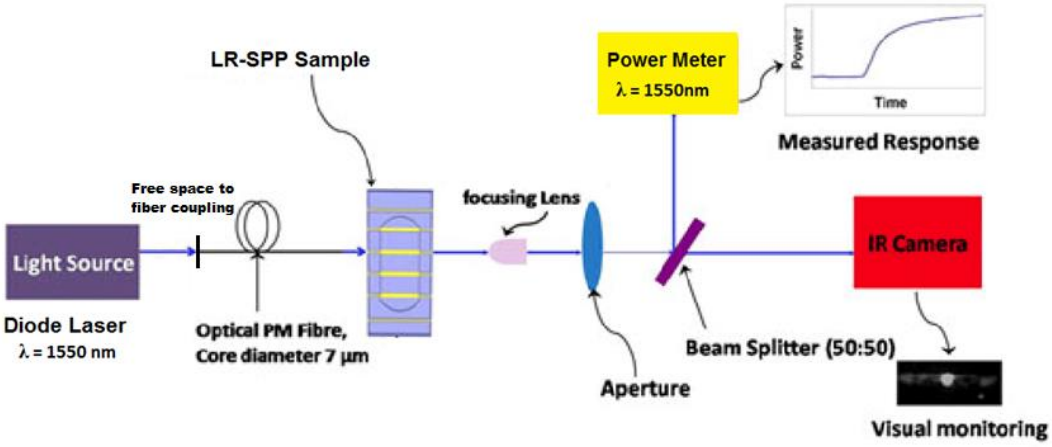

Figure 3.18. Schematic measurement setup for the characterization of LR-SPP stripes, which allows to visualize output power and mode outline.

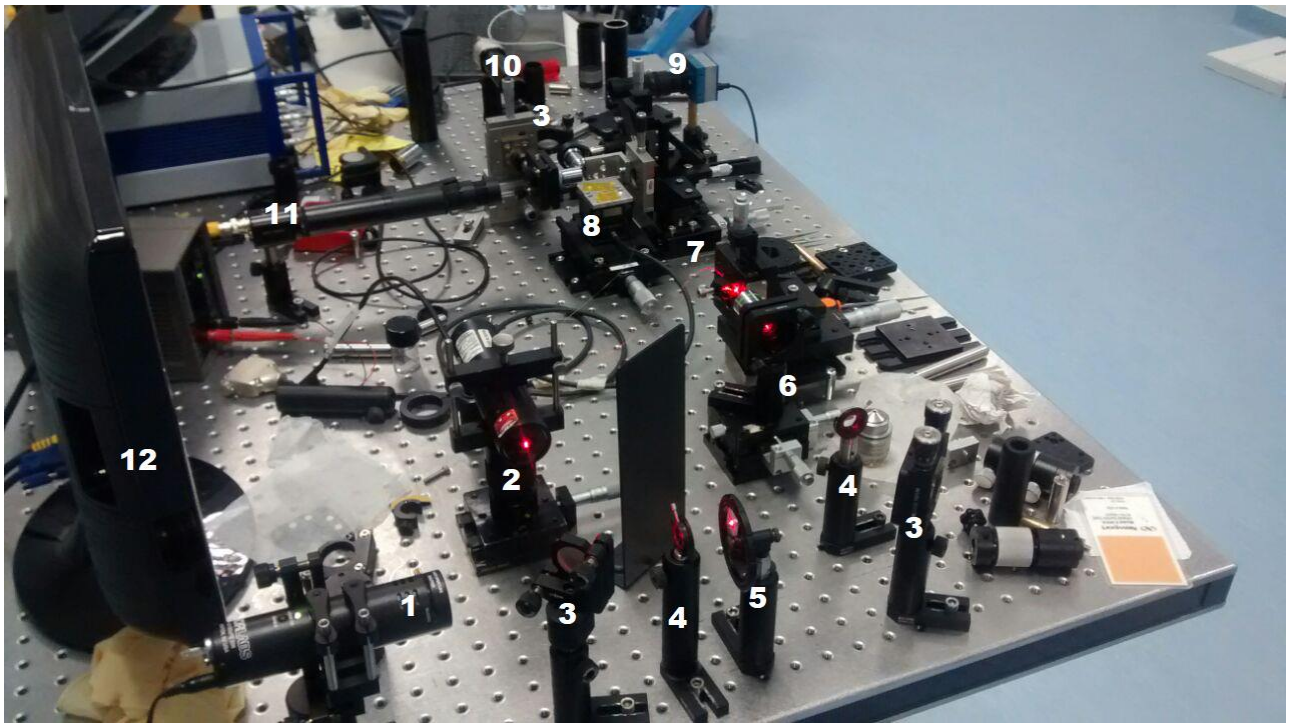

Figure 3.19. (1) Infra-Red laser source; (2) He-Ne 633nm laser source; (3) Mirror; (4) Iris; (5) Polarization rotator (actually, there is an attenuator); (6) Air to fiber coupling system (with 20X lens); (7) Polarization Maintaining single mode fiber; (8) Fiber to waveguide coupling, sample and

waveguide to air coupling (with 100X lens); (9) Infrared detector; (10) Visible detector; (11) Visible camera for top view; (12) Monitor for displaying the three cameras.

Since the setup was created from scratch (although the concept is almost a standard in literature), I have given multiple degrees of mechanical freedom to the optical elements, as shown in Fig.3.20: various translational and rotational holders are shown to have been extensively used.

Once the alignment light is correctly coupled (since it's 633nm, it is visible and thus allows an easy handling), the Infra-Red light is used; the critical (and time-consuming) parts are the couplings: free-space-laser to fiber, fiber to samples' stripes, and stripes' output to Infra-Red camera.

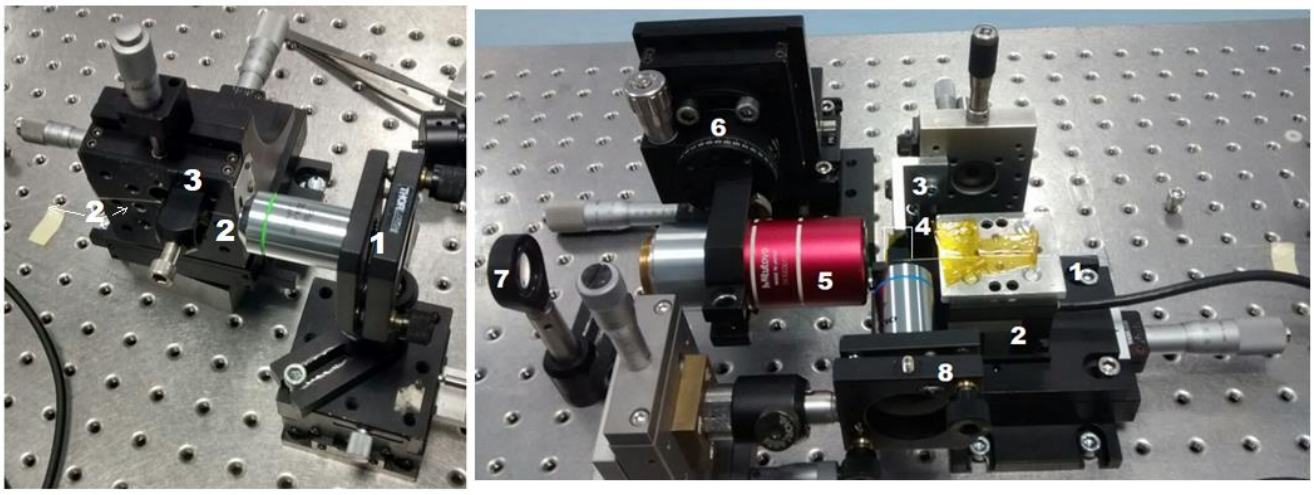

Figure 3.20. (Left) System for optical signal coupling from free-space to fiber: (1) 20X objective with holder; (2) polarization maintaining single mode fiber; (3) fiber holder with translation. (Right) System where the actual measurements happen, where the optical signal impinges from the fiber towards the sample, and the samples' output moves towards the cameras/detectors: (1) polarization maintaining single mode fiber; (2) fiber holder, made of manual axis translation and a precision quartz translation; (3) sample holder, with manual translation; (4) sample (sample is held vertically); (5) 100X objective towards the output cameras; (6) objective holder with translation and rotation; (7) lens with 10cm focal length; (8) 40X objective lens towards the top view camera.

The partial results of the measurements are shown in Fig.3.21; in particular, in 3.21b we can see at the output the effects of the interface: when the IR detector is translated vertically, only one of the circles of light, the one connected with the metal stripes, remains constant, while the others, created by the opacity of the interface, turn on and off; an iris (which acts as a space filter) is needed to "cut" the additional signal from the opaque interface.

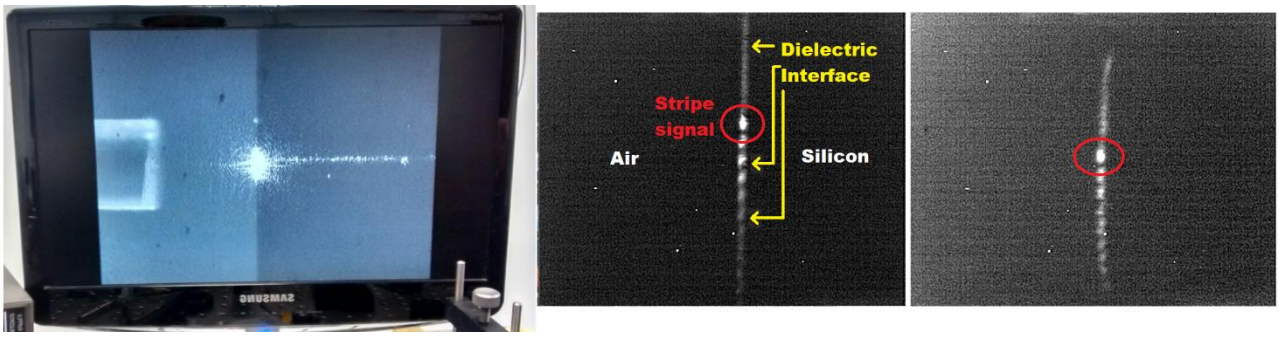

Figure 3.20. (Left) The image on the monitor shows the signal from the fiber impinging on the interface and coupling with the stripe, seen from top view. (Center and Right) Output of the sample, as seen from the infrared cameras; the stripe signal has been circled; the specific sample that has been measured had a small thickness of 15µm, with a single layer, while the others have 30µm, this may have impacted on the propagation loss of the stripe waveguides.

3.11 Conclusions Vertical Coupler

In this chapter I have investigated the possibility of using multi-planar plasmonic circuits to increase the complexity achievable by optical integrated circuits; vertical couplers are presented as the component that allows two planar circuits to communicate.

From section 1 to 5 an analysis on vertical couplers with long range surface plasmons has been presented; the results of the analysis have been published in [33] (see section 5 for the conclusions of the analysis). Vertical directional coupler may be reliable communication systems for the multi-planar circuits, if the guidelines given in the analysis are followed.

From section 6 to 9 I have proposed a plasmonic signal bridging system, which is composed of two planar circuits communicating through two vertical couplers, and is one of the possible applications of the vertical couplers. The structure has been designed and realized. Fig.3.20 is a partial result of the characterization, which confirms the working condition of the stripe waveguides; further measurements can confirm the effectiveness of the plasmonic signal bridging system.

3.12 References

[1] S. A. Maier. “Plasmonics: Fundamentals and Applications”, (Springer, 2010).

[2] P. Berini. “Long range surface plasmon polaritons,” Adv. Opt. Photonics 1, 484–588 (2009).

[3] G. D’Aguanno, Et al. “Quenched optical transmission in ultrathin subwavelength plasmonic gratings,” Phys. Rev. B 83, 035426 (2011).

[4] D. Sarid. “Long-range surface-plasma waves on very thin metal films,” Phys. Rev. Lett. 47(26), 1927–1930 (1981).

[5] P. Berini. “Plasmon polariton waves guided by thin lossy metal films of finite width: Bound modes of symmetric structures,” Phys. Rev. B 61, 10484–10503 (2000).

[6] J. J. Ju, Et al. “40 Gbit/s light signal transmission in long-range surface plasmon waveguides,” Appl. Phys. Lett. 91, 171117 (2007).

[7] B. Banan, Et al. “Multi-channel transmission through a gold strip plasmonic waveguide embedded in Cytop,” IEEE Photonics J. 5(3), 2201811 (2013).

[8] J. J. Ju, Et al. “Polymer-based long-range surface plasmon polariton waveguides for 10-Gbps optical signal transmission applications,” J. Lightwave Technol. 26(11), 1510–1518 (2008).

[9] A. Degiron, Et al. “Guiding light with long range plasmons,” Opt. Photonics News 19, 28–34 (2008).

[10] G. I. Stegeman, Et al. “Excitation of surface polaritons by end-fire coupling,” Opt. Lett. 8(7), 386–388 (1983).

[11] N. Mattiucci, Et al. “Long range plasmon assisted all-optical switching at telecommunication wavelengths,” Opt. Lett. 37, 121 (2012).

[12] R. G. Hunsperger. “Integrated Optics Theory and Technology” (Springer, 2009), Chap. 4–5, pp. 53–104.

[13] A. Boltasseva and S. I. Bozhevolnyi, “Directional couplers using longrange surface plasmon polariton waveguides,” J. Sel. Top. Quantum Electron. 12, 1233–1241 (2006).

[14] D. C. Zografopoulos and R. Beccherelli, “Long-range plasmonic directional coupler switches controlled by nematic liquid crystals,” Opt. Express 21(7), 8240–8250 (2013).

[15] V. A. Zenin, Et al. “Directional coupling in long-range dielectric loaded plasmonic waveguides,” Opt. Express 21(7), 8799–8807 (2013).

[16] A. Boltasseva, Et al. “Integrated optical components utilizing long-range surface plasmon polaritons,” J. Lightwave Technol. 23(1), 413–422 (2005).

[17] R. Charbonneau, Et al. “Demonstration of integrated optics elements based on long-ranging surface plasmon polaritons,” Opt. Express 13(3), 977–984 (2005).

[18] H. S. Won, Et al. “Vertical coupling of long-range surface plasmon polaritons,” Appl. Phys. Lett. 88, 011110 (2006).

[19] T. Srivastava and A. Kumar, “Comparative study of directional couplers utilizing long-range surface plasmon polaritons,” Appl. Opt. 49(12), 2397–2402 (2010).

[20] L. Carloni, P. Pande, and Y. Xie. “Networks-on-Chip in Emerging Interconnect Paradigms: Advantages and Challenges” (NOCS, San Diego, CA, 2009).

[21] K. Leosson, Et al. “Long range surface plasmon polariton nanowire waveguides for device applications,” Opt. Express 14(1), 314–319 (2006).

[22] T. Holmgaard, Et al. “Long-range dielectric loaded surface plasmon-polariton waveguides,” Opt. Express 18(22), 23009–23015 (2010).

[23] R. Charbonneau, Et al. “Passive integrated optics elements based on long-range surface plasmon-polaritons,” J. Lightwave Technol. 24(1), 477–494 (2006).

[24] A. W. Snyder and J. D. Love. “Optical Waveguide Theory” (Chapman and Hall, London, 1983), Chap. 18, p. 387.

[25] F. Liu, Et al. “Hybrid coupling between long-range surface plasmon polariton mode and dielectric waveguide mode,” J. Lightwave Technol. 29(9), 1265–1273 (2011).

[26] P. Berini and J. Lu, “Curved long-range surface plasmon-polariton waveguides,” Opt. Express 14(6), 2365–2371 (2006).

[27] J. Gosciniak, Et al. “Theoretical analysis of long-range dielectric-loaded surface plasmon polariton waveguides,” J. Lightwave Technol. 29(10), 1473–1481 (2011).

[28] S. L. Chuang, “Application of the strongly coupled-mode theory to integrated optical devices,” IEEE J. Quantum Electron. QE–23(23), 499–509 (1987).

[29] Y. Xie, Et al. “Fabrication of long-range surface plasmon polaritons waveguide by wet chemical etching,” J. Optics 16(6), 065006 (2014).

[30] J. T. Kim, Et al. “Gold stripe optical waveguides fabricated by a novel double-layered liftoff process,” ETRI J. 31(6), 778–783, 1225–6463 (2009).

[31] I. Slovinsky, Et al. “Propagation loss of long-range surface plasmon polariton gold stripe waveguides in the thin-film limit,” Plasmonics 8, 1613–1619 (2013).

[32] G. Y. Yeom, “Plasma-enhanced chemical vapor deposition of SiO2 thin films,” J. Korean Phys. Soc. 53(2), 892–896 (2008).

[33] B. Alam, A. Veroli and A. Benedetti. “Analysis on vertical directional couplers with long range surface plasmons for multilayer optical routing”. J. Appl. Phys. 120, (2016).

4 Narrow-beam optical antennas based on leaky waves with long range surface plasmons

Introduction

Optical antennas are a recent topic; although the correspondents in radiofrequencies and microwaves are now enabling technologies for mobile telephony, satellite communications and many other systems that use electromagnetic radiation, at optical frequencies the topic is deeply connected to recent studies such as integrated optics, plasmonics, nanofabrication, metamaterials.

Research on optical antennas has been focused mainly on field localization, which is the solution to the problem of correspondence between the nanoscopic dimensions of the devices and the scales of the wavelengths in play in the circuits[1]; in this direction, there are many works that concern the development of the capabilities to reveal millimetric, infrared, or visible waves [2-4], or optical antennas used as nano-probes for measurement of chemical or biological reactions [5]; another field of interest is the detection of individual photons for quantum applications [6].

An interesting category of optical antennas that is being developed in these very recent years are those based on leaky waves; this category of antennas has extensive theoretical and experimental literature in the microwaves [7], and the challenge is to be able to convert such knowledge to produce new devices working at optical frequencies. Although a first theoretical description of possible EM interactions within this type of antennas can be traced back several decades ago [8], it was necessary to wait until the development of computational methods of the past

decade to get the instrumentation needed to describe the phenomena involved [9] with sufficient accuracy.

Antennas based on leaky waves are attractive because they allow to obtain very narrow beams, mainly due to far field divergence: if the loss mechanism that causes the radiation is weak and gradual (guided mode in such path is leaky with small losses), the input signal needs a longer path to dissipate completely on the waveguide, and the resulting beam will be very narrow due to diffraction [7]. At optical frequencies (i.e. in the near-infrared), if the angle of such beam were electronically controllable, these antennas may find application in LIDARs[10-11], planar imaging[12], infrared communication in air [13,14].

Leaky waves are present in various types of nanostructured optical devices (i.e. in waveguide bends, tapers, etc.) and are usually an unwanted radiative event, while optical leaky-wave-antennas (OLWA) are structures designed to exploit this radiative phenomenon. All OLWAs have a similar configuration: a guided wave within a waveguide encounters a gradual radiation loss mechanism; it is possible to categorize the schemes proposed in the literature from the approach taken to induce losses. The most popular mechanisms is the insertion of a periodic perturbation; in [15] a structure with a Si_3N_4 waveguide intersected inside by periodic Silicon scatterers was proposed, and later the scheme was improved in [16] by inserting it in a ring resonator and in [17] by inserting it inside a Fabri-Perot resonator; in [18] silicon guides have been presented with gratings and waffles "(Rectangular sections). Loss may be caused also by slit apertures or a new material inserted within a waveguiding system, such as in [19,20]. Works that present also an experimental development are [18, 21]; in the first, despite the presence of broadband radiation, there are obvious signs suggesting a wide beam width and / or large secondary lobs, which are not the characteristics expected by an OLWA; the second is the experimental implementation of the work in [15], and shows a broadband radiation as per design (check if tight), although the radiated power came mainly from TM mode, while a good part of the overall power was still bound in TE.

The OLWA antenna proposed in this chapter involves an Au stripe supporting Long Range Surface Plasmon Polaritons (LR-SPPs) and an array of periodic scatterers supporting a broadband mode. Our analysis shows that such configuration allows to have a very directive main lobe, while also making the secondary lobes negligible; this work is made on the trail of [15,21], although the goal here is to be able to convert all

the power from the input into the radiated field, and not be limited to a portion; also, since the periodic perturbation is on the of the bound mode, we expect weaker secondary lobes.

In section 2 the proposed scheme is presented, as well as the setups for the analysis. In section 3 the numerical analysis has been presented (a particular effort has been dedicated to the implementation of Green's equations, which has been described in Appendix 2 to help readability). In section 4 I have shown the fabricated elements, as well as the plans for future evolution: the first level of circuit has been built, and needs to be measured before proceeding with the second level. The analysis of this device shows very promising results, although for a physical implementation the work is still in progress.

4.2 Antenna Geometry

We will work on quasi-TM mode, at C-Bandwidth around 1550nm of wavelength. The schematic representation of the antenna we propose, in three dimensions (3-D) and in two dimensions (2-D) as taken on the longitudinal plane in the middle, is shown in Fig.4.1. The bound mode from the input becomes leaky when it reaches the periodic scatterers (which act as perturbation), and then it returns bound at the output; actually, the signal on the metal stripe should be depleted after crossing the perturbation, when it reaches the output, and most of the power should have radiated broadband towards the y axis in both directions.

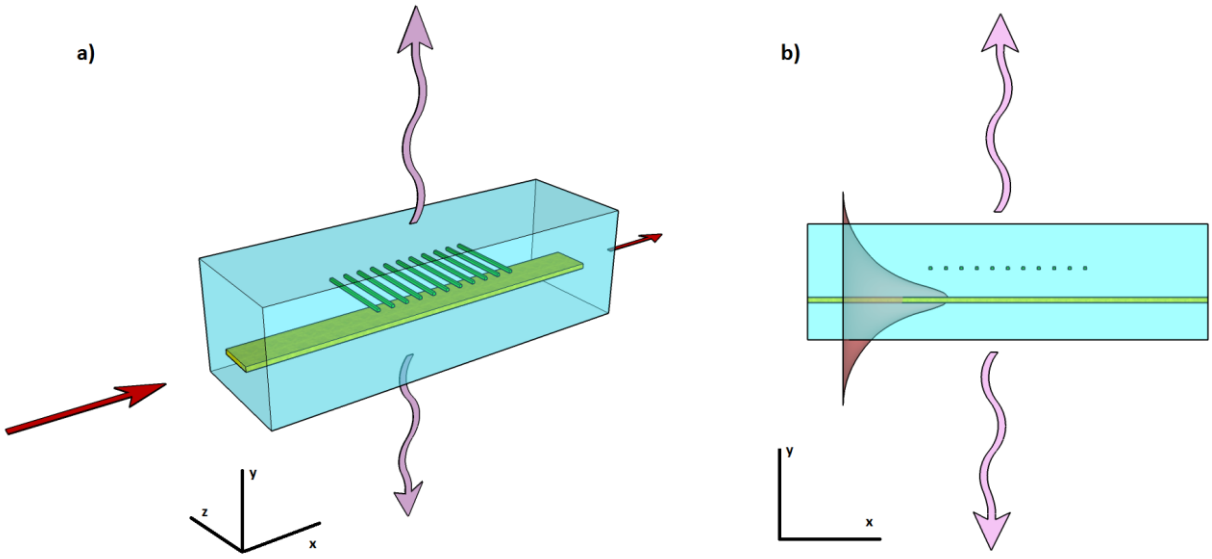

Figure 4.1. Unscaled schematic representation of the proposed device: a) The bound mode incoming from the waveguide becomes leaky in the area where the scatterers are present, and is radiated away; b) the plan is to build the scatterers at the tail of the bound quasi-TM mode

The stripes are made of Au, with 6µm width and 20nm thickness, within dielectric environment made of Su-8 (n=1.573); the final choice of the material for the array of scatterers shall be deduced after the analysis: we tried both dielectrics and metals, such as Air (n=1 at λ = 1.55µm), Si_3N_4 (n=1.995 at λ = 1.55µm), Au(ϵ_r = -93.0839 + i*11.1097 at λ = 1.55µm), Ag(ϵ_r = -129.17+ i*3.2841 at λ = 1.55µm).

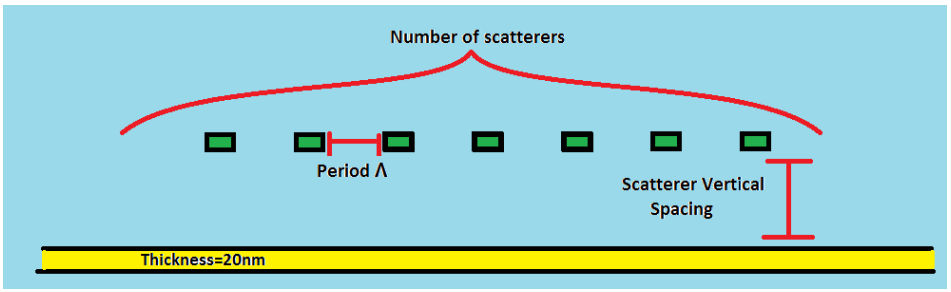

Figure 4.2. Schematic of the main parameters for the optimizations

The periodic array is placed on the tails of the main mode's field distribution; the vertical distance between this perturbation array and the stripe influences the strength of the perturbation, and this makes it one of the design parameters (Fig.4.2). A weaker perturbation (array farther from stripe) allows the loss to be weak and to have a very directive main lobe in far-field, but this requires the presence of big amount of scatterers; on the other hand, perturbations closer to the stripe allow to have a faster depletion of the input signal and thus a shorter length occupation of the overall element; the vertical distance is thus one of the main parameters to design.

The period of the perturbation has been defined using Floquet equations and numerical simulations, in the next section; the final value was very close to the purely analytical solution, which confirms the “weak perturbation” form the leaky waves approach.

Actually, the structure presented here radiates both upwards and downwards. In this work we shall focus on the scattered signal going upwards, as the other may be reflected in its opposite direction with the use of a Distributed Bragg Reflector on the bottom of this device (i.e. multiple stacked layers with the right periodicity [22]).

4.3 Numerical Analysis

4.3.1 Simulation setup

The starting point of the analysis is the definition of the period of the array of scatterers through Floquet equation; this method is a proven and reliable tool for 1-D periodic structures such as Bragg gratings, as shown in Appendix 1. The first step is to represent equation, with the addition of the dielectric in the environment (n≠1):

$$n_{transmitted}\frac{2\pi}{\lambda}\sin(\theta_m) = n_{reflected}\frac{2\pi}{\lambda}\sin(\theta_0) + m\frac{2\pi}{\Lambda} \rightarrow \theta_{S,n} = \arcsin\left[\sin(\theta_0) + m\frac{\lambda}{\Lambda}\right] \qquad (4.3.1)$$

Where $\mathbf{n_{transmitted}}$ and $\mathbf{n_{reflected}}$ are the refractive indices of the surrounding dielectrics, *m* is the mode number and Λ is the period of the grating. The goal is to obtain a single mode, so we will limit the modes to m=±1 (the sign refers to transmitted or reflected modes); we expect a broadband signal, so θ_m=0°; also, in our situation the wave-vector from the incoming field traveling on the Au stripe is incident from a parallel direction to the grating (θ_0=90°). For the broadband condition we have:

$$0 = 1 - \frac{\lambda_0}{n_{dielectric}\Lambda} \quad \rightarrow \quad \Lambda = \frac{\lambda_0}{n_{dielectric}} \qquad (4.3.2)$$

Condition (4.3.2) implies Λ=985nm; we will perform more accurate analysis around this central value.

The computational complexity for the direct simulation of far field of antennas is very demanding, especially when optical frequencies are involved. There are

various ways to analyze indirectly the far field profile, through a combination of analytical methods and simulations: equivalent aperture method [23], array factor method [24], Stratton Chu integral equation [15, 25-26]. The first two consider the array as a purely mathematical point object that creates a periodic perturbation, thus ignoring its e.m. effects as a physical object (i.e. fig 4 from [15]); also, while mainly analytical, those two methods still require simulations in order to obtain the effective index of the leaky mode. A bigger amount of information can be obtained through Stratton-Chu integral equation, which uses the information on the local field distribution in order to reconstruct the far-field radiation pattern; in such situation simulations are needed to compute the local field in the area over the scatterers, towards the direction of the radiation. In the present work we have used Green tensor method, which is an evolution of the Stratton-Chu approach. We have simulated an area around the LR-SPP stripe and the scatterers, extracted the local field distribution from the surrounding, and used it to obtain the far field profile by using Green's tensors, by applying what described in Appendix 2.

Three dimensional (3D) simulations of ultra-thin stripes supporting LR-SPPs is computationally demanding even with few tens of micrometers of length, mainly because the imaginary effective index (carrying information of the propagation loss) is on the same order of magnitude as the numerical error, if meshes don't have sizes of few nanometers. Since we expect to use hundreds of scatterers, the longitudinal extension of the simulation is expected to be over 100µm; so we discarded the possibility of a 3D simulation. Instead, we have focused on a 2D simulation toward the longitudinal plane x-y, with periodicity in x (longitudinal) direction (Fig.4.3).

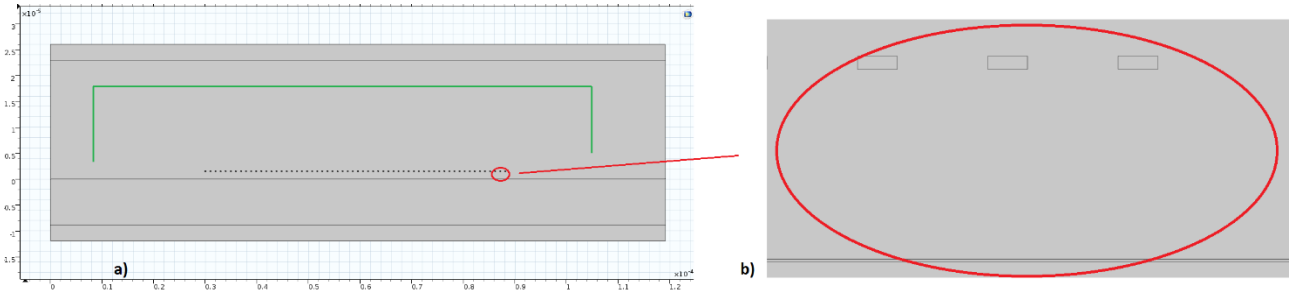

Figure 4.3. a) Representation of the CAD with an array of 60 elements; the lines toward which the field distribution has been extracted have been schematically represented in green. b) Zoom of the ending part, with three scatterers and the thin Au layer.

In practice, while we are producing a laterally finite stripe with width of 6µm, our analysis is limited to a slab; even though the width is bigger than a few

wavelengths, there are differences between the two approaches: the mode propagating through a slab is a quasi-TM very close to a perfect TM mode, while the fundamental mode in a laterally finite stripe has stronger longitudinal H field; despite the differences, the profile of the two modes is still similar, which validates the analogy.

4.3.2 Simulation results and analysis

Through the use of FEM simulations (COMSOL Multiphysics), the local fields of lines around the scatterers have been obtained; through formulas A.2.1.28-32 (Appendix 2) the equation A.2.1.37 could be solved. We have tested a variety of parametric variations of the base structure described in section 2.

Two results of interest are displayed in Fig.4.4, where two types of materials have been used: dielectric (represented in the image by Si_3N_4) and metal (represented by Au). The angle of the main lobe changes with the period of the array (50 elements), and is broadside when the period is close to 985nm, which is the purely mathematical solution of (4.3.2); angle change is related also to the material composing the scatterers, but it is a minimal variation. Another interesting thing that can be noticed with Fig.4 is the fact that there are strong secondary lobes when the scatterers are made of dielectrics (other than Si_3N_4, the same behavior was shown from air); Au based scatterers (as well as Ag) don't have such an issue.

This is due to the resonance within the dielectric scatterers themselves: due to fabrication difficulties, we have set a length of 300nm, which is comparable to around 1/3 of $\frac{\lambda}{n_{dielectric}}$ (thus, each scatterer acts as a resonant cavity).

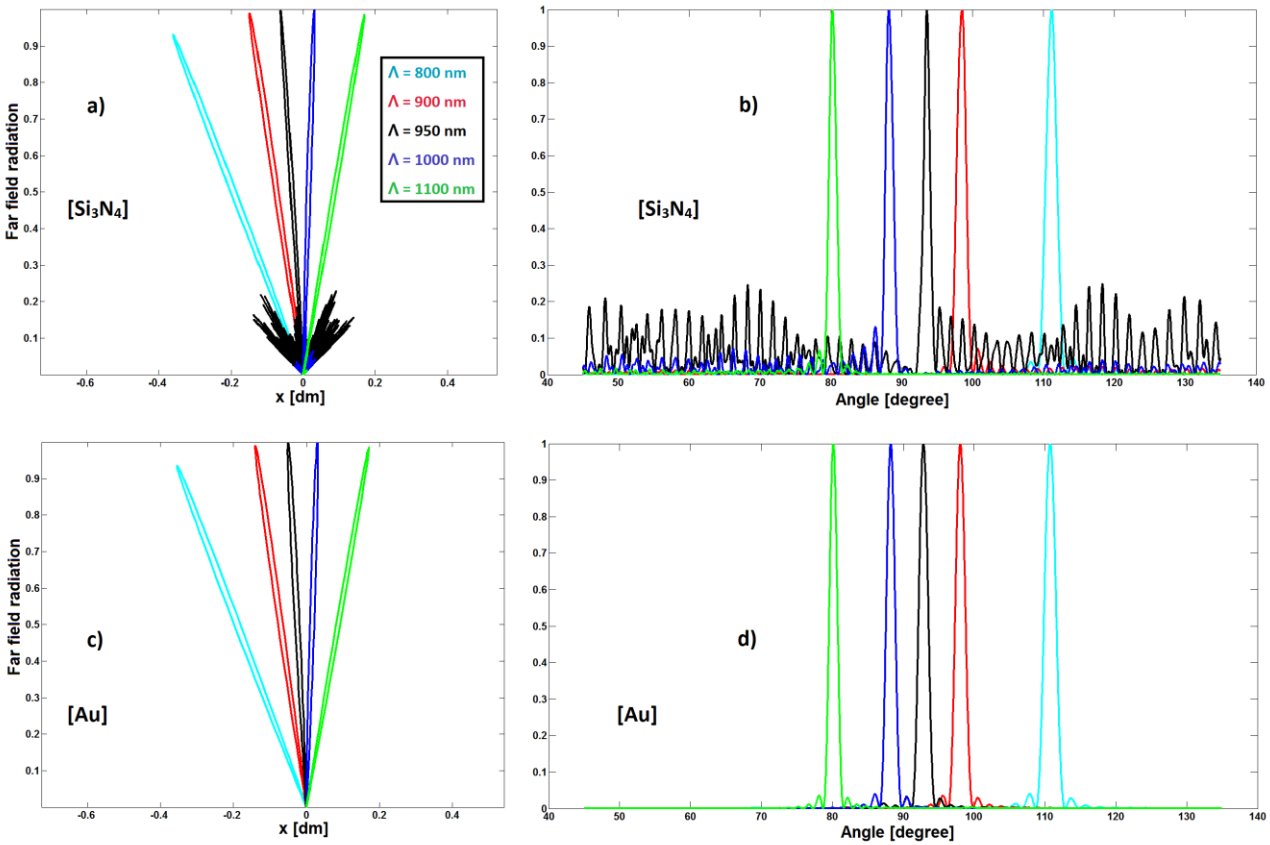

Figure 4.4. a) and c): Radiation pattern of the antenna; b) and d): normalized far field vs angle . In a) and b), Si3N4 has been used as scatterer material; in c) and d) Au has been used as scatterer's material

Another group of simulations has been performed in order to see the relation between the vertical distance from the Au stripe to the scatterers; parameter S_{21} describes formally the phenomena, but we have shown it more explicitly in Fig.4.5, where Au scatterers have been used. Overall, this configuration confirms the goals of the “plasmonic leaky wave antenna”: this analysis confirms that through the use of a plasmonic waveguide and a periodic array at the height of the tail of the bound mode, the perturbation acts slowly and gradually; the resulting main lobe is very directive, while secondary lobes are negligible.

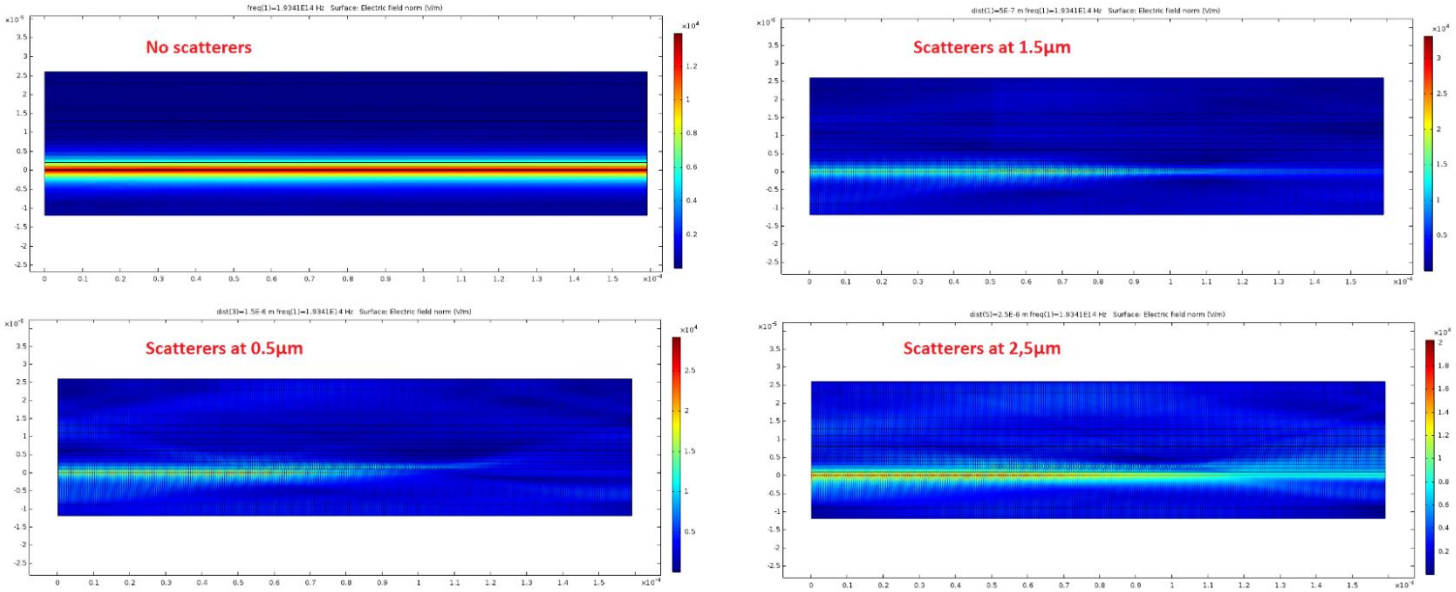

Figure 4.5: Field profile of the antenna when no scatterers are present, and when the array of scatterers is separated by the stripe of: 0.5µm, 1.5µm or 2.5µm. The deduction is immediate: the scatterers scatter away the signal of an amount indirectly proportional to the separation distance.

An additional advantage of metallic scatterers is the electric tunability through various types of modulation: photothermal [27] or electro-optical [28] modulation of the dielectric environment's refractive index.

4.4 Fabricated elements

The main idea is to build the proposed structure along one of the two branches of an Y-Splitter; the input signal from the main stripe would be split in an un-attenuated branch and another subject to the losses due to perturbation; measurement of the signal coming out from the two branches may give quantitative information. Still, it is also possible to test directly plasmonic leaky wave antennas built on s-bends and straight stripes for more qualitative information.

By using the same combination of parameters described in section 3 some y-splitters, s-bends, and straight stripes have been fabricated, all of them accompanied by markers for a later EBL alignment. Y-splitters needed additional care for the construction of the crotch: scattering in this point may be significant since, due to fabrication constraints, the middle corner should be large at least 1µm or 1.5µm;

because of the limits of contact photolithography, there may be also non-idealities, resulting in a lack of symmetry between the two split signals.

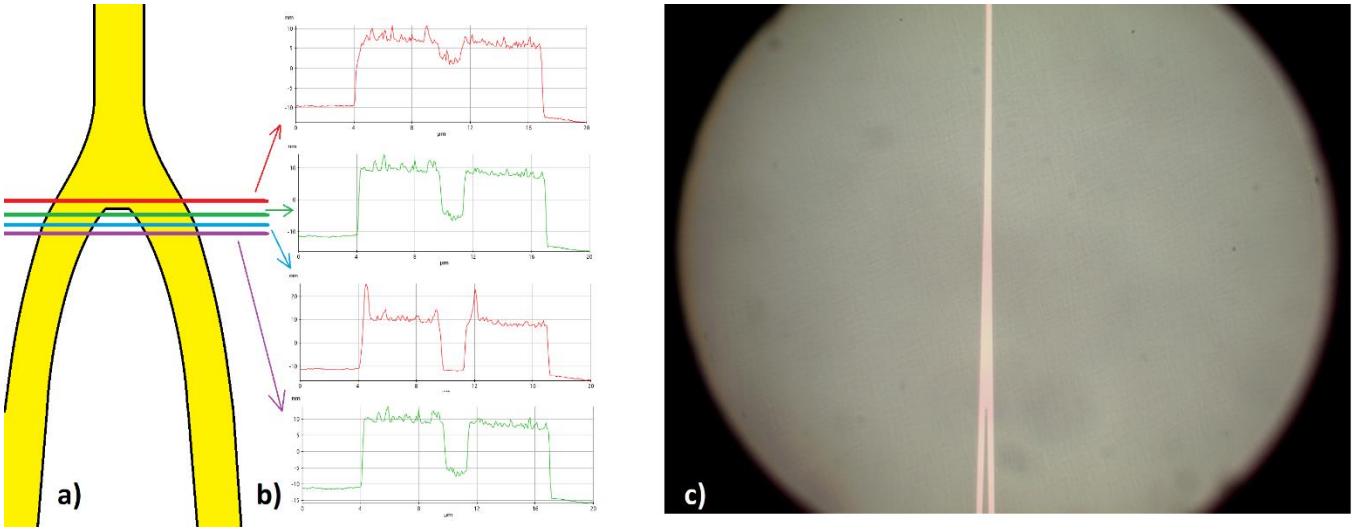

Figure 4.6: The crotch is represented through a scheme in a), through AFM images in b) and through an optical image in c) from top view. Actual waveguides had a more flat surface, and a better defined crotch

4.5 Conclusions

We have proposed a narrow beam optical antenna relying on leaky waves theory, based on a plasmonic metal waveguide and a periodic array that acts as a weak perturbation. The main goal is to produce a narrow beam broadside. The design of the grating was based on Floquet theory presented in appendix A.1, while the analysis of its interaction was done through a FEM analysis combined with analytical formulation taken from Green's Tensor, described in appendix A.2.

The analysis shows that there is a choice between the required number of the scatterers (equivalent to the length of the component) and the vertical spacing between the array and the plasmonic stripe, which controls the amount of the leakage; a longer length allows also to have a narrower beam. The material and the geometrical extension of the single scatterers are also important, as resonance phenomena may occur, creating uncontrollable scattering events; with metallic scatterers these resonances are not present and the resulting beam displays

negligible secondary beams. Additionally to confirming the requirements, this analysis suggests that tuning the angle is possible, which opens to the possible use of this component may be used as a small LiDAR.

Through bilayer lift-off, the waveguiding component of the optical leaky wave antenna has been realized, in three possible configurations: on one of the branches of an y-splitter, on a straight stripe, on a s-bend stripe. Those are now being characterized before proceeding with the fabrication of the periodic scatterers' array, and the final measurements for the verifications.

4.6 References

[1] P.Bharadwaj, B.Deutsch, and L.Novotny, "Optical Antennas", Advances in Optics and Photonics Vol. 1, Issue 3, pp. 438-483 (2009)

[2] Y. Salamin, W. Heni, C. Haffner, Y. Fedoryshyn, C. Hoessbacher, R. Bonjour, M. Zahner, D. Hillerkuss, P. Leuchtmann, D.L. Elder, L.R. Dalton , C. Hafner, J. Leuthold, "Direct Conversion of Free Space Millimeter Waves to Optical Domain by Plasmonic Modulator Antenna", Nano Letters, vol. 15, issue 12, pp. 8342-8346. (2015)

[3] F.J. Gonzalez, J. Alda, B. Ilic and G. Boreman, "Infrared antennas coupled to lithographic Fresnel zone plates", Appl.Opt. 43 6067–73, pp. 6067-73. (2004)

[4] S. Sederberg and A.Y. Elezzabi, "Sierpiński fractal plasmonic antenna: a fractal abstraction of the plasmonic bowtie antenna", Optics Express, Vol. 19, Issue 11, pp. 10456-10461 (2011)

[5] R. Won, "Surface plasmons: Optical antennas for sensing", Nature Photonics 1, 442 (2007)

[6] X.L. Chu, T. J. K. Brenner, X.-W. Chen, Y. Ghosh, J. A. Hollingsworth, V. Sandoghdar, and S. Gotzinger, "Experimental realization of an optical antenna designed for collecting 99% of photons from a quantum emitter", Optica, Vol. 1, Issue 4, pp. 203-208. (2014)

[7] C.A. Balanis, "Modern antenna handbook", John Wiley & Sons, p.325, 2008

[8] T. Tamir, "Leaky waves in planar optical waveguides", Nouvelle Revue d'Optique, Vol. 6, Num.5, p.273-284. (1975)

[9] F. Manticone, and A. Alù, “Leaky-Wave Theory, Techniques and Applications: From Microwaves to Visible Frequencies”, Proceedings of the IEEE, Vol. 103, No. 5, pp. 793-821, invited paper, (2015)

[10] C. K. Toth, “R&D of mobile LIDAR mapping and future trends”, in Proceeding of ASPRS 2009 Annual Conference (Baltimore, Maryland, 2009).

[11] N. Blaunstein, S. Arnon, N. Kopeika, A. Zilberman, “Applied Aspects of Optical Communication and LIDAR”, CRC Press. (2009)

[12] Q. Song, F. Qian, E. K. Tien, I. Tomov, J. Meyer, X. Z. Sang, and O. Boyraz, “Imaging by silicon on insulator waveguides,” Appl. Phys. Lett. 94(23), 231101. (2009)

[13] C. W. Oh, E. Tangdiongga and A. M. J. Koonen, "Steerable pencil beams for multi-Gbps indoor optical wireless communication," OSA Optics Letters, 39(18). pp. 5427-5430 (2014)

[14] M.A. Khalighi, M. Uysal, “Survey on Free Space Optical Communication: A Communication Theory Perspective”, IEEE Communications Surveys & Tutorials, Vol. 16 (4), (2014)

[15] Q. Song, S. Campione, O. Boyraz, and F. Capolino, “Silicon-based optical leaky wave antenna with narrow beam radiation”, Optics Express, Vol. 19, Issue 9, pp. 8735-8749 (2011)

[16] C. Guclu, O. Boyraz, and F. Capolino, "Theory of Optical Leaky-Wave Antenna Integrated in a Ring Resonator for Radiation Control," IEEE J. Lightwave Technology, Vol. 35, No. 1, pp. 10-18. (2017)

[17] C.Guclu, S.Campione, O.Boyraz, F.Capolino, “Concept of an Optical Leaky-Wave Antenna Embedded in a Fabry-Pérot Resonator”, IEEE Antennas and Propagation Society International Symposium, (2013)

[18] H. Hashiguchi, H. Arai, K. Kondo, T. Baba,” Optical leaky wave antenna using waffle waveguide”, IEEE iWEM Conference, 15681170. (2015)

[19] V. Ebrahimi, L. Yousefi, and M. M. Taheri, “Enabling inter- and intra-chip optical wireless interconnect by the aid of hybrid plasmonic leaky-wave optical antennas”, Optics Communications, Volume 382, Pages 119-126, (2017)

[20] Y.Wang, A.S.Helmy, and G.V.Eleftheriades, “Ultra-wideband optical leaky-wave slot antennas”, Optics Express Vol. 21, Issue 11, pp. 13184-13186 (2013).

[21] Q. Zhao, C. Guclu, Y. Huang, F. Capolino, O. Boyraz, “Experimental Demonstration of Directive Si3N4 Optical Leaky Wave Antennas With Semiconductor Perturbations”, Journal of Lightwave Technology, Vol. 34, Is.21, 4864-4871. (2016)

[22] J.W.Leem and J.S.Yu, “Broadband and wide-angle distributed Bragg reflectors based on amorphous germanium films by glancing angle deposition”, Optics Express Vol. 20, Issue 18, pp. 20576-20581 (2012)

[23] R. E. Collin, “Antennas and Radiowave Propagation”, McGraw Hill, p. 164 (1985)

[24] C. A. Balanis, “Antenna Theory: Analysis and Design”, Wiley, p. 286 (2005)

[25] E. J. Rothwell and M. J. Cloud, Electromagnetics, CRC Press, p. 418 (2008)

[26] J. A. Stratton, Electromagnetic Theory, McGraw-Hill, p. 424 (1941)

[27] S. Kaya, J.C. Weeber, F. Zacharatos, K. Hassan, T.Bernardin, B.Cluzel, J.Fatome, C.Finot, “Photo-thermal modulation of surface plasmon polariton propagation at telecommunication wavelengths”, Opt Express, Vol.21,Iss.19, p.22269-84 (2013)

[28] J.S. Schildkraut, “Long-range surface plasmon electrooptic modulator”, Applied Optics Vol. 27, Issue 21, pp. 4587-4590 (1988)

5 Precise detection of circular dichroism in a cluster of nano-helices by photoacoustic measurements

Introduction

In the last years, the ultimate nanofabrication frontier represented by 3D nanostructures is generating promising and versatile novel nano-photonics devices. In particular, 3D nanostructures with broken symmetry enable exciting complex interactions with chiral light, generating the typical forms of the optical activity, such as the optical rotation (OR), i.e., the polarization plane rotation of the incident light, and the circular dichroism (CD) [1,2], i.e., the different absorption levels for left and right circularly polarized (CP) waves [3]. Among the possible 3D chiral geometries, the helix architecture represents, because of its intrinsic chirality, an effective choice to manifest detectable chiral effects [4,5,6,7,8]. However, the engineering of the chiro-optical properties, such as the frequency as well as the absorbed and scattered portions of left- and right-handed circularly polarized light, requires the full control on the geometrical and spatial parameters and on material composition of the 3D nanostructures. Hence, great efforts have been made to develop flexible nanofabrication techniques for the realization of helical based structures with nanometer accuracy [9]. Recently, focused ion and electron beam induced deposition (FIBID/FEBID) have demonstrated the effective capability to tailor helical nanostructures as a function of application-driven chiro-optical properties [10,11,12,13,14], leading to the nanometer scale controlled fabrication of helix-shaped metal and dielectric nanostructures, organized in dense and ordered arrays of few micron area. Moreover, the FIBID/FEBID approach is particularly suitable for the building and the spatial localization of compact nano-devices as parts of embedded

systems, such as built-in-chip sensors and integrated optoelectronic filters, where it is of key importance the integration of nanostructured materials onto small areas.

When dealing with 3D nanostructured samples with limited patterned area, commonly used all optical (AO) measurements, though requiring low power levels of inspecting light, are heavily altered by the electromagnetic (e.m.) field escaping from the un-patterned substrate region, as well as by scattering effects. On the other hand, the photoacoustic (PA) technique, based on the generation of heat when a sample absorbs an incoming light beam [15,16], allows for the exclusive extraction of information from 3D nanostructures without being polluted by signals coming from the non-absorbing substrate. Sound- and heat-based approaches like PA [17,18,19,20], acousto-optic [21] and photothermal techniques already demonstrated to be successful for the detection of CD in other chiral media and for high precision imaging [22]. Here we extend this research to artificially structured materials, since PA technique already demonstrated to be reliable for the measurement of chiroptical effects in nanostructured samples [23,23].

In this paper, the CD of limited area nanohelices array fabricated by FIBID is studied by exploiting PA techniques, in addition to conventional all-optical (AO) measurements. This sample has been engineered in order to preserve the circular dichroism related to the helices' natural chirality and, at the same time, to limit the physical in-plane extension, the high precision measurements obtained by PA method allow to overcome physical limitations related to the natural diffraction of light, and combined with the large and tailorable chiro-optical effects demonstrated by this kind of artificial materials, concur to the development of novel photonic devices. By considering the precise internal structure of the helices' filament, numerical simulations have been performed to calculate the permittivity spectrum of the helix constitutive material, then we calculated the absorption spectra of the helices array, whose high CD levels confirmed the experimental results.

5.2 Sample description and experimental measurements

We investigated a sample consisting of an array of identical nano-helices designed to operate at near infrared (NIR) and visible (VIS) spectral regions, and realized by FIBID technique. Details on the helix construction can be found in ref.[10,14]. The helices consist of platinum-gallium-carbon (Pt-Ga-C) mixture, and are progressively grown upon a transparent dielectric multilayered substrate with a conductive layer [10]. The

helices are localized at the nodes of a square-based array with a 700nm lattice period (LP), covering a square area of 40x40 units (approximately with a side length of 28µm). The single helix has three loops (N=3), a wire section diameter (WD) of 110nm, an external diameter (ED) of 300nm, and the vertical pitch (VP) of 300nm (fig.1).

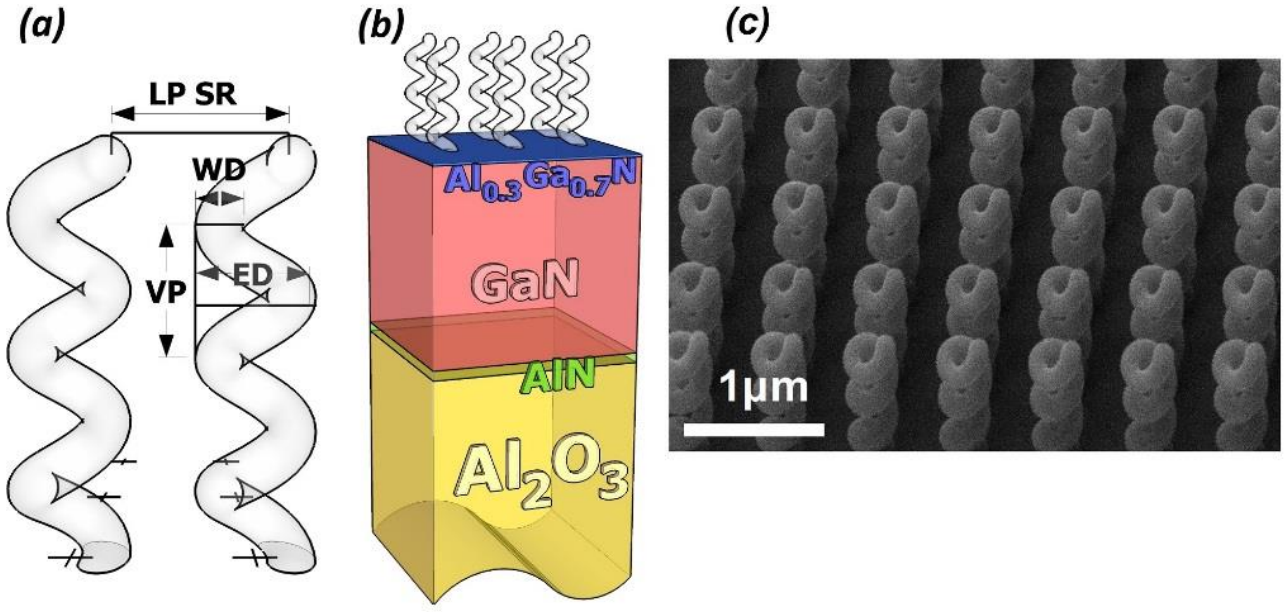

Figure 1. (a) Schematic view of the single helix, with another neighbor element. The wire diameter (WD) is 110 nm, the external diameter (ED) is 300 nm, and the vertical pitch (VP) is 300 nm. The helix is supposed to have a perfectly round shaped cross section. The lattice period (LP) of the square array is 700nm. (b) Schematic view of the substrate laying beneath the helices layer. It consists of a GaN/AlGaN heterostructure where a two dimensional electron gas allows for charge effect management during the helices growth by FIBID [10,24]. All the heterostructure is epitaxially grown on a thick (380 micron) Al2O3 substrate. (c) scanning electron microscope (SEM) view of the sample.

For AO and PA measurements we assembled two distinct experimental setups (figure 2), both controlled by a personal computer (PC). For AO measurements (fig.2-a) incident light coming from a Xenon arc lamp coupled to a monochromator passes through a linear polarizer and a wide-spectrum quarter wave plate (QWP), namely a Thorlabs AQWP05M-600 and a Thorlabs AQWP05M-980 for the λ ranges of (400-800) nm and (690-1200) nm, respectively. Incident light is focused onto the sample by means of 25X microscope objective, then detected by a photodetector (PD). Incident light is mechanically chopped at a frequency of 25 Hz used as reference for a lock-in amplifier.

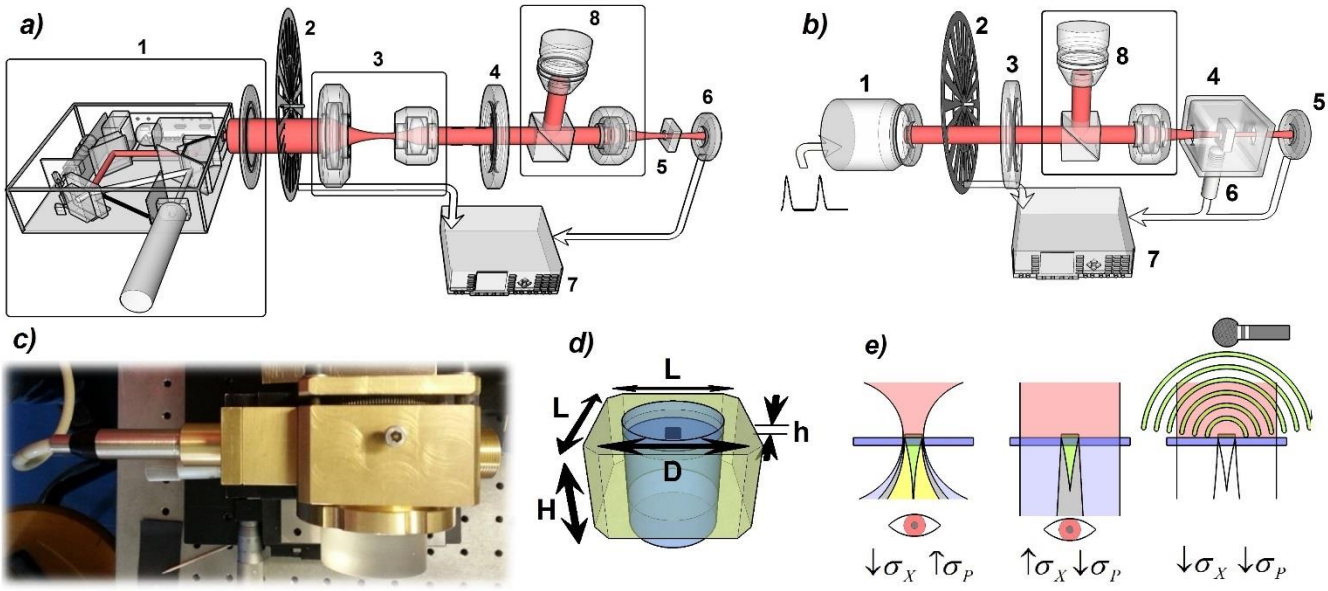

Figure 2. (a) Schematic view of the experimental setup for AO measurements. Here we display the polarized pump source (1), the chopper (2), the optic group of lenses (3) used to shrink the light source, the QWP (4), the sample (5) and the photodetector (6). A lock-in (7) control the signals and a set composed of a beam splitter and a microscope (8) is adopted to visualize and correctly aim the helices. (b) Schematic view of the experimental setup for PA measurements. We show the laser source (1), the chopper (2), the QWP (3), the PA chamber (4) containing the studied sample and the PD (6); the microphone (6) is partially installed inside the PA chamber; here again a lock-in (7) is connected to the main set-up. (c) PA chamber with Mic attached on its left side. (d) Schematic view of the main part of the PA chamber. L=6cm, H=3,5cm, D=4cm, h=1mm. Quartz glasses insulates the air chamber from external space. (e) Illustrative representation of a near-field optical (left), far-field optical (middle), and photoacoustic (right) measurement set-up. The colors associated to distinct zones refer to specific field characters: red = laser source; yellow = transmitted light through the helices with a high incidence angle; green = transmitted light through helices with normal incidence (desired data); grey = mixed field arising both from helices' region and nude substrate region; light grey = light purely transmitted by naked substrate. This representation simplifies the reasons behind the adoption of PA in the place of more common optical approach: if we want to observe the field emerging purely from helices (green), we must located the observer in close proximity of the helices, and use high-precision confocal systems; an excessive focusing will add unwanted plane components (high σ_P) to the measured field (yellow); a far-field optical set-up is easier to use, but it rather detects a mixed field (high σ_X) predominantly coming from the substrate (grey), and the resulting CD will be largely suppressed. The adoption of PA allows to detect the pure helices' footprint without the need of sophisticated systems like that of first AO set-up, still achieving the same precision and reliability.

The PA chamber is a brass container with a central circular cavity filled with quartz, with the exception of a small 1mm thick region filled with air and containing the sample (see fig.2c-d). The chamber features transparent apertures facing the incoming signals and the PD, plus a side channel for the Mic insertion, with plastic seals to grant a good acoustic insulation from the external environment. The modulation, operated by the chopper, has been added in order to recognize unwanted noises and spurious contributions, with its frequency and phase being used as markers

for the main signals. Together with the PD's, its control signals were monitored by a lock-in connected with the main PC. The sensitive microphone (Mic), used to ensure a clear record of the sound footprints of the optically absorbed power, was a Brüel&Kjær ANSI Type-4166 [25] combined with a Brüel&Kjær Pre-Amplifier Type-2619. Since the Mic-PreAmplifier system has its best signal-to-noise ratio (SNR) across 25 Hz, we set the modulation frequency to this value for the PA case.

5.3 Experimental Results

The main advantage of measuring PA signals resides in their purity in terms of unwanted field contributions coming from the nude substrate. This is graphically summarized in fig.2e. AO measurements can be performed either with tightly focused light (left side) or with slightly focused light (centre); while with the first choice one sacrifices the quality of the injected field (high σ_P), since high transverse momentum components are transmitted through the helices, in the second case a larger area is detected with respect to the helices' set region, thus capturing unwanted signals from the substrate (high σ_X). Therefore, reliable optical measurements on this kind of samples require the spatial selection of sample real image by using confocal set-up configurations [11]. As an alternative, PA measurements allow to overcome both these limitations, because they are based on the acoustic signal arising exclusively from the absorbing helices.

The results of the AO measurements have been assembled in a tridimensional function shown in fig.3a, where we plot the modulation of (normalized) light intensity reaching the PD as a function of the wavelength (λ) and of the QWP orientation angle. We estimate the average power impinging on the sample to be of the order of 1mW, while the PD registered signals of the order of 500μV; the z-axis has been rescaled to a common reference for the sake of simplicity since we are only interested in the ratio between opposite circular polarizations. From the 3D plot of fig.3a we extrapolated the circular dichroism data in transmission (CD_T) of fig.3b, after defining [26,27]:

$$CD_T = 2 \cdot \left(I_R - I_L \right) / \left(I_R + I_L \right) \tag{1}$$

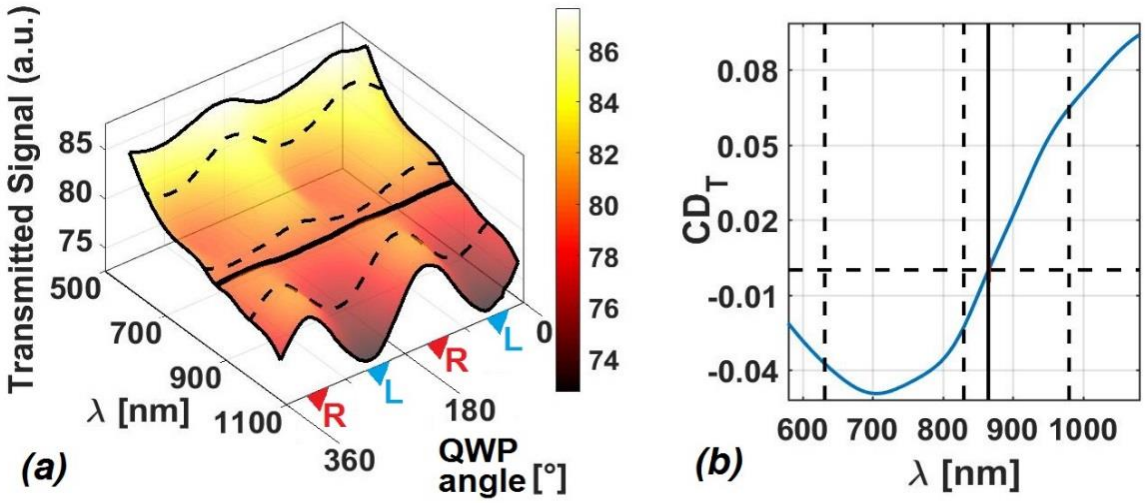

Figure 3. (a) Transmitted signal values (normalized for a common scaling factor) as a function of the vacuum wavelength λ and QWP orientation angle. (b) *CD$_T$* data extracted from (a) for the same wavelength range. We marked with dashed lines three wavelengths where we subsequently inspected the sample by means of the PA technique.

The linear transmission regime is well recognizable by the perfectly sinusoidal shape of the transmitted light intensity spectra at a fixed wavelength. As derived in the Supplementary Information section in Appendix A4, the square modulus of the total transmitted field T*(ω,z)* can be represented as follows:

$$T(\omega,z)=\alpha(\omega,z)T_{H+S}(\omega)+\beta(\omega,z)\sqrt{T_{H+S}(\omega)}+\gamma(\omega,z) \quad (2)$$

where T_{H+S} is the transmission of the helices+substrate system and the 3 coefficients α, β and γ are dispersive functions dependent on the diffraction of light and, with the exception of α, also on the pure substrate's transmittance, along with the vertical (z) position. Consequently, the CD_T profile measured in our experimental conditions is altered from the one belonging to the real helices-substrate system. The crossing point position between the LCP and RCP transmission curves (where $CD_T=0$) at λ=856nm is independent from diffraction effects since they affect at the same levels both the opposite circular polarizations, so it is a good reference for the experiments, which is expected at the same position also in PA measurements.

For the PA characterization we used four different laser sources, more precisely a 10mW CW Coherent Compass 315m green laser for λ=532nm, a 5mW He-Ne laser for λ=633nm, and two different 10mW Laser Diodes for λ=830nm and λ=980nm. The relative gaussian beam's diameter at the output were 0.6mm, 0.6mm, 0.5mm x

0.1mm (elliptical) and 3.5mm x 1.7mm (elliptical), respectively. The sample has been illuminated from the helices side.

CD_A values arise exclusively from the absorbing helices, so the corresponding *β* and *γ* values of (2) are now exactly null. To appreciate the inherent CD of the measurements, we defined a coefficient related to absorbance [28]:

$$CD_A = 2\cdot(A_R - A_L)/(A_R + A_L) \tag{3}$$

which can be directly calculated from the measured PA signals (see fig.4).

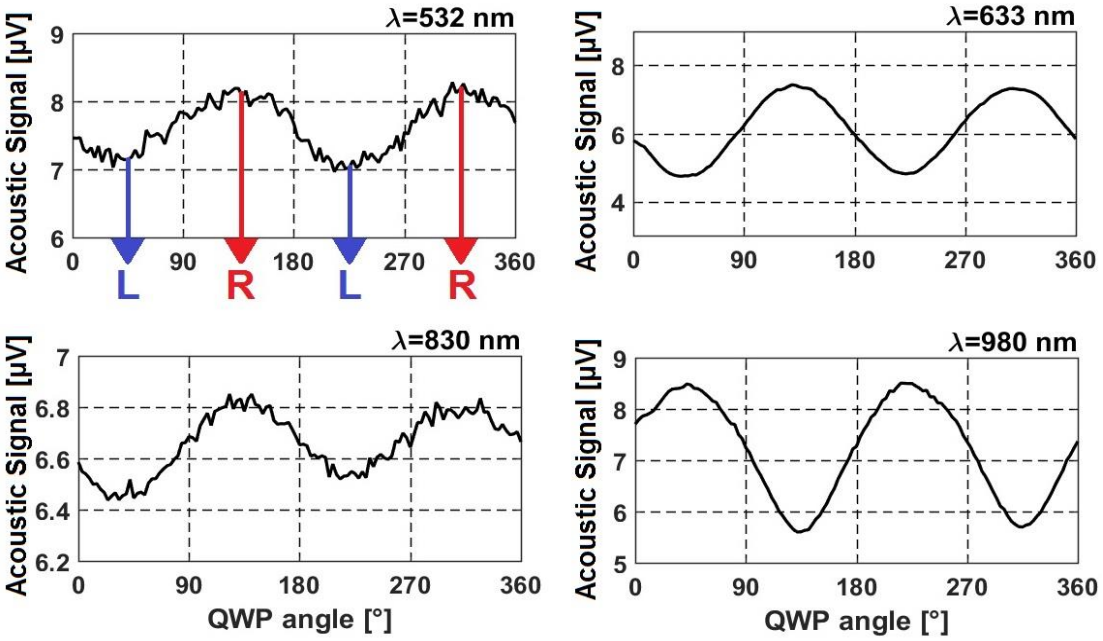

Figure 4. PA signal (in μV) as a function of the QWP orientation angle for four optical pumps; these spectra have been obtained under downward illumination. Extrapolated CD_A values are +0.14 @ λ=532nm, +0.41 @ λ=633nm, +0.1 @ λ=830nm, and -0.35 @ λ=980nm. The sound modulation was set at 25Hz, and the measurements were performed with a detail of 2 degrees and a time step of 5 seconds between each measurement.

For the first two lasers a chopper was physically part of the experimental apparatus, while for the two diodes it was replaced by a Newport Model-560 Laser Driver connected to their input port and controlled by the PC. Looking at fig.3 and 4, we notice that the sign of CD_A is naturally reversed with respect to CD_T's. This comes from obvious reasons, considering that when the sample presents the maximum transmission (high T value) it usually presents the minimum absorption (low PA signal) and vice versa, and that a generic dichroic layer the same reflectance for the two opposite CP senses [29,30].

Moreover, by comparing AO and PA experiments, the differences between CDT and CDA levels, at λ=633nm, λ=830nm and λ=980nm, could be related to the scattering and diffraction contributions in the transmission measurements which are absent in the PA ones. This effect allows to identify absorption and diffraction effects in the transmission measurements since photoacoustics is intrinsically insensitive to light scattering.

5.4 Numerical simulations

Aiming at having a more complete vision of the physical phenomenon, a detailed simulation of the entire optical process has been performed. We extensively used the Finite Difference Time Domain approach (FDTD, from Lumerical) for all the simulations.

The study of the helix permittivity has been carried out considering the compositional analysis data for this kind of FIBID nanostructures presented in ref. [12]. According to the analysis, the nanohelices are composed by Pt clusters embedded in a carbon matrix (Pt percentage around 55%, C percentage around 40%, with a small amount of residual gallium coming from ion implantation). Pt is present as irregular elliptical globes with average diameter of 8 nm, forming clusters with quite homogeneous distribution along the entire helix filament (see fig.A.4.2 of the Appendix 4). The carbon acts as a host in amorphous configuration, in good agreement with literature [31].

Due to the relatively high percentage of inclusions, the Maxwell-Garnett and Brüggeman [32,33,34] models cannot be considered acceptable to correctly evaluate the effective permittivities of the composite, so we add a further numerical step by performing a long series of simulations to emulate the random arrangement of Pt clusters in the carbon matrix. For each simulation, Pt clusters featured random positions and generic ellipsoidal shapes inside a C host, limiting the ellipsoids' side lengths to the values before mentioned and keeping fixed the materials' percentages according to the declared chemical composition. See ref.[12] for further details.

The Pt and C dielectric functions were extracted from Palik [35], *Djurišić* & *Li [36], respectively.* We included a composite material with C as the host medium and containing Pt ellipsoids into a FDTD box with a z extension of 1μm and large 0.5μm x

0.5µm on the Oxy plane, with couples of periodic boundary conditions at the Oxz and Oyz sides to emulate an infinite layer of homogeneous composite material. We illuminated the FDTD box with a vertical plane wave assuming a random arrangement of ellipsoids, and we extracted the composite material dispersion shown in fig.S2.

We used these spectra to perform a second stage of simulations, where we investigated the behavior of a periodic distribution of single-wired helices located upon the multilayered substrate and featuring a certain variance among their geometrical parameters under downward illumination, using the geometrical parameters of the sample shown in figure 1, including random variations to emulate the fabrication tolerances: VP was set to 300±10 nm, WD to 100±10 nm and ED to 300±20nm, with ± indicating the standard deviation. In addition, we assumed a description formula for the helix central line given by:

$$x(\theta)=\frac{ED-WD}{2}\cdot\cos(\theta),\qquad y(\theta)=\frac{ED-WD}{2}\cdot\sin(\theta)\qquad z(\theta)=\sqrt[p]{\left(1+\theta_0{}^p\right)\Big/\left(1+\left(\theta_0/\theta\right)^p\right)}H_{Tot},\ \theta\in[0,6\pi] \tag{4}$$

with ϑ_0=6π*(0.9±0.06), p=10±0.7, and H_{Tot}=3VP. This last expression allowed to emulate the helix vertical shrinking effect during the growth process along the third dimension (see reference [10]).

Each single simulation was performed assuming all the helices to be identical by setting again periodic boundary conditions at the Oxz and Oyz sides, and provided the single transmittances and reflectances needed to get the simulated absorption levels for the two circularly polarized incident beams shown in fig.5a. These data have been then employed for calculating CD_A shown in figure 5b, along with experimental data referred to the single wavelengths of 532nm, 633nm, 830nm, and 980nm (indicated as points A, B, C and D, respectively). We also calculated the effective refractive indexes [30] associated to the helices layer surrounded by vacuum for the two senses of circular polarization, as shown in fig.A.4.3 of Appendix A.4. The helices appear to resonate approximately at 261THz (λ=1150nm) and 441THz (λ=680nm) under normal plane incidence with left and right circular polarization, respectively.

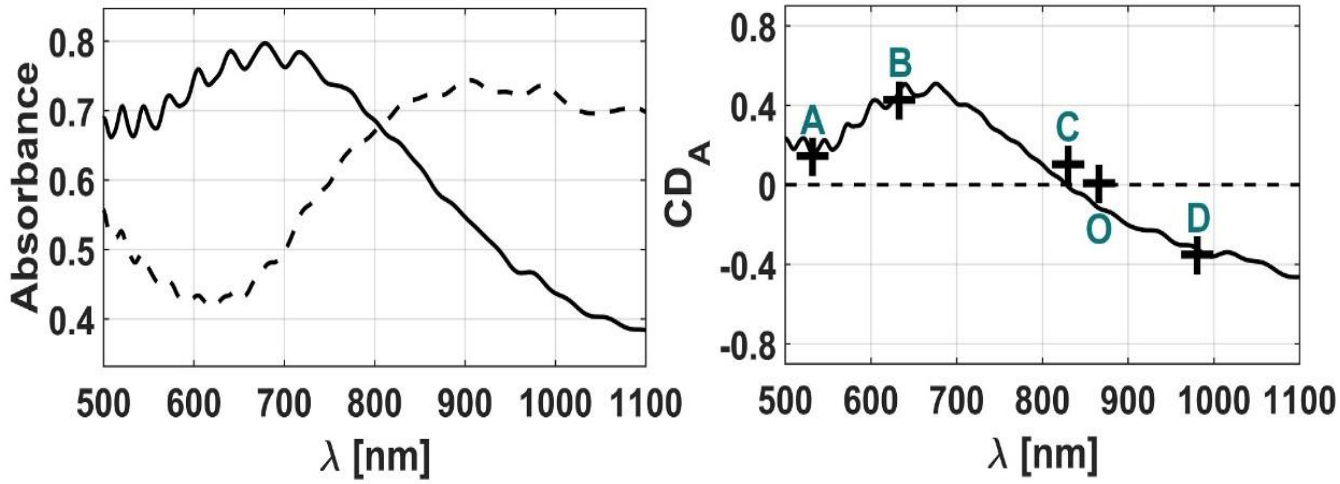

Figure 5. (a) average absorption levels (dashed for Left CP and straight for Right CP) for periodic triple turn helices aligned with LP=700nm, and featuring a central line described by the equations in (4), with VP=300±10nm, WD=110±10nm, ED=300±20nm,ϑ_0=6π*(0.9±0.06), p=10±0.7. (b) Corresponding CD_A spectrum as defined in (3); {A, B, C, D} indicate the CD_A values measured by means of the PA technique, while O indicates the AO crossing point.

The simulated spectra demonstrated to be in good agreement with the main experimental data, as can be seen by the close proximity of the [A,B,C,D,O] points from the straight line in the graph. Small discrepancies arise potentially due to negligible differences between the adopted dispersion curves and the ones related to the real composite material, and to fabrication tolerances in the helices geometry. Looking at fig.3b and 5b, we note also a small difference between the AO and PA crossing points, mainly due to small anisotropies on the experiment which naturally leads to spurious dichroism; this latter sums up with the real intrinsic dichroic of the helices' ensemble [12] and that of the substrate hosting the helices. A more detailed interpretation about this shift, which however is sufficiently small to be negligible, can be read in appendix A.4. As demonstrated by experimental measurements [11,12], the helices respond to the incoming electromagnetic field with low reflection levels and a good impedance match, acting as a wide band effective filter for circular dichroism both for the transmitted fields and the absorbed power.

5.5 Conclusions

We investigated the dichroic character of a nano-structured sample composed of an ordered ensemble of nano-sized helices fabricated by FIBID process built on a small area. We have optically characterized the nanohelix array by AO and PA techniques. By comparing optical and photoacoustic techniques, AO measurements are affected by high diffraction effects and, in addition, in the case of reduced sample area, empty area transmission hinders the purity of fields, while, PA measurement has allowed to obtain the pure and precise CD of the chiral sample by measuring scattering independent absorptions solely related to the helices.

An accurate numerical study allowed to perform a complete analysis of the electromagnetic phenomenon, confirming the experimental results. While the reduction of the array size helps to decrease fabrication time and eases placement inside integrated systems, it usually compromises CD detection, but thanks to the PA technique we have overcome this limitation. Since we obtained high CD values over a very large bandwidth for this sample, as per nature of this class of materials, we consider it a suitable candidate for innovative optical filters operating in the NIR, VIS and potentially UV frequency regions.

5.6 References

[1] Nordén, B., Rodger, A., Dafforn, T. *Linear Dichroism and Circular Dichroism: A Textbook on Polarized-Light Spectroscopy (Special Publication), 1st Edition* (Society of Chemistry, 2010)

[2] Bertolotti, M., Belardini A., Benedetti, A., Sibilia, C. Second harmonic circular dichroism by self-assembled metasurfaces [Invited], *JOSA B* 32, 7, 1287-1293 (2015)

[3] Balanis, C., A. *Antenna Theory - Analysis and Design, 3rd Edition* (John Wiley & Sons, 2005)

[4] Gansel, J. K. *et al.* Gold helix photonic metamaterial as broadband circular polarizer, *Science* 325, 5947, 1513-1515 (2009)

[5] Xiong, Z. *et al.* Assembling optically active and nonactive metamaterials with chiral units, AIP Advances 2, 041413 (2012)

[6] Yang, Z. *et al.* Polarization properties in helical metamaterials, Front. Of Optoelec. 5, 3, 248–255 (2012)

[7] Kaschke, J., Wegener, M. Gold triple-helix mid-infrared metamaterial by STED-inspired laser lithography, *Opt. Lett.* 40, 17, 3986-3989 (2015)

[8] Behera, S., Joseph, N-single-helix photonic-metamaterial based broadband optical range circular polarizer by induced phase lags between helices *J. App. Opt.* 54, 5, 1212-1219 (2015)

[9] Mark, A.G., Gibbs, J.B., Lee T.-C., Fisher, P. Hybrid nanocolloids with programmed three-dimensional shape and material composition, *Nature Mat.* 12, 3685, 802-807 (2013).

[10] Esposito M. *et al.* Three Dimensional Chiral Metamaterial Nanospirals in the Visible Range by Vertically Compensated Focused Ion Beam Induced-Deposition, *Adv. Opt. Mat.* 2, 2, 154–161 (2014)

[11] Esposito, M. *et al.* Nanoscale 3D Chiral Plasmonic Helices with Circular Dichroism at Visible Frequencies, *ACS Photonics* 2, 105-114 (2015)

[12] Esposito, M. *et al.* Tailoring chiro-optical effects by helical nanowire arrangement, *Nanoscale* 7, 18081-18088 (2015)

[13] Tasco, V. *et al.* Three-dimensional nanohelices for chiral photonics, *Appl. Phys. A* 122, 1–6 (2016)

[14] Esposito, M. et al. Triple-helical nanowires by tomographic rotatory growth for chiral photonics, *Nat. Comm.* 6, 6484 (2015)

[15] Mandelis, A. Principles and Perspectives of Photothermal and Photoacoustic Phenomena in *Progress in Photothermal and Photoacoustic Science and Technology, Vol 1* (Appleton & Lange, 1991)

[16] Wang, L. V. Photoacoustics Imaging and spectroscopy (CRC Press, 2009)

[17] Saxe, J. D., Faulkner, T. R., and Richardson, F. S. Photoacoustic detection of circular dichroism, *Chem. Phys. Lett.* 68, 71–76 (1979)

[18] Garcia, M.E., Brouder, Ch., Bennemann, K. H. Theory for the photoacoustic response to circularly polarized X-rays: How to detect magnetism by using a microphone, *Solid. State Comm.* 103, 6, 331-335 (1997)

[19] Uversky V. N., Permyakov, E. A. *Methods in Protein Structure and Stability Analysis* (Nova Science Publishers, 2007)

[20] Palmer, R. A., Roark, J. C., Robinson, J. C. Photoacoustic detection of natural circular dichroism in crystalline transition metal complexes in *Stereochemistry of Optically Active Transition Metal Compounds* (ed. Douglas, E. B., Saito, Y.) *ACS Symposium Series* 119, 20, 375-395 (1980)

[21] Matsuda, O., Larciprete, M. C., Li Voti, R., Wright, O. Fundamentals of picosecond laser ultrasonics, *Ultrasonics* 56, 3-20 (2015)

[22] Belardini, A.et al. Chiral light intrinsically couples to extrinsic/pseudo-chiral metasurfaces made of tilted gold nanowires, *Sci. Rep.* 6, 31796 (2016)

[23] Zelewski, S. et al. Photoacoustic spectroscopy of absorption edge for GaAsBi/GaAs nanowires grown on Si substrate, *Appl. Phys. Lett* 109, 182106 (2016)

[24] Esposito, M. et al. Programmable Extreme Chirality in the Visible by Helix-Shaped Metamaterial Platform, *Nano Lett.* 16, 9, 5823–5828 (2016)

[25] Brüel & Kjær, Product Data: Condenser Microphone Cartridges - Types 4133 to 4181, *http://www.bksv.com/doc/Bp0100.pdf* (Date of access:01/03/2017)

[26] Dorman, B.P., Hearst, J.E., Maestre, M.F. UV absorption and circular dichroism measurements on light scattering biological specimens, *Methods Enzymol.* 27, 767, 767-796 (1973)

[27] Benedetti, A., Belardini, A., Veroli, A., Centini, M., Sibilia, C. Numerical tailoring of linear response from plasmonic nano-resonators grown on a layer of polystyrene spheres, *Jour. of App. Phys.* 116, 164312 (2014)

[28] Ferenc Zsila M.D. Electronic Circular Dichroism Spectroscopy, *Pharm. Sci. Enc.* 7, 1–61 (2010)

[29] Landau, L. D., Lifshitz, E. M. *Electrodynamics of Continuous Media, Vol.8* of the *Course of Theoretical Physics* (Pergamon Press, 1960)

[30] Castanié, A., Mercier, J.-F., Félix, S., Maurel, A., Generalized method for retrieving effective parameters of anisotropic metamaterials, *Opt. Expr.* 22, 24, 29937-29953 (2014)

[31] De Teresa, J. M. et al. Origin of the Difference in the Resistivity of As-Grown Focused-Ion- and Focused-Electron-Beam-Induced Pt Nanodeposits. Jour. of Nanomat. 2009, 936863 (2009)

[32] Weiglhofer, W. S., Lakhtakia, A. & Michel, B. Maxwell Garnett and Bruggeman formalisms for a particulate composite with bianisotropic host medium. Microw. Opt. Technol. Lett. 15(4), 263–266 (1997)

[33] Tuck, C. Effective Medium Theory 1st Ed. (Oxford University Press, 1999)

[34] Weiglhofer, W. S., Lakhtakia, A. Introduction to Complex Mediums for Optics and Electromagnetics (SPIE Press, Bellingham, Wash, USA, 2003)

[35] Palik, E. D. Handbook of Optical Constants of Solids (Academic Press, 1998)

[36] Djurišić, A. B. & Li, E. H. Optical properties of graphite. Jour. of App. Phys., 85(10), 7404–7410 (1999)

6 Dichroic filter based on planar plasmonic metameterials with a bean-shaped cell element: theory, fabrication, experiment

Introduction

What makes Surface Plasmons unique and popular is the capacity to have sub-wavelength scale features and field localization [1]; those optical traits, added to metamaterials' properties, made them particularly successful in field such as near-field microscopy and chemical/biological sensing [2,3]. Plasmonic structures can also enhance interaction with circularly polarized light, and some exhibit strong chiroptical effect [4] (see chapter 2.8); in the recent years chiral plasmonic nanostructures have gained substantial interest [5,6].

These structures exhibit a high circular dichroism compared to common biomolecules [7,8]; but in a combination of both the plasmons may shift molecular chirality of many biomolecules from UV to visible, and amplify the natural circular dichroism of molecules [9]. This phenomenon is called Super Chirality, and many ways to exploit it are being researched in order to produce a high sensitivity device which can detect the handedness of a given molecule [10].

Over the years, many highly dichroic metasurfaces have been developed, and the literature is still in expansion [11]. Other than their extremely strong optical activity [12,13], which promises the ability to create compact broadband circular polarizers [14] and asymmetric transmission [15,16], chiral metamaterials have demonstrated a capacity to realize negative refractive indices, even when neither ε

nor μ is negative, as theoretically proposed in [17], and later independently discussed in [18,19]. This concept was then experimentally demonstrated in the microwave [20], terahertz [21] and optical regimes [22].

To the great variety of geometries that have been demonstrated corresponds a big variety of fabrication techniques and approaches, both top-down and down-top; in general, in quantitative terms of circular dicroism factor, the top-down approach is more successful. Notable three dimensional (3D) nanophotonic structures are the nano-helices [23,24] (see chapter 6) built with FIBID technique or Laser writing, bichiral plasmonic crystals built by combining laser writing with electroless plating [25], large area 3D gold spirals manufactured by colloidal hole-mask lithography in combination with tilted-angle rotation evaporation, and 3D L shape [26] through an "on edge" lithography. Stacked planar (2D) geometries are also present in literature, and such approach allows also to accomplish strong chiroptical responses; all of them can be all built by combining lithography with alignment in a layer-by-layer manner; between the most successful structure, we can list: twisted split rings [27], nanoparticle clusters[28], bilayer L-Shapes [29], nanorods with twists [30]. Other than 3D and stacked 2D structure, a few simple planar structures have been successful: gammadions [4], nanoslit pairs [31], split rings [32], and few others; their success was not due to the intrinsic chirality of their cell shape, but rather to their extrinsic chirality [32] due to oblique incidence, or to due to high field localization inducing non linearities[33,34]. Today, the highest CDF value reported in literature is 37% in a broad range from 500-1000nm [24]; as said, such values can be obtained through complex and expensive fabrication techniques, not accessible for most and hardly reproducible in an industrial environment.

In this chapter we present, design, fabricate and measure a new planar geometry in a plasmonic metamaterial array with a theoretical CDF of 60% and a measured value of 17% over a bandwidth of 100nm. During design step, shape variations around the perfect values have also been simulated and taken into account. The planar geometry helps not only to simplify the fabrication processes, which makes it more accessible, inexpensive and industrially feasible, but also to possible biological measurements, because of the regularity of the surface for the attachment of cells [35,36].

In section 2 we will present the geometry, report the numerical simulations and draw the theoretical considerations. In section 3 we will present the fabrication

processes of the array. In section 4 we will show the measurement setup and the first results. In the last section, the conclusions are drawn.

6.2 Theoretical and numerical analysis

The first geometry we tried was the spiral, because of the intrinsic chirality expected by its shape. So we tested the both logarithmic and archimedian spirals, obtaining average results, not reported in this work. But, when the archimedian spirals' shape is reduced to a fraction of its length, in particular when it's number of turns is less than 1 (we have tested around 0.35 and 0.5, and had a "bean"-like shape), we have noticed no decrease in CDF values connected to intrinsic chirality; a shorter length means a lower single element occupation and a higher density of elements in the same area, which boosts the overall CDF. Also, we have distributed the elements on the surface by using triangular arrays; the high field localization in the area where multiple elements are closed has an enhancement effect on CDF. In Fig.6.1 a and b the geometry is shown, along with the array map.

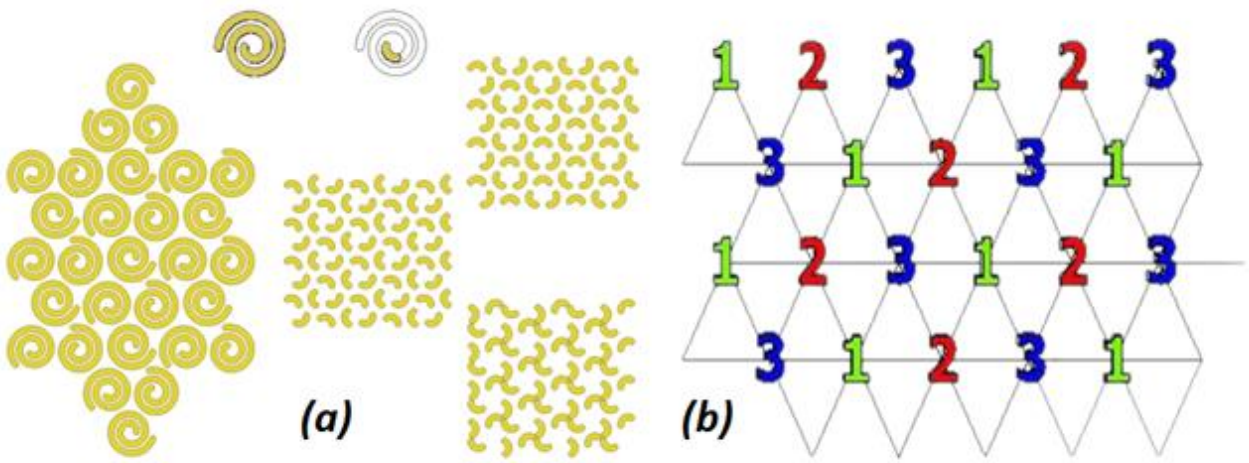

Figure 6.1. *(a)*The single unit is an Archimedean spiral: the elongated stripes have a variable angular extension; the units are rotated 120°. *(b)*The 2D profile follows an equilateral triangular scheme.

We have operated 3D FDTD simulation on the structures; the base unit cell for the numerical calculation is shown in Fig.6.2: a generic gold/silver Archimedean spiral section on a glass substrate; the mutual distance and the filament cross section have been set in in order to prevent collisions and deformations during the growing process; the array follows a triangular scheme of identical units rotated of 120° to prevent any form of linear on-plane anisotropy.

In addition to the array period (triangle side length), the single element of the array has been obtained by defining a combination of parameters from archimedian spirals' polar coordinates [37,38]: width, thickness, starting angle (origin is 0°), length, angle of the axis and gap of the spiral. This high number of parameters makes it computationally challenging to analyze the overall best combination of values for the highest CDF possible; instead, by taking into account of the fabrication constrains and degrees of freedom, we have focused more on a number of parameters (width, thickness, array spacing), less on others (length, angle), and almost nothing on the remaining; this way the simulations were more manageable, and we managed to find combinations where the high field localization allowed to consistently achieve high CDF.

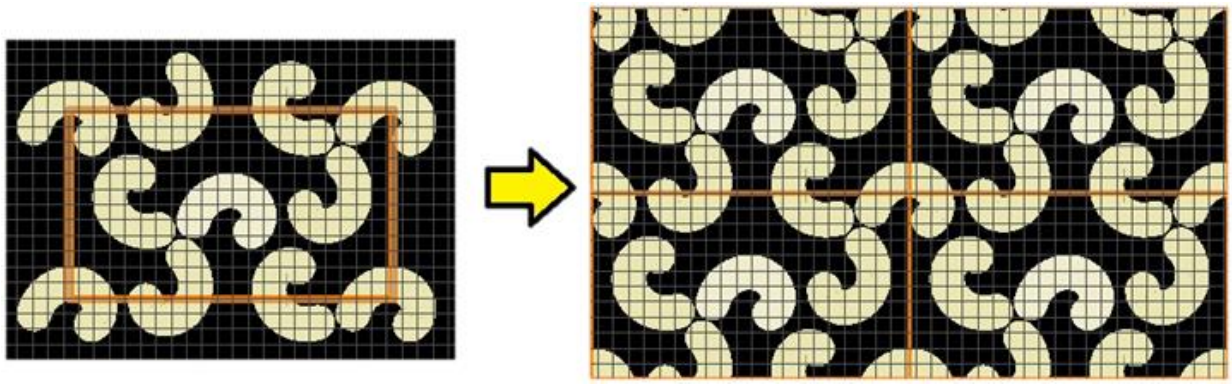

Figure 6.2. The base cell for the calculation method: the angular extension is chosen to ensure the best CD performances; with the PBC boundaries we can simulate all the device creating a perfect periodic distributions of identical units.

The 3D box is perfectly square but properly cut in order to reproduce the effect of a triangular distribution with the aid of PBC set at its boundaries, as can be seen in Fig.6.2. We have set PML on the top and bottom faces because we expect to measure transmitted value from incoming perpendicular beam (Fig.6.3).

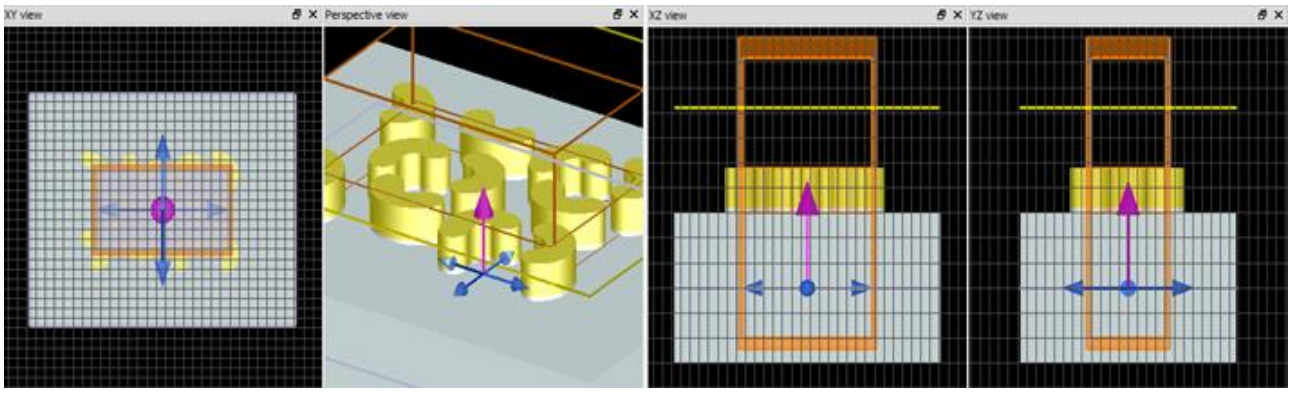

Figure 6.3. Lumerical FDTD 3D box interfaces are shown: the e.m. source is placed in the glass layer, under the gold structures, in the bottom of the simulation area.

We have sweeped through the three main parameters, namely array period, thickness, and width. We also tested both Au and Ag based structures. Examples are shown in Fig.6.4. The two values of interest were Transmission (Left and Right) and Circular Dichroism. 3D-FDTD simulation allowed the extraction of the main mode from the overall transmitted field; other than the search of the highest CD value (corresponding to a high difference between the two transmission of the left and right circularly polarized beams), we also wanted a transmission significantly higher than the noise. We defined the CD calculated as:

$$CD = 2\frac{T^{+}-T^{-}}{T^{+}+T^{-}} \tag{6.1}$$

where T^{+} and T^{-} are the output transmission spectra for left and right circularly polarized impinging waves.

We took into account of the variability of the parameters after fabrication: the array period has been considered always fixed, while thickness had a variability of ±2nm, and the width a variability of ±15nm (corresponding to lithographic non-idealities). As can be seen from Fig.6.4, there are multiple CD peaks over the various wavelengths, although the only peak that is always present is around 650nm.

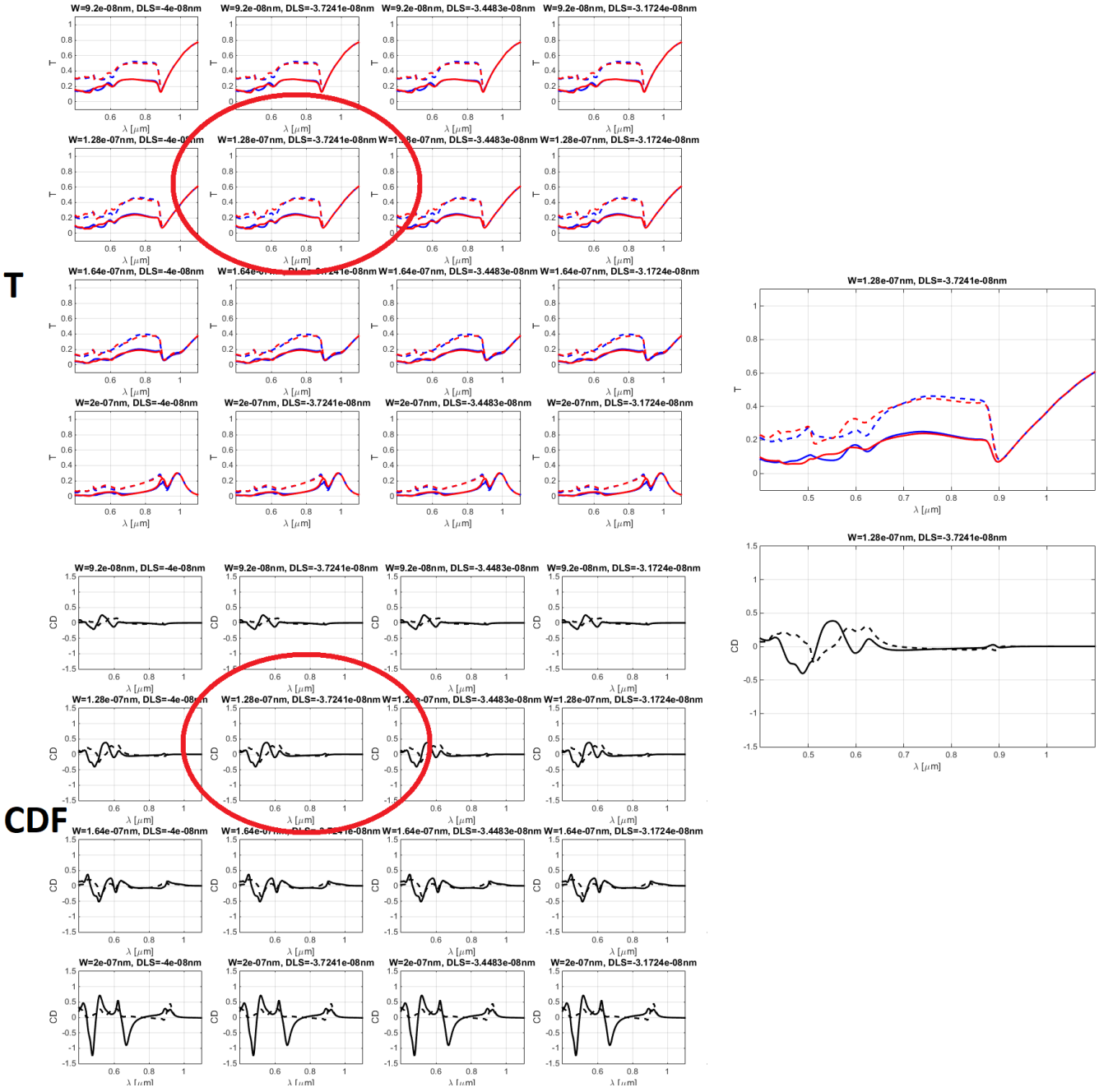

Figure 6.4. Example of the multiparametric sweep with Ag: we have sweeped the Width (W) and Spacing (DLS). The number of combinations and graphs was actually higher. In the graphs, dashed lines represent the overall Transmitted signal, while standard lines are the mode 0. In the transmission (T) graphs Red is Right Circular Polarization, while Blue is Left Circular Polarization.

6.3 Fabrication of the Nanobeans

Fabrication of the nano-beans surface has been operated through a lift-off process. A single layer of PMMA with around 650nm thickness has been patterned through Electron Beam Lithography; after the development of the PMMA, followed a thermal deposition of Au or Ag; finally, the lift-off was completed with the removal of PMMA with acetone. Each array covers 50x 50µm^2 and 100x100µm^2, although it is possible to produce bigger surfaces with this technique.

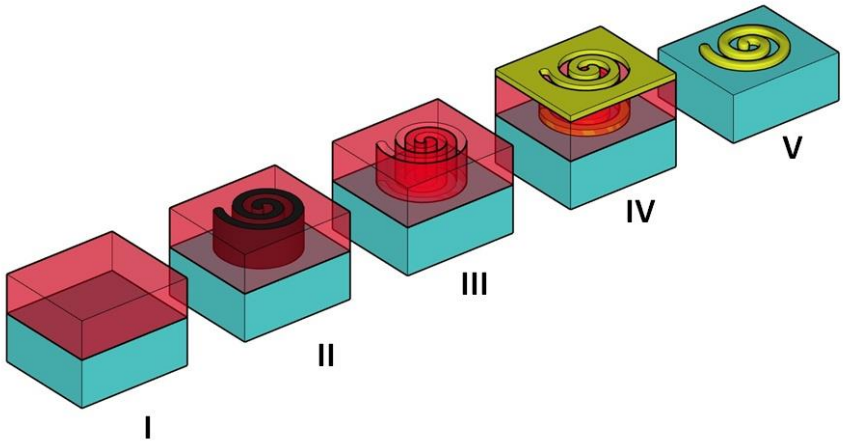

Figure 6.5. 3D schematic view of the fabrication process flow of the nano-beans.

As already stated, EBL requires tests in order to find the correct dosage values; a weak electron beam may not penetrate enough in the PMMA, and a too strong electron beam may create too big undercuts that undermine the final geometry. The use of glass substrates with an ITO layer helped to reduce undercut effects. We used two types of EBL machines, each with a different set of beam parameter, for two groups of samples: “A” and “B”, the first built with Ag, the second with Au. Images of fabricated elements from group A samples are shown in Fig.6.7.

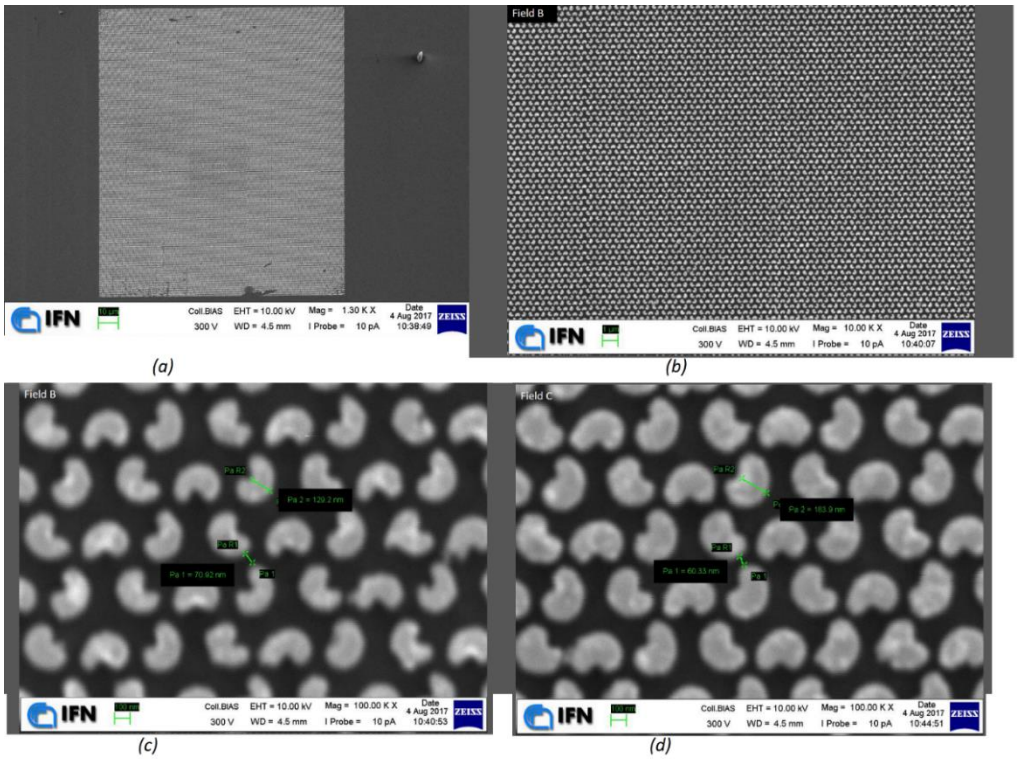

Figure 6.7. SEM images of a general view of the metasurface with Ag on SiO_2. The details are gradually zoomed from *(a)* to *(d).*

Images of areas from sample group B, are shown in Fig.6.8.

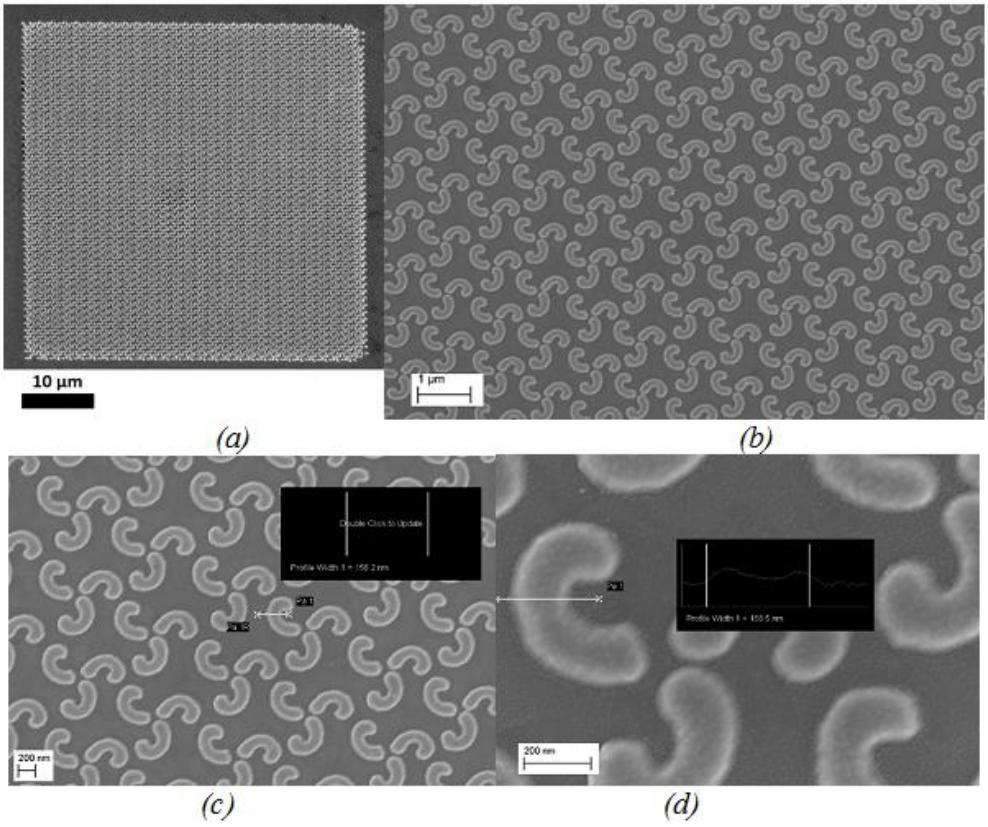

Figure 6.8. SEM images of a general view of the surface with Au on SiO_2. The details are gradually zoomed from *(a)* to *(d).*

6.4 Measurement setup and results

The concept idea and the setup of the measurements are shown in Fig.6.9. The sample was optically studied by normal incidence transmission on a home-made confocal setup. Light from a tungsten lamp was collimated and focused on the sample by an adjustable numerical aperture condenser (from 0.05 to 0.95). For normal incidence, the minimum numerical aperture was used, corresponding to a semi-aperture incidence angle of less than 3°. Circular polarization was obtained by means of a linear polarizer coupled to a broadband quarter wave-plate (Zeiss Microscopy, item number 445226-0000-000). Transmitted light was collected by a 10x 0.45 NA objective lens coupled to three cascaded (focusing, collimating and refocusing) lenses, and analysed with a CCD camera coupled to a mono-chromator. Optical transmission was evaluated with respect to the light transmitted through the bare glass substrate.

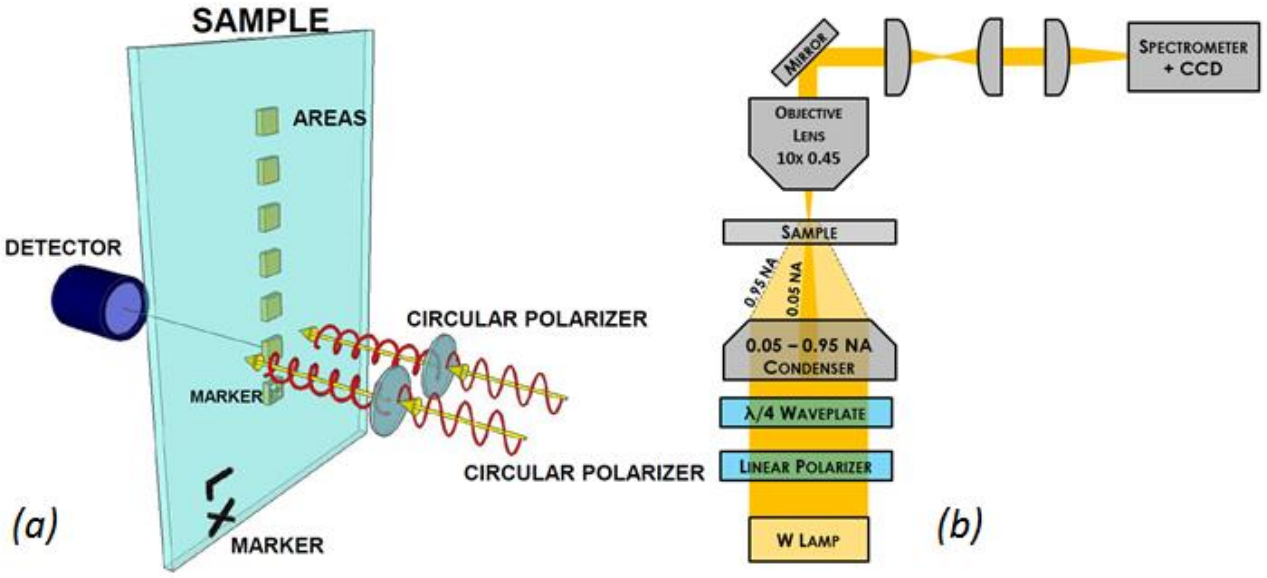

Figure 6.9. (a) Concept representation of the measurements on the samples. (b) Schematic view of the measurement setup.

CDF levels obtained from the measurements of samples from group A and B are shown in Figure 6.10; CD levels reach 17%, which is relatively high, although not yet close to the expected value of 60%. In Fig.6.11 the transmission levels from the output of two areas have been displayed (we have shown only two areas for the sake readability); as can be seen, Right Circular Polarization and Left Circular Polarization are not perfectly distinguished on a (0-to-1 scale), although a shift between the two is noticeable. In both groups the transmission issue is related to the fabrication: in group A the single elements were too symmetric due to overexposure, in group B the

thickness was just 60nm. Another group of samples is now being fabricated with corrections.

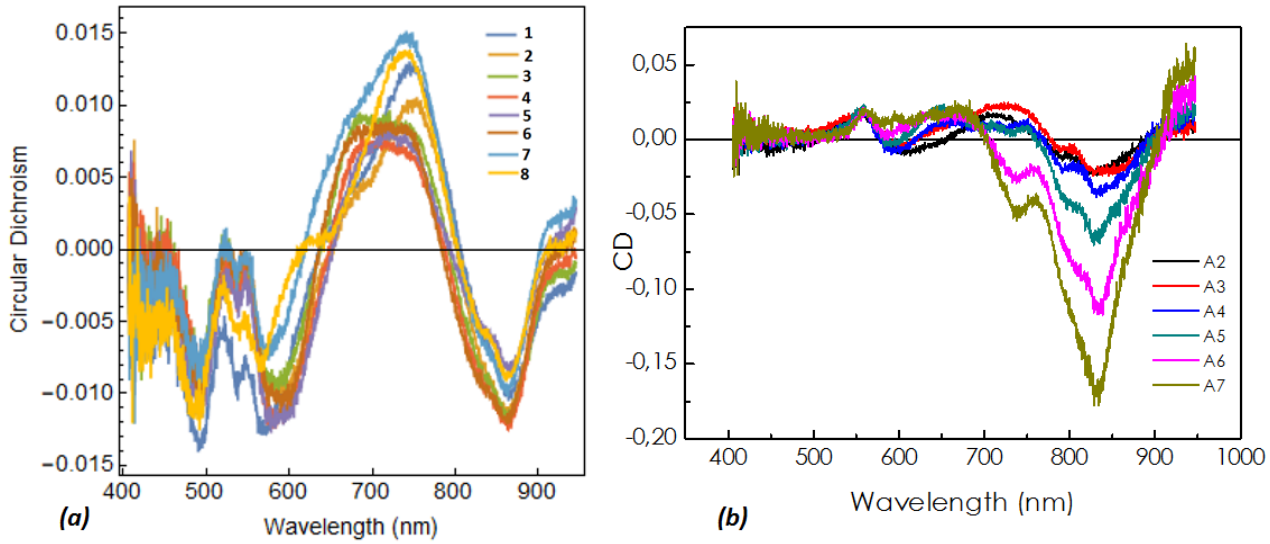

Figure 6.10. CD Measurement results for samples A (a) and B (b). The width of the nanobeans has been gradually increased from 100nm to 250nm in areas 8-1 and A1-A7. On the x-axis are the wavelength and on the y-axis the measured CD.

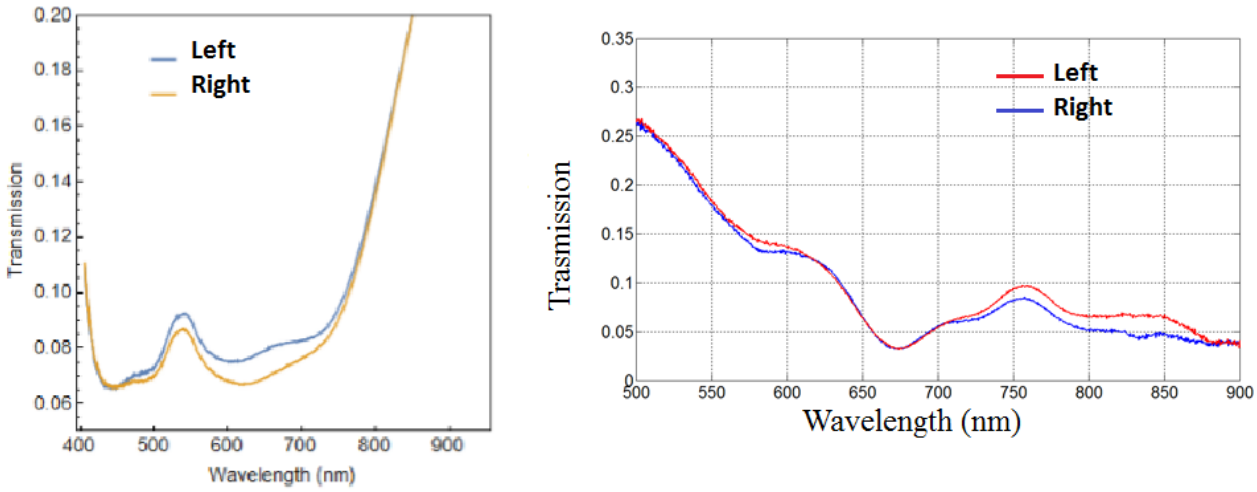

Figure 6.11. Transmission measurement for samples A (a) and B (b). Each graph represents a single line. On the x-axis are the wavelength and on the y-axis the measured CD.

The two samples A and B have each a specific issue due to the non-ideality of their geometries (which were far from their "tolerance level" we expected during design process). Au samples, while being perfectly constructed from top view (see Fig.6.8), had a rounded vertical profile, as shown in Fig.6.9; this meant that the high field localization changes towards z (see figure), resulting in different behavior

corresponding to different height; also, the thickness of the nano-beans should be 130nm, while the realized cell-elements have a thickness of 75nm; overall, it resulted in a slight reduction of CDF amplitude (17% is still one of the highest values in literature) and broadening of bandwidth. Ag samples, on the other hand, had very straight sidewalls, although from a top view the roundness of the nano-beans is noticeable from Fig.6.7, which is strongly different from the expected shape in Fig.6.2.

Another group of samples will be fabricated and measured, after these first samples' feedbacks, once the fabrication machines will be available again.

6.5 Conclusions and future developments

The nanobeans display a high CDF due to the field localization, which adds to the intrinsic chirality of their shape. We have engineered the geometrical parameters by selecting a few, while keeping the others fixed; we did this by following fabrication constrains and limitations. We have developed two groups of devices with both Ag and Au; despite having fabrication issues, which hindered mainly the transmission levels, we still obtained a relatively high CDF of 17%, which confirms the design; with a slightly better accuracy in lithography, we expect to be able to obtain higher CDF values, closer to the theoretical value of 67%. We had a bandwidth of 100nm around peaks close to 650nm with Ag and 800nm with Au.

This structure was built on a single layer, and has shown a good tolerance to fabrication non-idealities; this makes it more inexpensive than most of the geometries in literature, and helps its reproducibility on an industrial scale. Since the ultimate goal of these highly dichroic surfaces is to be applied in bio-sensing systems, this planar geometry is expected to be more successful than other complex geometries, as it is more suitable for the attachment of molecules than more complex tridimensional geometries.

6.6 References

[1] S. A. Maier, “Plasmonics: fundamentals and applications”, Springer Science Business Media LLC (2007).

[2] O. S. Wolfbeis, “Fiber-Optic Chemical Sensors and Biosensors”, Anal. Chem. 76, 3269-3284 (2004)

[3] K. Kurihara, H.Ohkawa, Y.Iwasaki, O.Niwa, T.Tobita, K.Suzuki, “Fiber-optic conical microsensors for surface plasmon resonance using chemically etched single-mode fiber”, Analytica Chimica Acta, 523, 2, 165–170 (2004)

[4] V. K. Valev, J.J.Baumberg, C.Sibilia, T.Verbiest, “Chirality and Chiroptical Effects in Plasmonic Nanostructures: Fundamentals, Recent Progress, and Outlook”, Adv. Mater. 25, 2517–2534 (2013)

[5] M.Schaferling, D.Dregely, M.Hentschel, H.Giessen,“Tailoring Enhanced Optical Chirality: Design Principles for Chiral Plasmonic Nanostructures”, Phys. Rev. X 2, 031010 (2012)

[6] A.O.Govorov, Z.Fan, P.Hernandez, J.M. Slocik and R.R. Naik, “Theory of Circular Dichroism of Nanomaterials Comprising Chiral Molecules and Nanocrystals: Plasmon Enhancement, Dipole Interactions, and Dielectric Effects”. Nano Lett. 10, 1374–1382 (2010)

[7] T.Cao, C.Wei, L.Mao and Y.Li, “Extrinsic 2D chirality: giant circular conversion dichroism from a metal-dielectric-metal square array”, Scientific Reports 4, 7442 (2014)

[8] A.Benedetti, B.Alam, M.Esposito, V.Tasco, G.Leahu, A.Belardini, R.Li Voti, A.Passaseo & C.Sibilia, “Precise detection of circular dichroism in a cluster of nano-helices by photoacoustic measurements”, Scientific Reports 7, 5257 (2017)

[9] A.O. Govorov, “Plasmon-Induced Circular Dichroism of a Chiral Molecule in the Vicinity of Metal Nanocrystals. Application to Various Geometries”, J. Phys. Chem. C 115, 7914–7923 (2011).

[10] N. A. Abdulrahman, Et al. “Induced Chirality through Electromagnetic Coupling between Chiral Molecular Layers and Plasmonic Nanostructures”. Nano Lett. 12, 977−983 (2012).

[11] Z. Wang, F. Cheng, T. Winsor and Y. Liu, “Optical chiral metamaterials: a review of the fundamentals, fabrication methods and applications”, Nanotechnology 27, 412001, pp.20 (2016)

[12] M.Kuwata-Gonokami, N.Saito, Y.Ino, M.Kauranen, K.Jefimovs, T.Vallius, J.Turunen and Y.Svirko, “Giant optical activity in quasi-two-dimensional planar nanostructures”, Phys. Rev. Lett., 95, 227401 (2005)

[13] Z.Li, M.Mutlu and E.Ozbay, “Chiral metamaterials: from optical activity and negative refractive index to asymmetric transmission”, J. Opt., 15, 023001 (2003)

[14] J.K.Gansel, M.Thiel, M.S.Rill, M.Decker, K.Bade, V.Saile, G.von Freymann, S.Linden and M.Wegener, “Gold helix photonic metamaterial as broadband circular polarizer Science”, 325, 1513–5 (2009)

[15] V.A.Fedotov, A.S.Schwanecke, N.I.Zheludev, V.V.Khardikov and S.L.Prosvirnin, “Asymmetric transmission of light and enantiomerically sensitive plasmon resonance in planar chiral nanostructures”, Nano Lett., 7, 1996–9 (2007)

[16] V.A.Fedotov, P.L.Mladyonov, S.L.Prosvirnin, A.V.Rogacheva, Y.Chen and N.I.Zheludev, “Asymmetric propagation of electromagnetic waves through a planar chiral structure”, Phys. Rev. Lett., 97, 167401 (2006)

[17] S.Tretyakov, I.Nefedov, A.Sihvola, S.Maslovski and C.Simovski, “Waves and energy in chiral nihility”, J. Electromagn. Waves Appl., 17, 695–706 (2003)

[18] J.B.Pendry, “A chiral route to negative refraction Science”, 306, 1353–5 (2004)

[19] C.Monzon and D.W.Forester, “Negative refraction and focusing of circularly polarized waves in optically active media”, Phys. Rev. Lett., 95, 123904 (2005)

[20] J.Zhou, J.Dong, B.Wang, T.Koschny, M.Kafesaki and C.M.Soukoulis, “Negative refractive index due to chirality”, Phys. Rev. B, 79, 121104 (2009)

[21] S.Zhang, Y-S.Park, J.Li, X.Lu, W.Zhang and X.Zhang, “Negative refractive index in chiral metamaterials”, Phys. Rev. Lett., 102, 023901 (2009)

[22] E.Plum, V.A.Fedotov, A.S.Schwanecke, N.I.Zheludev and Y.Chen, “Giant optical gyrotropy due to electromagnetic coupling”, Appl. Phys. Lett., 90, 223113 (2007)

[23] M.Esposito, V.Tasco, F.Todisco, A.Benedetti, D.Sanvitto and A.Passaseo, “Three dimensional chiral metamaterial nanospirals in the visible range by vertically compensated focused ion beam induced-deposition”, Adv. Opt. Mater, 2, 154–61 (2014)

[24] M. Esposito, V. Tasco, F. Todisco, M. Cuscuna`, A. Benedetti, D. Sanvitto, and A. Passaseo, “Triple-helical nanowires by tomographic rotatory growth for chiral photonics”, Nature communications, 7484. doi: 10.1038 (2015).

[25] A.Radke, T.Gissibl, T.Klotzbücher, P.V.Braun and H.Giessen, “Three-dimensional bichiral plasmonic crystals fabricated by direct laser writing and electroless silver plating”, Adv. Mater., 23, 3018–21 (2011)

[26] K.Dietrich, D.Lehr, C.Helgert, A.Tünnermann and E-B.Kley, “Circular dichroism from chiral nanomaterial fabricated by on-edge lithography”, Adv. Mater., 24, OP321–5 (2012)

[27] N.Liu, H.Liu, S.Zhu and H.Giessen, “Stereometamaterials”, Nat. Photon., 3, 157–62, (2009)

[28] M.Hentschel, M.Schäferling, T.Weiss, N.Liu and H.Giessen, “Three-dimensional chiral plasmonic oligomers”, Nano Lett., 12, 2542–7 (2012)

[29] C.Helgert, E.Pshenay-Severin, M.Falkner, C.Menzel, C.Rockstuhl, E-B.Kley, A.Tünnermann, F.Lederer and T.Pertsch, “Chiral metamaterial composed of threedimensional plasmonic nanostructures”, Nano Lett., 11, 4400–4 (2011)

[30] Y.Zhao, M.A.Belkin and A.Alù, “Twisted optical metamaterials for planarized ultrathin broadband circular polarizers”, Nat. Commun., 3, 870 (2012)

[31] E.Hendry, R.Mikhaylovskiy, L.Barron, M.Kadodwala and T.Davis, “Chiral electromagnetic fields generated by arrays of nanoslits”, Nano Lett., 12, 3640–4 (2012)

[32] E.Plum, X.X.Liu, V.A.Fedotov, Y.Chen, D.P.Tsai and N.I.Zheludev, “Metamaterials: optical activity without chirality”, Phys. Rev. Lett., 102, 113902 (2009)

[33] S.P.Rodrigues, S.Lan, L.Kang, Y.Cui and W.Cai, “Nonlinear imaging and spectroscopy of chiral metamaterials”, Adv. Mater., 26, 6157–62 (2014)

[34] V.K.Valev, J.Baumberg, B.De Clercq, N.Braz, X.Zheng, E.Osley, S.Vandendriessche, M.Hojeij, C.Blejean and J.Mertens, “Nonlinear superchiral meta-surfaces: tuning

chirality and disentangling non-reciprocity at the nanoscale", Adv. Mater., 26, 4074–81 (2014)

[35] A.L.Morel, R.M.Volmant, C.Méthivier, J.M.Krafft, S.Boujday, C.M.Pradier, "Optimized immobilization of gold nanoparticles on planar surfaces through alkyldithiols and their use to build 3D biosensors", Colloids Surf B Biointerfaces, 81, 1, 304-12 (2010)

[36] S.Unser, I.Bruzas, J.He and L.Sagle, "Localized Surface Plasmon Resonance Biosensing: Current Challenges and Approaches", Sensors, 15, 15684-15716 (2015)

[37] Archimedes of Syracusae, "On Spirals", library of Syracusae, (225 BC)

[38] W.H.Beyer, "CRC Standard Mathematical Tables", 28th ed. Boca Raton, FL: CRC Press, p. 225 (1987)

7 Conclusions

As can be seen by the variety of projects I have presented in this thesis, metamaterials, nanophotonics and plasmonics allow to exploit a wide range of physical phenomena that may be applied in many types of devices; also, some concepts from those disciplines may be combined to produce specific effects or enhancements. The applications are very diverse: intra-chip communication, computation, imaging and chemical/biological sensing. Those research fields have developed greatly in the last 15 years, and present a mature theory and experimental demonstrations that imply potential applications in multiple directions.

The main goal of my research activities was to produce elements that may be consistently used in devices, with characteristics such as performance enhancement, repeatability of the performances, cost effectiveness and addition with preexisting circuit elements. In order to achieve this, I have worked in all phases of development, in particular analysis, design and fabrication, while I have been involved in measurements to a lower extent. As can be seen in chapter 2, the fundamentals are multiple: plasmonics (with focus on long range surface plasmons), metamaterials, circular dichroism in materials, and main fabrication instruments for a top-down approach.

In chapter 3, an analysis on vertical directional couplers with long range surface plasmons has been presented, along with its fabrication; the goal of the analysis was to discern information about all interactions in play in the structure and to find suitable parametric choices to design it. In order to compute the interaction in the s-bend region, a new method has been introduced and used; the analysis shows that the "additional" coupling is strong and significant. At the same time, the interaction can be controlled by tuning the geometrical parameters, in particular the bend radius. What makes this circuital element unique is the topological advantage it may give to Optical Integrated Circuits based on LR-SPPs: the use of polymeric claddings permits to stack multiple circuital layers, capable of communicating through the vertical directional coupler; with surface plasmons this can be achieved without increasing significantly the crosstalk between circuits. With this new element, efficient multi-planar circuit built with stripes supporting long range surface plasmons can be built

in order to satisfy the needs for the production of complex network systems. In addition to the published analysis, I have also realized the elements through bilayer lift-off method, previously planned in section 3; the details of the fabrication processes are shown, and the characterization is still in process; the first measurements shows the effectiveness of the stripe waveguides.

In chapter 4 I have proposed, analyzed, designed and partially fabricated a narrow beam optical antenna based on leaky waves approach and long range surface plasmon technology. The structure is made by combining a waveguiding system with a periodic perturbation, represented by an ultrathin plasmonic stripe and a Bragg grating, respectively; the numerical analysis has been operated through a combination of analytical method and FEM simulations, where Green's tensor has been used to compute the far-field. Three main parameters influence significantly the output of the structure, all regarding the scatterers' array: the distance from the stripes, the period, and the materials; once defined, it is possible to control the narrow beam. We have noticed that the use of dielectric scatterers may create resonances which create uncontrollable secondary lobes; this can be solved by using metals. A possible electro-optical tuning has been envisioned, in particular with the angle of the beam; if confirmed, this circuit element may be used in "frontier" applications such as integrated LIDARs, in planar imaging, or infrared communication in air. The waveguides have been realized, as well as markers for the following steps of fabrication; the fabricated structures are being measured before completion of the antenna.

In chapter 5 are presented the results of measurements and post-measurements analysis of compact samples of nano-helices built by means of a focused ion beam technique. The reduced area coverage of the nano-helices was meant to compensate the complexity of the fabrication of single nano-helices, and helps also in the production of built-in-chip sensors. We operated two types of optical measurements; direct all-optical measurements revealed the sample's dichroic character with insufficient details because of scattering and diffraction interference; on the other hand, photoacoustic measurements resulted to be a possible alternative investigation, since they directly deal with absorbed power and allow to get clear evidences of the differential selection for the two opposite polarization states. Multi-level numerical simulations confirmed the experimental results, proving once again the reliability of photoacoustic technique and the versatility of this class of dichroic artificial materials. Since we obtained high CD values (0.37) over a very large

bandwidth (500nm-1000nm) with this small sample, as per nature of this class of materials, without ruining significantly the performances in comparison with samples with bigger area coverage, we can state that integration of CD measurement systems, which are of great interest in chemical/biological biosensing can be achieved with photoacoustics.

In chapter 6 a new planar nanostructured metamaterial is proposed as an alternative approach to nano-helices; we have analyzed, designed, fabricated, and measured this new geometry, which we called “nano-beans”. With this metasurface it is theoretically possible to achieve high CD values of 0.60 and we have achieved with our preliminary devices values around 0.17. We designed the geometric parameters to obtain both an intrinsic CD and an enhancement in CD due to field localization; we also ensured reduced performance variations due to fabrication non-idealities. Fabrication was operated with EBL lithography, thermal evaporation and lift-off; to have more differentiated transmission levels new samples are now being realized; we developed samples with Ag and Au structures, which resulted in peak centered around 650nm and 850nm respectively. Like the nano-helices, this metastructure can be used as circular dichroic filters in chemical/biological sensors; the advantages are multiple: ease of construction (also in industrial scale), performance tolerance to fabrication non-idealities, high CD and planar interface for adhesion of molecules.

Handling different stages of device development required not only an increase in design complexity, but also organizational feats for the gathering of fabrication and measurements instruments. Along with my group, we have collaborated with multiple organizations: CNIS, Sapienza, for access to Electron Beam Lithography machine; CNR-ARTOV for access to clean room; CNR-IFN for access to another EBL and evaporators; University of Ottawa, SITE, for the access to clean room with instrumentations focused on surface plasmons; Department of Information Engineering, Electronics and Telecommunications (DIET), Sapienza, for logistic support; Department SBAI for the access to optical measurements; CNR-Nano Lecce for FIBID fabrication and optical measurements. Fabrication requirements are given by the capabilities of specific machines; design variations are given by feedbacks from fabricated samples. The top-down approach of fabrication has proven to be successful, repeatable and reliable.

Something that I think should be explored is the use of hybrid optical integrated circuits, made of a combination of different technologies, in order to profit from the strong points of each one of them; this could be an interesting direction, in vision of the fact that today there are multiple options for various applications; a starting point may be the design of an efficient signal coupling between different technologies. Overall, as proven also by the works presented in this thesis, we confirm the efficacy of devices made through nanophotonics, plasmonics and metamaterials, as well as their versatility. As of today, there are already in the market some sensors made of these technologies, but we believe that most of the industrial potential is yet to be expressed, and that the number of possible applications should also increase in these years.

7.1 Author's bibliography

PUBLICATIONS:

[1] B. Alam, A. Veroli and A. Benedetti. "Analysis on vertical directional couplers with long range surface plasmons for multilayer optical routing". J. Appl. Phys. 120, (2016)

[2] A. Benedetti, **B.Alam**, M. Esposito, V. Tasco, G. Leahu, A. Belardini, R. Li Voti, A.Passaseo & C.Sibilia, "Precise detection of circular dichroism in a cluster of nano-helices by photoacoustic measurements", Scientific Reports 7, 5257 (2017)

PROCEEDINGS:

[3] B. Alam, A. Veroli, A. Benedetti. "Multilayer optical routing by means of vertical directional coupler with long range surface plasmons". Poster subsmission at Nano Innovation 2016.

[4] A. Veroli, **B. Alam**, L. Maiolo, F. Mura, R. Camminiti, F. Todisco, M. De Giorgi, L. Dominici, A. Benedetti. "Planar plasmonic bean-Like nano structures for high dichroic filtering: theory, fabrication and esperiment". Poster subsmission at Nano Innovation 2016.

[5] M. Muzi, A. Veroli, A. Buzzin, **B. Alam**, G. De Cesare, D. Caputo, L. Maiolo, M. Marrani, F. Frezza. "Nano-sieve filter for microfluidic sensing on lab-on-chip". Poster subsmission at Nano Innovation 2016.

Appendices

A.1 Scattered Field by a Plasmonic Structure with a Chirped Distribution of Scatterers under Plane Incidence.

A.1.1 Constant grating period Λ

The physical structure is compounded by many scatterers (in the following also referred to as 'defects') located at discrete positions identified by their respective x_n, while their y values are assumed as identical (and for the sake of simplicity we assume that it equals 0). For the case of periodic distribution of scatterers with a fixed lattice period, we can write:

$$x_n = x_0 + n\Lambda \tag{A.1.1}$$

The incident field impinges across the structure with a certain angle of incidence and wavelength, and it is assumed to travel inside the *Oxy* plane, so I can be modeled as follows:

$$U_0(x)\big|_{y=0} = e^{\iota\frac{2\pi}{\lambda}\sin(\theta_0)x} = e^{\iota\beta x} \tag{A.1.2}$$

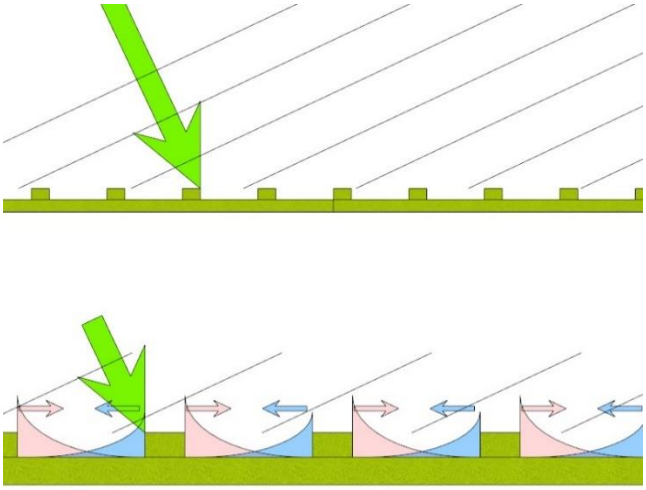

Figure A.1.1. Sequence of scatterers (in the presented case, ridge-type elements) illuminated by an impinging wave. In the bottom set, a magnified portion shows the opposite SPPs travelling along the surface between the several scatterers. The green arrow indicates the k vector of the incoming wave impinging across the plasmonic grating. The SPP are primarily excited by the incoming wave, and their complex amplitude is determined after multiple reflections across the scatterers. The ones impinging across the scatterers from both sides contribute, together with the initial impinging wave, to the total field scattered by each single scatterer.

The scatterers will radiate a propagative filed according to their shape and material; at large distances from their barycenter, the scattered field will assume the typical profile of a cylindrical wave, with a

multiplicative complex constant given by the interaction of the incoming field with the same scatterers (which is of course dependent both on the angle of incidence of the input plane wave and on the mutual distance between scatterers):

$$\begin{aligned} U_{\mathrm{S},n}(x,y) &= \alpha(\theta_0,\Lambda)\cdot H_0^{(1)}\left(k_0\sqrt{(x-x_n)^2+y^2}\right)\cdot U_0(x_n) = \\ &= \alpha(\theta_0,\Lambda)\cdot H_0^{(1)}\left(k_0\sqrt{(x-x_n)^2+y^2}\right)\cdot c\cdot e^{\imath n\beta\Lambda} \end{aligned} \tag{A.1.3}$$

where *H* denotes the Hankel function; the total scattered field will be so:

$$U_{\mathrm{S}}(x,y) = \alpha(\theta_0,\Lambda)\cdot c\cdot\sum_{n=-\infty}^{+\infty} H_0^{(1)}\left(k_0\sqrt{(x-x_n)^2+y^2}\right)\cdot e^{\imath n\beta\Lambda} \tag{A.1.4}$$

The scattered field (evaluated at a fixed *y* value given by y_L) can be decomposed in to a complete and continuous set of plane waves by the Fourier transform of complex amplitude *A*:

$$\begin{aligned} A(k_X) &= \int H_{\mathrm{S}}(x,y_L)e^{-\imath k_X x}dx = \\ &= \alpha(\theta_0,\Lambda)\cdot c\cdot\int\sum_{n=-\infty}^{+\infty} H_0^{(1)}\left(k_0\sqrt{(x-x_0-n\Lambda)^2+(y_L)^2}\right)\cdot e^{\imath n\beta\Lambda}\cdot e^{-\imath k_X x}dx = \\ &= \alpha(\theta_0,\Lambda)\cdot c\cdot\sum_{n=-\infty}^{+\infty}\left[\int H_0^{(1)}\left(k_0\sqrt{(x-x_0-n\Lambda)^2+(y_L)^2}\right)\cdot e^{-\imath k_X\left[x-(x_0+n\Lambda)\right]}dx\right]\cdot e^{-\imath k_X(x_0+n\Lambda)}\cdot e^{\imath n\beta\Lambda} \end{aligned} \tag{A.1.5}$$

At this point, we remind the relation between the classic 1D and 2D Green's scalar function for homogeneous media, which are solution of the following equations:

$$\begin{aligned} -\left(\frac{\partial^2}{\partial x^2}+k_X^2\right)g_{1D}(k_X,x-x') &= \delta(x-x') \\ -\left(\frac{\partial^2}{\partial x^2}+\frac{\partial^2}{\partial y^2}+k_{X,Y}^2\right)g_{2D}\left(k_{X,Y},\sqrt{(x-x')^2+(y-y')^2}\right) &= \delta(x-x')\delta(y-y') \end{aligned} \tag{A.1.6}$$

and which are given by the following expressions:

$$\begin{aligned} g_{1D}(x-x') &= -\frac{e^{\imath k_X|x-x'|}}{2\imath k_X} \\ g_{2D}(x-x') &= -\frac{\imath}{4}H_0^{(1)}\left[k_{X,Y}\sqrt{(x-x')^2+(y-y')^2}\right] \end{aligned} \tag{A.1.7}$$

The required relation is:

$$\frac{e^{i\sqrt{k_{X,Y}^2-k_Y^2}|x-x'|}}{2\imath\sqrt{k_{X,Y}^2-k_Y^2}}=\int_{\square}\frac{\imath H_0^{(1)}\left(k_{X,Y}\sqrt{\left(x-x'\right)^2+\left(y-y'\right)^2}\right)}{4}e^{-\imath k_Y\left(y-y'\right)}dy$$

$$\rightarrow\qquad -\frac{2e^{i\sqrt{k_0^2-k_X^2}|y_L|}}{\sqrt{k_0^2-k_Y^2}}=\int_{\square}H_0^{(1)}\left(k_0\sqrt{\left(x-x'\right)^2+\left(y_L\right)^2}\right)e^{-\imath k_X\left(x-x'\right)}dx \tag{A.1.8}$$

So making advantage of the last relation in (8), we write:

$$A\left(k_X\right)=\alpha\left(\theta_0,\Lambda\right)\cdot c\cdot\sum_{n=-\infty}^{+\infty}\left[\int_{\square}H_0^{(1)}\left(k_0\sqrt{\left(x-x_0-n\Lambda\right)^2+\left(y_L\right)^2}\right)\cdot e^{-\imath k_X\left[x-\left(x_0+n\Lambda\right)\right]}dx\right]\cdot e^{-\imath k_X\left(x_0+n\Lambda\right)}\cdot e^{\imath n\beta\Lambda}=$$

$$=\alpha\left(\theta_0,\Lambda\right)\cdot c\cdot\left[-\frac{2e^{i\sqrt{k_0^2-k_X^2}|y_L|}}{\sqrt{k_0^2-k_X^2}}\right]\cdot\sum_{n=-\infty}^{+\infty}e^{-\imath k_X\left(x_0+n\Lambda\right)}\cdot e^{\imath n\beta\Lambda}= \tag{A.1.9}$$

$$=\alpha\left(\theta_0,\Lambda\right)\cdot c\cdot\left[-\frac{2e^{i\sqrt{k_0^2-k_X^2}|y_L|}}{\sqrt{k_0^2-k_X^2}}\right]\cdot e^{-\imath k_X x_0}\cdot\sum_{n=-\infty}^{+\infty}e^{\imath n\Lambda\left(\beta-k_X\right)}$$

The last summatory can be reformulated taking into consideration the two alternative representations of a series of Dirac functions:

$$\sum_{m=-\infty}^{+\infty}\delta\left(x-a-mT\right)=\sum_{p=-\infty}^{+\infty}a_p\cdot e^{\imath p\frac{2\pi}{T}x},\quad a_p=\frac{1}{T}e^{-\imath p\frac{2\pi}{T}a} \tag{A.1.10}$$

Thus, we can rewrite eq.9 as follows:

$$A\left(k_X\right)=c\cdot\left[-\frac{2e^{i\sqrt{k_0^2-k_X^2}|y_L|}}{\sqrt{k_0^2-k_X^2}}\right]\cdot e^{-\imath k_X x_0}\cdot\alpha\left(\theta_0,\Lambda\right)\cdot\frac{2\pi}{\Lambda}\cdot\sum_{m=-\infty}^{+\infty}\delta\left(k_X-\beta-m\frac{2\pi}{\Lambda}\right) \tag{A.1.11}$$

Last equation shows how the scattered field's spectrum is actually a discrete spectrum, where the plane components are non-zero provided that:

$$k_X=\beta+m\frac{2\pi}{\Lambda} \tag{A.1.12}$$

which is nothing else than the Bragg's conservation law of momentum. The previous equation can be even reformulated by explicating the scattered field's angle:

$$\frac{2\pi}{\lambda}\sin\left(\theta_S\right)=\frac{2\pi}{\lambda}\sin\left(\theta_0\right)+m\frac{2\pi}{\Lambda}\qquad\rightarrow\qquad\theta_{S,n}=\arcsin\left[\sin\left(\theta_0\right)+m\frac{\lambda}{\Lambda}\right] \tag{A.1.13}$$

A.1.2 Super-chirped grating

In case of a strongly chirped grating, where the grating period is fast variable and with a saw tooth profile, the situation gets more complicated, since the x_n positions are no longer divided by a constant distance as in (1); we assume for instance that the scatterers' spatial distribution is given by:

$$x_{n,m} = x_0 + m\cdot\Lambda_1 + \frac{m(m-1)}{2}\cdot\Delta\Lambda_1 + n\cdot\Lambda_T$$
$$n,m\in\mathbb{Z}, \qquad 0\le m\le M-1, \qquad \Lambda_T = M\cdot\Lambda_1 + \frac{M(M-1)}{2}\cdot\Delta\Lambda_1 \tag{A.1.14}$$

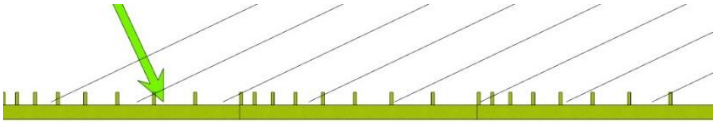

Figure A.1.2. Sequence of scatterers for the Chriped Grating configuration. In this case one can no longer assume the SPPs' complex amplitude to be constant for all the scatterers. This happens only relatively, and for all those featuring the same m-index (with the usual exception of a phase difference).

We now make a first assumption, which we assume to be a first order approximation to understand the behavior of a chirped distribution of scatterers: we shall assume that the complex amplitude α is a quite independent on the mutual distance between scatterers, and thus that it still remains constant for all of them. This last assumption is true only when the mutual distance is fixed, or in the case of inhomogeneous distributions, when the reflected plasmonic field does not impinge effectively across the scatterers. Under this hypothesis, the total scattered field in (1.5) changes as:

$$\begin{aligned}
&A(k_X) = \int_{\mathbb{R}} H_S(x,y_L)e^{-\imath k_X x}dx = \\
&= \alpha(\theta_0)\cdot c\cdot\int_{\mathbb{R}}\sum_{n=-\infty}^{+\infty}\sum_{m=0}^{M-1}\left\{H_0^{(1)}\left[k_0\sqrt{(x-x_{n,m})^2+y_L^2}\right]\cdot e^{\imath\beta x_{n,m}}\right\}\cdot e^{-\imath k_X x}dx = \\
&= \alpha(\theta_0)\cdot c\cdot\sum_{n=-\infty}^{+\infty}\sum_{m=0}^{M-1}\left[\int_{\mathbb{R}} H_0^{(1)}\left(k_0\sqrt{(x-x_{n,m})^2+y_L^2}\right)\cdot e^{-\imath k_X(x-x_{n,m})}dx\right]\cdot e^{\imath(\beta-k_X)x_{n,m}} = \\
&= c\cdot\left[-\frac{2e^{i\sqrt{k_0^2-k_X^2}|y_L|}}{\sqrt{k_0^2-k_X^2}}\right]\cdot\alpha(\theta_0)\cdot\sum_{n=-\infty}^{+\infty}\sum_{m=0}^{M-1}e^{\imath(\beta-k_X)x_{n,m}} = c\cdot\left[-\frac{2e^{i\sqrt{k_0^2-k_X^2}|y_L|}}{\sqrt{k_0^2-k_X^2}}\right]\cdot F_{\beta,M}(\theta_0,k_X)
\end{aligned} \tag{A.1.15}$$

Once again, the scattered field profile will adopt a discrete distribution in the k_X dominium, and the only non-zero component will be the ones spectrally located in positions determined by the recasting of the double summatory at the last hand side of eq.2 into a summatory of Dirac functions:

$$F_{\beta,M}(\theta_0,k_X) = \alpha(\theta_0)\cdot\sum_{n=-\infty}^{+\infty}\sum_{m=0}^{M-1}e^{\imath(\beta-k_X)x_{n,m}} = \alpha(\theta_0)\cdot\left(\sum_{n=-\infty}^{+\infty}e^{\imath(\beta-k_X)n\Lambda_T}\right)\cdot\left(\sum_{m=0}^{M-1}e^{\imath(\beta-k_X)\left[m\Lambda_1+\frac{m(m-1)}{2}\Delta\Lambda_1\right]}\right) =$$

$$= \alpha(\theta_0) \cdot \left[\frac{2\pi}{\Lambda_T} \cdot \sum_{p=-\infty}^{+\infty} \delta\left(k_X - \beta - p\frac{2\pi}{\Lambda_T} \right) \right] \cdot \left(\sum_{m=0}^{M-1} e^{\iota(\beta - k_X)\left[m\Lambda_1 + \frac{m(m-1)}{2}\Delta\Lambda_1 \right]} \right) \tag{A.1.16}$$

If the hypothesis of constant complex amplitudes is removed, the previous equation must be replaced with the following:

$$F_{\beta,M}(\theta_0, k_X) =$$

$$= \sum_{n=-\infty}^{+\infty} \sum_{m=0}^{M-1} \alpha_m(\theta_0, \Lambda_m) e^{\iota(\beta - k_X) x_{n,m}} = \left(\sum_{n=-\infty}^{+\infty} e^{\iota(\beta - k_X) n\Lambda_T} \right) \cdot \left(\sum_{m=0}^{M-1} \alpha_m(\theta_0, \Lambda_m) e^{\iota(\beta - k_X)\left[m\Lambda_1 + \frac{m(m-1)}{2}\Delta\Lambda_1 \right]} \right) =$$

$$= \left[\frac{2\pi}{\Lambda_T} \cdot \sum_{p=-\infty}^{+\infty} \delta\left(k_X - \beta - p\frac{2\pi}{\Lambda_T} \right) \right] \cdot \left(\sum_{m=0}^{M-1} \alpha_m(\theta_0, \Lambda_m) e^{\iota(\beta - k_X)\left[m\Lambda_1 + \frac{m(m-1)}{2}\Delta\Lambda_1 \right]} \right) \tag{A.1.17}$$

Before inspecting the case under investigation, we test this last more general result for the previous case of constant periodicity. Indeed, the constant Λ grating can be studied again by means of formula 4, by assuming the substitutions:

$$\Delta\Lambda_1 = 0 \qquad \Lambda_T = M \cdot \Lambda_1 \qquad \alpha_m(\theta_0, \Lambda_m) = \alpha(\theta_0, \Lambda_1) \tag{A.1.18}$$

which give:

$$F_{\beta,M}(k_X) = \alpha(\theta_0, \Lambda_1) \cdot \left[\frac{2\pi}{M\Lambda_1} \cdot \sum_{p=-\infty}^{+\infty} \delta\left(k_X - \beta - p\frac{2\pi}{M\Lambda_1} \right) \right] \cdot \sum_{m=0}^{M-1} e^{\iota(\beta - k_X)[m\Lambda_1]} =$$

$$= \alpha(\theta_0, \Lambda_1) \cdot \left[\frac{2\pi}{M\Lambda_1} \cdot \sum_{p=-\infty}^{+\infty} \delta\left(k_X - \beta - p\frac{2\pi}{M\Lambda_1} \right) \right] \cdot \frac{e^{\iota(\beta - k_X) M\Lambda_1} - 1}{e^{\iota(\beta - k_X)\Lambda_1} - 1} =$$

$$= \alpha(\theta_0, \Lambda_1) \cdot \left[\frac{2\pi}{M\Lambda_1} \cdot \sum_{p=-\infty}^{+\infty} \delta\left(k_X - \beta - p\frac{2\pi}{M\Lambda_1} \right) \cdot \frac{e^{-\iota p 2\pi} - 1}{e^{-\iota p\frac{2\pi}{M}} - 1} \right] =$$

$$= \alpha(\theta_0, \Lambda_1) \cdot \left[\frac{2\pi}{M\Lambda_1} \cdot \sum_{p=-\infty}^{+\infty} \delta\left(k_X - \beta - p\frac{2\pi}{M\Lambda_1} \right) \cdot M \cdot \delta^0_{\mathrm{mod}\left(\frac{p}{M},1\right)} \right] =$$

$$= \alpha(\theta_0, \Lambda_1) \cdot \frac{2\pi}{\Lambda_1} \cdot \sum_{n=-\infty}^{+\infty} \delta\left(k_X - \beta - n\frac{2\pi}{\Lambda_1} \right) \tag{A.1.19}$$

and the former is exactly the term also appearing in (1.11).

A.1.3 Slowly chirped grating

We start supposing that the period function has a generic dependence of the *x* position. We choose a central wavelength λ_C such that the chirped grating will focus the field across a point located at the vertical distance *h* and at the horizontal position x_f:

$$x_f = x + h \cdot \tan\left[\arcsin\left(\sin\left(\theta_{Inc}\right) - n\frac{\lambda_C}{\Lambda(x)}\right)\right] = x + h \cdot \frac{\sin\left(\theta_{Inc}\right) - n\frac{\lambda_C}{\Lambda(x)}}{\sqrt{1 - \left[\sin\left(\theta_{Inc}\right) - n\frac{\lambda_C}{\Lambda(x)}\right]^2}} \tag{A.1.20}$$

The focusing at λ_C is the same for all the x points of scattering, so x_f must not be a function of x; on behalf of this, we remind that:

$$\tan\left\{\arcsin\left[f(x)\right]\right\} = \frac{f(x)}{\left[1 - f^2(x)\right]^{\frac{1}{2}}} \quad \rightarrow \frac{d\tan\left\{\arcsin\left[f(x)\right]\right\}}{dx} = \dot{f}(x)\frac{1 + f(x) - f^2(x)}{\left[1 - f^2(x)\right]^{\frac{3}{2}}} \tag{A.1.21}$$

so we get:

$$0 = \frac{\partial x_f}{\partial x} = 1 + h \cdot n\frac{\lambda_C}{\Lambda^2(x)} \cdot \frac{\partial\Lambda(x)}{\partial x} \cdot \frac{1 + \left[\sin\left(\theta_{Inc}\right) - n\frac{\lambda_C}{\Lambda(x)}\right] - \left[\sin\left(\theta_{Inc}\right) - n\frac{\lambda_C}{\Lambda(x)}\right]^2}{\left\{1 - \left[\sin\left(\theta_{Inc}\right) - n\frac{\lambda_C}{\Lambda(x)}\right]^2\right\}^{\frac{3}{2}}} \tag{A.1.22}$$

We stress that the projected chirped grating is functional provided that the chirping is extremely slow, that is:

$$\left|\frac{\partial\Lambda\ x}{\partial x}\right| \ll 1 \tag{A.1.23}$$

To calculate the analytical expression of the grating period as a function of x is a very difficult task; thus we prefer to make explicit the period derivative as follows:

$$\frac{\partial\Lambda(x)}{\partial x} = -\frac{\Lambda^2(x)}{h \cdot n \cdot \lambda_C} \cdot \frac{\left\{1 - \left[\sin\left(\theta_{Inc}\right) - n\frac{\lambda_C}{\Lambda(x)}\right]^2\right\}^{\frac{3}{2}}}{1 + \left[\sin\left(\theta_{Inc}\right) - n\frac{\lambda_C}{\Lambda(x)}\right] - \left[\sin\left(\theta_{Inc}\right) - n\frac{\lambda_C}{\Lambda(x)}\right]^2} \tag{A.1.24}$$

and perform a recursive calculation by adopting a finite difference approach:

$$\Lambda\left(x_{k+1}\right)=\Lambda\left(x_k\right)-\Delta x_k\cdot\frac{\Lambda^2\left(x_k\right)}{h\cdot n\cdot\lambda_C}\cdot\frac{\left\{1-\left[\sin\left(\theta_{Inc}\right)-n\frac{\lambda_C}{\Lambda\left(x_k\right)}\right]^2\right\}^{\frac{3}{2}}}{1+\left[\sin\left(\theta_{Inc}\right)-n\frac{\lambda_C}{\Lambda\left(x_k\right)}\right]-\left[\sin\left(\theta_{Inc}\right)-n\frac{\lambda_C}{\Lambda\left(x_k\right)}\right]^2} \tag{A.1.25}$$

The presented form is just one possible kind of discretization of the continuous formula shown in (5); precisely, it consists in the simplest form obtained by following the direct-euler version of the finite difference approach. The calculation of the spatial function *Λ* can now proceed by numerical means and being determined after having stated the first value of the *Λ* function.

To study the behavior of this later class, we firstly calculate the integral plasmonic reflectances *R*, which in this instance are different when observed under opposite directions; SPPs impinging from left to right experience the overall reflection represented by the coefficient:

$$\begin{aligned}&R_i^{\rightarrow}=r+\frac{t^2e^{+\imath2\beta d_{i/i+1}}R_{i+1}^{\rightarrow}}{1-rR_{i+1}^{\rightarrow}e^{+\imath2\beta d_{i/i+1}}},\qquad R_{i+1}^{\rightarrow}=r+\frac{t^2e^{+\imath2\beta d_{i+1/i+2}}R_{i+2}^{\rightarrow}}{1-rR_{i+2}^{\rightarrow}e^{+\imath2\beta d_{i+1/i+2}}},\quad ....\\&\Rightarrow\qquad\Delta R_{i/i+1}^{\rightarrow}\approx+\frac{t^2e^{+\imath2\beta d_{i+1/i+2}}R_{i+1}^{\rightarrow}}{\left[1-rR_{i+1}^{\rightarrow}e^{+\imath2\beta d_{i+1/i+2}}\right]^2}\imath2\beta\Delta d_{i/i+1}\end{aligned} \tag{A.1.26a}$$

Similarly, for SPPs impinging from right to left, we have:

$$\Delta R_{i-1/i}^{\leftarrow}\approx-\frac{t^2e^{+\imath2\beta d_{i-2/i-1}}R_{i-1}^{\rightarrow}}{\left[1-rR_{i-1}^{\rightarrow}e^{+\imath2\beta d_{i-2/i-1}}\right]^2}\imath2\beta\Delta d_{i/i+1} \tag{A.1.26b}$$

If the variations of the scatterers' mutual distances are slow, we can rightfully assume that the system locally behaves as a constant distance grating, where SPPs experience the same overall reflection *R*:

$$\begin{aligned}&R=r+t^2\cdot\frac{R\cdot e^{\imath2\beta(\Lambda-W)}}{1-R\cdot r\cdot e^{\imath2\beta(\Lambda-W)}}\\&\rightarrow\qquad\left[r\cdot e^{\imath2\beta(\Lambda-W)}\right]\cdot R^2+\left[\left(t^2-r^2\right)\cdot e^{\imath2\beta(\Lambda-W)}-1\right]\cdot R+r=0\\&\rightarrow\qquad R=\frac{-\left(t^2-r^2\right)\cdot e^{\imath2\beta(\Lambda-W)}+1-\sqrt{1+\left(t^2-r^2\right)^2\cdot e^{\imath4\beta(\Lambda-W)}-2\left(t^2+r^2\right)\cdot e^{\imath2\beta(\Lambda-W)}}}{2r\cdot e^{\imath2\beta(\Lambda-W)}}\end{aligned} \tag{A.1.27}$$

with *r* and *t* being the complex plasmonic coefficients, and *W* the width of the single defect. At this point, we define two aiding functions:

$$F_R=\frac{R\cdot e^{\imath2\beta(\Lambda-W)}}{1-R^2\cdot e^{\imath2\beta(\Lambda-W)}}\quad g_R=\frac{e^{\imath\beta(\Lambda-W)}}{1-R\cdot r\cdot e^{\imath2\beta(\Lambda-W)}} \tag{A.1.28}$$

We then calculate the SPPs impinging from left(right) to right(left) at the n^{th} position due to the SPPs promoted at the k^{th} position from the left and right sides, respectively:

$$p_n^{L/R} = p_{L/R,k} \cdot \left[\left(g_R \cdot t \right)^{|n-k|} \cdot F_R \right] + p_{R/L,k} \cdot \left[R \cdot e^{\iota\beta(\Lambda - W)} \cdot \left(g_R \cdot t \right)^{|n-k|+1} \cdot F_R \right] \quad \text{(A.1.29a)}$$

Actually, the effect will be considerable just for small n-k differences, and it will be associated to a particular region of the chirped grating, where the grating period can be considered approximately constant. The overall contribution will be:

$$p_n^{L/R} = \sum_{|n-k| \square\ p} \left\{ p_{L/R,k} \cdot \left[\left(g_R \cdot t \right)^{|n-k|} \cdot F_R \right] + p_{R/L,k} \cdot \left[R \cdot e^{\iota\beta(\Lambda - W)} \cdot \left(g_R \cdot t \right)^{|n-k|+1} \cdot F_R \right] \right\} \quad \text{(A.1.29b)}$$

Considering that the SPPs excited at the *k*-th scatterer has a phase which depends on the illumination angle, we get:

$$p_n^{L/R} = \sum_{|n-k| \square\ p} \left\{ p_{L/R} \cdot \left[\left(g_R \cdot t \right)^{|n-k|} \cdot F_R \right] + p_{R/L} \cdot \left[R \cdot e^{\iota\beta(\Lambda - W)} \cdot \left(g_R \cdot t \right)^{|n-k|+1} \cdot F_R \right] \right\} \cdot e^{+\iota k_0 \sin(\theta_I)\Lambda k} \quad \text{(A.1.30)}$$

All the scatterers radiate as a function of the impinging SPPs given by the previous formula, and the emitted power will be dependent also on the observation angle:

$$\Psi_{Tot}\left(\theta_O\right) = \sum_{n=-N}^{+N} \left[p_n^L \cdot \Psi_S\left(\theta_O\right) + p_n^R \cdot \Psi_S\left(-\theta_O\right) \right] \cdot e^{+\iota\Phi_0} \cdot e^{-\iota k_0 \sin(\theta_O)\Lambda n} \quad \text{(A.1.31)}$$

A.1.4 The scattered field and secondary effects

The total reflected field is a summation of several contributions. We first proceed in expressing the back scattered field as follows:

$$S\left(\theta\right) = R_0\left(\theta_{Inc}\right) \cdot \delta\left(\theta - \theta_{Inc}\right) + S_1\left(\theta\right) + S_2\left(\theta\right) \quad \text{(A.1.32)}$$

The first contribution (R_0) refers to the specular reflection from the planar component of the structure. The second one is the first order of scattering, and is composed of two distinct contributions:

$$\begin{aligned} S\left(\theta\right) &= \sum_{n=-\infty}^{+\infty} \Psi_0\left(\theta\right) e^{+\iota\beta n\Lambda} \cdot e^{-\iota k_0 n_B n\Lambda \sin(\theta)} + \sum_{n=-\infty}^{+\infty} \Theta_n\left(\theta\right) \cdot e^{-\iota k_0 n_B n\Lambda \sin(\theta)} \\ &= \Psi_0\left(\theta\right) \cdot 2\pi \cdot \sum_{n=-\infty}^{+\infty} \delta\left[\beta\Lambda - n \cdot 2\pi - k_0 n_B \Lambda \sin\left(\theta\right) \right] + \sum_{n=-\infty}^{+\infty} \Theta_n\left(\theta\right) \cdot e^{-\iota k_0 n_B n\Lambda \sin(\theta)} \end{aligned} \quad \text{(A.1.33)}$$

The first contribution (proportional to Ψ_0) refers to the directly scattered field by a single defect:

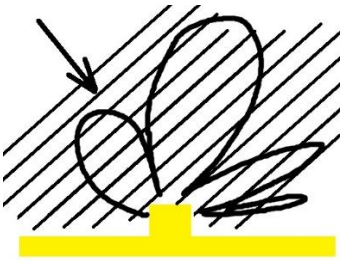

Figure A.1.3. Field scattered by a single defect after being illuminated by the input plane wave. In the text is indicated with $\Psi_0(\vartheta)$.

The second contribution arises from the multiple reflections of surface plasmons excited by the input field and traveling along the metal plateau. They cross several defects and produced other reflected and transmitted plasmons while scattering field on the outer space, till their total consumption. To evaluate these plasmons, first we must calculate the total reflectance seen by a generic plasmon impinging across a generic defect:

$$\begin{aligned} & R = r + t^2 \cdot \frac{R \cdot e^{\imath 2\beta(\Lambda - W)}}{1 - R \cdot r \cdot e^{\imath 2\beta(\Lambda - W)}} \\ \rightarrow \quad & \left[r \cdot e^{\imath 2\beta(\Lambda - W)} \right] \cdot R^2 + \left[\left(t^2 - r^2 \right) \cdot e^{\imath 2\beta(\Lambda - W)} - 1 \right] \cdot R + r = 0 \\ \rightarrow \quad & R = \frac{-\left(t^2 - r^2 \right) \cdot e^{\imath 2\beta(\Lambda - W)} + 1 - \sqrt{1 + \left(t^2 - r^2 \right)^2 \cdot e^{\imath 4\beta(\Lambda - W)} - 2\left(t^2 + r^2 \right) \cdot e^{\imath 2\beta(\Lambda - W)}}}{2r \cdot e^{\imath 2\beta(\Lambda - W)}} \end{aligned} \tag{A.1.34}$$

where *r* and *t* are the complex plasmonic coefficients, and *W* is the width of the single defect. Then we define two aiding functions:

$$F_R = \frac{R \cdot e^{\imath 2\beta(\Lambda - W)}}{1 - R^2 \cdot e^{\imath 2\beta(\Lambda - W)}} \quad g_R = \frac{e^{\imath\beta(\Lambda - W)}}{1 - R \cdot r \cdot e^{\imath 2\beta(\Lambda - W)}} \tag{A.1.35}$$

and we get:

$$p_n^{L/R} = \sum_{k=-\infty}^{+\infty} p_{L/R,k} \cdot \left[\left(g_R \cdot t \right)^{|n-k|} \cdot F_R \right] + p_{R/L,k} \cdot \left[R \cdot e^{\imath\beta(\Lambda - W)} \cdot \left(g_R \cdot t \right)^{|n-k|+1} \cdot F_R \right] \tag{A.1.36}$$

Since we have initially considered an infinite disposition of defects, the only difference among the promoted SPPs along the grating resides in the relative phase, we get:

$$\begin{aligned} p_n^{L/R} = & \; p_{L/R} \cdot F_R \cdot \sum_{k=-\infty}^{+\infty} \left(g_R \cdot t \right)^{|n-k|} \cdot e^{\left(\imath\Phi_0 + \beta\Lambda k \right)} + \\ & + p_{R/L} \cdot \left(R \cdot F_R \cdot e^{\imath\beta(\Lambda - W)} \right) \cdot \sum_{k=-\infty}^{+\infty} \left(g_R \cdot t \right)^{|n-k|+1} \cdot e^{\left(\imath\Phi_0 + \beta\Lambda k \right)} = p_0^{L/R} \cdot e^{\imath\beta T n} \end{aligned} \tag{A.1.37}$$

Finally, the field scattered by each defect will be:

$$\Theta_n(\theta) = e^{\imath\beta\Lambda \cdot n} \cdot \left[p_0^L \cdot \Theta_\beta^L(\theta) + p_0^R \cdot \Theta_\beta^R(\theta) \right] \tag{A.1.38}$$

where the Θ functions inside the square brackets in (7) represent the scattered field under plasmonic impinging from left and right, respectively. Once again, the assumption of perfectly constant grating constant Λ makes the second summatory at the last hand side in (2) reduce to a summation of Dirac's deltas.

The second–order term S_2 represents the contributions coming from second-order scattering, i.e. the scattered field after a first process of scattering; this term is not necessarily negligible, because the multiple reflections can delete (or at least weaken) a first order scattering while enhance the 2nd order, thus increasing the percentage of scattered power by this latter. Among the several components of S_2, the more prominent ones are the scattered field by each defect after the interception of the first-order scattered field by close defects, and the field scattered by multiple-reflecting plasmons promoted during the same interception. **The S_2 term is dependent on the multiple scattering process and cannot be easily calculated.**

The interception of 1st order scattered field is strongly dependent on the scatterers shape and reciprocal distance, and can be almost completely suppressed by choosing the correct class of defects; for instance, a grooved defect shows quite a null S_2 contribution for a strongly reduced angular tail of its scattering profile.

In case of terminated sequence of defects, the situation gets more complicated. First of all, the total reflectance seen by plasmons while crossing a defect is no more constant, but is dependent on the defect position, and must be calculated for each scatterer; moreover, its value is different according to the impinged side by the plasmons, thus we define the following reflection coefficients, analogue to the one in (3):

$$R_k^L \qquad R_k^R \tag{A.1.39}$$

The procedure to calculate these two quantities requires two steps, and is described in [1]. The breaking symmetry introduces more variability to the plasmon complex envelopes p introduced in (5-6), so the dependence on the position affects also the term inside the square brackets in (7) through the dependence of the p coefficients (while the standard scattering functions Θ remain the same). The values of this coefficients can be calculated again as described in ref.1.

Other than this, the interruption of the defects' line introduces a greater complication for the calculation of S_2, since this term is doubly dependent on the multiple scattering and consequently its evaluation under the assumed hypothesis becomes almost impossible.

[1] A. Benedetti · A. Veroli · C. Sibilia · F. A. Bovino, "*Numerical evaluation of irradiation diagram by plasmonic gratings and slit apertures*", JOSA B, Vol. 32, Issue 4, pp. 676-682 (2015).

A.1.5 Numerical examples

We show some profiles of the scattered field. For instance, we start with the case of a plane wave with a fixed wavelength (ranging from 400nm to 1100nm) impinging with a ϑ_I angle of incidence comprised inside the [20°-70°] range of angle across a plasmonic grating featuring a Λ=500nm period:

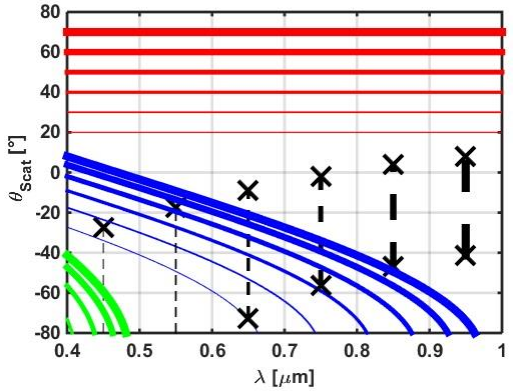

The red lines refer to the reflected (specular) 0-mode, the blue lines refer to the scattered 1-mode, and the green lines to the 2nd order of scattering; dashed segments indicate the non-superposition (monochromatic) angular zones, where only the 1-mode is present. In the following picture, we have a similar situation but with Λ=750nm:

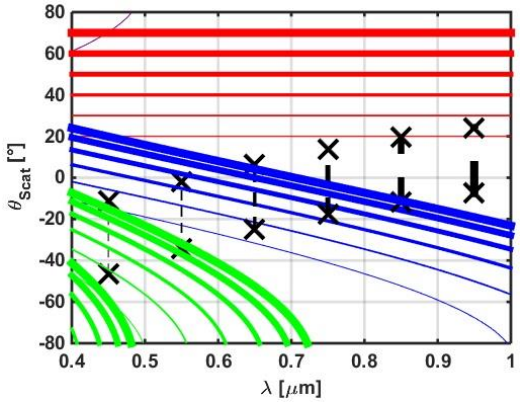

Note that here also the 3rd order of scattering appears together with the 2nd one. A -1-mode appears forward scattered.

A.2 Application of Green's Equations for the determination of the far field

A.2.1 Determination of Green's Tensor

We start from Maxwell's equation for non-magnetic materials:

$$\begin{aligned}&\vec{\nabla}\wedge\vec{E}=j\omega\mu_0\vec{H}\\&\vec{\nabla}\wedge\vec{H}=\vec{J}-j\omega\varepsilon_0\varepsilon_B\vec{E}\\&\left[\vec{E}=\vec{E}\left(\vec{r}\right),\vec{H}=\vec{H}\left(\vec{r}\right),\vec{J}=\vec{J}\left(\vec{r}\right)\right]\end{aligned}\qquad\text{(A.2.1)}$$

There are multiple combinations between the two equations; one of the most popular is:

$$\vec{\nabla}\wedge\vec{\nabla}\wedge\vec{E}-k_B^2\vec{E}=+j\omega\mu_0\vec{J}\qquad\text{(A.2.2)}$$

where $k_B^2=\frac{\omega^2}{c^2}\varepsilon_B$; by taking the divergence of the first of (A.2.1), we have:

$$\vec{\nabla}\cdot\vec{H}=0\ \rightarrow\ \vec{H}=\vec{\nabla}\wedge\vec{A}\qquad\text{(A.2.3)}$$

It should be underlined that (A.2.3) comes from the non-magneticity of the domain; again from the first of (A.2.1), we have:

$$\vec{\nabla}\wedge\left(\vec{E}-j\omega\mu_0\vec{A}\right)=0\ \rightarrow\ \vec{E}-j\omega\mu_0\vec{A}=-\vec{\nabla}V\qquad\text{(A.2.4)}$$

Vector A and scalar V are not univocally defined; from (A.2.3) we deduce that vector *A* can be defined from a vector that represents the gradient of a scalar function of the position vector:

$$\vec{A}=\vec{A_0}+\vec{\nabla}\Phi\qquad\text{(A.2.5)}$$

Scalar V can be also defined along with a scalar function:

$$\begin{aligned}&\vec{E}=+j\omega\mu_0\vec{A}-\vec{\nabla}V=+j\omega\mu_0\vec{A_0}+j\omega\mu_0\vec{\nabla}\Phi-\vec{\nabla}V=\\&=+j\omega\mu_0\vec{A_0}-\vec{\nabla}\left(V-j\omega\mu_0\Phi\right)\ \rightarrow\ V=V_0+j\omega\mu_0\Phi\end{aligned}\qquad\text{(A.2.6)}$$

So, once a scalar function Φ is chosen, rules (A.2.5) and (A.2.6) must be followed to obtain other A and V functions. If we put what we have defined in (A.2.5) and (A.2.6) inside the second of (A.2.1), we have:

$$\vec{\nabla}\wedge\vec{\nabla}\wedge\vec{A}=\vec{\nabla}\left(\vec{\nabla}\cdot\vec{A}\right)-\nabla^2\vec{A}=\vec{J}+k_B^2\vec{A}+j\omega\varepsilon_0\varepsilon_B\vec{\nabla}V$$
$$\nabla^2\vec{A}+k_B^2\vec{A}=-\vec{J}+\vec{\nabla}\left(\vec{\nabla}\cdot\vec{A}-j\omega\varepsilon_0\varepsilon_B V\right) \qquad \text{(A.2.7)}$$

We can simplify (A.2.7) by choosing:

$$\vec{\nabla}\cdot\vec{A}=j\omega\varepsilon_0\varepsilon_B V \qquad \text{(A.2.8)}$$

Condition (A.2.8) is not very restraining: if we choose a pair of A_0-V_0 that does not satisfy the condition, we can always take a function Φ that makes the condition satisfied; i.e. if we suppose:

$$\vec{\nabla}\cdot\vec{A_0}-j\omega\varepsilon_0\varepsilon_B V_0=\varphi \qquad \left[\varphi=\varphi\left(\vec{r}\right)\right] \qquad \text{(A.2.9)}$$

where obviously φ is not identically zero in the domain, then we will certainly have a Φ which verifies:

$$\vec{\nabla}\cdot\vec{A}-\nabla^2\Phi-j\omega\varepsilon_0\varepsilon_B V-k_B^2\Phi=\varphi$$
$$-\nabla^2\Phi-k_B^2\Phi+\vec{\nabla}\cdot\vec{A}-j\omega\varepsilon_0\varepsilon_B V=\varphi$$
$$-(\nabla^2\Phi+k_B^2\Phi)=\varphi\rightarrow L(\Phi)=\varphi\rightarrow\Phi(\vec{\mathrm{r}})=\int_T\varphi\left(\vec{r}\right)g\left(\vec{r}\right)d\tau \qquad \text{(A.2.10)}$$
$$g_L\left(\vec{r}\right)=\frac{e^{jk_B|\vec{r}|}}{4\pi|\vec{r}|}$$

L is defined a “deterministic problem”and $g_L(r)$ is “Green’s function”, which solves it, by [1].

So, overall, two functions A_0 and V_0 are chosen (first is vectorial the second is scalar); the (A.2.9) is calculated, and from that a function Φ is estracted, which allows to have other two values of A and V that verify condition (A.2.8) as well as what follows:

$$-\left(\nabla^2\vec{A}+k_B^2\vec{A}\right)=\vec{J}$$
$$L\left(\vec{A}\right)=\vec{J}\ \rightarrow\ A_i\left(\vec{r}\right)=\int_T J_i\left(\vec{r}\right)g_L\left(\vec{r}\right)d\tau,\quad i=x,y,z \qquad \text{(A.2.11)}$$
$$g_L\left(\vec{r}\right)=\frac{e^{jk_B|\vec{r}|}}{4\pi|\vec{r}|}$$

If we combine the base property of magnetic potential vector (A.2.4) with condition (8), we have:

$$\vec{E} = +j\omega\mu_0\vec{A} - \vec{\nabla}V = +j\omega\mu_0\vec{A} - \vec{\nabla}\frac{\vec{\nabla}\cdot\vec{A}}{j\omega\varepsilon_0\varepsilon_B} = +j\omega\mu_0\left(\overline{\overline{I}} + \frac{\vec{\nabla}\vec{\nabla}}{k_B^2}\right)\vec{A} = \left(\overline{\overline{I}} + \frac{\vec{\nabla}\vec{\nabla}}{k_B^2}\right)j\omega\mu_0\vec{A} \qquad \text{(A.2.12)}$$

This form is not satisfactory since we still have magnetic potential vector A; so, we process more by reformulating (A.2.11) as:

$$-\left(\nabla^2 + k_B^2\right)j\omega\mu_0\vec{A} = j\omega\mu_0\vec{J} \qquad \text{(A.2.13)}$$

Using (A.2.2), we can redefine the deterministic problem as:

$$\begin{cases} j\omega\mu_0\vec{J} = \vec{f}\left(\vec{r}\right) \\ j\omega\mu_0\vec{A} = \vec{A'} \end{cases} \qquad \text{(A.2.14)}$$

Thus, we have:

$$\begin{cases} \left(\vec{\nabla}\wedge\vec{\nabla}\wedge - k_B^2\overline{\overline{I}}\right)\vec{E} = \vec{f}\left(\vec{r}\right) \\ L\left(\vec{A'}\right) = \vec{f}\left(\vec{r}\right) \\ \vec{E} = \left(\overline{\overline{I}} + \frac{\vec{\nabla}\vec{\nabla}}{k_B^2}\right)\vec{A'} \end{cases} \qquad \text{(A.2.15)}$$

Now, we will consider a situation where the point source of the field is not the origin, but another point r'; so the position vectors of the fields change $r \to r - r'$, and $r \to r'$ happens for the sources. By combining the equations in (A.2.15), and remembering that g_L is the solution to the deterministic problem [], we have:

$$\begin{aligned} &\vec{E} = \left(\overline{\overline{I}} + \frac{\vec{\nabla}\vec{\nabla}}{k_B^2}\right)\int_T g_L\left(\vec{r},\vec{r'}\right)\vec{f}\left(\vec{r'}\right)d\tau' = \int_T\left[\left(\overline{\overline{I}} + \frac{\vec{\nabla}\vec{\nabla}}{k_B^2}\right)g_L\left(\vec{r},\vec{r'}\right)\right]\vec{f}\left(\vec{r'}\right)d\tau' \\ &\left(\overline{\overline{I}} + \frac{\vec{\nabla}\vec{\nabla}}{k_B^2}\right)g_L\left(\vec{r},\vec{r'}\right) = \overline{\overline{G_M}}\left(\vec{r},\vec{r'}\right) \end{aligned} \qquad \text{(A.2.16)}$$

The first equation of (A.2.16) connects the electric field to the sources *f(r')* (corresponding to the impressed currents J_{si}). As shown in (A.2.16), the relationship inside the integral can be represented by the operator $\overline{\overline{G_M}}$, called "Green's tensor".

Now we want to obtain the equivalent matrix of G_M; for simplicity, the following passages from equation (A.2.17) to equation (A.2.24) consider a point source in the origin (r'=0).

First, we have to recall the polar equivalent of the ∇ function:

$$\vec{\nabla}\frac{e^{jkr}}{4\pi r}=\left(\hat{r}\frac{\partial}{\partial r}+\frac{\theta}{r}\frac{\partial}{\partial\theta}+\frac{\varphi}{r\sin(\theta)}\frac{\partial}{\partial\varphi}\right)\frac{e^{jkr}}{4\pi r}=\hat{r}\frac{\partial}{\partial r}\left(\frac{e^{jkr}}{4\pi r}\right) \tag{A.2.17}$$

If we use it twice, the relationship becomes:

$$\vec{\nabla}\vec{\nabla}\frac{e^{jkr}}{4\pi r}=\vec{\nabla}\left[\left(jk-\frac{1}{r}\right)\frac{e^{jkr}}{4\pi r}\hat{r}\right] \tag{A.2.18}$$

In order to find a more explicit form of (A.2.18), we should use the polar relationships:

$$\begin{array}{lll}\dfrac{d\hat{r}}{dr}=0 & \dfrac{d\hat{r}}{d\theta}=\theta & \dfrac{d\hat{r}}{d\varphi}=\sin(\theta)\varphi\\ \dfrac{d\theta}{dr}=0 & \dfrac{d\theta}{d\theta}=-\hat{r} & \dfrac{d\theta}{d\varphi}=\cos(\theta)\varphi\\ \dfrac{d\varphi}{dr}=0 & \dfrac{d\varphi}{d\theta}=0 & \dfrac{d\varphi}{d\varphi}=-\hat{r}\sin(\theta)-\theta\cos(\theta)\end{array} \tag{A.2.19}$$

Gradient operator, expressed in spherical coordinates, has the vectorial expression:

$$\vec{\nabla}\{\ \}=\frac{1}{r^2\sin(\theta)}\left[\frac{d}{dr}\left(r^2\sin(\theta)\hat{r}\{\ \}\right)+\frac{d}{d\theta}\left(r\sin(\theta)\theta\{\ \}\right)+\frac{d}{d\varphi}\left(r\varphi\{\ \}\right)\right] \tag{A.2.20}$$

Inserting (18) into (20), we have:

$$\vec{\nabla}\left\{\left(jk-\frac{1}{r}\right)\frac{e^{jkr}}{4\pi r}\hat{r}\right\}=\frac{1}{r^2\sin(\theta)}\left[\frac{d}{dr}\left(r^2\sin(\theta)\hat{r}\hat{r}\left(jk-\frac{1}{r}\right)\frac{e^{jkr}}{4\pi r}\right)+\frac{d}{d\theta}\left(r\sin(\theta)\hat{\theta}\hat{r}\left(jk-\frac{1}{r}\right)\frac{e^{jkr}}{4\pi r}\right)+\frac{d}{d\varphi}\left(r\varphi\hat{r}\left(jk-\frac{1}{r}\right)\frac{e^{jkr}}{4\pi r}\right)\right]=$$

$$=\frac{1}{r^2\sin(\theta)}\left[\sin(\theta)\frac{d}{dr}\left(\hat{r}\hat{r}\left(jk-\frac{1}{r}\right)\frac{e^{jkr}r}{4\pi}\right)+\left(jk-\frac{1}{r}\right)\frac{e^{jkr}}{4\pi}\frac{d}{d\theta}\left(\sin(\theta)\theta\hat{r}\right)+\left(jk-\frac{1}{r}\right)\frac{e^{jkr}}{4\pi}\frac{d}{d\varphi}\left(\varphi\hat{r}\right)\right] \tag{A.2.21}$$

Considering what expressed in (A.2.19), formula (A.2.21) becomes:

$$\vec{\nabla}\left\{\left(jk-\frac{1}{r}\right)\frac{e^{jkr}}{4\pi r}\hat{r}\right\}=\frac{1}{r^2\sin(\theta)}\left[\sin(\theta)\hat{r}\hat{r}\left(\left(jk-\frac{1}{r}\right)\frac{e^{jkr}r}{4\pi}\left(\frac{1}{r}+jk\right)+\frac{1}{r^2}\frac{e^{jkr}r}{4\pi}\right)+\right.$$
$$\left.+\left(jk-\frac{1}{r}\right)\frac{e^{jkr}}{4\pi}\left(\cos(\theta)\theta\hat{r}-\sin(\theta)\hat{r}\hat{r}+\sin(\theta)\theta\theta\right)+\left(jk-\frac{1}{r}\right)\frac{e^{jkr}}{4\pi}\left(-\hat{r}\sin(\theta)\hat{r}-\theta\cos(\theta)\hat{r}+\varphi\sin(\theta)\varphi\right)\right]=$$
$$=\frac{1}{r^2\sin(\theta)}\left[-\sin(\theta)k^2\frac{e^{jkr}r}{4\pi}\hat{r}\hat{r}\hat{r}+\left(jk-\frac{1}{r}\right)\frac{e^{jkr}}{4\pi}\cos(\theta)\widehat{\theta r}-\sin(\theta)\left(jk-\frac{1}{r}\right)\frac{e^{jkr}}{4\pi}\hat{r}\hat{r}+\sin(\theta)\left(jk-\frac{1}{r}\right)\frac{e^{jkr}}{4\pi}\widehat{\theta\theta}+\right.$$
$$\left.-\left(jk-\frac{1}{r}\right)\sin(\theta)\frac{e^{jkr}}{4\pi}\hat{r}\hat{r}-\left(jk-\frac{1}{r}\right)\frac{e^{jkr}}{4\pi}\cos(\theta)\widehat{\theta r}+\left(jk-\frac{1}{r}\right)\frac{e^{jkr}}{4\pi}\sin(\theta)\widehat{\varphi\varphi}\right]=$$
$$=\frac{1}{r^2\sin(\theta)}\left[-\sin(\theta)k^2\frac{e^{jkr}r}{4\pi}\hat{r}\hat{r}\hat{r}+\left(jk-\frac{1}{r}\right)\frac{e^{jkr}}{4\pi}\cos(\theta)\widehat{\theta r}-\sin(\theta)\left(jk-\frac{1}{r}\right)\frac{e^{jkr}}{4\pi}\hat{r}\hat{r}+\sin(\theta)\left(jk-\frac{1}{r}\right)\frac{e^{jkr}}{4\pi}\widehat{\theta\theta}+\right.$$
$$\left.-\left(jk-\frac{1}{r}\right)\sin(\theta)\frac{e^{jkr}}{4\pi}\hat{r}\hat{r}-\left(jk-\frac{1}{r}\right)\frac{e^{jkr}}{4\pi}\cos(\theta)\widehat{\theta r}+\left(jk-\frac{1}{r}\right)\frac{e^{jkr}}{4\pi}\sin(\theta)\widehat{\varphi\varphi}\right]=$$
$$=\frac{1}{r^2\sin(\theta)}\left[-\sin(\theta)k^2\frac{e^{jkr}r}{4\pi}\hat{r}\hat{r}\hat{r}-2\left(jk-\frac{1}{r}\right)\sin(\theta)\frac{e^{jkr}}{4\pi}\hat{r}\hat{r}+\sin(\theta)\left(jk-\frac{1}{r}\right)\frac{e^{jkr}}{4\pi}\widehat{\theta\theta}+\right.$$
$$\left.+\left(jk-\frac{1}{r}\right)\frac{e^{jkr}}{4\pi}\sin(\theta)\widehat{\varphi\varphi}\right]=$$
$$=\frac{1}{r^2}\left[-k^2\frac{e^{jkr}r}{4\pi}\hat{r}\hat{r}\hat{r}-3\left(jk-\frac{1}{r}\right)\frac{e^{jkr}}{4\pi}\hat{r}\hat{r}+\left(jk-\frac{1}{r}\right)\frac{e^{jkr}}{4\pi}\hat{r}\hat{r}+\left(jk-\frac{1}{r}\right)\frac{e^{jkr}}{4\pi}\widehat{\theta\theta}+\left(jk-\frac{1}{r}\right)\frac{e^{jkr}}{4\pi}\widehat{\varphi\varphi}\right]=$$
$$=\left(jk-\frac{1}{r}\right)\frac{e^{jkr}}{4\pi r^2}\bar{\bar{I}}-\left(k^2\frac{e^{jkr}}{4\pi r}+3\left(jk-\frac{1}{r}\right)\frac{e^{jkr}}{4\pi r^2}\right)\hat{r}\hat{r} \qquad \text{(A.2.22)}$$

If we insert the result in (A.2.22) into the expression in (A.2.16), we can easily find that:

$$\bar{\bar{G}}=\frac{e^{jkr}}{4\pi r}\bar{\bar{I}}+\frac{1}{k^2}\left[\left(jk-\frac{1}{r}\right)\frac{e^{jkr}}{4\pi r^2}\bar{\bar{I}}-\left(k^2\frac{e^{jkr}}{4\pi r}+3\left(jk-\frac{1}{r}\right)\frac{e^{jkr}}{4\pi r^2}\right)\hat{r}\hat{r}\right]=$$
$$=\bar{\bar{I}}\frac{e^{jkr}}{4\pi r}+\left(\frac{jkr-1}{k^2r^2}\right)\frac{e^{jkr}}{4\pi r}\bar{\bar{I}}+\frac{\left(-k^2-\frac{3jkr-3}{r^2}\right)}{k^2}\hat{r}\hat{r}\frac{e^{jkr}}{4\pi r}= \qquad \text{(A.2.23)}$$
$$=\left[\bar{\bar{I}}+\left(\frac{jkr-1}{k^2r^2}\right)\bar{\bar{I}}+\frac{3-3jkr-k^2r^2}{k^2r^2}\hat{r}\hat{r}\right]\frac{e^{jkr}}{4\pi r}$$

From which we can finally define Green's 3D tensor:

$$\bar{\bar{G}}=\left[\bar{\bar{I}}+\left(\frac{jkr-1}{k^2r^2}\right)\bar{\bar{I}}+\frac{3-3jkr-k^2r^2}{k^2r^4}\vec{r}\vec{r}\right]\frac{e^{jkr}}{4\pi r} \qquad \text{(A.2.24)}$$

Again, if the sources are not in the origin (r'≠0), the equations would be:

$$\bar{\bar{G}}=\left[\bar{\bar{I}}+\frac{jkR-1}{k^2R^2}\bar{\bar{I}}+\frac{3-3ik_BR-k_B^2R^2}{k_B^2R^4}RR\right]\frac{e^{(ik_BR)}}{4\pi R} \qquad \text{(A.2.25)}$$

where ***r=|R|=|r-r'|*** is the relative distance between the source and the observing point.

Formula (A.2.25) is useful to obtain the field profile in 3 dimensions when there is a point source. In our situation, we have a 2 dimensional simulation, and the corresponding source has a linear distribution of points. In this situation, it is necessary to use 2D Green tensor, which can be developed in Fourier space [2], or be deduced from the 2D Green's function [1,3],

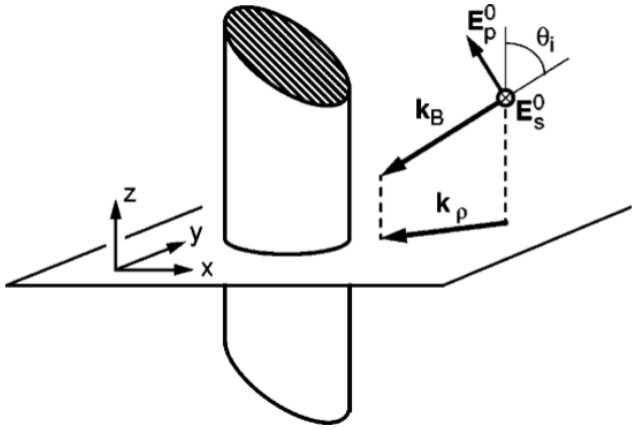

$$g_{2D}^{B}(r,r') = \frac{i}{4}H_0(k_\rho\rho)e^{ik_z z} \tag{A.2.26}$$

Where $\rho = (x-x', y-y')$, K_ρ is the is the propagation vector projected on the plane, Kz is the propagation vector on the axis not present in the plane, and H_i is the Henkel function of the first kind $H_i^{(1)}$ [4].

The elements of the matrix are harder to obtain analytically, so here we will focus on the situation when the incident field is inside the xy plane $K_B=K_\rho$[2,3]:

$$G^B(\rho,\rho') = \begin{pmatrix} G_{xx}^B & G_{xy}^B & 0 \\ G_{xy}^B & G_{yy}^B & 0 \\ 0 & 0 & G_{zz}^B \end{pmatrix} \tag{A.2.27}$$

$$G_{xx}^B(\rho,\rho') = \frac{i}{4}sin^2(\theta)H_0\left(k_\rho\rho\right) + \frac{i}{4}\frac{\cos(2\theta)}{k_B\rho}H_1\left(k_\rho\rho\right) \tag{A.2.28}$$

$$G_{xy}^B(\rho,\rho') = \frac{i}{4}\frac{\sin(2\theta)}{2}H_2\left(k_\rho\rho\right) \tag{A.2.29}$$

$$G_{yy}^B(\rho,\rho') = \frac{i}{4}cos^2(\theta)H_0\left(k_\rho\rho\right) - \frac{i}{4}\frac{\cos(2\theta)}{k_B\rho}H_1\left(k_\rho\rho\right) \tag{A.2.30}$$

$$G_{zz}^{B}(\rho,\rho') = \frac{i}{4} H_0\left(k_\rho \rho\right) \tag{A.2.31}$$

Relations (A.2.27-31) can be used to solve the first of (A.2.16) in order to find the local field from a linear source J_{si}. But in our present situation we have field E and H "sampled" in the simulation from a line, while we need the impressed currents as a source to use in (A.2.16); in the following section, I describe the method I used to define an "equivalent impressed current".

A.2.2 Solution through equivalent impressed current from field distribution in a monitor window

The inhomogeneous distribution of field can be obtained by a superposition of surface distributions of electric and magnetic currents. The combination of these two kinds of emitters grants the perfect replacement of the incoming field with equivalent sources; they can be evaluated with ease by considering the interior region replaced by perfect vacuum, with no scatterers and internal field, and the exterior coinciding with the real external region; so the boundary conditions are [1]:

$$\begin{aligned} n \wedge \left(\overrightarrow{E^+} - \overrightarrow{E^-}\right) &= -\overrightarrow{k_m} = n \wedge \overrightarrow{E_0} \\ n \wedge \left(\overrightarrow{H^+} - \overrightarrow{H^-}\right) &= +\overrightarrow{k_e} = n \wedge \overrightarrow{H_0} \end{aligned} \tag{A.2.32}$$

The surface current densities must be converted properly into volume current densities by means of the dirac function:

$$\begin{aligned} \overrightarrow{J_e}\left(\vec{r}\right) &= \overrightarrow{k_e}\left(\vec{r_\partial}\right) \cdot \delta\left(\vec{r} - \vec{r_\partial}\right) \\ \overrightarrow{J_m}\left(\vec{r}\right) &= \overrightarrow{k_m}\left(\vec{r_\partial}\right) \cdot \delta\left(\vec{r} - \vec{r_\partial}\right) \end{aligned} \tag{A.2.33}$$

Now we must incorporate these terms inside the Helmholtz vector equation, and consequently inside the Green's formula:

$$\begin{cases}\vec{\nabla}\wedge\vec{E}=-\vec{J_m}+\iota\omega\mu_0\vec{H}\\ \vec{\nabla}\wedge\vec{H}=+\vec{J_e}-\iota\omega\varepsilon_0\vec{E}\end{cases}\rightarrow\begin{cases}\vec{\nabla}\wedge\vec{E_1}=\iota\omega\mu_0\vec{H_1}\\ \vec{\nabla}\wedge\vec{H_1}=+\vec{J_e}-\iota\omega\varepsilon_0\vec{E_1}\end{cases}+\begin{cases}\vec{\nabla}\wedge\vec{E_2}=-\vec{J_m}+\iota\omega\mu_0\vec{H_2}\\ \vec{\nabla}\wedge\vec{H_2}=-\iota\omega\varepsilon_0\vec{E_2}\end{cases} \tag{A.2.34}$$

Since the first contribution is composed by an electric source, we already know its solution (A.2.16); for the sake of simplicity we will jump directly to the second one. In this case, we could again solve the problem taking into consideration the electric field:

$$\begin{aligned}&\vec{\nabla}\wedge\vec{\nabla}\wedge\vec{E_2}=-\vec{\nabla}\wedge\vec{J_m}+\iota\omega\mu_0\vec{\nabla}\wedge\vec{H_2}=-\vec{\nabla}\wedge\vec{J_m}+\iota\omega\mu_0\left(-\iota\omega\varepsilon_0\vec{E_2}\right)=+k_0^2\vec{E_2}-\vec{\nabla}\wedge\vec{J_m}\\ &\rightarrow\quad\vec{\nabla}\wedge\vec{\nabla}\wedge\vec{E_2}-k_0^2\vec{E_2}=-\vec{\nabla}\wedge\vec{J_m}\\ &\rightarrow\vec{E_2}=-\int_{V'}\overline{\overline{G}}\left(\vec{r}-\vec{r}'\right)\square\vec{\nabla}'\wedge\vec{J_m}\left(\vec{r}'\right)d\tau'=-\int_{V'}\left[\left(\overline{\overline{I}}+\frac{\vec{\nabla}\vec{\nabla}}{k_0^2}\right)g\left(\vec{r}-\vec{r}'\right)\right]\square\vec{\nabla}'\wedge\vec{J_m}\left(\vec{r}'\right)d\tau'\end{aligned} \tag{A.2.35}$$

Alternatively, it is more convenient to proceed by considering the magnetic field as the primary one, then evaluating the electric field from its solution:

$$\begin{aligned}&\vec{\nabla}\wedge\vec{\nabla}\wedge\vec{H_2}=-\iota\omega\varepsilon_0\vec{\nabla}\wedge\vec{E_2}=+\iota\omega\varepsilon_0\vec{J_m}-\iota\omega\varepsilon_0\left(+\iota\omega\mu_0\vec{H_2}\right)=+k_0^2\vec{H_2}+\iota\omega\varepsilon_0\vec{J_m}\\ &\rightarrow\quad\vec{\nabla}\wedge\vec{\nabla}\wedge\vec{H_2}-k_0^2\vec{H_2}=+\iota\omega\varepsilon_0\vec{J_m}\\ &\rightarrow\vec{H_2}=+\iota\omega\varepsilon_0\int_{V'}\overline{\overline{G}}\left(\vec{r}-\vec{r}'\right)\square\vec{J_m}\left(\vec{r}'\right)d\tau'=+\iota\omega\varepsilon_0\int_{V'}\left[\left(\overline{\overline{I}}+\frac{\vec{\nabla}\vec{\nabla}}{k_0^2}\right)g\left(\vec{r}-\vec{r}'\right)\right]\square\vec{J_m}\left(\vec{r}'\right)d\tau'\\ &\rightarrow\vec{E_2}=\frac{\vec{\nabla}\wedge\vec{H_2}}{-\iota\omega\varepsilon_0}=-\vec{\nabla}\wedge\int_{V'}\left[\left(\overline{\overline{I}}+\frac{\vec{\nabla}\vec{\nabla}}{k_0^2}\right)g\left(\vec{r}-\vec{r}'\right)\right]\square\vec{J_m}\left(\vec{r}'\right)d\tau'=-\int_{V'}\vec{\nabla}g\left(\vec{r}-\vec{r}'\right)\wedge\vec{J_m}\left(\vec{r}'\right)d\tau'=\\ &=-\int_{V'}\left[\vec{\nabla}g\left(\vec{r}-\vec{r}'\right)\wedge\overline{\overline{I}}\right]\square\vec{J_m}\left(\vec{r}'\right)d\tau'\end{aligned} \tag{A.2.36}$$

So the final expression of the electric field is the sum between (A.2.16) and the result of (A.2.5):

$$\begin{aligned}&\vec{E_1}+\vec{E_2}=+\iota\omega\mu_0\int_{V'}\overline{\overline{G}}\left(\vec{r}-\vec{r}'\right)\cdot\vec{J_e}\left(\vec{r}'\right)d\tau'-\int_{V'}\left[\vec{\nabla}g\left(\vec{r}-\vec{r}'\right)\wedge\overline{\overline{I}}\right]\cdot\vec{J_m}\left(\vec{r}'\right)d\tau'=\\ &=+\iota\omega\mu_0\int_{S'}\overline{\overline{G}}\left(\vec{r}-\vec{r}'\right)\cdot\vec{k_e}\left(\vec{r}'\right)dS'-\int_{S'}\left[\vec{\nabla}g\left(\vec{r}-\vec{r}'\right)\wedge\overline{\overline{I}}\right]\cdot\vec{k_m}\left(\vec{r}'\right)dS'=\\ &=+\iota\omega\mu_0\int_{S'}\overline{\overline{G}}\left(\vec{r}-\vec{r}'\right)\cdot\left[n\wedge\vec{H_0}\right]dS'+\int_{S'}\left[\vec{\nabla}g\left(\vec{r}-\vec{r}'\right)\wedge\overline{\overline{I}}\right]\cdot\left[n\wedge\vec{E_0}\right]dS'\end{aligned} \tag{A.2.37}$$

A.2 References

[1] G.Gerosa, P.Lampariello, “Lezioni di campi elettromagnetici Ed.II”, Edizioni Ingegneria 2000, chapter 9 (2006)

[2] A. Castaiux, C. Girard, A. Dereux, O. J. F. Martin, and J.P. Vigneron, “Electrodynamics in complex systems: Application to near-field probing of optical microresonators”, Phys. Rev. E 54, 5752 (1996)

[3] O.J.F.Martin, “Electromagnetic scattering in polarizable backgrounds”, Phis.Rev.E, 58, 3, 3909-3915 (1998)

[4] A. D. Yaghjian, “Electric Dyadic Green‘s Functions in the Source Region”, Proc. IEEE, 68, 248 (1980)

A.3 Nano-sieve filter for microfluidic sensing on lab-on-chip

With technologies acquired in the assemblage of the gold grating, in particular with the features of the EBL instrument, it is possible to realize a wide range of different devices. In this subsection is reported how is possible to produce a polyimide sieve for biomedical applications in microfluidic systems.

During last years we have assisted to an increasing interest on the integration of opto-electronic and mechanical devices in lab-on-chip systems for biomolecular detection [1, 2]and analysis of cell culture behavior [3, 4]. An important task is to operate an efficient mechanical separation of the suspended particulate of a biological material in order to simplify its study and characterization; from this point of view we have studied a new fabrication method to produce a **polyimide-based nano-sieve** for biomedical applications in microfluidic systems.

We have chosen the polyimide for different reasons: it is lightweight, flexible, resistant either to heat and chemicals and it can form stable bonds with most of metals. It is traditionally used as stress buffer/passivation layer over semiconductor circuitry and now It is having extensive use in MEMS applications.

For the design of the nano-sieve it was decided to start with an orthogonally alterned groove patterns (fig. 1).

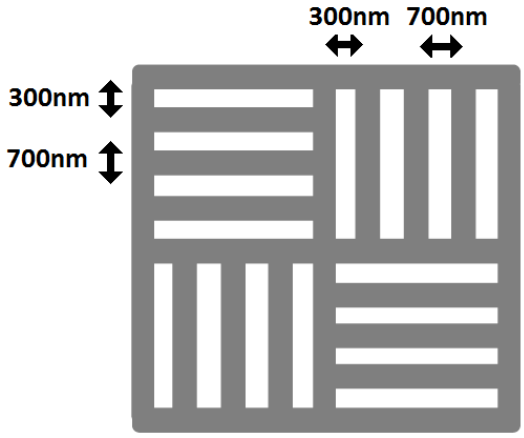

Figure 1. Schematic 2D vision of the design used for the polyimide nano-sieve: the width of the lines is 300nm spaced 700nm.

The width of the stripe lines is 300nm spaced 700nm and the thickness of the polyimide is 6µm; so, the device turns out to have an high aspect ratio (1:20). Therefore the following fabrication method can be replicated implementing various

geometries (keeping the same aspect ratio) in order to sifting different kinds of suspended cells/particulate.

In fig. 2 is reported the fabrication process flow for the device:

I. Oxidized silicon substrate.

II. Deposition of a 6 µm-thick polyimide film by spin-coating on the silicon substrate and curing in a vacuum oven.

III. Vacuum evaporation of a 40 nm- thick Al film.

IV. Spin coating of a 600 nm-thick PMMA e-resist layer.

V. Electron Beam Lithography (Area Dose = 500 µC/cm^2) to imprint the nano-sieve geometry on the PMMA film.

VI. Pattern definition on the Al film by wet etching.

VII. Pattern imprinting on the polyimide film by Reactive Ion Etching (RIE).

VIII. Peeling of the **nano-sieve** from the substrate.

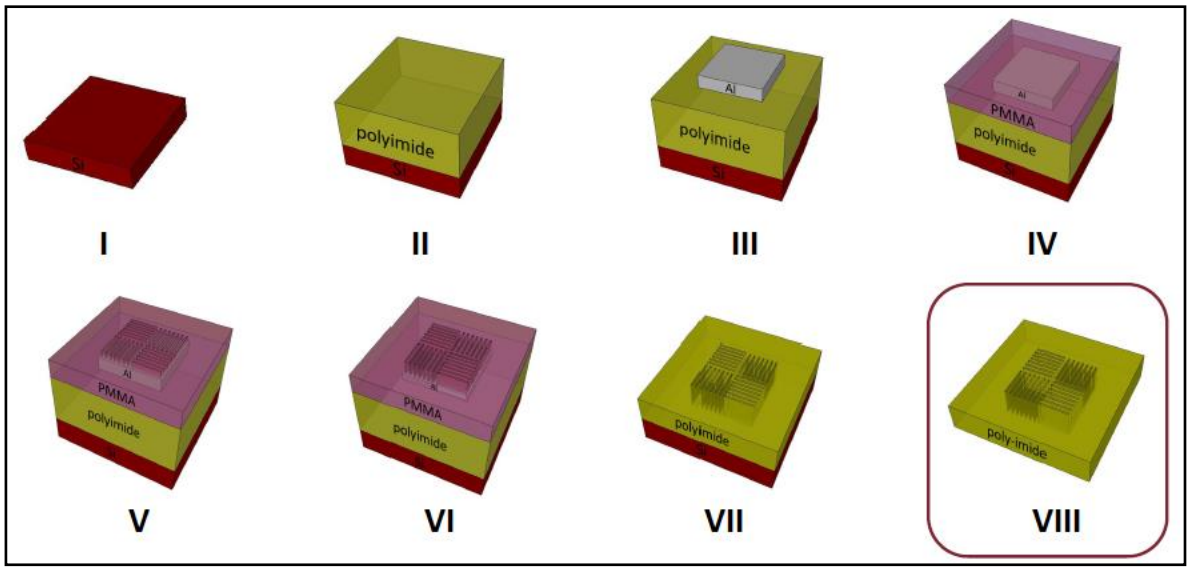

Figure 2: 3D schematic view of the fabrication process flow of the polyimide nano-sieve.

The device, successfully manufactured is shown in fig. 3.

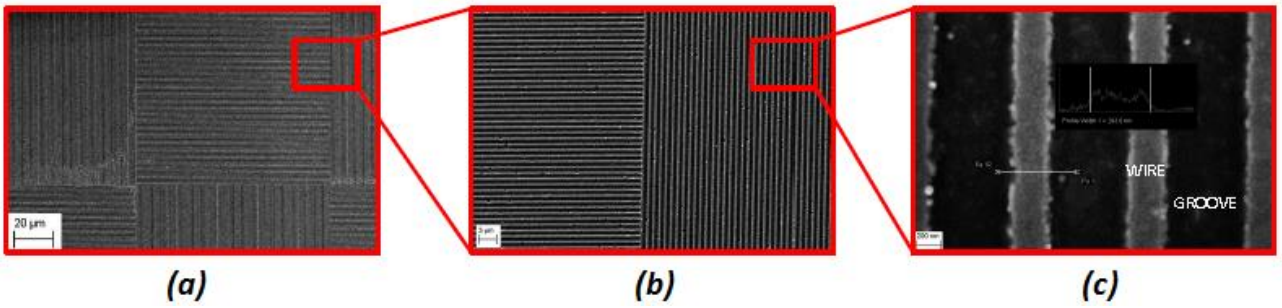

Figure 3. The SEM images of a general view of the device is zoomed in to inspect the geometry details: *(a)*geometry overview; *(b)*orthogonal grooves pattern; *(c)* polyimide wires (300 nm wide) and grooves (700 nm wide).

From the results it is clear that the fabrication procedure for manufacturing nano-sieve devices is correct, reaching an aspect ratio of **1:20**. The polyimide structure will be implemented in a more complex microfluidic networks to analyse biological material in lab-on-a-chip systems.

A.3 References

[1] D. Caputo, et al. "Lab-on-glass system for DNA analysis using thin and thick film technologies."MRS Proceedings. Vol. 1191. Cambridge University Press, 2009.
[2] B. Alam, Et al. "Analysis on vertical directional couplers with long range surface plasmons for multilayer optical routing."Journal of Applied Physics120.8 (2016).
[3] F. Frezza, Et al. “In silico validation procedure for cell volume fraction estimation through dielectric spectroscopy”. Journal of biological physics, vol. 41(3), 223-234, (2015).
[4] M. Muzi, Et al, “Hierarchical in silico validation procedure for biomass estimation techniques based on dielectric spectroscopy”, Proceedings of: XX RINEM, September 10th-14th, 2014, Padua, Italy.

A.4 Supplementary Information of: Precise detection of circular dichroism in a cluster of nano-helices by photoacoustic measurements.

A.4.1 Permittivity function of the filament composing the helix, and helices' layer spectral properties.

In order to perform all the 3D simulations of the helixes, we firstly needed to know the internal filament refractive index spectrum. We managed this stage by means of an effective refractive index approach.

The effective refractive indexes employed in the simulations take into account the filament internal composition already described in Ref.[1]. The filament is composed of large clusters of tiny Pt and Ga spheroids located inside a homogeneous amorphous carbon host environment. The Pt and Ga inclusions' percentages are estimated to be around 55% and 5%, approximatively, with the reaming part of volume occupied by the host C. The large average diameter of the spheroids (ranging from 6 to 12nm both for Pt and Ga) suggests that setting the canonical refractive indexes spectra is still a good assumption and that an evaluation of the e.m. properties by means of an effective medium approximation seemed to be possible, so we enclosed a random arrangement of spheroids in a large FDTD box with periodic boundary conditions (PBC) and illuminated this system with a plane wave with normal incidence (as shown in fig. S1).

A sufficiently large extension is set to suppress any spurious reflection coming from the opposite termination of the FDTD box, and a monitor collects the complex values of reflected field for the wavelengths of interest (approximately [0.3 μm -1.6 μm]). After some numerical passages, we retrieved the reflection coefficients of the overall compounds, and we finally calculated the required refractive indexes by taking advantage of the following formula:

$$n(\lambda) = n_{Host}(\lambda) \cdot \frac{1 - r(\lambda)}{1 + r(\lambda)}$$

where n_{Host} is the host refractive index and r the complex reflection coefficient.

where n_{Host} is the host (air) refractive index and r the complex reflection coefficient.

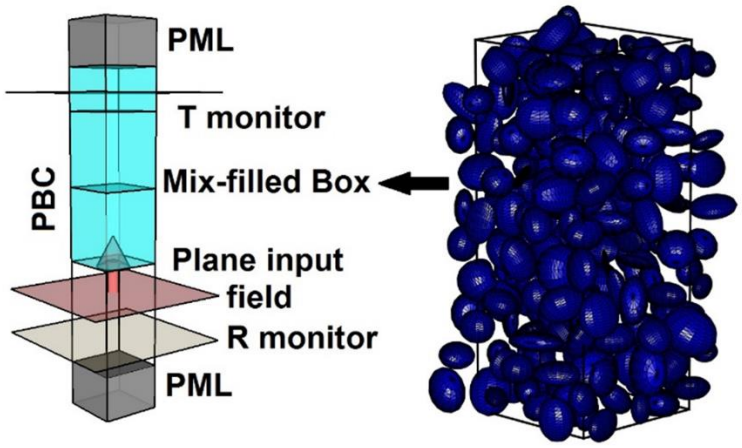

Figure S1. On the left, schematic view of the entire FDTD system. A linearly polarized plane wave vertically directed toward the top impinges on stacked boxes filled with the mixture. An example of mixture is displayed on the right, with a 40x40x100nm box filled by the inclusions, and whose background index is set to the carbons. The spheroids in the picture feature an average diameter of 8nm, and they randomly cover 30% of the total volume.

The Pt, Ga and C spectra used for this purpose are shown in the top line of fig.S2. Thanks to the numerical calculations, we obtained the final index spectrum shown in the bottom graph of fig.S2. The final mixture presents a strong metal character, which suggests the presence of surface plasmon polaritons along the helixes' bodies when they are illuminated.

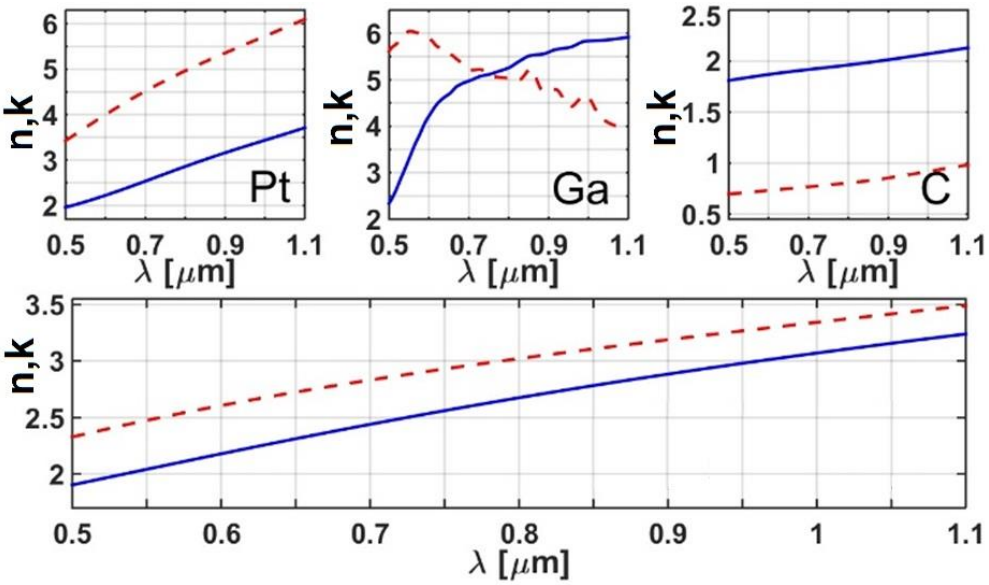

Figure S2. (Above) the dispersion spectra adopted for the 3 materials and (below) the resulting dispersion adopted for the filament's material, calculated with the random cluster simulation technique. Real indexes are plotted in blue straight lines, while red dashed lines refer to imaginary indexes.

We adopted a similar procedure to calculate the effective phase index for a virtual layer composed of helices floating in the vacuum. We calculated the complex reflection and transmission coefficients of the

helixes layer and, together with the assumption of an effective thickness of 950nm, we calculated the effective refractive index of an equivalent homogeneous slab layer [2], whose profile we show in fig. S3.

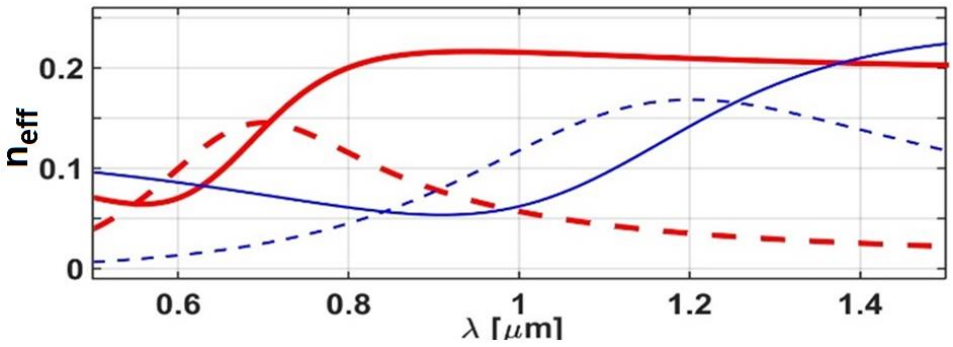

Figure S3. Effective refractive index spectra for the opposite sense of polarization. Straight (dotted) lines refer to the real (imaginary) part. Red-thick (blue-thin) lines refer to the right (left) circular polarization.

The spectra are different for the two signs of circular polarization. Indeed, these indexes correspond to relative permittivities which present the typical Drude-Lorentz resonant profile:

$$n^{L/R}(\omega)=\sqrt{\varepsilon_r^{L/R}(\omega)}=\sqrt{\varepsilon_\infty-\frac{\left(\omega_P^{L/R}\right)^2}{\omega^2-\left(\omega_0^{L/R}\right)^2-\imath\omega\gamma^{L/R}}} \tag{5}$$

with *L* and *R* indicating the left and right circular polarization, and ε_r the relative permittivity. Good fit parameter values are ε_∞ =0.12, $\omega^L{}_P$=4.9415·10^{14}, $\omega^R{}_P$=8.0667·10^{14}, $\omega^L{}_0$=17.4707·10^{14}, $\omega^R{}_0$=28.5203·10^{14}, γ^L=8.1772·10^{14}, γ^R=15.5254·10^{14}. Consequently, the helices appear to resonate approximately at 261THz and 441THz under normal plane incidence with left and right circular polarization, respectively.

The simulations for the absorption spectra have included also the presence of the substrate, which is composed of a multilayered structure (see fig.1). The refractive index spectra adopted for the 4 involved materials are summarized in the plots of fig.S4. We used dispersions retrieved from Barker & Ilegems (ordinary axis, 1973) [3] for the GaN layer, from Pastrňák & Roskovcová (ordinary axis, 1966) [4] for the AlN layer, from Malitson &Dodge (synthetic sapphire, ordinary axis, 1972) [5] for the Al_2O_3 substrate, and our own measurements for the Al0.3Ga0.7N.

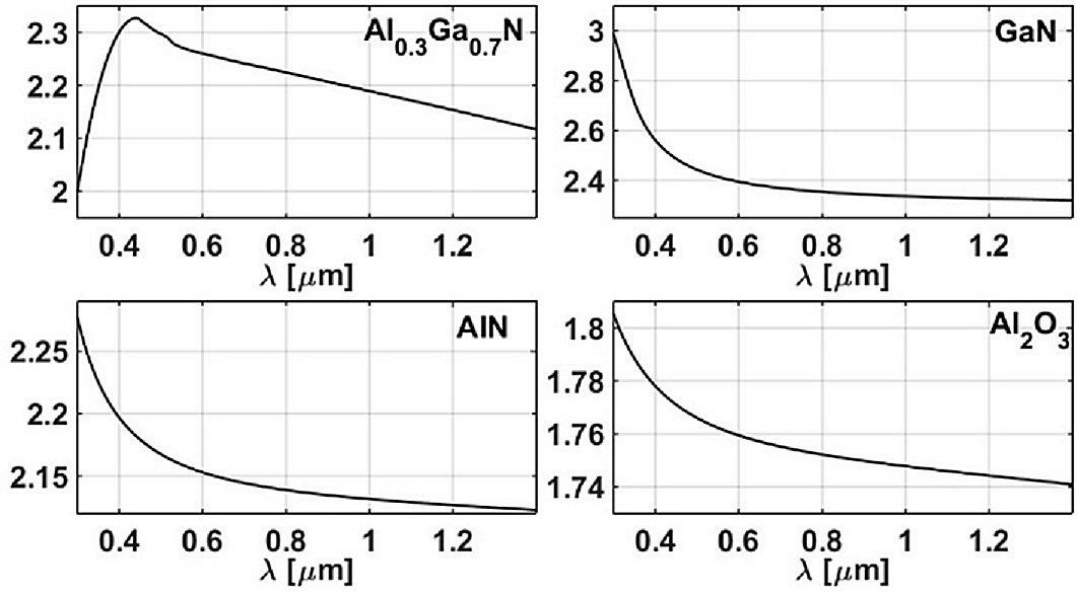

Figure S4. Refractive index spectra for the four materials compounding the multilayered substrate. The materials are perfectly lossless in the observed wavelength region. See fig.1 for the substrate internal structure.

A.4.2 Crossing point shifts and anisotropy effects.

Small anisotropies on the experiment naturally leads to spurious dichroism that sums up with the real intrinsic dichroic character of the helices' ensemble; these anisotropies are both related to the helices [6] and the hosting substrate. These secondary dichroism leads to a weak shift of few nanometers for the two circular polarization absorption crossing point (i.e., the wavelength at which the total dichroism is null), and at analytical level to the break of proportionality between the CD related to transmittance (CD_T), on one hand, and the CD related to absorbance (CD_A), on the other hand.

Indeed, we know that under ideal conditions, CD_T and CD_A must be proportional (with a dispersive coefficient):

$$CD_A = 2\frac{A_R - A_L}{A_R + A_L} = 2\frac{T_L - T_R}{2\cdot(1-R)-(T_R+T_L)} = -CD_T \cdot \frac{1}{\frac{2\cdot(1-R)}{T_R+T_L}-1} = -CD_T \cdot \frac{1}{\frac{1-R}{T_{Lin}}-1} = -CD_T \cdot \frac{T_{Lin}}{A_{Lin}} \quad (6)$$

where R is the common reflectance for the two polarizations [2], where A_{Lin} and T_{Lin} refer to the absorbed and transmitted spectra under linear polarization. In presence of anisotropies, the incidence (and consequent partial absorption) of a left/right circular polarization gives rise also to the transmission of polarizations with opposite circular sign:

$$CD_A = 2\frac{A_R - A_L}{A_R + A_L} \approx 2\frac{T_L - T_R + T_{R,L} - T_{L,R}}{2\cdot(1-R)-(T_R+T_L)} = \left(-CD_T + \frac{T_{R,L} - T_{L,R}}{T_{Lin}}\right)\cdot\frac{1}{\frac{1-R}{T_{Lin}}-1} \tag{7}$$

with $T_{R,L}$ ($T_{L,R}$) being the transmittance of right (left) circular polarization promoted by the incidence of left (right) circular input field.

A.4.3 Diffraction effects in Circular Dichroism.

The diffraction properties of light naturally contribute to deform the CD detected in transmission and to a second shift of the crossing point along the spectrum. To better explain this fact, we take advantage of a scalar approach and to the paraxial approximation to characterize the output field observed across the central axis (x'=0 & y'=0) beneath the helices at different heights as the superposition of two distinct contributions, one coming from the vertical stack of helices and substrate, and one coming from the naked substrate. Assuming that no anisotropies take place in this instance, and approximating the input field to an infinite plane wave, this output field is estimated to be:

$$\begin{aligned} E_O(z) \approx E_I \cdot \Bigg\{ t_{H+S}(\omega)\cdot\left[e^{i\kappa_0 z}\cdot\iint_{S_H} e^{+i\frac{\kappa_0}{2z}\left(x'^2+y'^2\right)}dx'dy' \right] + \\ + \left[t_S(\omega)\cdot e^{i\kappa_0 z}\cdot\iint_{R^2,S_H} e^{+i\frac{\kappa_0}{2z}\left(x'^2+y'^2\right)}dx'dy' \right]\Bigg\} = E_I\cdot\left[c_1(\omega,z)\cdot t_{H+S}(\omega)+c_2(\omega,z)\right] \end{aligned} \tag{8a}$$

where E_I is the input electric field, S_H is the sample surface covered by helices, R^2-S_H is remaining unpatterned surface, and c_1 and c_2 are:

$$\begin{aligned} c_1(\omega,z) &= e^{i\kappa_0 z}\cdot\iint_{S_H} e^{+i\frac{\kappa_0}{2z}\left(x'^2+y'^2\right)}dx'dy' \\ c_2(\omega,z) &= t_S(\omega)\cdot e^{i\kappa_0 z}\cdot\iint_{R^2,S_H} e^{+i\frac{\kappa_0}{2z}\left(x'^2+y'^2\right)}dx'dy' \end{aligned} \tag{8b}$$

Consequently, the transmitted intensity will be:

$$\begin{aligned} \Pi_O(z) = \frac{|E_O(z)|^2}{2\zeta_0} \approx \frac{|E_I(z)|^2}{2\zeta_0}\cdot\left|c_1(\omega,z)\cdot t_{H+S}(\omega)+c_2(\omega,z)\right|^2 = \\ = \Pi_I\cdot\left|c_1(\omega,z)\cdot t_{H+S}(\omega)+c_2(\omega,z)\right|^2 \end{aligned} \tag{9}$$

So the transmittance will be a dispersive, z-dependent function:

$$T(\omega,z)=\frac{\Pi_O(z)}{\Pi_I}\approx\left|c_1(\omega,z)\cdot t_{H+S}(\omega)\right|^2+2\cdot\mathrm{Re}\left[c_1(\omega,z)\cdot c_2^*(\omega,z)\cdot t_{H+S}(\omega)\right]+\left|c_2(\omega,z)\right|^2=$$
$$=\left|c_1(\omega,z)\right|^2\cdot T_{H+S}(\omega)+2\cdot\mathrm{Re}\left[c_1(\omega,z)\cdot c_2^*(\omega,z)\cdot e^{i\Phi_{t_{H+S}}(\omega)}\right]\cdot\left|t_{H+S}(\omega)\right|+\left|c_2(\omega,z)\right|^2= \quad (10)$$
$$=\alpha(\omega)\cdot T_{H+S}(\omega)+\beta(\omega,z)\cdot\sqrt{T_{H+S}(\omega)}+\gamma(\omega,z)$$

having actuated the following replacements:

$$\alpha(\omega)=\left|c_1(\omega,z)\right|^2=\left|e^{i\kappa_0 z}\cdot\iint_{S_H}e^{+i\frac{\kappa_0}{2z}\left(x'^2+y'^2\right)}dx'dy'\right|^2$$
$$\beta(\omega,z)=2\cdot\mathrm{Re}\left[c_1(\omega,z)\cdot c_2^*(\omega,z)\cdot e^{i\Phi_{t_{H+S}}(\omega)}\right] \quad (11)$$
$$\gamma(\omega,z)=\left|c_2(\omega,z)\right|^2=\left|t_S(\omega)\cdot e^{i\kappa_0 z}\cdot\iint_{\square^2,S_H}e^{+i\frac{\kappa_0}{2z}\left(x'^2+y'^2\right)}dx'dy'\right|^2$$

Among *β* and *γ*, which represent the spurious contribution to the exact transmittance which is related only to the region of superposition of helices and substrate, the coefficient *γ* appears to be stronger and more influent to the increasing difference among CD_T and CD_A. Indeed, considering eq.(10a), we have:

$$CD_T=\frac{\alpha(\omega)\cdot\left[T_{H+S,Right}(\omega)-T_{H+S,Left}(\omega)\right]+\beta(\omega,z)\cdot\left[\sqrt{T_{H+S,Right}(\omega)}-\sqrt{T_{H+S,Left}(\omega)}\right]}{\alpha(\omega)\cdot\frac{T_{H+S,Right}(\omega)+T_{H+S,Left}(\omega)}{2}+\beta(\omega,z)\cdot\frac{\sqrt{T_{H+S,Right}(\omega)}+\sqrt{T_{H+S,Left}(\omega)}}{2}+\gamma(\omega,z)}=$$

$$=\frac{CD_{T,H+S}+\dfrac{\beta(\omega,z)\cdot\left[\sqrt{T_{H+S,Right}(\omega)}-\sqrt{T_{H+S,Left}(\omega)}\right]}{\alpha(\omega)\cdot\dfrac{T_{H+S,Right}(\omega)+T_{H+S,Left}(\omega)}{2}}}{1+\dfrac{\beta(\omega,z)\cdot\dfrac{\sqrt{T_{H+S,Right}(\omega)}+\sqrt{T_{H+S,Left}(\omega)}}{2}+\gamma(\omega,z)}{\alpha(\omega)\cdot\dfrac{T_{H+S,Right}(\omega)+T_{H+S,Left}(\omega)}{2}}} \quad (12)$$

and considering eq.6 we shall have:

$$CD_T=\frac{-CD_{A,H+S}\cdot\left(\dfrac{1-R_{H+S}}{\dfrac{T_{H+S,Right}(\omega)+T_{H+S,Left}(\omega)}{2}}-1\right)+\dfrac{\beta(\omega,z)\cdot\left[\sqrt{T_{H+S,Right}(\omega)}-\sqrt{T_{H+S,Left}(\omega)}\right]}{\alpha(\omega)\cdot\dfrac{T_{H+S,Right}(\omega)+T_{H+S,Left}(\omega)}{2}}}{1+\dfrac{\beta(\omega,z)\cdot\dfrac{\sqrt{T_{H+S,Right}(\omega)}+\sqrt{T_{H+S,Left}(\omega)}}{2}+\gamma(\omega,z)}{\alpha(\omega)\cdot\dfrac{T_{H+S,Right}(\omega)+T_{H+S,Left}(\omega)}{2}}} \quad (13)$$

The presence of the coefficients β and γ in the denominator at the right-hand side of eq.13 leads to an evident reduction of the measured CD_T values. Eq.6 explains also why any crossing point of absorption-related CD should be the same of transmittance-related CD (excluding anisotropies

described In previous section), since the convergence of the two CP transmittances to a common value deletes both the term in the numerator at the last member of eq.13 and CD_T, thus implying the annihilation of CD_A.

A.4.4 Dichroic character dependence on illumination direction.

A second set of measurements, performed reversing the studied sample, revealed a certain dependence of the CD spectrum on the direction of illumination. We show the collective experimental data set in figure S5.

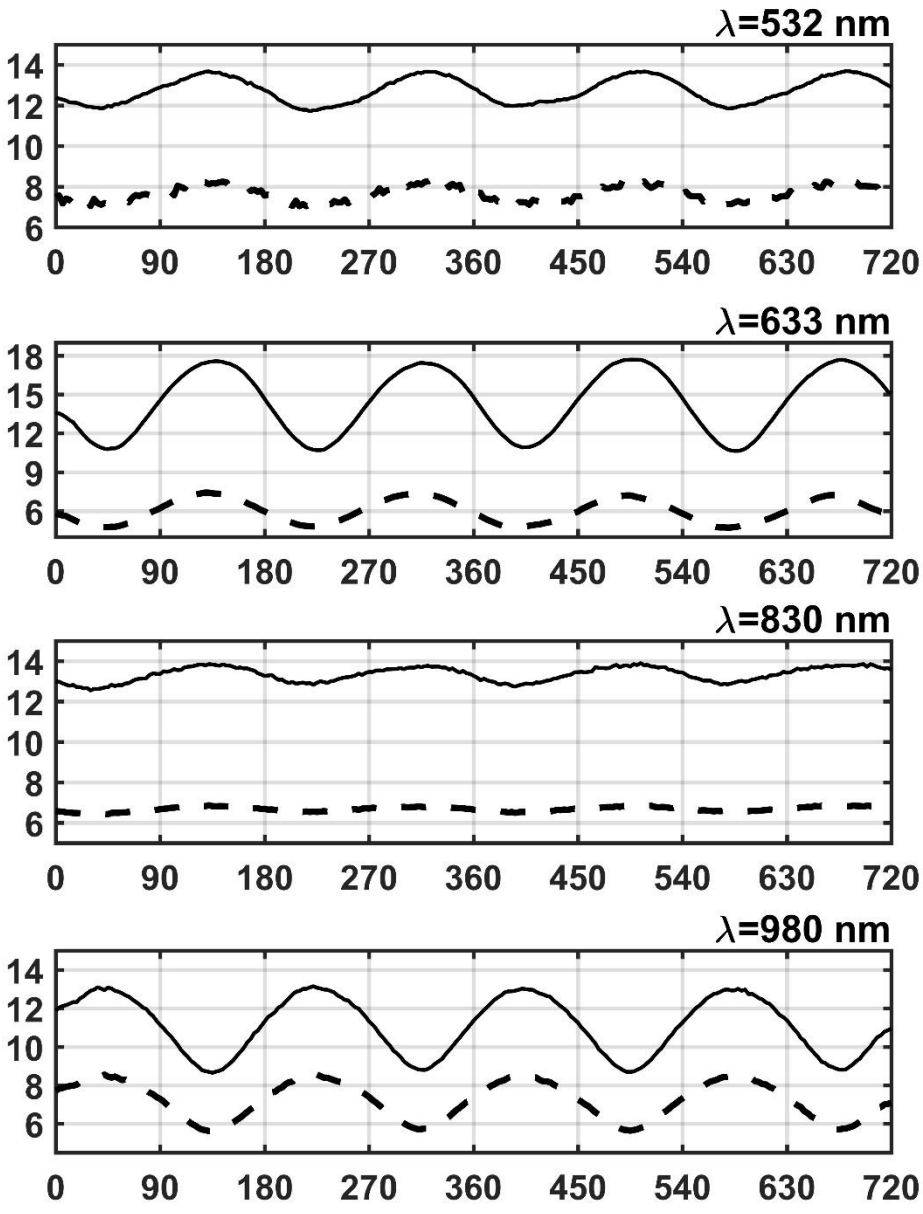

Figure S5. Acoustic signal as a function of the quarter wave phase plate for the 4 investigated wavelengths under upward and downward illumination, plotted in straight and dashed lines, respectively. The upward set of experimental data is the same plotted also on the main publication.

Despite showing extremely similar values, there were small percentage differences in the CD spectra (less than 10%) for the two sets of data related to the downward and upward illumination. These differences can be related to substrate effects on the measurements rather than real systematic errors, and in order to better understand this last effect, we performed a further simulation changing position and illumination direction of the source plane in the numerical setup.

To understand the origins of this discrepancy, we start stating that the absorption of two counterpropagating waves in a lossy layer is given by:

$$A = \varepsilon_0 \int_H \left\{ \int_S \mathrm{Im}\left[\varepsilon_r\left(\vec{r}\right)\right] \cdot \left\| \overrightarrow{E^{\uparrow}}\left(\vec{r}\right) e^{+\imath\beta_1 z} + \overrightarrow{E^{\downarrow}}\left(\vec{r}\right) e^{-\imath\beta_2 z} \right\|^2 dS \right\} dz =$$

$$= \varepsilon_0 \int_H \left\{ \int_S \mathrm{Im}\left[\varepsilon_r\left(\vec{r}\right)\right] \cdot \left[\left\| \overrightarrow{E^{\uparrow}}\left(\vec{r}\right) \right\|^2 e^{-2\mathrm{Im}(\beta_1)z} + \left\| \overrightarrow{E^{\downarrow}}\left(\vec{r}\right) \right\|^2 e^{+2\mathrm{Im}[\beta_2]z} \right] dS \right\} dz +$$

$$+ \varepsilon_0 \int_H \left\{ \int_S \mathrm{Im}\left[\varepsilon_r\left(\vec{r}\right)\right] \cdot \left[2\,\mathrm{Im}\left[\overrightarrow{E^{\uparrow}}\left(\vec{r}\right) \overrightarrow{E^{\downarrow *}}\left(\vec{r}\right) e^{+\imath\left(\beta_1 + \beta_2^*\right) z} \right] \right] dS \right\} dz \approx$$

$$\approx \varepsilon_0 \int_H \left\{ \int_S \mathrm{Im}\left[\varepsilon_r\left(\vec{r}\right)\right] \cdot \left[\left\| \overrightarrow{E^{\uparrow}}\left(\vec{r}\right) \right\|^2 e^{-2\mathrm{Im}(\beta_1)z} + \left\| \overrightarrow{E^{\downarrow}}\left(\vec{r}\right) \right\|^2 e^{+2\mathrm{Im}[\beta_2]z} \right] dS \right\} dz = A^{\uparrow} + A^{\downarrow} \tag{14}$$

with S and H being the surface and thickness of the lossy volume. Assuming that two counterpropagating waves are travelling along the helices layer, we calculate the absorption for downward and upward illumination truncating this process after the first reflection step:

$$A^{\downarrow}_{R/L} \approx A_{H,R/L} + \left(1 - A_{H,R/L} - R_H\right) \cdot \frac{R_{S,\downarrow}}{\left|1 - r_{S,\downarrow} r_H\right|^2} \cdot A_{H,L/R} \approx A_{H,R/L} + \left(1 - A_{H,R/L} - R_H\right) \cdot R_{S,\downarrow} \cdot A_{H,L/R} \tag{15a}$$

$$A^{\uparrow}_{R/L} \approx \frac{1 - R_{S,\uparrow}}{\left|1 - r_{S,\uparrow} r_H\right|^2} A_{H,R/L} \approx \left(1 - R_{S,\uparrow}\right) \cdot A_{H,R/L} \tag{15b}$$

where now *H* refers to coefficients consistent with a pure helices' layer inserted into a vacuum host, and *S* refers to the pure (lossless) substrate. The pedices *R/L* refer to left and right circular polarization, respectively, while the arrows indicating the input illumination direction. Lower *r* and upper *R* refer to complex reflection coefficient and reflectance, respectively. We have introduced the $|1-r_S{*}r_H|^2$ factor to include the effect of multiple reflections between the helices' layer and the substrate, although in the following we will neglect it for the sake of simplicity; indeed, this coefficient is extremely close to 1 and it would just give rise to negligible 2nd order effects. In addition to this, we will neglect scattered modes associated to wavelengths smaller than the horizontal *Λ*

step of the helices' array. The helices' reflection spectra is non-dichroic, since dichroic effects appear only across transmitted fields [2].

The CD of absorption under downward illumination is:

$$CD_A^{\downarrow} = 2\frac{A_R^{\downarrow} - A_L^{\downarrow}}{A_R^{\downarrow} + A_L^{\downarrow}} \approx 2\frac{\left(A_{H,R} - A_{H,L}\right)\cdot\left(1 - R_{S,\downarrow} + R_H \cdot R_{S,u}\right)}{\left(A_{H,R} + A_{H,L}\right)\left(1 + \left(1 - R_H\right)\cdot R_{S,\downarrow}\right) - 2A_{H,R}\cdot R_{S,\downarrow}\cdot A_{H,L}} = \\ = CD_{A,H}\frac{1 - \left(1 - R_H\right)\cdot R_{S,\downarrow}}{1 + \left(1 - R_H\right)\cdot R_{S,\downarrow} - 2\cdot R_{S,\downarrow}\cdot\dfrac{A_{H,R}\cdot A_{H,L}}{A_{H,R} + A_{H,L}}} \tag{16}$$

while the one for upward illumination is:

$$CD_A^{\uparrow} \approx 2\frac{A_R^{\uparrow} - A_L^{\uparrow}}{A_R^{\uparrow} + A_L^{\uparrow}} = CD_{A,H} \tag{17}$$

Finally, the ratio between these CD expressions is:

$$\frac{CD_A^{\downarrow}}{CD_A^{\uparrow}} \approx \frac{1 - \left(1 - R_H\right)\cdot R_{S,\downarrow}}{1 + \left(1 - R_H\right)\cdot R_{S,\downarrow} - 2\cdot R_{S,\downarrow}\cdot\dfrac{A_{H,R}\cdot A_{H,L}}{A_{H,R} + A_{H,L}}} \tag{18}$$

In the following we show the reflection and dichroic absorption spectra of the helices layer, and the reflection spectra of the pure substrate under downward illumination. This latter is calculated neglecting multiple reflections internal to the Al_2O_3 layer, since usually they are not consistent with thick etalons like the Al_2O_3 bottom layer. Thus, the reflectance is calculated as:

$$R_{S,\downarrow} \approx R_{Multilayer} \tag{19}$$

The resulting spectrum of the CD_A ratio defined in (18) is plotted in figure S6.

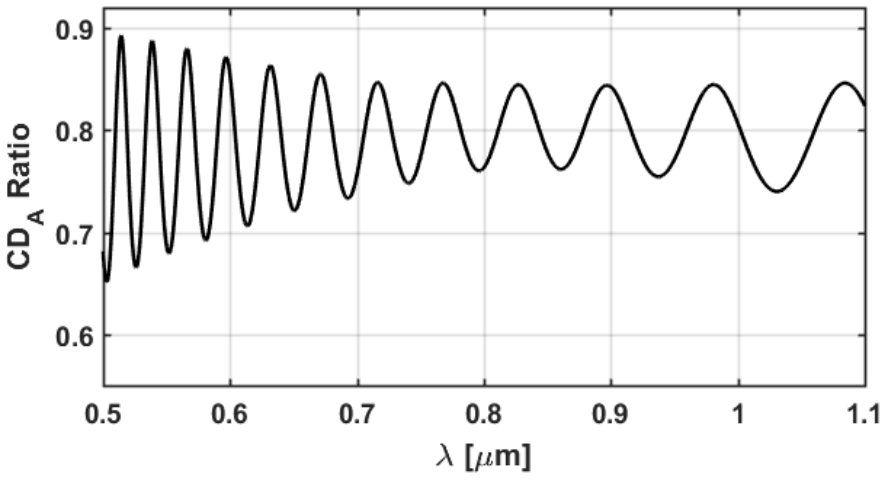

Figure S6. CD_A ratio spectrum. The average value is almost perfectly constant (0.79) along the entire observed spectrum, with oscillations due to the etalon effect of the GaN layer in the substrate.

To confirm our speculations, we performed also a second simulations' stage setting simultaneously 3 different cases of illuminations: downward illumination, upward illumination and the case of absent substrate (having the helix quite similar terminations, there is no need to make distinctions between illumination sides on this last case). Random variations to the helix geometrical parameters and an averaging procedure has been again applied as done in the main simulation stage.

Looking at figure S7, we see that the upward and vacuum CD_A profiles are quite similar each other, with upward CD_A appearing slightly stronger then downward CD_A, consistently with the prediction of the theory.

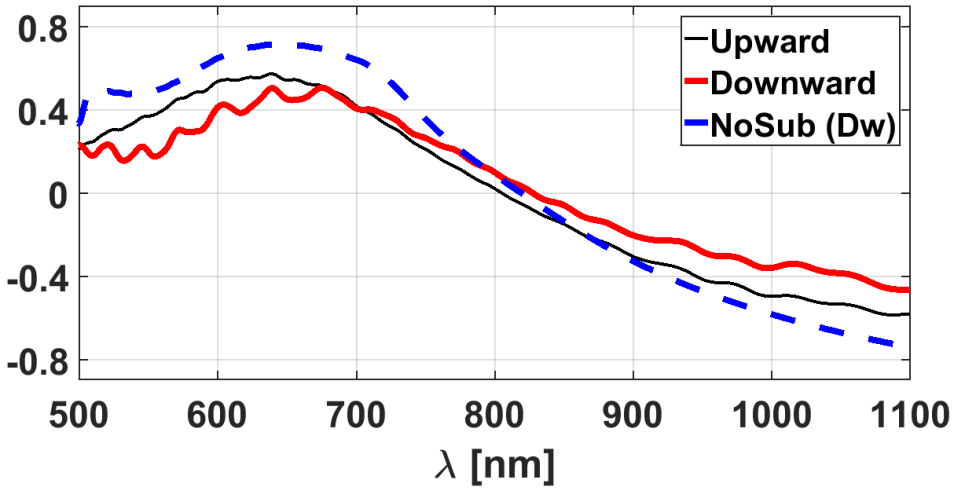

Figure S7. CD_A ratio spectrum for 3 different cases of illumination. The downward illumination case is evidently more affected by the etalon effects. Among the 2 cases where the substrate is involved, the upward illumination one is the closest to the no-substrate case in the range λ>~750nm (where scattered modes are perfectly absent).

The ratio between the 2 variants of CD_A is roughly 80% above the crossing region approximately located at λ~810nm. Below this wavelength (especially below 700nm, which is the array horizontal lattice period), diffraction orders start to affect the internal scattering process, and the overall response progressively diverges from the one of a homogeneous layer. See also the major spectral modulation of downward CD_A with respect to the upward and vacuum variant, consistently with the modulation of the CD_A-ratio function as defined in (18).

Other than this, we see that theoretically vacuum CD_A should be similar to the upward variant, but numerically the former appears to be slightly stronger than the latter. This can be explained by considering again that in our previous derivation we neglected superior diffraction orders (excited at wavelengths lower than the array lattice period); this difference is potentially

enhanced by surface plasmon excitation internal to the helices layer; more precisely, this latter effect is weakened or strengthened according to the field localization and to the phase relations taking place inside the meta-structure [7].

Other differences are mainly due to the large set of random variations of geometrical parameters during the simulation stage which we performed to simulate the fabrication tolerances; the meaning of this step was to average the electromagnetic properties but added certain modifications on the final CD spectra.

A.4.5 References

1. Esposito, M. et al. Programmable Extreme Chirality in the Visible by Helix-Shaped Metamaterial Platform, *Nano Lett.* **16**, 9, 5823–5828 (2016)
2. Castanié, A., Mercier, J.-F., Félix, S., Maurel, A., Generalized method for retrieving effective parameters of anisotropic metamaterials, *Opt. Expr.* **22**, 24, 29937-29953 (2014)
3. Barker, A. S. Jr.; Ilegems, M. Infrared Lattice Vibrations and Free-Electron Dispersion in GaN, *Phys. Rev. B* **7**, 2, 743-750 (1973)
4. Pastrňák, J.; Roskovcová, L. "Refraction Index Measurements on AlN Single Crystals, *Phys. Stat. Sol.* **14**, 1, K5-K8 (1996)
5. Malitson, I. H.; Dodge, M. Refractive Index and Birefringence of Synthetic Sapphire, *J. Opt. Soc. Am.* **62**, 1405 (1972)
6. Esposito, M. et al. Triple-helical nanowires by tomographic rotatory growth for chiral photonics, *Nat. Comm.* **6**, 6484 (2015)
7. Tuccio, S.; Centini, M.; Benedetti, A.; Sibilia, C., *Jour. of Opt. Soc. Am. B* **30**, 2, pp.450-455 (2013)